2019

Computational Study of Neuronal Oscillations In Motor Control Circuits

Ferrario, Andrea

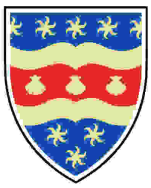

UNIVERSITY OF
PLYMOUTH

Computational Study of Neuronal Oscillations In Motor Control Circuits

by

Andrea Ferrario

A thesis submitted to the University of Plymouth
in partial fulfilment for the degree of

DOCTOR OF PHILOSOPHY

School of Computing, Electronics and Mathematics

April 2019

Acknowledgements

I am deeply grateful to my supervisor and mentor Roman Borisyuk, for introducing me to the fascinating world of mathematical neuroscience and dynamical systems. Thank you Roman for giving me the opportunity to start this doctorate and for your constant motivation and help throughout these past years. Many thanks also go to my second supervisor and friend Bob Merrison-Hort: thank you for teaching me many programming skills and for our thought provoking discussions. I also thank Roman's wife Galina, Bob's wife Jenny and their children Andrew and Laura for making me feel like a part of their families, which made my time in Plymouth most enjoyable.

Special thanks go to all the collaborators working on the tadpole project, and especially to Alan Roberts, Steve Soffe, Stella Koustikou, Edgar Buhl, and Wenchang Li. It has been a pleasure to work alongside such talented, enthusiastic and friendly researchers. I am grateful to all of you for sharing your knowledge and for our interesting project meetings, which aided me greatly in my research. I would also like to thank my examiners, Professors Sue Denham and Krasimira Tsaneva-Atanasova, for their useful corrections and for their positive comments on this manuscript.

Many thanks go to the many friends met in Plymouth, who made my past three years pleasant and motivated me to complete this doctorate. I will start with three people I consider as brothers: Riccardo, Massimiliano and Valerio, but also to Vincenzo, Luca Stirnimann, Salvatore, Luca Surace, Giovanni Carmantini, Frank, Ilaria, Martina, Emmanuel, Vittoria, Mario, Pat, the Cangelosi family, Daniel, Jacek, Luca, Giovanni Nicolazzo, Damien, Felice, Joe, Matt, Marie, Benita, Giuseppe, Liam and Eva. Special thanks go also to my best "Italian" friends: Luo, Geno, Rana, Mitch, Pie and Steti.

I also thank my family: my parents, Marco and Carla, my sister Maria, my brother Pietro, his wife Anna and my nephews Guglielmo and Alberto. Your support, kindness and love have helped me to live this experience away from home and to never discourage. Without each one of you I simply would have not been able to complete this doctorate.

Lastly, I want to thank the love of my life, Hannah. Without your love and patience I would have never been able to maintain my mental sanity and complete this work.

Abstract

In this thesis we used mathematical and computational models to study neuronal networks that control motor behaviours. Specifically, we modelled two neuronal circuits from two opposite ends of the brain complexity spectrum: the swimming circuit of the hatchling *Xenopus* tadpole and the human basal ganglia.

Due to its relative simplicity, tadpole is a unique animal for studying locomotion using both experiments and models. This allowed us to define three biologically-realistic spiking models to clarify the interplay between the architecture of synaptic connections (structure) and the network's ability to generate activities that correspond to its swimming behaviour (function).

First, we investigated how the structural variability of individual circuits produces similar behaviours. To answer this question, we defined a probabilistic model of connectivity and dynamics for the neurons in the spinal cord. Simulations of the model showed that the swimming behaviours generated by different connectivities are remarkably similar. We used graph theory measures to characterise structural properties of networks underlying swimming. For example, we applied them to (1) predict the swimming period and (2) detect key neurons and connections that promote the swimming rhythm.

Second, we built a minimal model of the central pattern generator (CPG) which reproduces all the experimentally recorded oscillatory regimes: swimming and synchrony - anti-phase and in-phase oscillations between two body sides, respectively. Using bifurcation theory, we defined stabilities for these regimes and demonstrated the existence of bi-stablity for a physiological range of parameters. Considering a vicinity of the critical parameter values of a saddle-node bifurcation, we explained how long-lasting synchrony transitions can appear both in model and experiment.

Third, we expanded our CPG model by adding three sensory pathways. Our modelling is based on available anatomical and physiological data and on our new probabilistic approach for modelling connections. The expanded model contains approximately 1700 neurons and about 100,000 connections. The model reproduces the experimentally recorded neuronal activities during the initiation, acceleration, continuation, modulation and termination of locomotion. Therefore, it can describe the complete swimming behaviour of the tadpole in response to sensory inputs.

Inspired by our study of oscillations and synchronisation in the tadpole nervous system, we proposed a theoretical model of action selection in the basal ganglia. We use a mathematical formalism known as Arnold tongues to explain how modulatory inputs from the cortex can partially synchronise subsets of neurons in the basal ganglia and generate a rhythmic action. This mechanism can explain how the transitions between multiple oscillatory states might work, thus effectively resolving the switching between competing actions. Although theoretical, the model could serve as a qualitative tool to understand the basic working principles of action selection. For example, model simulations match experimental recordings in rodents showing that the cortex can synchronise neurons in the basal ganglia and generate Arnold tongues synchronisation.

Authors declaration

At no time during the registration for the degree of Doctor of Philosophy has the author been registered for any other University award without prior agreement of the Doctoral College Quality Sub-Committee.

Work submitted for this research degree at the University of Plymouth has not formed part of any other degree either at the University of Plymouth or at another establishment.

This study was financed with the aid of a studentship from Plymouth University. Some of the work presented in this thesis was funded by the BBSRC.

Relevant scientific seminars and conferences were regularly attended at which work was often presented. Two papers have been accepted for publication in refereed journals.

Word count for the main body of this thesis: **56890**

Signed: _____

Date: _____

Journal Publications:

Ferrario, A., Merrison-Hort, R., Soffe, S. R., Li, W. C., & Borisyuk, R. *Bifurcations of Limit Cycles in a Reduced Model of the Xenopus Tadpole Central Pattern Generator.* The Journal of Mathematical Neuroscience 2018, 8(1), 10.
DOI: https://doi.org/10.1186/s13408-018-0065-9

Ferrario, A., Merrison-Hort, R., Soffe, S. R., & Borisyuk, R. *Structural and functional properties of a probabilistic model of neuronal connectivity in a simple locomotor network.* eLife 2018, 7: e33281.
DOI: https://doi.org/10.7554/eLife.33281.001

Koutsikou, S., Merrison-Hort, R., Buhl, E., Ferrario, A., Li, W. C., Borisyuk, R., Soffe,S. R., & Roberts, A. *A simple decision to move in response to touch reveals basic sensory memory and mechanisms for variable response times.* The Journal of Physiology 2018.

DOI: https://doi.org/10.1113/JP276356

Book Chapter:

Merrison-Hort, R., Yousif, N., Ferrario, A., & Borisyuk, R. *Oscillatory Neural Models of the Basal Ganglia for Action Selection in Healthy and Parkinsonian Cases.* In Computational Neurology and Psychiatry Springer, Cham, 2017. p. 149-189. DOI: https://doi.org/10.1007/978-3-319-49959-8_7

Oral Conference Presentations:

"An action selection mechanism driven by partial synchronization in a computational model of the basal ganglia", with Robert Merrison-Hort and Roman Borisyuk. Presented at the 2nd ICMNS (International Conference of Mathematical Neuroscience, Antibes), France, June 2016

"A Probabilistic Model of Neuronal Connectivity in the Xenopus Tadpole Spinal Cord: Network Properties and Functionality", with Robert Merrison-Hort and Roman Borisyuk. Presented at the 3rd ICMNS, Boulder, USA, May 2017

Poster Conference Presentations:

"Graph properties of Xenopus Tadpole's connectome", with Roman Borisyuk and Robert Merrison-Hort. Presented at:

- 25th CNS (Computational Neuroscience) Meeting, Jeju, Korea, July 2016
- APRIL (Applications of Personal Robotics for Interaction and Learning) summer school, Cefalu, Italy, July 2016

"Structural Properties of a Probabilistic Model of Neuronal Connectivity in a Simple Vertebrate Animal", with Robert Merrison-Hort and Roman Borisyuk. In collaboration with Alan Roberts and Steve Soffe. Presented at the SfN (Society for Neuroscience) Conference, Washington DC, USA, November 2017

"Bifurcation Analysis of a Central Pattern Generator Microcircuit in the Xenopus Tadpole Spinal Cord", with Roman Borisyuk and Robert Merrison-Hort. Presented at:

- SIAM (Society for Applied and Industrial Mathematics) conference in dynamical systems, Snowbird, USA, July 2017
- ISN (Integrated Systems Neuroscience) workshop, Manchester, UK, September 2017

"A computational model of sensory pathway integration and motor decision making in the Xenopus tadpole", with Roman Borisyuk, Stella Koutsikou, Wen-Chang Li, Robert Merrison-Hort, Steve Soffe and Alan Roberts. Presented at the SfN Conference, San Diego, USA, November 2018

List of Abbreviations

EEG - Electroencephalograms

LFP - Local field potentials

dIN - Descending excitatory interneuron

cIN - Commissural inhibitory interneuron

aIN - Ascending inhibitory interneuron

dlc - Dorsolateral commissural neuron

dla - Dorsolateral ascending neuron

RB - Rohon beard neuron

CPG - Central pattern generator

MZ - Marginal zone

DT - Dorsal tract

GPi - Internal part of the globus pallidus

STN - Subthalamic nucleus

PD - Parkinson disease

BG - Basal ganglia

NMDA - N-methyl-D-aspartate

AMPA - α-amino-3-hydroxy-5-methyl-4-isoxazolepropionic acid

NBQX - quinoxaline derivative, 2,3-dihydroxy-6-nitro-7-sulfamoylbenzo quinoxaline

PIR - post inhibitory rebound

SyC - Synchrony limit cycle

SwC - Swimming limit cycle

2-SyC - Double-period synchrony limit cycle

LP - Fold of limit cycles

PD - Period-doubling bifurcation

PFK - Pitchfork bifurcation

TR - Neimark-Sacker bifurcation

LPD - Fold-flip bifurcation

VT - Virtual tadpole

Contents

List of Figures

Chapter 1

Introduction

This thesis is devoted to the study of neuronal mechanisms underlying oscillations in motor circuits. Animals and humans spend the entire course of their lifetime executing a variety of stereotypical rhythmic movements, such as as swimming, walking and breathing. What leads to the generation of these movements?

Contemporary neuroscience states that these behaviours can be explained by specific patterns of oscillatory activities generated by specialised neuronal circuits in the brain [Marder, 2015]. It is well-known that theoretical principles and mechanisms of these circuits are universal and they work at many levels of the nervous system organisation, from simple animals up to humans [Marder and Calabrese, 1996, Kandel et al., 2000]. One such principle is the principle of synchronisation [Pikovsky et al., 2003], according to which oscillatory units can coordinate their activities to work together as one global oscillator. Another example is partial synchronisation, a state of a network in which only some oscillatory units become synchronised during a limited time period [Kazanovich and Borisyuk, 2006].

We attempted to clarify how motor neuronal circuits generate oscillations and synchronise to achieve motor functions. To answer this question we studied two neuronal circuits: the swimming circuit in the two day old *Xenopus* tadpole and the basal ganglia. Each of these circuits controls locomotion by synchronising the activity of multiple oscillating neurons. Therefore, in both of these circuits we studied how this synchronisation occurs.

The *Xenopus* tadpole is a unique animal for studying locomotion from both an exper-

imental and a modelling perspectives. On one hand, its nervous system is relatively simple; so simple that it can only generate two types of movements: swimming and struggling. One the other hand, it is complex enough to be able to select, generate and modulate movements in response to sensory signals from the external environment. These two features have allowed us to design biologically-realistic spiking neuronal models aiming to clarify some important and challenging questions.

Firstly, what are the neuronal mechanisms beyond the generation of a complete swimming episode? We answer this question using one of our models, which includes most of the neurons active during swimming (about 1500). Model simulations clarify the neuronal processing leading to the initiation, continuation, modulation and termination of anti-phase swimming oscillations, and can therefore explain a whole episode of swimming at the neuronal level.

Secondly, what mechanisms can lead to the generation of all oscillatory patterns of activities that have been recorded during swimming? We used bifurcation theory to study a reduced circuit and find the existence and stabilities of all the experimentally recorded regimes. One is a swimming regime which is characterised by anti-phase oscillations between opposite body sides, and one a regime of synchronous in-phase spiking between the two body sides.

Thirdly, how do neurons in the swimming neuronal circuit generate connections? And what are the structural properties of these connections that lead to the generation of swimming oscillations? For the connectome of some animals answering the first question is still not possible, because the number of connections is too high. In the case of tadpoles, however, we suggest a new "probabilistic model" approach to finding the pair-wise connectivity and successfully use it to generate and analyse connections in multiple individuals. We then mapped this connectivity to a functional spiking neuronal model to simulate the circuit dynamics and identify some of the neurons and connections that are key for producing and controlling the swimming rhythm.

In the case of the basal ganglia, we demonstrated a plausible mechanism of the ac-

tion selection problem. Our approach to modelling this mechanism is mostly based on the principle of partial synchronisation and some constraints coming from experimental neurobiology. This model suggests a theoretical mechanism for the selection and switching between multiple actions, which is interpreted in terms of phase-locking of different groups of oscillating neurons in the basal ganglia.

1.1 Thesis outline

In chapter 2, we review the experimental and modelling studies on the anatomy and behaviour of the *Xenopus* tadpole and on the basal ganglia. All other chapters of this thesis include an introductory selection which reviews the information relevant to that specific chapter.

In chapter 3, we describe the probabilistic model of the neuronal connectivity in the tadpole spinal cord. Our primary goal is to clarify the relationship between the topological properties of the architecture of synaptic connections and the network's ability to generate behaviour, commonly known as structure-function problem. Clarifying this relationship is often difficult because the neuronal connectivity of most animals varies considerably across individuals of the same species. To clarify this problem, we develop a probabilistic meta-model that generalises the neuronal connectivity of multiple individuals. We calculate of structural characteristics of this connectivity and we compare them with the neuronal circuits of other species. We use the probabilistic model to generate neuron-to-neuron connectivity and we combine this connectivity with a functional model of Hodgkin-Huxley neurons to simulate the oscillatory neuronal dynamics corresponding to the animal's swimming behaviour. These simulations can explain the basis of key experimental findings and make new predictions for experimental testing.

In chapter 4, we study a reduced spiking neuronal model representing one segment of the tadpole spinal cord. In experiments, neurons in each of these segments oscillate in anti-phase between left-right half-centres (swimming oscillations). However, the same neurons can also generate transient bouts of in-phase oscillations between left-right centres (synchrony oscillations). In this chapter, we use our reduced model to inves-

tigate the origins of these two activity patterns. Using the reduced model allows us to find the minimal conditions for the generation of biologically-realistic patterns of oscillations and for providing a mathematical description of how these oscillations appear. Although highly reduced, our model contains a detailed description for spike generation and synaptic transmission, which allows model simulations to accurately mimic physiological recordings. The reduced model can generate outputs that closely match all the activities seen in experimental recordings, including synchrony and swimming oscillations. We use bifurcation analysis to show the critical boundaries separating different dynamical regimes and demonstrate the existence of parameter regions where swimming and synchrony are bi-stable. Our results can explain the appearance of long-lasting synchrony bouts seen at the beginning and during a swimming episode.

In chapter 5, we describe a spiking neuronal model of the tadpole nervous system which includes three sensory pathways and the spinal central pattern generator, called the Virtual Tadpole (VT) model. We use the VT model to clarify how somatosensory modulatory inputs can initiate and terminate swimming in tadpoles. Swimming can be initiated in two sensory modalities - skin touch, head touch - and terminated by head pressure. Anatomical and physiological experiments have identified the sensory modalities that lead to the decision to start/stop the animal's swimming behaviour. The VT model is an extension of our previous anatomical and functional models described in chapter 3. Based on these experiments we model the connectivity and dynamics of the new neuronal populations participating in the sensory modalities. Firstly, we use the probabilistic model defined in chapter 3 to generalise the static neuronal connectivity of these populations based on the connectivity of previously modelled neurons. Secondly, we model the dynamical properties of each neuronal type using the Hodgkin-Huxley formalism and with parameters that fit experimental recordings. The final model represents the most complete and biologically realistic reconstruction of a vertebrate neuronal network and it can generate the whole swimming behaviour of tadpoles. With the term "whole" we mean that the VT model (1) includes most of the active neurons in the entire nervous system and (2) simulates the complete temporal dynamics of these neurons, from

the initiation to the termination, through the continuation and modulation of swimming. External modulatory input mimics the tactile and visual contribution of the external environment in each modality. In agreement with experiments, the model suggests two distinct mechanisms for swimming decision-making: touch of the trunk skin stimulation generate slow and variable accumulation of excitation to threshold, and provide a simple mechanism of working memory. Head pressure and touch produce much faster and less variable decisions, similar to reflexes. In summary, the VT model simulates a detailed and biologically plausible sequence of information processing from the internal representation of different sensory modalities, integration and decision-making, action selection, and movement generation.

In chapter 6, we attempt to clarify the physiological role of synchronisation in the context of action selection by modelling the mechanism of switching between multiple competing motor tasks. This problem is particularly important because it could help to treat impulsive movements in patients affected by Parkinson's disease. We propose a theoretical neuronal spiking model of the basal ganglia, a collection of brain nuclei involved in action selection and other motor functions. Our hypothesis is that different motor programs correspond each to a different groups of partially synchronised oscillators and the action selection is achieved by transition between these groups. We use this paradigm to explain a potential mechanism of action selection based on partial synchronisation by periodic cortical forcing. This model is motivated by experimental studies showing this type of synchronisation occurs in both normal and Parkinsonian conditions. Using numerical simulations and bifurcation analysis, we find regions of phase-locking synchronisation under variation of cortical input parameters, called Arnold tongues. Our model shows how these synchronisation regions can explain the transition between different oscillatory states and could be used as a qualitative tool to understand the basic working principles of action selection.

Finally, Chapter 7 summarises the thesis contribution and the Appendix contains copies of published papers.

Chapter 2

Background

In this chapter we review previous experiments and models related to our research studies. We start off by outlining previous experiments and models that have studied the role of oscillation and synchronisation in neuronal circuits. In the second part we review some key findings related to the neuronal circuits that have been the focus of our studies: the swimming circuit in the Xenopus tadpole and the basal ganglia.

2.1 The importance of oscillations and synchronisation in the brain

Brain oscillations are rhythmic patterns of brain activity recorded in variety of experimental setups such as electroencephalograms (EEG), local field potentials (LFP), single/multiunit electrodes, etc.

After Berger firstly recorded oscillatory activities in the brain [Berger, 1929], brain rhythms have been classified into the several bands in the frequency spectrum: α (8-13 Hz), δ (1-4 Hz), θ (4-8 Hz), β (13-30 Hz) and γ (30-70 Hz) [Buzsáki and Draguhn, 2004]. Oscillations at each of these frequencies manifest themselves during a multitude of behaviours [Buzsáki and Draguhn, 2004]. For example, δ oscillations appear during cognitive processes such as attention [Herrmann et al., 2016], while γ oscillations during object representation tasks [Ritz and Sejnowski, 1997]. Singer [1993] give a detailed review of the frequency bands and their emergence during many behaviours. Particularly relevant in the field of motor control are β oscillations in the human basal ganglia (BG), a collection of subcortical nuclei believed to play a critical role in generating movements. A remarkable fact suggesting the importance of oscillations in underlying the function of the brain is that the identification of different abnormalities in the state of the brain, such as anesthesia and coma, can be based solely on the frequency spectrum of EEG

oscillations [Singer, 1993, Voss and Sleigh, 2007]. However, this should not lead us to thinking that this spectrum is the signature of any behaviour, simply because different functions can be associated with oscillations at the same frequency. For example, α oscillations are recorded during both memory and attention [Herrmann et al., 2016].

Besides being found at different frequency levels, brain oscillations appear also at multiple spatial scales, ranging from the activity of single neurons up to entire brain regions. Recordings made with EEG and LFP instrumentations reveal the activity of an ensemble of neurons in the brain scalp and neuronal tissue, respectively. The fact that these recordings show oscillations indicates that a large number of neurons must be engaged in a synchronous rhythmic activity to generate what are typically called "macroscopic oscillations". Indeed, if these oscillations were not the result of synchronous rhythmic activity of many single neurons, the weak currents associated with membrane potential and synaptic activity of single neurons would not be detectable [Singer, 1993].

Current belief in neuroscience is that oscillations and synchronisations play a key role in various brain functions. These activities correspond to different cognitive processes such as sensory processing [Engel et al., 2001, Kahana et al., 2001], pattern recognition [Gray et al., 1989, Llinas and Ribary, 1993], memory [Buzsáki and Draguhn, 2004, Başar et al., 2001], attention [Herrmann et al., 2016, Fries et al., 2001, Borisyuk and Kazanovich, 2004], hearing [Lakatos et al., 2008, Rankin et al., 2015, Wang and Chang, 2008], perception and emotions [Kahana et al., 2001, Varela et al., 2001], object representation [Ritz and Sejnowski, 1997], cicardian clock [Moore, 1983], feature binding and binocular rivalry [Schillen and König, 1994, Engel et al., 1999, Singer, 1993, Singer and Gray, 1995, Borisyuk et al., 1998], dreaming and sleeping [Llinas and Ribary, 1993, Kahn et al., 1997, Steriade et al., 1993]. Moreover, oscillations appear in motor circuits which control rhythmic movements such as breathing, walking, swimming, flying, etc [Grillner and Kashin, 1976, Roberts et al., 1998, Grillner et al., 2008, Golubitsky et al., 1999, Marder and Bucher, 2001, Arshavsky et al., 1993, Dimitrijevic et al., 1998, Marder and Calabrese, 1996, Grillner, 2006, Eisenhart et al., 2000, Marder and Bucher, 2001].

For this reason clarifying the neural mechanisms underlying oscillations and synchronisations is believed to be a crucial part of understanding how the brain operates. In the next sections we review some modelling studies which have suggested how the structural and dynamical properties of neuronal circuits can account for the generation of these oscillations and synchronisations. We do not attempt to cover all the literature in this field of research, as there are many existing books and reviews that do this in great detail, such as [Izhikevich, 2007, Ashwin et al., 2016].

One of the most famous and widely used models describing how a neuron can generate electrical activity is the one formalised by the two British scientists Hodgkin and Huxley [Hodgkin and Huxley, 1952a]. Their model dissects the biophysical mechanisms underlying the generation of the action potential (or spike), a fast rise of the neuron membrane potential followed by a rapid decrease. Since the work of Hodgkin and Huxley a variety of different neuronal models have been developed, such as the Izhikevich, integrate-and-fire models and many others [Izhikevich, 2003, Brette and Gerstner, 2005, Izhikevich, 2007]. These models describe neurons using systems of ordinary differential equations, and they can generate many complex phenomena, including oscillations and chaos [Glass and Mackey, 1988, Izhikevich, 2007, Chua et al., 2012].

In these models, oscillations can appear spontaneously in absence of any input, or due to forcing by an external stimulus [Izhikevich, 2007]. One typical example relates to the firing of neurons in response to depolarising current injections: some neurons, if injected with a sufficiently strong current, exhibit oscillatory patterns of action potentials (tonic spiking). This property is called neural excitability [Izhikevich, 2000, Rinzel and Ermentrout, 1998]. The firing frequency of excitable neurons depends on the amplitude of the injected current, and the curve describing this dependency (current-frequency curve) is typically monotonically increasing. The current-frequency curve of excitable neurons can be either continuous (Class 1 excitability) or discontinuous (Class 2 excitability). The remaining set of neurons can only fire one action potential in response to current injection, independently of the amplitude of the current (Class 3 neurons). One example

of a Class 3 neuron excitability is the one of excitatory descending spinal interneuron (dINs) neurons in tadpoles [Soffe et al., 2009], as we will discuss later in this chapter.

In the past decades, many advances in the study of neuronal oscillations have been reached thanks to the theory of dynamical systems [Guckenheimer and Holmes, 2013]. In particular, bifurcation theory offers a qualitative description of how such systems change their dynamics under parameter variation [Kuznetsov, 2013]. For example, consider the transition between quiescence and repetitive spiking states in neurons injected with current, as mentioned in the previous paragraph. This transition is marked by the crossing of the system at a critical value of the current amplitude below which the neuron is quiescent and above which it produces oscillatory firing. This value is commonly referred to as a bifurcation point, that is, a critical parameter value that determines a "drastic" change in behaviour. For example, bifurcations determining the transition between quiescence and oscillatory firing can be one of four types: a saddle-node, a saddle-node on invariant circle, a sub- or a super-critical Andronov-Hopf (AH) bifurcation [Kuznetsov, 2013]. The analysis of bifurcations can explain a number of neurocomputational properties of single neurons, including excitability [Rinzel and Ermentrout, 1998], subthreshold oscillations [Shilnikov and Rulkov, 2004], post-inhibitory rebound [Wang and Rinzel, 1992] and resonance [Baer et al., 1989]. For example, when crossing a super- or sub-critical Andronov-Hopf bifurcation, neurons exhibit small amplitude oscillation in the membrane potential that can promote post-inhibitory rebound firing [Izhikevich, 2000]. This is another characteristic feature displayed by dINs in tadpoles which we will consider throughout the thesis.

Other than tonic firing, there are other more complex oscillatory modes that single cells (not necessarily neurons) can exhibit and that have been explained using bifurcation theories. Two of these examples are bursting and mixed-mode oscillations. Bursting is a dynamical mode characterized by alternations between quiescence and repetitive firing, while mixed-model oscillations are patterns of intermittent low-amplitude and high-amplitude oscillations [Desroches et al., 2012]. These phenomena have been

observed in electrophysiological recordings of single-cell activity. Cortical chattering neurons [Gray and McCormick, 1996], respiratory neurons in the pre-Botzinger complex [Butera Jr et al., 1999], endocrine cells [Tsaneva-Atanasova et al., 2010] and the lobster stomatogastric ganglion cells [Gola and Selverston, 1981] are examples of cell bursters, while entorhinal cortex layer II neurons [Dickson et al., 2000] and pituitary cells [Vo et al., 2010] are examples of neurons exhibiting mixed-mode oscillations. The transitions between two dynamical states (quiescence from/to spiking and low from/to high amplitude oscillations) in both bursting and mixed-mode oscillations typically occurs because of the different time scales of the variables in the system. Using a geometric approach to the study of dynamical systems, bifurcation and singular perturbation theories have unveiled many mechanisms underlying these complex oscillations. Thanks to these approaches we now have full classifications for different types of bursting [Izhikevich, 2000, Coombes and Bressloff, 2005] and mixed-mode [Golubitsky et al., 2001] oscillations that is based on the bifurcation structure of the various models.

In addition to single cells, it is well known that the dynamics of a neuronal network models comprised of excitatory and inhibitory neurons can be oscillatory [Ashwin et al., 2016, Buzsáki and Draguhn, 2004, Selverston and Moulins, 1985]. For example, a study [Borisyuk, 2002] of spiking integrate-and-fire type neurons with random connections demonstrated that an oscillatory regime is stable and exists for a broad range of parameter values after crossing an Andronov-Hopf bifurcation.

Experiments have shown that spinal circuits can produce fictive movements without any input from the brain in many animals, including tadpoles [Li et al., 2006] and cats [Pearson and Rossignol, 1991]. This has led to the general concept of central pattern generators (CPGs): specialised neuronal circuits in the spinal cord that are capable of autonomously generating rhythmic activity in the absence of forcing by periodic external stimuli [McCrea and Rybak, 2008, Marder and Bucher, 2001]. The ability of these circuits to generate oscillations depends on both the properties of the neurons and on their interactions [Bargmann and Marder, 2013].

For example, using a simplified CPG model Skinner et al. [1994] considered two relaxation-oscillator neurons (n_1 and n_2) coupled by reciprocal inhibition. Synapses were assumed to have the same constant threshold and to be instantaneous, so that each neuron can either be in an active or in an inhibited state. The model shows four different mechanisms which can generate anti-phase oscillations. Two of these mechanisms are driven by the intrinsic properties of the neurons (case 1), and the other two by the properties of the synapses (case 2). In case 1, the dynamics of n_1 starts from an inhibited (active) state and it escapes (release) from it after crossing a fold bifurcation and jumping to its active (inhibited) state. At the same time, n_2 starts from an active (inhibited) state and jumps to its inhibited (active) state after the jump of n_1. In the second two cases, n_1 starts from its active (inhibited) state and jumps to its inactive state after crossing the synaptic threshold. Meanwhile, the n_2 starts from its active (inhibited) state and jumps to its active state when n_1 crossed the threshold.

Although oscillations in neural circuits have been studied for decades, we still struggle to understand many aspects of their functioning [Bargmann and Marder, 2013, Marder and Taylor, 2011, Roberts et al., 2010]. One reason is that many of the circuits' properties are largely unknown, due to the lack and variability of experimental data. To overcome this limitation, biologically-inspired models have been successfully developed to test experimental hypotheses and make suitable predictions. However, these models are often difficult to validate because they can be either too complex, therefore difficult to analyse, or too abstract, therefore restrictive in their predictions. A possible solution is to model neural circuits with few number of neurons and behaviours. This would guarantee models to be simple enough to be analysed, for example, by using computer simulations. In addition to selecting such circuits, these models should be designed to incorporate as many biological details as possible to increase their predictive power. In a more general picture, the hope is that the study of these circuits could help us to understand some general principles for the brain functioning in even more complex circuits. This would allow stepping forward in the ambitious goal of understanding how the human brain works. This modelling paradigm can be achieved, for instance, by mod-

elling the main behaviour of the neuronal circuit in the two-day-old hatchling *Xenopus* tadpole.

2.2 The structure and function of the tadpole swimming circuit

Oscillatory activity patterns corresponding to (fictive) swimming can robustly be initiated and sustained for some seconds by stimulating the skin of tadpoles even when these animals are deprived of all body parts except for a 1.5 mm long segment consisting of parts of the hindbrain and spinal cord (shown in Figure 2.1 A, these results are summarised in Li et al. [2006]). Therefore, we presume that the neural circuit located in this segment - which we call "swimming circuit" throughout all the thesis - contains the CPG generating the swimming rhythm and at least one sensory modality responsible for the start of the CPG and motor activity in response to skin stimuli. In this thesis we mainly consider the study of this swimming circuit, but we also extend our studies to model other sensory modalities located in other parts of the hindbrain and trigeminal ganglia [Roberts et al., 2010].

According to the present knowledge [Roberts et al., 2010], which has been accumulated over decades of experimental and modelling studies, the swimming circuit contains roughly 1500 neurons divided into only eight cell types. Seven of these types are divided based on their anatomical and functional properties [Sautois et al., 2007, Roberts et al., 2014]. The remaining one - the hindbrain extension neurons (hINs) - is a hypothetical neuronal class that has not yet been identified anatomically nor physiologically. However, we have evidence that suggest that these neurons exist, and that they are involved in initiating swimming via the skin stimulation [Koutsikou et al., 2018]. We will discuss and investigate the role of these neurons in chapter 5.

Here, we review the properties of the remaining seven neuronal types, which have been studied in detail using anatomical measurements and electrophysiological recordings, combined with computational modelling. It is thanks to these studies that we now have a clear picture of the role of these cell types during tadpole's swimming behaviour.

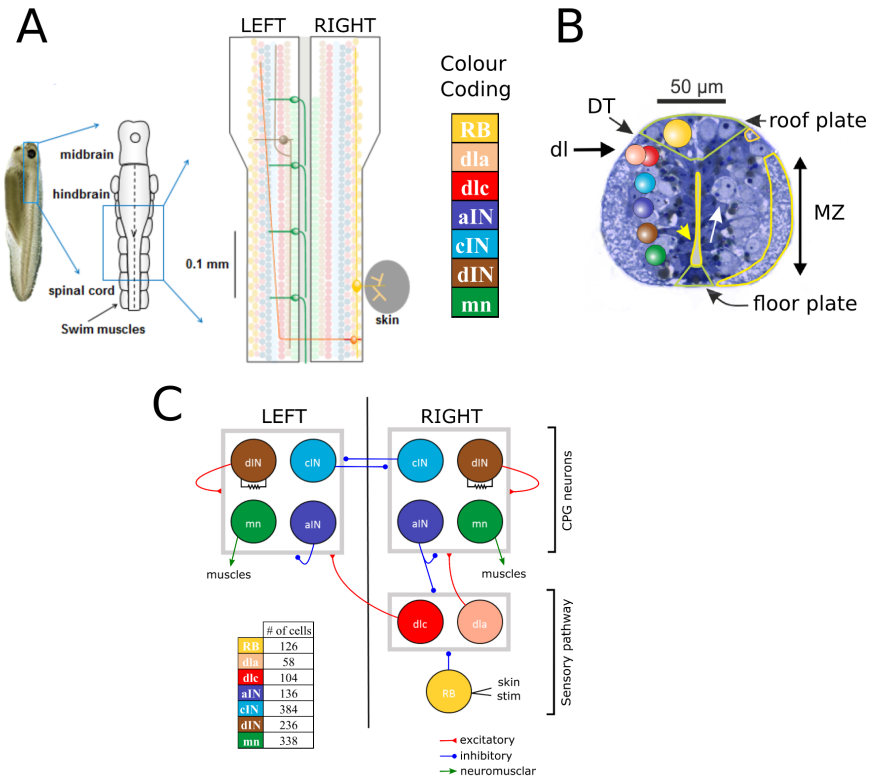

Figure 2.1: Organisation of the swimming neuronal network in the *Xenopus* tadpole. A. Left: Photo of a 5 mm long hatchling Xenopus tadpole, stage 37/38. Middle: Zoom of the two-dimensional of the CNS seen from top with its subdivisions (midbrain, hindbrain and spinal cord). Right: Zoom of the indicated region of hindbrain and rostral spinal cord after opening the body in half along the midline like a book, showing the division of the body into left and right sides. This diagram shows examples of cell bodies positions (filled circles), dendrites (straight horizontal lines) and axons (lines extending also vertically). The floor plate separates left and right side of the CNS (grey rectangle). The colour coding used to identify each cell type is the same one used throughout the whole thesis. B. Transverse section of the spinal cord, showing the neuron somata (white arrows), typical position of cell bodies of different types (coloured circles), the roof and floor plates (green oulines), dorsal tract (DT) and marginal zone (MZ). Dorslateral (dl) somata separate the MZ from seonsory axons in the DT. C. Diagram showing the different populations within the swimming network and the synaptic connections between them (lines with markers; red=excitatory, blue=inhibitory). Connections ending on the border of each symmetrical half-centres (grey square) represent connections to any cell-type in the corresponding half-center. Descending interneurons (dINs) are locally coupled by gap junctions. Note that neuronal populations in the sensory pathway are only shown for one side of the body, but are present on both sides. Parts A and C are taken from [Ferrario et al., 2018a], and part B from [Roberts et al., 2014]

2.2.1 The anatomy of the circuit

Anatomically, neurites (cell bodies, axons and dendrites) are located in special positions within the spinal cord. Figure 2.1B shows a transverse section of the spinal cord and the dorso-ventral position of the cell bodies of the different cell types. The body is symmetrical under mid-line reflection. Therefore, all anatomical properties described for one side are obviously valid for the other side, too. On each body side, cell bodies are organised in sequence from top (ventral end) to bottom (dorsal end) according to the neuronal type. This sequence repeats in a series of longitudinal columns along the body (coloured circles in Figure 2.1A-B). The dorso-ventral disposition of neurons in this sequence is controlled by different sensitivities to chemical gradients resealed from the roof and floors plates during development. These gradients control also the growth of axons in the cord and the positions of dendrites. Figure 2.1A shows simplified diagram of the swimming circuit opened dorsally like a book, showing location of cell types, axons and dendrites of the different neural types in a two dimensions. After following a short path in dorso-ventral direction starting from the soma, axons tend to grow longitudinally in ascending or descending directions. Some of these axons branch in two, with one branch growing in ascending and the other in descending directions. Dendrites extend dorso-ventrally, covering more surface to be crossed by growing axons. During these developmental processes neurites distribute in special positions in the spinal cord, where synapses can form. A result of this special positioning of neurites is that some synaptic connections between neural types are more likely to form, while others are less likely. Figure 2.1C shows a schematic diagram of the synaptic connectivity between the different neural types. The anatomy of the different neuronal types and the properties of their synaptic connections is presented below; more details can be found in [Roberts et al., 2014, Li et al., 2007a].

Rohon-Beard neurons (RBs) are excitatory sensory cells innervating the skin. They release glutamate neurotransmitters on post-synaptic sites and spike in response to stimulation or touch of the skin. Their axons grows longitudinally in the dorsal tract

(DT), where they form synapses with dlas and dlcs.

Dorsolateral ascending (dlas) and commissural interneurons (dlcs) are excitatory sensory pathway cells releasing glutamate. They are located in a region separating the DT from a thin lateral area called marginal zone (MZ), where all cells except RBs are located. Their dendrites extend towards the DT, where they are likely to be contacted by RB axons. The axons of dlas run ventrally towards the MZ and then in an ascending direction. The axons of dlcs travels contralaterally (to the other side of the body) passing through the floor plate.

Ascending (aINs), commissural (cINs) and descending interneurons (dINs) are believed to form the CPG population responsible for the maintenance of swimming oscillations over time. Cell bodies, dendrites and axons of all three cell types are located in the MZ, where these neurons are likely to form synapses with all other neural types except RBs. While aINs and cINs are inhibitory cells by releasing glycine, dINs are excitatory cells by co-releasing glutamate and acetylcholine. Opposite to dINs and aINs, cINs have axons running contralaterally. DINs are also electrically connected via gap junctions.

Motor neurons (mns) are excitatory cell that release acetylcholine. Their cell bodies are ventrally located, and their dendrites lie in the MZ, where they receive input from CPG neurons. Mns form special neuromuscolar synapses controlling the contraction of muscles, and enable the animal to swim. They have very short axons and, consequently, they form few synapses with nearby cells and muscles organised in longitudinal segments.

Electrophysiological pairwise recordings have revealed the connection probabilities for each pair of neural types [Li et al., 2007a]. Analysis of these data suggest that the formation of synapses does not depend on cell-to-cell specific factors, but it can rather be explained simply by the crossing of axons and dendrites in the spinal cord [Li et al., 2007a, Borisyuk et al., 2014]. By using the numerous anatomical and physiological data gathered throughout the years, previous studies [Borisyuk et al., 2008, 2011, 2014,

Davis et al., 2017] have shown how modelling of the neuronal connectivity in the tadpole swimming circuit is possible through a 'developmental' approach, whereby connections between neurons are not prescribed but appear as a result of the intersection between (simulated) growing axons with dendrites. This anatomical model mimics the realistic growth of axons in the spinal cord, including axon branching, physical constraints (barriers) and projections to opposite body sides (commissural axons). Following biological realism, the axon growth is guided by the concentration of chemical gradients controlled by model parameters that have been optimised to produce the same statistical characteristics as real measurements. Other model specifications (including soma positions and dendritic extents) are assigned from the distributions of experimental data and from general biological knowledge. The model includes several stochastic components; therefore, each model simulation generates a different pattern of connectivity ('anatomical connectome'). In this thesis we use this model to define a probabilistic model that generalises the connectivity of many stochastically generated anatomical connectomes (chapter 3). Since clarifying some details of the anatomical model is crucial for understanding the results presented in this chapter, we give a brief description of the model in the next subsection.

2.2.2 The anatomical model

The anatomical model generates the complete neural connectivity in the spinal cord using a "developmental" approach that mimics axon growth [Borisyuk et al., 2014] of all the cells and synaptic formations. This model is based on numerous anatomical data of the Xenopus tadpole spinal cord neurons. Here, we give a brief description of the model, but full details can be found in [Borisyuk et al., 2014, Roberts et al., 2014].

It is important to note that the anatomical model provides a way of generating many different connectomes, such that the random variation observed between generated connectomes has the same statistical properties as measurements taken from different individual animals. Here, we set out to reveal the fundamental features of the neuronal connectivity that underlie the ability of the swim network to function robustly.

The model spatial structure

Tadpole's spinal cord is approximated as a 2D rectangular plate where neuronal bodies, dendrites and axons are located (Figure 2.1). The third dimension (i.e. the thickness of the spinal cord "tube") was ignored as this is very thin (10 μm thick). In the model description, variables and correspond to the rostro-caudal distance (RC) from the midbrain-hindbrain border (referred to as "rostro-caudal distance") and the dorso-ventral distance (DV) from the ventral mid-line border (referred to as "dorso-ventral distance"), respectively. Positive (Negative) values of correspond to positions on the left (right) side of the body. We consider a limited area of the spinal cord, where $(x, y) \in [500\mu m, 2000\mu m] \times [-145\mu m, 145\mu m]$.

Axon growth model

We describe the axon growth using discrete time iteration map (with time step 1ms). The map is described by three variables (x_n, y_n, θ_n), where x_n represents RC coordinate, y_n the DV coordinate and θ_n the growth angle of the axon at each time step $n(n = 0, 1, ..., N)$. The map for the growth angle depends on a "stiffness" term, which is the tendency of the growth angle to grow straight, and by the influence of environmental cues (according to chemical gradients), which deviate the growth cone from a straight path. The chemical gradients functions $G_{RC}(x, y)$ and $G_{DV}(x, y)$ depend on the current position of the axon and that will determine the change of the growth angle at each time step on the RC and DV axis, respectively. Additionally, a uniform random variable ϵ_n is included to provide an additional degree of freedom at each time step. The map is described by the following equations:

$$x_{n+1} = x_n + \Delta cos\theta_n$$

$$y_{n+1} = y_n + \Delta sin\theta_n$$

$$\theta_{n+1} = \theta_n - G_{RC}(x_n, y_n)sin\theta_n + G_{DV}(x_n, y_n)cos\theta_n + \epsilon_n$$

Here, the elongation parameter $\Delta = 1\mu m$; ϵ_n uniformly distributed in the interval $[-\alpha, \alpha]$. To start the axon growth simulation we assume that the axon initial positions coincide

with the soma positions. The initial value for the growth angle θ_0 and the axon length $L = N \cdot \delta$ (which will determine the number of iterations of the map) are randomly selected from the distribution of experimentally measured initial angles and axon lengths. The gradient functions $G_{RC}(x, y)$ and $G_{DV}(x, y)$ depend on various parameters that describe the properties of the chemical gradients in the 2D space. Previous studies revealed that the axons of the same neuron type tend to grow in specific regions of the spinal cord, suggesting that such axons could be controlled by the same gradients. Thus, the parameters of the gradient functions in the model were selected to reproduce the statistical properties of the axons of each specific cell type separately. Some of these parameters were selected according to general biological knowledge on the distribution and properties of the chemical gradients. The remaining parameters were estimated using an optimisation technique that minimises a custom cost function measuring the similarity between statistical properties of simulated and experimentally measured axons. For a detailed description of the gradient functions $G_{RC}(x, y)$ and $G_{DV}(x, y)$, the cost function and the optimisation technique see Borisyuk et al. [2014].

Anatomical and physiological studies in tadpoles have revealed that there are physical constraints to the axons growth, and these have been added in the anatomical model. In particular, longitudinal barriers delimited by DV coordinates $y = \pm 125$ delimit the area where axons of all neuron types except RBs grow (called marginal zone). Coordinates $y \in (127, 137)$ on the left body side ($y \in (-137, -127)$ for the right body side, respectively) delimit the region where RB axons can grow (called dorsal tract area).

Branching and contralateral axons

The axon of tadpole spinal neurons typically splits into two branches during its growth. We call primary axon the branch that starts from the soma and continues to grow following the growth direction before the branching point. Secondary axons grow from the branching and towards the opposite direction of the primary axon (rostro-caudally). The RC direction of primary axon of each neuron type is known from anatomy of neurons. In the model we thus consider growth of primary axons and secondary axons as

two consecutive processes. All primary axons grow first, and after that secondary axon growth starts at a specified branching point. The coordinates of branching points are selected randomly from the distribution of available experimental data for each neuron type.

The axon of commissural neurons (dlcs and cINs) starts to grow on the cell body side and then rapidly navigates on the opposite body side after crossing the floor plate due to the influence of strong DV gradients. After crossing, DV gradients change their sensitivity and become weak, and the axon starts to deviate towards ascending direction. Secondary axons are positioned on the contralateral side and grow in the descending direction. At the beginning, commissural neurons grow in the ventral direction according to the axon growth equations with specially adjusted parameter values. After crossing the boundary of the ventral plate on the opposite side the axon growth is described by the same equations but with another regular set of parameter values (for details see Borisyuk et al. [2014]).

Synapses and Full Connectome

Dendrites are assumed to be fixed bars extending dorso-ventrally. Thus, each dendrite is represented by a pair of DV positions, one corresponding to its lower (ventral) bound and on to its upper (dorsal) bound. For each neuron, cell body positions and dendritic bounds are sampled from the distributions of experimentally measured data for each specific cell type.

In model simulations the number of neurons of each type is fixed and it is the same for both sides of the body. In reality, although biological data are limited, total numbers of spinal neurons and the population sizes of individual neuron types do not appear to vary greatly between animals (perhaps $\pm$ 10-15% at most) at this early stage of development. Any variation in these numbers is small compared to the differences from the previous developmental stage to the following stage.

For each pair of pre- and post- synaptic neurons, a connection is generated whenever the pre-synaptic axon crosses the dendritic bar of the post-synaptic neuron with some

probability. Such probability depends on pre and post synaptic cell types and was estimated from various experimental pairwise recordings (for details see [Borisyuk et al., 2014]). During the initial pre-crossing stage we assume that the axon of commissural neurons cannot produce synapses. Since the model uses several number of random variables, each simulation of the anatomical model generates a different connectome.

2.2.3 Functional model

In a next study [Roberts et al., 2014] the connectivity of each anatomically generated connectome has been mapped onto a functional model composed of spiking units of Hodgkin-Huxley type, with parameters chosen to match known tadpole electrophysiology [Sautois et al., 2007, Dale, 1995, Winlove and Roberts, 2012]. The resulting functional model reliably produces activity patterns similar to those seen in cell recordings during fictive swimming [Roberts et al., 2014].

In the next sections we review the spiking neuronal models used to describe the activity of the different neuronal types in the tadpole connectome. We start off by describing one of the most popular models describing the activity of neurons, the Hodgkin-Huxley model, as this model was used to model the dynamical features of the seven cell types in the functional model.

2.2.3.1 The Hodgkin-Huxley model

In the early 50s Alan Hodgkin and Andrew Huxley derived a set of non-linear equations that describe the dynamics of the squid giant axon-work for which they received the Nobel prize [Hodgkin and Huxley, 1952a,b,c]. The Hogkin-Huxley model is essentially a four-dimensional system of ordinary differential equations describing the dynamics of the cell membrane by ionic channels, which is able to reproduce highly non-linear phenomena of neurons called action potentials, which is at the basis of neural transmission.

In this model, the cell membrane is thought as a circuit with capacitance C which acts as parallel resistors consisting of different ionic channels (sodium: Na^+, potassium: K^+, and non-specific leakage: LK). Each of these channels is a pore forming protein

in the cell membrane allowing the flow of charged ions (currents) between the inside and the outside of the cell.

The voltage or membrane potential - i.e. the voltage difference between the interior and the exterior of the cell - regulates the proportion of opened and closed of K^+ and Na^+ channels (voltage gated), but not LK ions, which are always open.

Typically, the concentration of K^+ ions is higher in the inside of the cell, while the concentration of Na^+ ions is higher outside of the cell. Due to this difference in concentrations, when the channels are in the open state, a chemical force mediated by a cellular pumps attracts Na^+ ions from the outside to the inside of the cell, and it repels K^+ ions from the inside to the outside the cell.

While ions of each type (K^+ or Na^+) move due to this force, they create an excess of charge on either the inside or the outside of the cell. This activates an electrical force that contrast the continuous movement of ions in a single direction. These two forces balance each other creating an equilibrium where the voltage is at rest. The reversal potentials (Nernst potential) E_{Na}, E_k and E_{lk} represent the equilibrium at which these forces are balanced for each type of ion. This means that, when the voltage of the cell is equal to the reversal of one ion type, the corresponding ionic current is zero.

This proportion of opened and closed ionic channels is modelled in the Hodgkin-Huxley formalism by considering two variables for the Na^+ current and one variable for the K^+ current.

According to the Hodgkin-Huxley model, the voltage across the membrane varies according to the following equation:

$$C\frac{dV}{dt} = g_{lk}(E_{lk} - V) + m^3 h g_{Na}(E_{Na} - V) + n^4 g_K(E_K - V) + I_{ext}$$

Where I_{ext} is an external source of current, g_{lk},g_{Na},g_K and E_{lk},E_{Na},E_k are the maximal conductance and equilibrium potential of the sodium, potassium and leakage currents, respectively. The variables m, h and n are the gating variables of the sodium and potas-

sium channels and their integer powers represent the number of molecules involved in the dynamics of each channel. Each of these gating variables evolves according to an equation of the following form (where X is m, h or n):

$$\frac{dX}{dt} = \alpha_X(V)(1 - \alpha_X(V))(1 - X) - \beta_X(V)X$$

The function α_X is the forward rate function (specified in ms^1) at which the corresponding gating molecule moves from its configuration where ions are blocked to its configuration where ions can flow. Conversely β_X are backwards rate functions, which determine how quickly gating molecules move from the unblocked to the blocked configuration. The functions α_X and β_X follow the form:

$$f(V) = \frac{A + BV}{C + exp[(V + D)/E]} \tag{2.1}$$

where A, B, C, D and E are parameters determined using experimental voltage clamp protocols.

The Hodgkin-Huxley equations can show a variety of dynamics seen in experimental recordings, including excitability, tonic spiking and bursting. Extended versions of the Hodgkin-Huxley model consider more currents and equations than the ones considered in their seminal work, leading to even more complex and interesting dynamical behaviours.

Although being biologically realistic the four dimensional Hodgkin-Huxley system usually has computational limitations, especially if extended with multiple ionic currents. For this reason, several simplified models have been developed. The Morris-Lecar [Morris and Lecar, 1981] and FitzHugh-Nagumo [FitzHugh, 1961] models are examples of two dimensional systems of ordinary differential equations that demonstrate many of the same basic features of the Hodgkin-Huxley model, but they cannot reproduce complex behaviours like bursting. Existing two-dimensional models are able to reproduce a different firing patterns (including bursting), but take into account a reset condition. Ex-

amples of these models are Izhikevich neuron model [Izhikevich, 2003] (which is used in chapter 6 to model neurons in the basal ganglia) and the adaptive exponential leaky integrate and fire model [Brette and Gerstner, 2005].

Models of the neurons in the tadpole's swimming circuit

To simulate the activity in the functional model each cell type in the tadpole connectome has been modelled using the Hodgkin-Huxley formalism with more ionic currents than the ones described in the original model. The equation governing the membrane potential (V) for each neuron i is:

$$C\frac{dV}{dt} = I_{lk} + I_{Na} + I_{Kf} + I_{Ks} + I_{Ca} + I_{syn} + I_{gj} + I_{ext}$$

The capacitance C of all neurons is $C = 10pF$, which corresponds to a density of $1.0\mu F/cm^2$ for a total surface area of $10^{-5}cm^2$. The terms I_{Na}, I_{Kf}, I_{Ks} and I_{Ca} represent transmembrane currents mediated by different ions, respectively: non-specific leak, sodium, fast potassium, slow potassium and calcium. The terms and represent the summed inputs from chemical synapses (I_{syn}) and gap junctions (I_{gap}), while I_{ext} is an external source of injected current. Although the different neuron types in the tadpole spinal cord have different electrophysiology, for simplicity we use the model of a motoneuron from for most model neurons, as this shows characteristics (e.g. repetitive firing in response to injected current) that are broadly shared by all of the neuron types. The exception to this is dINs, which have special properties such as only firing a single spike in response to current injection and the ability to fire post-inhibitory "rebound" spikes. Model dINs differ from non-dINs in the following ways:

- Parameter values governing membrane properties are different (Tables 2.2 and 2.1).
- Only dINs contain a calcium current. For non-dINs, we set $I_{ca} = 0$.
- Only dINs make gap junction connections (and only with other dINs).

	g_{lk}	e_{lk}	g_{Na}	e_{Na}	g_{Kf}	e_{Kf}	g_{Ks}	e_{Ks}
dIN	1.4	-52	240.5	50	12	-80	9.6	-80
non-dIN	2.47	-61	110	50	8	-80	1	-80

Table 2.1: Maximal conductance (in nS) and equilibrium potential (in mV) of each ionic channel in the model neurons.

dIN/others	Rates	A(ms^{-1})	B($ms^{-1}mV^{-1}$)	C(-)	D(mV)	E(mV))
Ca	α_r	4/-	0/-	1/-	-15.3/-	-13.6/-
if $v < -25$	β_r	1.2/-	0/-	1/-	10.6/-	1/-
if $v > -25$	β_r	1.3/-	0/-	1/-	5.4/-	12.1/-
K-fast	α_f	5.1/3.1	0.1/0	5.1/1	-18.4/-27.5	-25.4/-9.3
	β_f	0.5/0.4	0/0	0/1	28.7/9	34.6/16.2
K-slow	α_s	0.5/0.2	8.2e^{-3}/0	4.6/1	-4.2/-3	-12/-7.7
	β_s	0.1/0.05	-1.3e^{-3}/0	1.6/1	2.1e5/-14.1	3.3e5/6.1

Table 2.2: Parameters defining the rate functions of the model neurons rounded to the first decimal digit for dINs and all other neuronal types in the functional connectome model (- sign indicates that the cell type has no contribution of the specific channel variable, units of measures are given in the first row of each parameter; parameter C is dimensionless.

Membrane Channels

The leak, sodium and potassium channel currents are given by the following equations:

$$I_{lk}(v) = \bar{g}_{lk}(v - e_{lk})$$

$$I_{Na}(v) = \bar{g}_{Na} h m^3 (v - e_{Na})$$

$$I_{Kf}(v) = \bar{g}_{Kf} n_{Kf}^4 (v - e_K)$$

$$I_{Ks}(v) = \bar{g}_{Ks} n_{Ks}^2 (v - e_K)$$

The parameters e_{lk}, e_{Na} and e_K give the reversal potential for the leak, sodium and potassium channels respectively, and the parameters $\bar{g}_{lk}$, $\bar{g}_{Na}$, $\bar{g}_{Kf}$ and $\bar{g}_{Ks}$ give their maximum conductances (these parameter values are given in 2.1). The gating variables

h, m, n_f and n_s are governed by equations 2.2-2.5, where $X = h, m, n_f, n_s$.

$$\tau_X(v) = (X_\infty(v) - X) \tag{2.2}$$

$$X_\infty(v) = \alpha_X(v)(\alpha_X(v) + \beta_X(v))^{-1} \tag{2.3}$$

$$\tau_X(v) = (\alpha_X(v) + \beta_X(v))^{-1} \tag{2.4}$$

$$\alpha_X(v), \beta_X(v) = \frac{A + Bv}{C + exp((D + V)/E)} \tag{2.5}$$

The values of the parameters A, B, C, D and E in the functions were taken from Sautois et al. [2007] for non-dINs and from Roberts et al. [2014] for dINs, and are shown in table 2.2. As in Roberts et al. [2014], model dINs contain a calcium-mediated current which is modelled according to the Goldman-Hodgkin-Katz equation. This current is calculated as:

$$I_{Ca}(v) = h_{Ca} p_{Ca} z F x \frac{S_{in} - S_{out} exp(-x)}{1 - exp(-x)}$$

$$x = \frac{zFv}{RT}$$

Here, p_{Ca} is the permeability of the membrane to calcium ions (analogous to maximum conductance) and z is their ionic valence (+2). S_{in} and S_{out} are the concentration of calcium in and outside of the cell, respectively. F is Faraday's constant, and R is the ideal gas constant, while T is the temperature in Kelvin. Parameters of the calcium current are $p_{Ca} = 14.25 cm^3/ms$, $F = 96485 C/mol$, $R = 8.314 J/(K \cdot mol)$, $T = 300K$, $S_{in} = 10^{-7} mol/cm^3$, $S_{out} = 10^{-5} mol/cm^3$. Finally, h_{Ca} is the gating variable associated with the calcium current, which is governed by the standard gating equations 2.2-2.5 - although note from table 2.2 that two different sets of parameters are used for this equation based on whether the membrane potential is above or below -25mV.

Synaptic Currents

The probabilistic and anatomical connectomes provides detailed information on connectivity in the spinal cord - specifically a list of synaptic connections between neurons. We use this information to build a functional model that simulates the spiking activity of

all the swimming network. This allows us to study one of the fundamental problems of neuroscience: the relationship between connection structure and functionality.

The synaptic current that arises in a neuron is the combination of three different subtypes of synaptic receptor: excitatory AMPA and NMDA and inhibitory glycine:

$$I_{syn} = I_{ampa} + I_{nmda} + I_{inh}$$

Each synaptic current is calculated using the following equation, where $X = ampa, nmda, inh$:

$$I_X = \sum_j \bar{g}^X_{i,j} f_X(v_i) \sum_{s \in S_j(t)} \Delta_X(exp((s + \delta_{i,j} - t)/\tau^X_c) - exp((s + \delta_{i,j} - t)/\tau^X_o))$$

Here, $\bar{g}^X_{i,j}$ is the maximum conductance ("strength") of synaptic connection of type X from neuron to neuron . If the connectome does not include a connection from i to j then $\bar{g}^X_{i,j} = 0$, otherwise it is selected according to the type of the pre- and post- synaptic neurons, based on paired recordings. Pre-synaptic neuronal type determines the synapse type X. Inhibitory neuron types are cIN and aIN; excitatory ones are the remaining cell types. The synaptic strengths used in the model are typically the ones given in table 2.3, except for few values that were modified to match the physiology of neurons and synapses (details are given in [Roberts et al., 2014]). Specifically, the maximal conductance of AMPA synapses from RBs to dli neurons are set to $8nS$, the maximal conductance of AMPA synapses from dINs to aINs are set to $0.1nS$, the maximal conductance of NMDA synapses from dIN to dINs are set to $0.1nS$, and the maximal conductance of NMDA synapses from dlc to dINs are set to $1nS$ (to guarantee the start of swimming on the unstimulated side). The set $S_j(t)$ contains the times of all the spikes that neuron j has fired up to the current time t. Each spike generates a post-synaptic current (PSP) that rises according to the time constant τ^X_o and decays according to τ^X_c. The normalising constant Δ_X is set such that the peak of the sum of the exponential is 1, meaning that following a spike the conductance rises to a maximum of $\bar{g}^X_{i,j}$. The values selected for the time and normalising constants are given in 2.3 and they are

X	NMDA	AMPA	INH
τ_o^X (ms)	0.5	0.2	1.5
τ_c^X (ms)	80	3	4
Δ_X (-)	1.25	1.25	3.0
E_X (mV)	0	0	-75
g_X (nS)	0.29	0.593	0.435

Table 2.3: Parameters of the synaptic models.

based on previous modelling [Roberts et al., 2014]. To mimic synaptic strength variability, Gaussian noise with standard deviation 5% of the mean was added to the maximum conductance of each individual synapse.

The synaptic delay between two neurons, $\delta_{i,j}$, consists of a constant and distance-dependent part:

$$\delta_{i,j} = \delta_C + \delta_D |P_i - P_j|$$

Here, P_i and P_j are the positions of neurons i and j along the rostro-caudal axis, δ_C is the constant delay and δ_D is the speed of synaptic transmission. We set $\delta_C = 1ms$ and $\delta_D = 0.0035ms/\mu m$. Finally, the function determines how the synaptic current depends on the post-synaptic voltage. For AMPA and inhibitory synapses this has a simple linear (Ohmic) form:

$$f_X(v) = E_X - v$$

Where $X = ampa, inh$ and E_X is the equilibrium (reversal) potential of the synapse type (2.3). As a result of magnesium block, NMDA synapses have an additional non-linear voltage dependence, which we include by adding a sigmoidal scaling term to :

$$f_{NMDA}(v) = (E_{nmda} - v)(1 + 0.05 \cdot exp(-0.08 \cdot v))^{-1}$$

Gap Junctions

As mentioned above, descending interneurons (dINs) are electrically coupled to other nearby dINs via gap junctions. The gap junction current is calculated using a simple

Ohmic relationship:

$$I_{gj} = \sum_{j \in G_i} \bar{g}_{gj}(v_j - v_i)$$

Here G_i is the set of indexes of all dINs that are on the same side of the body as neuron i and are located within D_{gj} of neuron on the rostro-caudal axis, where we set $D_{gj} = 100\mu m$. The parameter $g_{gj} = 0.2nS$ gives the conductance of gap junctions.

2.2.4 The neuronal dynamics during swimming and synchrony

Hatchling *Xenopus* tadpoles spend the majority of their lifetime attached under the surface of the water or attached onto solid object using its cement gland. When the skin of the animal is touched or the light dims, the tadpole starts to swim. A swimming episode typically stops spontaneously after minutes, during which the neurons generate a pattern of antiphase oscillations between left and right sides with a frequency of 10-25Hz. Some of these neurons activate the rhythmic contraction of muscles that enable the animal to swim. It is also possible that the tadpole suddenly bumps into a solid object. When this happens, swimming terminates prematurely.

In neurobiological experiments, tadpoles are immobilised using a neuromuscular blocker (α-bungarotoxin). The activities of the neurons in the swimming circuit have been studied intensively using whole cell recordings collected over many years combined with simulations of the functional model. These studies gave us a detailed picture of the dynamical properties of the different neuronal types and their role during swimming. Some of these features appear to be critical for the generation of swimming activity, such as the ones related to dINs. Analysis of dINs' recordings highlighted some unique properties (properties 1-5) that can be summarised in the following points [Soffe et al., 2009, Koutsikou et al., 2018, Li et al., 2009, Dale, 1995, Li et al., 2006]:

1. The firing of dINs precedes and drives the firing of all other CPG neurons and mns at each swimming cycle via synaptic excitation.

2. The simultaneous activation of single dINs by electrical stimulation is likely to trigger the start of a swimming episode.

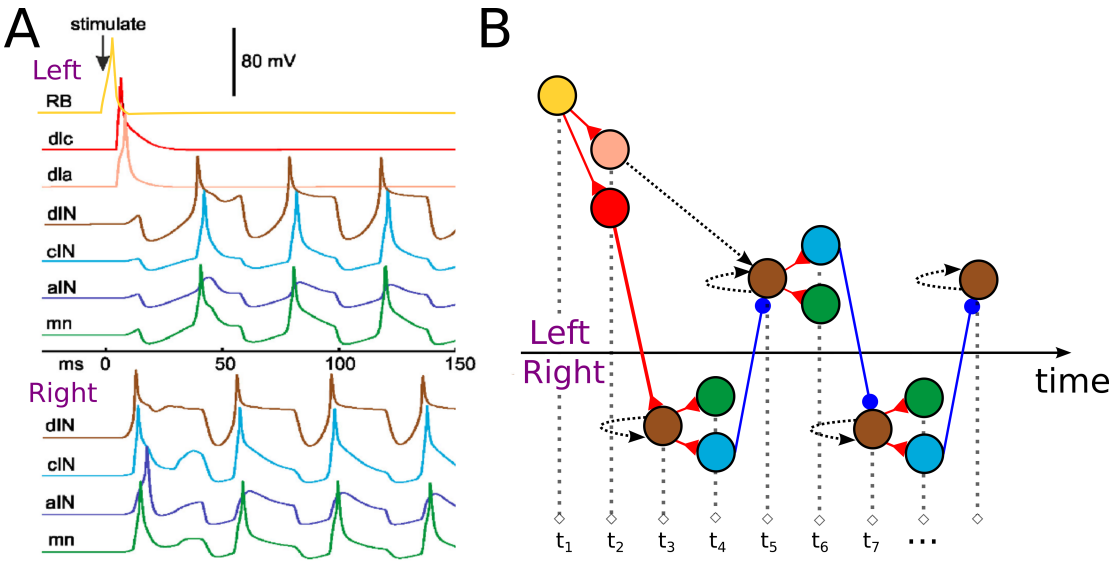

Figure 2.2: Visualisation of the dynamics for neurons of different types. Colours follow the standard coding of 2.1.
A. Each panel shows the voltage dynamics of one representative neuron of each type during a single simulation of the functional connectome, from Roberts et al. [2014]. 2 Stimulations of two left RBs (arrow) trigger a stable pattern of anti-phase oscillatory activity between the left-right sides. B. Schematic diagram showing the time of spiking and synaptic transmissions events $t_1, t_2, ...$ happening during the swimming episode shown in panel A (time is not on scale). Coloured dots represent spikes. Connectivity lines indicate the key synaptic connections activated during each time event and promoting the rhythm. NMDA synapses are shown by dotted black arrows. The other connections indicate excitatory and inhibitory synapses as in Figure 2.1C. For more details, see the text.

3. dINs can spike on post inhibitory rebound (PIR) if their membrane potential is sufficiently high.

4. They can only fire at most one spike in response to positive current injection (thus exhibiting the "Class 3" excitability).

5. They are recurrently coupled via both excitatory glutamatergic synapses and electric coupling (gap junctions). These connections excite and promote the synchronous firings of the dIN population on each side during every swimming cycle.

Next, we will briefly describe the results from one simulation of the functional model, where model dINs incorporate the special properties described above. These simulations can partially reproduce the activities of neurons of each type during one episode

of swimming.

Figure 2.2 A and B clarify the mechanisms leading to the start and the continuation of swimming oscillations in the functional model, by describing the sequence of spiking and synaptic events from the stimulations of the skin to the establishment of the swimming rhythm. Panel A shows the voltage activities of one representative neuron per type from a typical random simulation of the functional connectome. Panel B shows a schematic diagram explaining the sequence of spiking events and synaptic transmissions $t_1, ..., t_7$ leading to the establishment of the swimming oscillatory dynamics (see next paragraphs). For more details on panel A see Roberts et al. [2014].

To mimic the skin touch or stimulation, two left RBs are injected with brief depolarising current at time $t = 0$, which ultimately leads to the left-right antiphase oscillatory firing of motor neurons, which is defined as "swimming". Stimulation causes RBs to fire a single spike each at $t = t_1$, which activates most dlas and dlcs on the left side at $t = t_2$. These dlcs activate most right dINs at $t = t_3$ (property 4), which fire at most one spike each (property 4) in a synchronous fashion (property 5). Right dINs release NMDA currents which sets their voltage at high voltage levels. The summed excitation of these dINs causes single and synchronous bombarding of most right CPGs at $t = t_4$, including cINs (but not aINs, property 1). Right cINs inhibit left dINs and causes them to spike on PIR at $t = t_5$ (see note 1 below). After spiking, left dINs fire synchronously, releasing NMDA in their population and activating most left CPGs at $t = t_6$. At this time, left cINs inhibit right dINs and cause them to fire on PIR at $t = t_7$ (property 3). After $t = t_7$, the same process repeats like in the previous cycle and a stable pattern of anti-phase CPG oscillations appears (2.2).

Note 1: dla firings at $t = t_2$ releases NMDA currents into dINs at $t = t_2$, which enables their PIR spiking at $t = t_5$ (property 3).

Note 2: In this simulation synapses from dlcs were made stronger than the ones from dlas (see above) in order to start swimming oscillations on the unstimulated side. Ex-

changing these strengths results in the start of swimming on the stimulated side (for more details, see [Roberts et al., 2014]) and leads to a similar dynamics.

2.2.5 An overview of the sensory pathways

In tadpoles there are four sensory pathways which respond to the input signal from the external environment. These pathways activate in response to sensitive, mechanical or light stimuli and integrate these signals in the neuronal circuit to make movement decisions. Sensory cells in each of these pathways are responsible for the integration and they are located in different positions in the body. Here is an overview of the sensory pathways and cells, and of their role:

- **Skin touch -** The whole body surface is innervated by sensory RB neurons in the spinal cord [Roberts, 1980, Clarke et al., 1984] located under the skin [Boothby and Roberts, 1995]. The skin is excitable and propagates a single action potential when stimulated anywhere on the spinal cord [Roberts et al., 2010, Roberts, 1969], which can initiate swimming.

- **Head touch -** The head is innervated by sensory neurons in the trigeminal ganglia located under the skin [Roberts, 1980, Buhl et al., 2012, 2015]. Similar to the skin touch pathway, the touch of the head propagates single action potential when stimulated and can lead to the initiation of swimming.

- **Pineal eye -** Tadpoles have a pineal eye that is excited by light dimming [Foster and Roberts, 1982, Roberts, 1978]. Dimming of the light can lead to the initiation of swimming [Jamieson and Roberts, 2000]. If the light is dimmed when the tadpole is moving, swimming accelerates and the animal turns upward moving spirally towards the water surface [Jamieson and Roberts, 1999, 2000, Roberts et al., 2000]. Once it reaches the surface, the animal stops and attaches to it [Boothby and Roberts, 1992].

- **Head Pressure -** Sensory neurons innervate the head skin and cement gland and they are excited by mechanical pressure of the head, such as when tadpoles

bump into objects. This leads to the termination of swimming behaviour [Roberts and Blight, 1975, Roberts, 1980, Perrins et al., 2002].

In this thesis we study tadpoles that at the developmental stage 37/38. At this stage tadpoles have lateral eyes, but they do not seem to influence their behaviour. Little is known about the function of the nose in olfaction, the inner ears, sense of balance and if reflexes can be activated by Mauthner neurons [Roberts et al., 2010]. However, Mauthner neurons are present [Van Mier and Ten Donkelaar, 1984] and it has been suggested that they can drive trunk flexions in young larvae [Sillar and Robertson, 2009]. We therefore concentrated on these mechanical and light stimuli, because enough experimental evidences are known to model the corresponding pathways.

2.2.6 Synchrony in the functional model

As we previously described, a "normal" swimming behaviour is controlled by anti-phase activity of CPG neurons and muscle contractions between the two body sides. However, a puzzling observation that is rarely seen in experimental recordings is that the activity on both sides of the tadpole's body can show transient synchrony bouts, with CPG neurons and muscle active in-phase on both sides [Kahn and Roberts, 1982a,b, Soffe et al., 1984, Li et al., 2014a]. This synchronous firing has double the frequency of swimming and occurs more frequently at the beginning of a swimming episode. Figure 2.3 shows dIN and MN activity during synchrony and swimming. It is somewhat remarkable that the same very simple network can generate two different patterns of oscillatory activity, and we will use a computational model to investigate the conditions and mechanisms of synchrony in chapter 4.

2.3 The structure and function of the basal ganglia

In this section, we mainly review previous models related to the study of the basal ganglia and, in particular, action selection. Our aim here is to highlight that principles of neuronal oscillations and synchronisation are considered to be critical aspects of the general functioning of this circuit. A more systematic and complete review of the

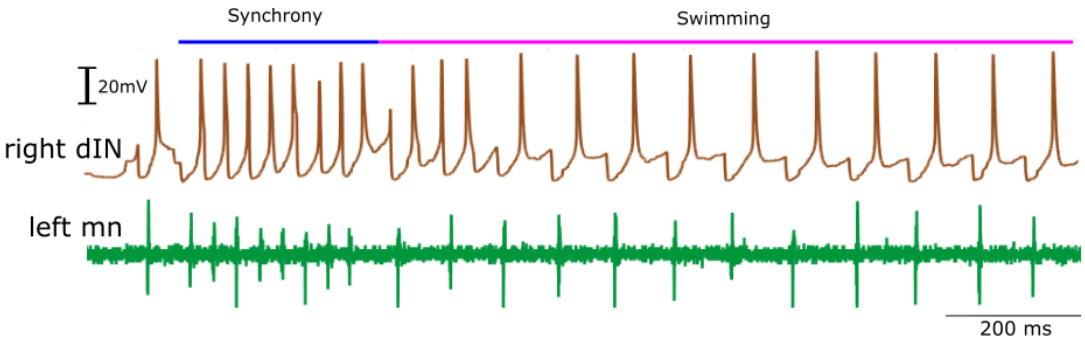

Figure 2.3: Pairwise recordings from a right dIN and left mn during following stimulation of the trunk skin. For an initial period of time (blue time line), activities of both neurons are locked in in-phase oscillations (synchrony). This is followed by a second time period (fuchsia time line), where the same activities are in anti-phase. Note how the frequency of synchrony is double that of swimming, and that dIN period becomes aperiodic in the transition from synchrony to swimming.

anatomy and function of the BG can be found in our published book chapter Merrison-Hort et al. [2017], with a particular emphasis on the role of deep brain stimulation for treating Parkinson's disease.

The basal ganglia (BG) are a group of subcortical nuclei in the brain of vertebrates which are thought to play a role in movement generation and action selection [Redgrave et al., 1999]. Oscillatory neuronal activity in the BG is the focus of much research, since many studies have shown that increased oscillatory synchronisation, particularly in the β band (10-30 Hz) is linked to the motor symptoms of Parkinson's disease [Joundi et al., 2012]. There are a number of reasons why widespread pathological oscillations may cause motor deficits, for example they may impair the ability to relay information [Mallet et al., 2008]. It has also been proposed that, in health, sporadic beta oscillations act as a global signal for maintenance of the current motor activity [Jenkinson and Brown, 2011]. For example, Hutchison et al. [2004] put forward the hypothesis that beta oscillations are enhanced in Parkinson's disease and prevent the generation of voluntary movements.

As well as these pathological oscillations, however, it has been proposed that oscillations may play a functional role in the physiological BG [De Lau and Breteler, 2006]. Previous works showed that the BG may be organised into multiple parallel "channels"

[Joundi et al., 2012, Merrison-Hort et al., 2013], with each channel corresponding to actions and/or body regions and/or specific muscles. These channels are believed to be organised both topographically and by frequency of oscillations [Alexander and Crutcher, 1990, Williams et al., 2002]. In a previous population-level modelling study it was shown that oscillations can be generated within the BG if they are considered as a set of weakly coupled parallel channels [Jankovic, 2008]. In the context of action selection, these channels must be coordinated to resolve the competition between different motor outputs [Chersi et al., 2013, Redgrave et al., 1999]. We will discuss this in chapter 6, where we propose a model of the mechanism of action selection in a sub-network of the BG formed by neurons in the subthalamic nucleus (STN) and in the internal part of the globus pallidus (GPi). In our model, activation of GPi groups represents the activation of a combination of BG channels representing an action.

There are several hypotheses related to synchronization of neural activity for explaining how these oscillations might appear and lead to the network function/dysfunction. Results reported in Bar-Gad et al. [2004] showed a complex phase-locking synchronisation between a stimulus and its response in most neurons in the globus pallidus. Some neurons increased their firing rate but the majority of neurons displayed partial inhibition during the stimulus train. The activities of simultaneously recorded neurons display rate correlation but no spike-to-spike correlation. *In vivo* experiments in epileptic and Parkinsonian rats show that BG neurons acts as self-sustained oscillators and can partially synchronise to external periodic stimuli [Velazquez et al., 2015]. Moreover, cortical input appears to be synchronised to neurons in the BG and contributes to generating oscillations. For example, oscillations in the STN-GPi network have been shown to be phase-locked to the cortical modulatory input and are abolished under transient inactivation of this cortical input [Magill et al., 2000]. Other experiments have shown that oscillations in Parkinsonian rats are also modulated by cortical rhythms [Magill et al., 2001].

Although significant progress has been made towards our understanding of how the

BG controls movements, many questions remain unanswered. Models have attempted to answer many of these questions, including the mechanisms that lead to pathological activities in PD and the restoration of physiological activity via deep brain stimulation. Network models of the BG can be divided into essentially two classes:

- Spiking models, in which equations represent the activity of individual neurons, possibly within one or more synaptically coupled populations.
- Models of interactive nuclei, where each nucleus (or population of neurons) is described by averaged population-level equations.

Here, we will briefly review these two approaches to computationally modelling neuronal activity, and describe how each has been applied to the study of the BG.

Probably the most well-known computational model of the BG is that of Terman et al. [2002]. This is a conductance-based spiking model of the interconnected subthalamic nucleus and globus pallidus, where each neuron is of single compartment Hodgkin-Huxley type, with a (simplified) set of ion channels chosen to represent the main electrophysiological features of the neurons in each nucleus. This model was used to investigate the emergence of different patterns of spiking behaviour, such as rhythmic bursting, under conditions of simulated Parkinson's disease. In a later paper the model was improved with parameter changes and the addition of thalamo-cortical relay neurons, and this revised model was used to consider the effects of deep brain stimulation on the activity in the network [Rubin and Terman, 2004]. A more advanced single compartment model of 500 neurons within the BG network was built by McIntyre and Hahn [2010], and was similarly used to investigate the effects of STN. These models have many advantages: since they are built of reasonably biologically-realistic conductance-based neurons, their outputs can be easily compared with electrophysiological data, and because they consist of networks of such neurons they can be used to examine how different patterns of synaptic connectivity produce different outputs. However, these models do not make use of any anatomical information about the spatial distribu-

tion of their constituent neurons. This limits their utility for studying the effects of spatially heterogeneous stimulation, such as deep brain stimulation, and makes it difficult to compare the results of simulations with spatially averaged experimental recordings, such as local field potentials.

A well-known larger scale spiking model of the BG is that developed by Humphries et al. [2006a]. This model comprises 960 spiking neurons across five BG nuclei, where each nucleus is divided into three parallel "channels". Each neuron in the model is based on the leaky integrate-and-fire formalism, with additional currents added to neurons in each sub-population to better reflect their physiological behaviour. Although the model does not contain any synaptic plasticity mechanisms, and cannot therefore exhibit learning, it is able to demonstrate robust selection of outputs based on simulated cortical input, in line with the proposed action selection role of the BG. Furthermore, this model is able to reproduce a number of experimental characteristics of the BG under both healthy and parkinsonian conditions. Chersi et al. [2013] developed a model that is similar to that of Humphries et al. [2006a], but with the addition of cortical and thalamic populations and a much larger number of neurons: 14,600 in total. These neurons are also of the leaky integrate-and-fire type, and are similarly organised into distinct channels. The main improvement in this model is the addition of spike timing dependent plasticity (STDP). Chersi and colleagues claim that their model may represent how the BG are able to facilitate learning of habitual motor responses to sensory input, and they demonstrate this by showing that a "virtual primate" is able to learn to perform a simple behavioral task when driven by the model.

The circuit formed by the reciprocally connected subthalamic nucleus (STN) and globus pallidus (GP) has been particularly well studied using models of interactive nuclei at the population level of modelling [Willshaw et al., 2002, Merrison-Hort et al., 2013, Holgado et al., 2010, Nevado-Holgado et al., 2014] as this circuit has been hypothesized to act as a neuronal pacemaker that generates pathological rhythms in Parkinson's disease.

Taking inspiration from these models, we will also consider this pacemaker property in our model of the STN neurons in chapter 6. The advantage of relatively simple mathematical models such as these is that they permit detailed mathematical analysis of the network, which can be used to determine, for example, the conditions under which oscillatory activity can occur. Another advantage of averaged models is that because they are computationally straightforward to simulate and typically have only a small number of parameters, they can be used alongside optimisation techniques in order to fit experimental measurements, such as average spike rates. This allows macroscopic-scale characteristics of the network, for example the relative overall synaptic connection strengths between populations, to be determined [Nevado-Holgado et al., 2014]. However, since these models are averaged over time and often represent the activity of many neurons as a single equation, they are unable to address many questions that are likely to be very important for understanding BG (dys)function. For example, averaged models cannot be used to study the information carried by precise spiking patterns, or to unravel the role played by the circuits formed between neurons of the same nucleus.

Chapter 3

A probabilistic model of neuronal connectivity in the *Xenopus* tadpole spinal cord

In this chapter we use computational models to clarify the relationship between the structure and function of a neuronal circuit. Although, in most animals, this connectivity varies between individuals, behaviour is often similar across a specie. What fundamental structural properties are shared across individual networks that define this behaviour? We describe a probabilistic model of connectivity in the hatchling Xenopus tadpole spinal cord which, when combined with a spiking model, reliably produces rhythmic activity corresponding to swimming. The probabilistic model allows calculation of structural characteristics that reflect common network properties, independent of individual network realisations. We use these characteristics to study examples of neuronal dynamics, in the complete network and various sub-networks, and this allows us to explain the basis for key experimental findings, and make predictions. We also study how structural and functional features differ between detailed anatomical connectomes and those generated by our new, simpler, model.

Information processing in the brain is based on the communication between spiking neurons that are embedded in a network of synaptic connections. Clarifying the interplay between network connectivity and functionality is a key part of understanding how the brain generates functional behaviours [Sporns et al., 2005, Marder and Calabrese, 1996, Newman, 2003]. Studying this relationship is difficult because nervous system connectivity usually varies considerably between individuals. Despite this variation each individual behaves in approximately the same way, especially in the case of simple animals. This commonality of behaviour suggests that there are some fundamental organisational principles that underlie the structure of a species' nervous system. How can we identify these fundamental properties that are shared across individuals and allow the nervous system to function correctly?

In this chapter we attempt to answer this question in the case of the hatchling Xenopus tadpole. Whole cell recordings and anatomical measurements of neurons, combined with computational modelling, have uncovered many important details regarding the neuronal network that controls swimming in hatchling tadpoles [Roberts et al., 2010, 2014].

We describe a new probabilistic model of connectivity, which is generalised from a large number of connectomes generated by the anatomical model (see chapter 2). This probabilistic model is a matrix that specifies the probability of connection between each pair of neurons. Being derived from multiple biologically realistic (anatomical) connectomes, the probabilistic model reflects the anatomical structure of the biological system. An important advantage of the probabilistic model is that it is simple enough that we can analyse the properties of the model itself, rather than individual connectome realisations. We use the probabilistic model to calculate structural properties of the tadpole network. These results are general, and therefore should reflect the fundamental organisational principles that we aim to uncover here.

A potential advantage of the probabilistic model is that it can be used to easily generate connectome realisations by sampling from the probability matrix, without detailed simulation of neuronal growth. This enhances its potential value as a tool for studying the functional properties of the network when combined with an appropriate physiological model. Multiple functional simulations of probabilistic connectomes demonstrated a reliable pattern of rhythmic activity, qualitatively like tadpole swimming and as seen in previous modelling [Roberts et al., 2014]. Thus, the generalised probabilistic model shares structural and functional properties with the real biological object.

A common approach for studying the relationship between the structure and function of neuronal networks is to use methods from graph theory, a branch of mathematics that applies to a variety of scientific fields, including linguistics, sociology, physics, biological and neural sciences [Newman et al., 2002, Albert and Barabási, 2002]. These methods are increasingly used to study connectivity of different neuronal networks [Bullmore and

Sporns, 2009, Kaiser, 2011, Rubinov and Sporns, 2010, Bassett and Sporns, 2017]: *C. elegans* [Varshney et al., 2011, Kaiser and Hilgetag, 2006], vertebrate systems [Stobb et al., 2012], cat and macaque cortical structures [Sporns et al., 2007, de Reus and van den Heuvel, 2013, Humphries et al., 2006b].

In this chapter some of these measures are discussed and applied to analyse and compare the tadpole connectome with the ones of other animals. By combining these measures with the functional model, we show that the neuronal connectivity in the tadpole has some specific structural features, and we suggest how this specificity relates to its swimming behaviour. For example, we found that the network has an abundance of reciprocal connections and we demonstrate the importance of these connections by showing how, by removing them, the network is not able to reproduce normal patterns of swimming oscillations.

The comparisons with other animals show interesting similarities and differences. For example, similar to the *C. elegans* connectome [Varshney et al., 2011, Kaiser and Hilgetag, 2006], the tadpole connectome has low density, low average path length, high robustness, modular organisation, minimal number of long distance connections and the same overrepresented motifs - including feed-forward loops. Differently from *C. elegans* and other animals, we found that the overrepresented motifs in the tadpole and zebrafish spinal connectomes are more similar to null-model networks possessing a random rather than ring-like topologies. In the case of tadpoles, we also demonstrate that the network is not of the small-world type [Watts and Strogatz, 1998]. Overall, these comparisons suggest that graph measures describe properties of each specific neuronal circuit, and should therefore be used with care. In tadpoles, we both speculate and demonstrate using simulations a possible functional role of each of this measures.

It was shown that the *C. elegans* connectome is also heterogeneous and has a hub structure [Towlson et al., 2013]: most neurons have a low number of connections but there are several highly connected "hubs". Hubs have been identified in many brain networks [Achard et al., 2006, Eguiluz et al., 2005], they are likely to be formed at an

early stage of development [Varier and Kaiser, 2011] and are thought to be critical to guarantee the robustness of the network [Albert et al., 2000, Barabási and Albert, 1999]. However, not all brain circuits have hubs; for example, they have not been found in the brainstem reticular formation [Humphries et al., 2006b] or zebrafish nervous system [Stobb et al., 2012]. Using the probabilistic model, we estimate the heterogeneity [Hu and Wang, 2008, Estrada, 2010] and connection degree distributions [Barabási and Albert, 1999, Sporns et al., 2007, Varshney et al., 2011] of the tadpole's spinal cord network. We found that the generalised tadpole network is not scale-free and that hubs do not exist; therefore in this respect the generalised tadpole network differs from the *C. elegans* connectome.

When comparing the simulations of the functional model using anatomical and probabilistic connectomes, we found some quantitative differences. These differences revealed that caution is required to avoid pitfalls when employing the probabilistic approach to study real biological activity. Specifically, we found the variance in the number of incoming connections (in-degree) or out-going connections (out-degree) of each neuron is higher in anatomical rather than a probabilistic connectomes. As a result of this finding, we observed that the period of the rhythm was longer in probabilistic connectomes. We can explain why the generalisation process affects the swimming period, and show how it is possible to accurately predict the period of swimming using only structural properties of the connectome. We then show how, by making suitable parameter adjustments, we can match the functionality of the probabilistic connectomes to that of the animal and anatomical connectomes. This makes it possible to use the probabilistic approach as a tool for studying real biological activity as well as fundamental structural properties of networks.

Despite the differences between anatomical and probabilistic models, we demonstrate several important advantages of using the probabilistic model in comparison to the anatomical one. For example, we could predict the position of commissural interneurons (cINs) that are active during swimming, which cannot be explained by the anatomi-

cal model. Specifically, our simulations show that cINs in rostral positions are less likely to fire reliably than those in caudal positions. Moreover, the probabilistic model allowed us to easily design new computational experiments that helped to clarify the following experimental findings.

By studying the connectivity of CPG neurons specifically, we show that the minimal swimming subnetwork includes neurons of two types: inhibitory commissural interneurons (cINs) and excitatory descending interneurons (dINs). Similar to experiments with the surgically isolated half semi-CNS [Soffe, 1989], we found that the network of interconnected dINs on one body side could still generate rhythmic activity even without commissarial inhibition. It is known from experimental measurements that some dINs have both descending and ascending axons [Roberts et al., 2010]. Our simulations of the model without ascending dIN axons show that the ascending connections play a key role in swimming and their deletion leads to pathological activity.

To summarise, in this chapter we design a simple probabilistic model (meta-model) which reflects some structural features of anatomical connectomes. We also show that it can be used to study how these features relate to real behaviour by making suitable adjustments in synaptic strengths. We consider this investigation of the tadpole spinal cord as an important example of a technique that can be widely applied to study the nervous system of other animals.

3.1 Derivation of the probabilistic connectivity model

The probabilistic connectivity model is derived from multiple connectomes generated by our existing anatomical model: a developmentally-inspired model which is biologically realistic and incorporates a large number of biological measurements [Borisyuk et al., 2014, Li et al., 2007a, Borisyuk et al., 2011]. The anatomical model simulates axon growth guided by chemical gradients, with model parameters that are chosen by fitting the generated axons to experimental measurements. As the growing axons intersect dendrites, which are allocated along the body according to experimental measurements, synapses form and make connections between neurons. Here we explain

some details of the anatomical model that are important for understanding the new probabilistic model (for more details about the anatomical model, see the Introduction). The anatomical model includes N=1382 neurons of the seven types known to generate the swimming response. The network is divided between neurons in the sensory pathway (RB, dlc and dla), CPG neurons (dIN, cIN and aIN), and output motor neurons (mn). Sensory pathway neurons deliver sensory stimulation to CPG neurons. CPG neurons are responsible for the generation and maintenance of the swimming activity pattern. Motor neurons (mn) deliver CPG output to muscles and generate locomotion. The model is simplified by fixing the number of cells for each neural type, with neurons of each type equally divided between the left and right body sides (Table 3.1). Simulation of the anatomical model results in a network with approximately 83,000 synapses on average. For a full description of the anatomical model and its implementation, see [Borisyuk et al., 2014, Roberts et al., 2014].

Importantly, the anatomical model includes stochastic components, so repeatedly running the model produces different connectomes with different numbers of connections and connection distributions. In particular, rostro-caudal coordinates of neurons can vary between connectomes. However, since the number of neurons of each type is kept constant it is possible to find a one-to-one correspondence between any two generated connectomes. First, we ordered the cell types (RB, dla, dlc, aIN, cIN, dIN, mn) and second, for each cell type we ordered neurons of that type according their longitudinal position (or the rostro-caudal (RC) coordinate) in ascending order from head to tail. For example, in any connectome neuron #1 is the most rostral RB neuron on the left side of the body, while neuron #62 is the most caudal left-side RB ; neurons #63-126 are the right-side RB neurons; neurons #127-146 and neurons #147-174 are the dla neurons on the left and right sides respectively, etc. This ordering of cells is universal and does not depend on a particular connectome; therefore, we can enumerate all neurons in a universal way, providing a one-to-one correspondence between generated connectomes.

	RB	dlc	aIN	cIN	dIN	mn	dla
nuumber of cells	126	104	136	384	236	338	58

Table 3.1: Number of cells for each neural type in the connectome model

To define the probabilistic model we used the universal enumeration of neurons and considered the matrix of probabilities $P = (p_{i,j})$ where $p_{i,j}$ is the probability that there is a synaptic connection from neuron i to neuron j. Here N=1382 is the total number of neurons. We defined the random Bernoulli variable $X_{i,j} \in 0, 1$ where $X_{i,j} = 1$ means that there is a directed connection from i to j and the probability $Pr(X_{i,j} = 1) = p_{i,j}$. To calculate an estimate of this probability $(\hat{p}_{i,j})$, we generated K=1000 connectomes and calculated the frequency of appearance of this directed connection: $\hat{p}_{i,j} = \frac{M}{K}$, where M is the number of connectomes with a connection from neuron i to neuron j. The RC-coordinate of each neuron is defined by the averaging the RC-coordinates across the K generated connectomes. The central limit theorem provides the error estimation of each entry of the probability matrix $p_{i,j}$: the length of the binomial confidence interval with 95% confidence is given by $e_{i,j} \approx 2\frac{1.96}{\sqrt{M}}\sqrt{\hat{p}_{i,j}(1-\hat{p}_{i,j})}$. The maximum of this error's estimate corresponds to $\hat{p}_{i,j} = 0.5$, therefore, $max_{i,j}(e_{i,j}) \approx 0.06$.

The probabilities of directed connections between all neurons of the swimming network are shown in Figure 3.1A. All probabilities are between $\hat{p}_{i,j} = 0$ (no connections) to $\hat{p}_{i,j} = 0.69$. To visualise these probabilities we use a colorscale, where white colours correspond to $\hat{p}_{i,j} = 0$, blue and red colours correspond to high inhibitory and excitatory connection probabilities, respectively. Note: here and below we use the same notation $\hat{p}_{i,j}$ for both the probabilities and their estimates.

As an example, 3.1B shows the sub-matrix corresponding to aIN-aIN inhibitory connections. There is a white diagonal line which results from the fact that neurons cannot make connections with themselves. In fact, similar almost-diagonal lines can be seen in all of the other sub-matrices due to a feature of the growth model that prevents neurons contacting very nearby neurons. Close to the diagonal line in 3.1B the shading is very bright, but this fades to blue away from the diagonal. This results from the fact that

the probability of two neurons being connected decreases with the distance between them. For aINs, the shading is brighter below the diagonal line, which reflects the fact that their axons are mainly in the ascending direction, making a given aIN more likely to contact aINs that are located more rostrally. While the aIN-aIN example is relatively simple to understand, neurons with more complicated growth patterns have sub-matrices with more complex structure - for example in the case of dIN-dIN connections. The matrix P can be used to generate a specific adjacency matrix of directed connections (connectome) $A = (a_{i,j})$, where $a_{i,j} \in \{0, 1\}$ and $a_{i,j} = 1$ indicates existence of the connection from neuron i to neuron j. This matrix A is a particular realisation of independent Bernoulli variables. We then used these specific adjacency matrices ("probabilistic connectomes") to explore their functional properties by mapping the connectomes onto our functional model to study the spiking activity in the swim network in response to stimulation.

3.2 Graph theory methods

We assume that a structure of the neuronal network is represented by a graph, which includes units (nodes) and connections (edges). In our study of tadpoles, nodes represent neurons and edges represent directed synaptic connections from an origin node to a destination node. We do not consider a connection from the node to itself. We can order nodes in the graph according to indexes $j = 1, ..., N$, where N is the total number of nodes. In fact we do not distinguish between graphs and networks and use both terms.

A tadpole connectome (anatomical or probabilistic) can be represented as a binary adjacency matrix $A = (a_{ij})$, where a_{ij}=1 indicates the presence of a connection from node i to node j, and $a_{ij} = 0$ indicates the absence of such connection. The probabilistic matrix of connectivity P shown in 3.1 is a weighted graph $P = (p_{ij})$, where p_{ij} is the probability of directed connection from node i to node j.

Equivalently, a graph G can be considered as a pair of two sets: $G = (V, E)$, where V is the set of N nodes and E is the set of edges. Elements of E are direct connections

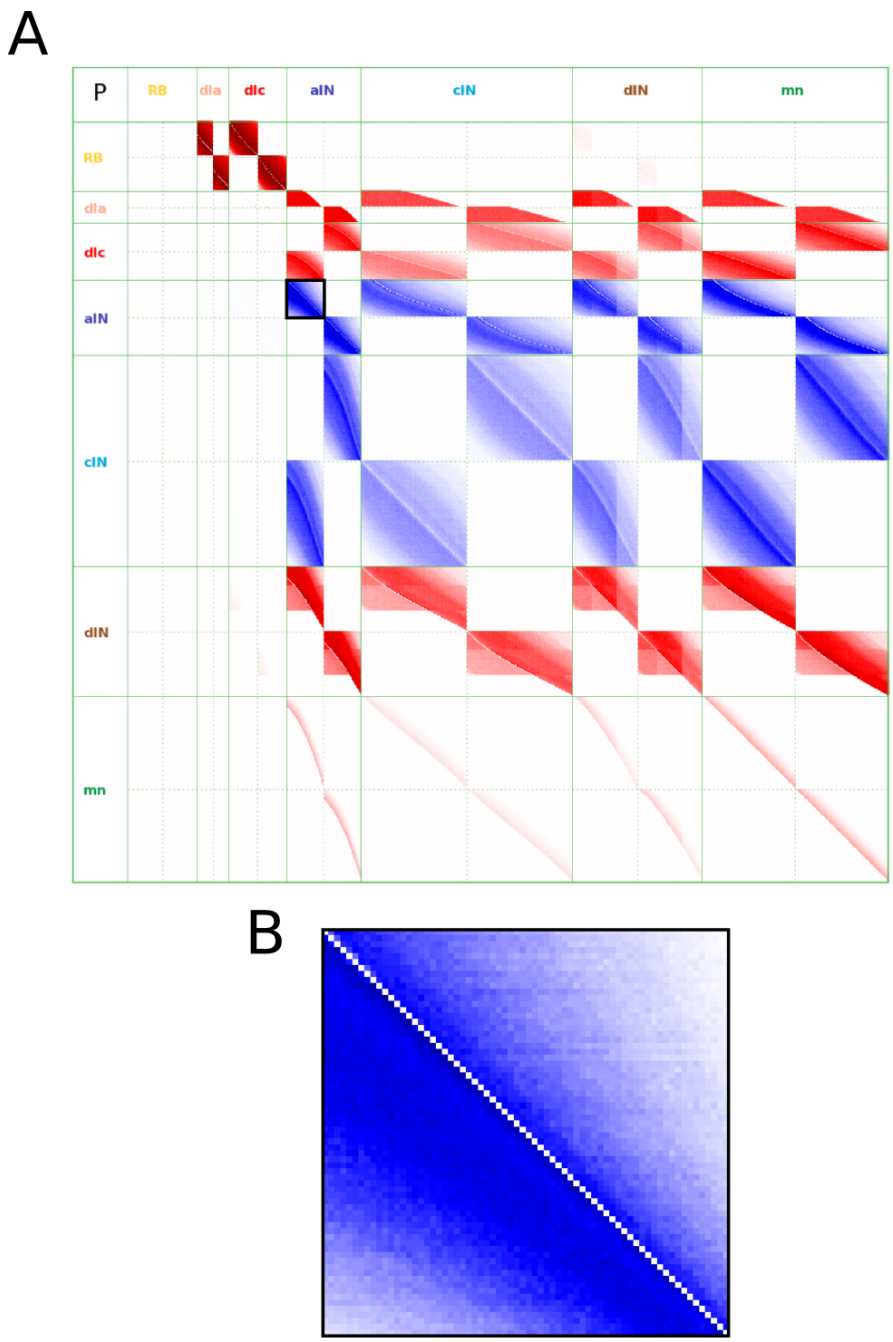

Figure 3.1: Visualisation of the probability matrix P. A. Image representation of the complete matrix $P = (p_{i,j})$, where the intensity of the pixel in row i and column j represents the value of the probability $p_{i,j}$. White intensity corresponds to connection probability zero and blue/red intensity corresponds inhibitory/excitatory connection with probability one. Rows and columns corresponding to neurons of each of the seven types are separated by solid green lines. These lines separate the matrix into symmetrical sub-blocks. Within each sub-block vertical and horizontal dotted lines separate the left body side (top rows and left columns) from the right body side (bottom rows and right columns). In each sub-block neurons are ordered according to increasing rostro-caudal position B. Zoom of the left body side aINaIN sub-block (marked by a red square in A)

between pair of elements in V. Therefore for each edge $e \in E$ there are two nodes $u, v \in V$ connected by a directed connection, and we write $e = e(u, v)$, where e represents a binary or weighted connection from node u to node v.

3.2.1 Network density

The density of a binary network $W = (w_{ij})$ is the proportion of existing edges in the network $k = \sum_{i,j=1}^{N} w_{ij}$ relative to the total possible number of connections $N(N-1)$. Therefore, the density ranges from 0 (graph with no connections) and 1 (fully connected graph), and it is a measure that indicates the sparseness of the network. The density of brain networks is typically small. For example, a density of 0.03 was found in the nematode worm C. elegans [Kaiser and Hilgetag, 2006], while the density of cortical areas and pathways interconnecting them ranges between 0.1 and 0.3 [Kaiser, 2011].

3.2.2 Degrees

The degree is a measure of the centrality of individual nodes of a graph. For directed networks, it consists in counting the number of incoming connections I_j (in-degree) or outgoing connections O_j (out-degree) of each node j. For an adjacency matrix $A = (a_{ij})$ these degrees are given by the following formulas:

$$I_j = \sum_{i=1}^{N} a_{ji} \quad O_j = \sum_{i=1}^{N} a_{ij} \tag{3.1}$$

The probabilistic matrix $P = (\hat{p_{ij}})$ can be used to generate single connectome realisations drawn by independent Bernoulli random variables (see previous paragraph). Therefore, the in-degree I_j and the out-degree O_j for each node j are also random variables, and we can analytically derive their mathematical expectations using the following formulas:

$$< I_j >= \sum_{i=1}^{N} p_{ji} \quad < O_j >= \sum_{i=1}^{N} p_{ij} \tag{3.2}$$

These formulas follow from the fact that the random variables I_j and O_j have the Pois-

son binomial distribution [Sprott, 1958]. Similarly, the formulas for the standard deviation of these random variables are the following:

$$std(I_j) = \sqrt{\sum_{i=1}^{N} p_{ji}} \quad std(O_j) = sqrt\sum_{i=1}^{N} p_{ij}$$

3.2.3 Scale-free graphs and degree heterogeneity

A key structural property of a graph is whether or not it is a scale-free graph. A scale-free graph contains some "hub" nodes with the large number of connections in comparison with other nodes. Networks with hubs are important because they are particularly robust to removal of random nodes [Barabási and Albert, 1999]. One way in which a network can be categorised as scale-free is by quantifying the heterogeneity of its nodes' in- or out-degrees. We use the so-called heterogeneity index H [Hu and Wang, 2008] for in- and out-degree distributions to estimate the variability of in and out-degrees. We compute this index to confirm that it is less than the threshold for scale-free networks [Hu and Wang, 2008]. The heterogeneity is given by the following formula:

$$H = \frac{\sum_{i=1}^{N}\sum_{j=1}^{N}|d_i - d_j|}{2N^2\bar{d}}$$

Here d_i is either in- or out-degree of neuron i, $\bar{d} = \sum_i d_i$ is the average degree (either in- or out-), and N is the number of neurons. Note, we calculate the heterogeneity index using the probabilistic model without considering any particular connectome.

3.2.4 Strongly connected component and path length

The strongly connected component of a binary graph $G = (V, E)$ is a sub-graph $G' = (V', E')$ containing the maximal number of nodes and edges of G such that all node pair are connected by a direct or a sequence of intermediate edges (called a path). In symbols this writes:

$u, v \in V'$ if $\exists e(u, w_1), e(w_1, w_2), ..., e(w_m, v) \in E$ for some $m \in \mathbb{N}$ and $w_1, ..., w_m \in V'$

By definition, every pair of nodes in the strongly connected component $G' = (V', E')$ of a graph $G = (V, E)$ is connected by a path. The length of any of paths is equal to the number m of edges connecting nodes u and v. The shortest path length $d_{u,v}$ for each pair of nodes $u, v \in V'$ is the path with minimal length connecting u and v. Therefore, the shortest path length is the length of the shortest communication pathway between nodes, and it is the most effective way to quickly transfer information across nodes. The average path length of the graph G is simply defined as the average length of the shortest paths between all node pairs in the strongly connected component G' [Watts and Strogatz, 1998]:

$$L = \frac{1}{N(N-1)} \sum_{u,v \in V': u \neq v} d_{u,v}$$

The average path length L is therefore a global characteristic indicating how effective is the synaptic integration between nodes. Generally, paths of various lengths other than the shortest path could be important for processing the information in networks. In brain networks, however, longer paths are likely to be a less effective method of synaptic integration rather than short paths. The shortest path length has been popular and used, together with the clustering coefficient (see next sections), to demonstrate the small world property in several real world networks [Watts and Strogatz, 1998], which will be discussed further in the results section. We use Tarjan's algorithm [Tarjan, 1972] to compute numerically the strongly connected component and Dijkstra's algorithm [Dijkstra, 1959] to compute the shortest path of the tadpole's connectome.

3.2.5 Clustering coefficient

The clustering coefficient is a local measure of segregation around individual nodes. It involves counting the number of triangles around such nodes, with high number of such triangles implying segregation. Locally, the clustering coefficient of a node j is the fraction of triangles t_j around the node, or equivalently, the probability CC_j that the neighbours of node j are connected between each others. Globally, the clustering

coefficient of the whole network is defined by the average clustering coefficient of all nodes. For undirected networks (networks where all edges are bidirectional) this simply writes as:

$$CC = \frac{1}{N}\sum_j CC_j = \frac{1}{N}\sum_j \frac{t_j}{d_j(d_j-1)}, \tag{3.3}$$

where t_j is the number of triangles around node j, and d_j is the degree of node j (equivalent to both in- or our-degrees). If $d_j = 0$ or 1, the clustering coefficient for node j is 0. In the case of directed networks, the clustering coefficient depends on the directionality of connections and can therefore be defined in four different ways for any neuron j in the network [Fagiolo, 2007]: the inward, outward, middle and cycle clustering coefficients. Figure 3.2 shows a definition of these coefficients for each node in a generic graph defined by an adjacency matrix $A = (A_{ij})$. For weighted graphs $W = (w_{ij})$, the matrix A in these formulas is replaced by $\hat{W} = (w_{ij}^{1/3})$. To calculate the clustering coefficients for the whole graph in the case of directed connections, we simply average the local clustering coefficients across all the nodes in the graph, like in the case of a directed network (Equation 3.3). We will refer to the clustering of the network simply as the inward, outward, middle and cycle clustering coefficients, and use the abbreviations CC^{in}, CC^{out}, CC^{mid} and CC^{cyc}, respectively. On the right side of Figure 3.2 we report a simple interpretation of each of these local measures.

Note 1. It is obvious from this figure that the cycle clustering coefficient only counts the number of cyclic triangular patterns (or cycle loops), while all the other three clustering coefficients count the number of feed-forward loops.

Note 2. It is easy to prove that any commissural neuron i in the tadpole connectome is such that $CC_i^{mid} = 0$. Indeed, by contradiction method, let us consider a commissural neuron i which receives a connection from a sender neuron and sends the connection to a receiver neuron. Then, according to the definition of middle clustering coefficient, the sender neuron would be connected to one neuron on each side. Therefore, it contradicts to the property of tadpole neurons: a neuron can be either ipsilateral or commissural.

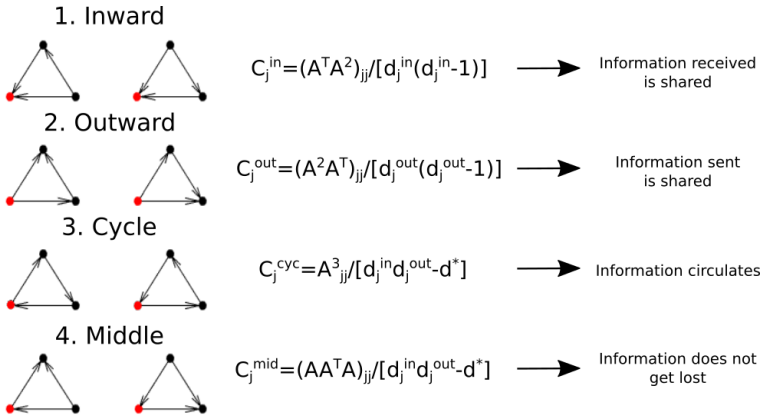

Figure 3.2: Local clustering coefficients measures for a node j (red dot) in a binary or weighted directed network A. Depending on the directions of connections of neighbouring nodes (black dots), there are four clustering coefficient (from top to bottom). In this figure, d_j^{in} and d_j^{out} are the in- and out-degrees of node j, respectively. d_j^* is the number of nodes that have reciprocal connections with node j. In the right, we report a simple interpretation of each clustering coefficients.

3.2.6 Null graphs

Typically, some of the structural properties of a network occur significantly more or less often than we would expect if these networks were organised in a random or ordered (lattice) topologies [Bullmore and Sporns, 2012]. Indeed, these properties often fall in between completely random and completely ordered networks (called "null-models") that can be constructed from our network of study (called "original network"). We will use these null-models to compare some of their graph properties with the properties of the tadpole connectome and of other animals' connectomes. By making these comparisons we will show that some of these properties are lost in the randomisation process used to construct these null-models. Thus, we will demonstrate that the connectivity of our original network is specific (not random nor lattice), and we suggest how such specificity might be related the network function. We refer to random and lattice null-models as benchmark random and lattice networks, respectively. In the next section we are going to explain how to construct these networks.

Benchmark random and lattice networks are artificial graphs generated from the original network (Figure 3.3) using a randomisation algorithm. These networks have the

same number of nodes and the same node degrees as the original network (degree-preserving). These properties guarantee that the comparisons we are going to make are not biased. Both benchmark random networks are generated using a Markov chain rewiring algorithm that starts by considering the original network and fixing a (large) number $c >> 1$ of iteration steps [Maslov and Sneppen, 2002]. The algorithm iterates c times searching for four nodes $u, v, w, t \in V$ that are connected through edges $e(u, v)$ and $e(w, t)$, but not by edges from $e(u, w)$ and from $e(v, t)$ (Figure 3.3). Once the algorithm detects such nodes, it deletes $e(u, v)$ and $e(w, t)$ from the network and adds two new edges $e(u, w)$ and $e(v, t)$ (rewiring step). When the number of iterations reaches c, the network is considered fully randomised. This network will be our random benchmark network. For creating a lattice benchmark network the algorithm works in a similar way, except for an additional condition on the rewiring step based on the distance between node indexes. To define this distance, we rewire nodes according to their indexes. Therefore, let us change reference to nodes u, w, v, t with indexed nodes i_1, j_1, i_2, j_2, respectively. The additional condition for rewiring in the lattice network generation is:

$$|i_1 + j_2| + |i_2 + j_1| < |i_1 + j_1| + |i_2 + j_2|$$

This condition guarantees that the reconnected network is organised as a ring or lattice (Figure 3.3).

3.2.7 Motifs measures

The clustering coefficient is a particular case of a more general graph property called motifs. The clustering coefficient measures the number of triangular motifs, i.e. patterns of three connected nodes in the network. In general, motifs are defined as sub-network of any size $M = 2, 3, 4, ...$, where M is the number of nodes in the motif pattern considered, such as $M = 3$ for triangular motifs or $M = 4$ for square motifs. For $M = 2$ nodes (non-ordered pair of nodes A and B) there are two types of motifs: 1) a connection in one direction, $A \rightarrow B$, 2) a bidirectional connection, $A \leftrightarrow B$. For $M = 3$ nodes, there are 13 different triangular motifs in which three nodes can be connected. Figure 3.4

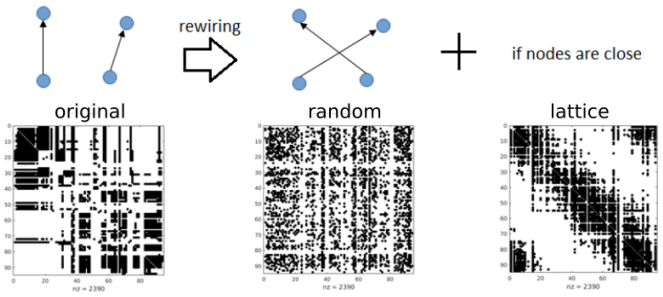

Figure 3.3: Sketch of the rewiring algorithms for generating benchmark random and lattice networks with an example network, the macaque cortex on one hemisphere, obtained from [Kaiser and Hilgetag, 2006]. The algorithm start from an original network (bottom left) and ends by generating either a random (bottom center) or a lattice network (bottom right). In each rewiring step, two edges (top left) are destroyed and two new edges generated (top center). In the case of a lattice generation, an additional condition on the vicinity of the nodes is given. More details are given in the text.

shows these 13 triangular motifs and their indexing (note that these indexes are used in the Result section to identify motifs). For $M = 4$ nodes, there are 199 different square motifs. We do not report a figure showing all these different motifs and their indexes for $M > 3$, as it is not relevant for the results presented in this chapter.

Note. The definition of motifs which we use, corresponds to the definition of structural motifs in some other works (see [Sporns and Kötter, 2004] for more details).

Of particular interest are "over-represented" motifs occurring in a network significantly more often than in random benchmark networks (see null model section). By having this property, over-represented motifs are believed to have some functional significance in the network [Milo et al., 2002, Kaiser, 2011]. To decide if a motif is overrepresented in the original network, we compare the motif counts between the original and benchmark random networks. Specifically, we generated 100 random benchmark networks and calculated the frequency of occurrence of each motif in the original (N_{real}) and in these random networks ($N_{rand} \pm SD$), following the approach described in Milo et al. [2002]. To detect if a motif is over-represented in the original network we checked if 1) the probability that this motif occurs more times in random lattice networks rather than in the original network is smaller than $P = 0.01$ (P-value), 2) this motif appears at least 4 times in the original network , 3) the number of appearances in the original network

Figure 3.4: Overview of all possible 13 triangular motifs.

is significantly larger than in the randomised networks: $N_{real} - N_{rand} > 0.1N_{rand}$. 4) The Z-score of over-represented motifs is positive and sufficiently high ($Z > 20$). This Z-score is defined as $Z = (N_{real} - N_{rand})/SD$, to quantify the significance of the over-representation of such motif in the original network.

The histogram of the number all motifs of a selected size M is called the motif spectrum of the network for that size, and it is indexed using the same motif indexes (like the indexes shown in Figure 3.4). Plotting the motif spectra of a network and its benchmark random networks helps to quickly visualise which motifs are likely to be over-represented and to make comparisons between these networks. In addition to this visualisation, we will use a normalised Euclidean distance between these motif spectra to quantify similarities. Given the vector of frequencies for the real network $f = (f_1, ..., f_N)$ and for the mean frequencies $f^X = (f_1^X, ..., f_N^X)$ from several repetition of random or lattice networks X, this distance is given by:

$$d = d(f, f^X) = \frac{\sqrt{\sum_{i=1}^{N}(f_i - f_i^X)^2}}{\sum_{i=1}^{N} f_i}$$

3.2.8 Functional model of spiking activity

Graph theoretical approaches describe the structural properties by considering networks as static objects. However, brain networks are not static objects, as their function depends on the relationship between their intrinsic structural and dynamical properties [Bassett et al., 2018, Bassett and Sporns, 2017]. Therefore, to investigate the function of the tadpole connectome in more detail, we simulate the spiking activity using the connectomes generated by the probabilistic model. We produced specific adjacency matrices from the probability matrix and used them in a functional model described in the Introduction and in [Ferrario et al., 2018a, Roberts et al., 2014]. Simulations of neu-

ral activity described in this chapter were performed using NEURON 7.3 [Carnevale and Hines, 2006] with a fixed time-step of 0.01ms.

3.3 Results

PART I - Structural Properties

3.3.1 Modular structure defined by the degree measure

All neurons in the tadpole connectome can be divided into three main groups, based on what we know about their function during swimming (see the Introduction and Roberts et al. [2010, 2014]):

- **Sensory and sensory pathway neurons (RB, dIc and dIa) - starters:** They are active only at the start of a swimming episode (<15ms after stimulation). They internally represent the sensory stimuli and transmit it to neurons in the other two groups for further processing.
- **Interneurons (INs - aINs, cINs, dINs):** They are CPG neurons responsible for processing the sensory input, rhythm generation and transmission to output motor neurons. Except for aINs, interneurons tend to fire at almost every cycle of swimming. For this reason, they are believed to be responsible for the generation and maintenance of swimming oscillations.
- **Motor neurons (MNs):** They are the "output" neurons and their firing controls the contraction of muscles.

Figure 3.5 shows a schematic diagram of these three functional groups (starters, IN and MN) in tadpole. Arrows represent directional synaptic contacts between members of each group. Numbers above each arrow are the average out-degree across all neurons in the pre-synaptic group to all neurons in the post-synaptic group. Remarkably, this connectivity diagram, which is based on only structural connectivity of the network (the degrees), confirms the main functional

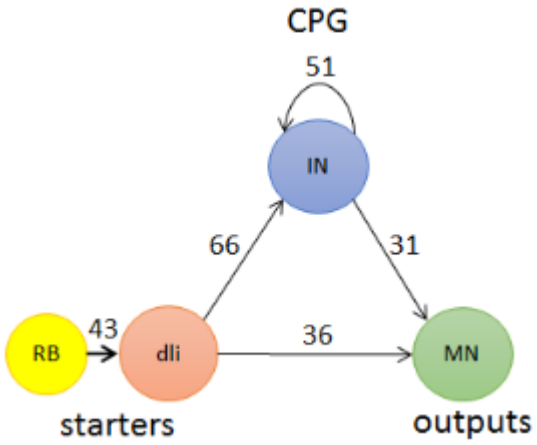

Figure 3.5: Classification of neurons in the connectome. We divide neurons between sensory/sensory pathway neurons (RB, dlas, dlcs), interneurons (IN) and motoneurons (MN). Numbers along each arrow represent the average number of connections a single neuron in the presynaptic group forms towards neurons in the postsynaptic group. Average numbers of connections that appear less than 5 times are ignored.

role of each neural group. Starters receive no connections from other groups, which confirms their role as "input" cells. They also send many connections to CPG neurons and mns, suggesting their role as transmitters. The fact that the CPG population have many recurrent connections suggests that their role is to process the information and sustain it over time. MNs receive many connections, but they do not send connections to other neurons and this suggests their role as output cells.

3.3.2 Network density and average path length

A common structural feature among many neuronal circuits is sparseness of connections. This can be easily observed from Figure 3.1, where low probabilities occur more often than high probabilities. Another way to show this is to measure the network density, which is the total number of connections in the network relative to the number of potential connections. Assuming that the network has E edges and N nodes its density is $d = E/(N(N-1))$. As expected, the density of the tadpole connectome is low, $d = 0.09$. This is similar, for ex-

ample, to the density of the nematode worm C. elegans, $d = 0.03$ [Kaiser and Hilgetag, 2006].

The network density essentially measures the probability that any randomly picked nodes in the network are connected by a directed connection. This concept leads to the definition of a minimal path between a sender node and a receiver node, which is the minimal number of directed connections from the sender to the receiver, or minimal path length. This measure can be extended to the whole network by defining its strongly connected component (see Methods). Since neurons tend to form connections mostly with other spatially neighbouring neurons [Bullmore and Sporns, 2012], we would expect a high average path length in both the tadpole and *C.elegans* connectomes. However, it turns out that these lengths are much lower than in a lattice benchmark topologies and much higher than in a random benchmark network (Table 3.2). Having this property has been suggested to enhance a quick signal integration and synchronisability in the network [Watts and Strogatz, 1998, Bullmore and Sporns, 2012].

In the case of tadpoles, we randomly generated 80 connectomes using the probabilistic model and we calculated the strongly connected component for each of these connectomes. The number of neurons in the highest populated strongly connected component is 1103 ± 6.7 (80% of the total population). Remarkably, the *C. elegans* connectome has a similar fraction of cells in its highest populated strongly connected component (85% of the total population) [Varshney et al., 2011].

We hypothesise that this feature might enhance robustness of a network to random removal of connections. In the case of tadpole, we tested this hypothesis by removing a percentage of connections in the network and checking if simulations of the functional model (see Introduction) could still generate a robust

	Real	Random	Lattice
Xenopus tadpole	2.3	2.2	5
C. elegans	4	3	5.2

Table 3.2: Average path length in tadpoles and C. elegans in the original, randomised and lattice-random networks.

anti-phase swimming oscillatory activity (repeating the results of Roberts et al. [2014]). Simulations with connectomes where less than 40% of connections have been randomly removed, generate swimming oscillations for every randomly generated connectome. After removing 40% of connections, simulations still produce swimming oscillations with a realistic period (average is 63 ms) in 87% of simulations. Removing 45% of connections, only 25% of simulations generate swimming oscillations. Removing more than 45% of these connections results in no simulations generating swimming oscillations. These results demonstrate that the network is indeed very robust, as we need to remove more than 40% of connections to destroy its functionality.

3.3.3 Distributions of connection lengths

The results presented in the previous section have shown that tadpole's connectome and other neuronal circuits have similar structural properties, including a low density of connections, low path length and high robustness. Another shared topological feature is the tendency of these networks to form an unexpectedly high number of long range connections. There are multiple interpretations on the functional role of this property. Firstly, it would allow propagating the information more quickly in the network by minimising the number of processing paths [Kaiser and Hilgetag, 2006]. Secondly, it would minimise the metabolic costs by generating shorter connections [Bullmore and Sporns, 2012].

To clarify if the tadpole also shows this feature, we analysed the distribution of lengths between each neuronal pair in the connectome. We perform this analysis for each neuronal type. Figure 3.6 shows the normalised distributions of

connection lengths for each of these types. To calculate these distributions, we compute the connection distances for all pairs of neurons and group them according to the pre-synaptic neuronal type. These distances have been calculated as the sum of all axon segments produce by the axon growth model, starting from the pre-synaptic neuronal soma to position where synapses are located (see chapter 2 for more details). Black dotted lines define a lower bound $x_{low} = 150\mu m$ for the probability of forming short connections $G(x) = P(x \leq x_{low})$, while blue dotted lines define an upper bound $x_{up} = 850\mu m$ for the probability of forming long connections $F(x) = P(x \geq x_{up})$. These lower and upper bounds have been arbitrarily chosen to show a qualitative feature in the connection length distributions. The results represented in this figure can be summarised in the following statements:

- For each cell type, short connections are more likely than long ones. However, if pre- and post-synaptic cells are too close to each other, then the connection is less likely to be formed. The reason is that axons start to grow from the pre-synaptic soma position in some direction before reaching a position where the post-synaptic dendrite is located. As a result of this, the distributions are skewed and their medians are located at intermediate distance values.

- Compared to the other ipsilateral neuronal types, dlc and cIN demonstrate few short distance connections (low values of $G(x)$=0 and 0.04, respectively). The reason is that the axons of dlcs and cINs initially travel in the floor plate and then contralaterally before they can form synaptic contacts with other neurons.

- Dlas and dlcs exhibit longer connections than all other neuronal types (higher values of $F(x) = 0.2$ and 0.16, respectively).

- Mns have very short connections.

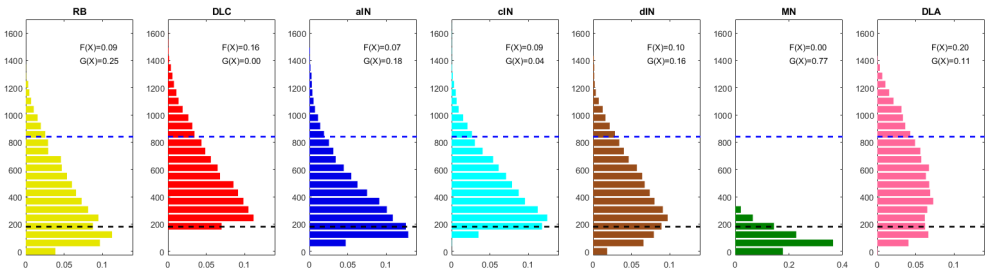

Figure 3.6: Connection length distributions for the different cell types. The black dotted lines are set to a lower bound $x_{low} = 150\mu m$ for the probability of forming a low-range connection $G(x) = P(x \leq x_{low})$, while the blue dotted line are set to an upper bound $x_{up} = 850\mu m$ for the probability of forming long connections $F(x) = P(x \geq x_{up})$.

The fact that axons from dlas/dlcs are longer suggests that these neurons favour the integration of the information via a higher number of direct mono-synaptic connections. This would allow a quick and reliable communication between distal regions. Considering the role of dlas/dlcs in initiating the swimming activity, this property would guarantee sensory signals to be well distributed throughout the spinal cord and quickly propagated to guarantee a reliable start of the swimming dynamics. On the contrary, the fact that CPG neurons do not exhibit such long connections suggests that the CPG sub-network favours the segregation of the information. This latter interpretation is in line with previous ideas suggesting that CPGs are organised in longitudinally segmented clusters, such as in the lamprey [Cohen et al., 1982]. The fact that mns have such short connections confirms their role as output cells.

Overall, our results are in agreement with the analysis of other neuronal circuits, by showing that also the tadpole connectome minimises - to some extent - the number of long range connections, by favouring short range ones. Moreover, we suggested some functional interpretation about the relationship between the length of connections and their functional role.

3.3.4 Clustering coefficients

Analysis of the complete cionnectome

Each panel of Figure 3.7 shows one clustering coefficient (inward, outward, middle, cycle and total) for the tadpole connectome (red dotted line) and 100 random benchmark networks generated from the tadpole original connectome (see Methods section). In the case of the tadpole connectome, the clustering measures are obtained from one probabilistically generated connectome (i.e. one probabilistic connectome, see Methods section), but we found similar results when repeating the same analysis on multiple generated connectomes. On the x-axis of each panel we vary the number of rewiring steps in the algorithm used to generate the benchmark random networks. The black and green lines in Figure 3.7 show the average and standard deviation clustering coefficients for the random benchmark networks. Since these networks are equal to the tadpole connectome at $x = 0$ (at the first iteration of the rewiring algorithm), the red dotted lines and black curves start from the same clustering measures. At increasing values of x the clustering coefficients for the benchmark random networks separate from the corresponding values for the tadpole connectome and they converge to some asymptotic values. These values represent the clustering coefficients for a fully randomised benchmark network, and they should be compared with the values for the tadpole connectome (red dotted lines).

Each clustering coefficient is higher for the tadpole connectome than for ranges generated by the random benchmark networks, except for the cycle clustering coefficient CC^{cyc}. These results show that, on average across all neurons in the connectome, the inward, outward and middle neighbours (Figure 3.2) tend to be more mutually connected than if the network was randomly organised. These results and the ones obtained on the average path length (see above) show that the tadpole connectome is small-world, if we define this property using

any clustering coefficient except of CC^{cyc} [Watts and Strogatz, 1998, Bullmore and Sporns, 2012]. The fact that the tadpole network has lower CC^{cyc} than benchmark random networks shows that the tadpole connectome cannot be considered a small-world network in this respect. This contradicts a commonly believed principle stating that all brain networks have the small-world architecture [Telesford et al., 2011, Bullmore and Sporns, 2012].

What do our results tell us about the structure of the tadpole connectome? The cycle clustering coefficient of a selected neuron measures probability that its neighbouring neurons complete a feedbackward triangular motif, while all the other clustering coefficients (i.e. CC^{in},CC^{out} and CC^{mid}) define the probability that such neighbours complete a feedforward triangular motifs (see the definition of the clustering coefficients in the Methods section). Therefore, the results presented in the previous section show that the tadpole connectome has an over-represented number of feedforward triangular motifs and an under-represented number of feedbackward triangular motifs, when compared to a degree-matched random topology. This suggest that these feedfoward motifs are important building blocks for a proper functioning of the tadpole swimming network. Interestingly, the over-represention of feed-forward loop motifs were also found in the connectome of *C. elegans* [Milo et al., 2002].

The functional significance of feed-forward and feed-backward loops in the these circuits is still unclear. A previous modelling study on the human locomotor CPG suggested that these motifs could help to stabilise gait modulations [Iosa et al., 2015]. We speculate a second potential advantage of these motifs in the case of the tadpole swimming circuit. It is known [Kahn and Roberts, 1982c] that the activity of neurons during each cycle of swimming progresses from the head to the tail. Since feed-forward loops help to integrate and propagate the information in a preferential (forward) direction, we suggest that the over-representation of these motifs in the tadpole connectome could help to generate this progres-

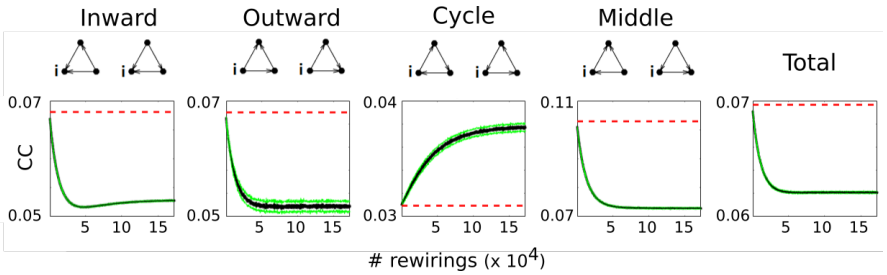

Figure 3.7: Clustering coefficients for the global network (red dotted lines) and for 100 random networks at varying number of rewiring steps. The black and green curves show the mean and mean $\pm$ standard deviation curves for the random networks.

sion. A confirmation of this intuition comes from simulations of the functional model [Roberts et al., 2014]. This model reliably reproduces head to tail progression that is remarkably similar to experimental recordings [Roberts et al., 2014, Soffe et al., 2009]. Therefore, it is likely that the feed-forward connectivity incorporated in the tadpole connectome encapsulates the key mechanisms for reproducing this progression (see also Figure 3.7).

CPG subnetwork Evidences from the lamprey studies suggest that swimming CPGs are organised in longitudinally segmented clusters, and that this organisation should be favoured by having a segregated structure [Cohen et al., 1982]. To test if this segregation is present also in the tadpole CPG, we calculated the level of segregation in this subnetwork - i.e. the subnetwork constituted by dINs, aINs and cINs - using the clustering coefficients.

Figure 3.8 compares the clustering coefficients calculated from the CPG subnetwork (red dotted line) and from 100 random benchmark network realisations (black and green curves). The description of this figure is similar to the one of Figure 3.7 (see previous section).

All clustering coefficients measured for the CPG subnetwork are higher than for the random benchmark networks, except for the middle clustering (and, as a consequence of this, also the total clustering coefficient). This implies that the inward, outward and cyclic triangles are overrepresented motifs in the CPG cir-

cuit and they are therefore likely to be important for the functioning of the circuit. Since the network is formed by both ascending (cINs) and descending neurons (dINs), it is not so surprising that cyclic triangular motifs are overrepresented.

Why is the middle clustering of the CPG network higher than the one of the random networks? We have previously shown (see the Methods section) that the middle clustering coefficient of all commissural neurons - including cINs - is zero. Therefore, these neurons have a null contribution to the measure of the middle clustering coefficient for the whole network. The percentage of cINs in the CPG subnetwork is higher than all other CPG neuronal types (53%). Therefore, CC^{mid} for the whole CPG subnetwork is dominated by the zero cIN contribution. Instead, in the case of the benchmark random networks, the contribution of the cINs in CC^{mid} is positive and non-zero, and increases with the number of rewiring steps. In fact, the randomisation algorithm iteratively swaps any pair of randomly picked edges, including ipsilateral and contralateral connections. By swapping these connections, we obviously lose ipsilateral and commissural properties of the neurons. The number of contralateral neurons therefore decreases with increasing the number of swaps and, as a result of this, also the middle clustering coefficient tends to decrease.

Overall, our results on the tadpole CPG partially support the hypothesis of the segregation of CPG networks [Cohen et al., 1982], by showing that the tadpole CPG is segregated according to almost all clustering measures (outward, inward and cycle clusterings coefficients) except for the middle clustering coefficient.

3.3.5 Analysis of motifs

Overrepresented triangular motifs

In this section, we report the analysis of motifs in the tadpole connectome. Previous studies analysed motifs in brain networks and they found that some motifs are overrepresented in these circuits [Sporns and Kötter, 2004, Varshney et al.,

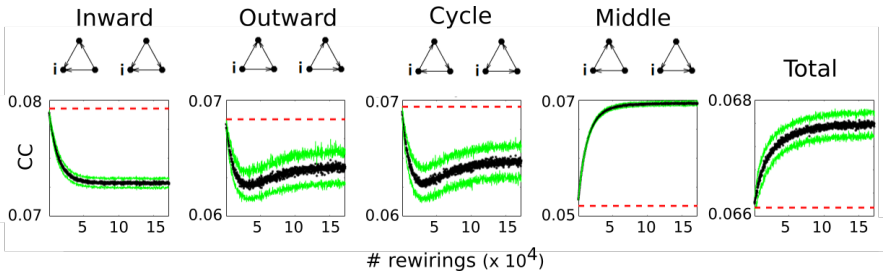

Figure 3.8: Clustering coefficients for the CPG subnetwork (red) and average across 100 random networks at varying number of rewiring steps.

2011]. For this reason, overrepresented motifs - which we will call "motifs" from now on, for simplicity - are believed to have some functional significance in these networks [Rubinov and Sporns, 2010, Kaiser, 2011].

In Figure 3.9, the left panel shows the frequency of each motif in (black circles) and in 100 benchmark random networks (green crosses) relative to the average frequency across all the benchmark random networks. Bars in the right panel of Figure 3.9 show the z-score values of each triangular motif. Black bars represent motifs that are overrepresented (based on the approach described in the Methods section), while red bars represent motifs that our approach does not classify as overrepresented (we call these "non-overrepresented motifs").

Overrepresented motifs are the ones with indexes ids = 5,8,11,12 and 13 (Figure 3.4). We notice that these results are statistically robust, since the Z_{score} of all these overrepresented motifs are much higher than the threshold $Z_{score} = 20$. Remarkably, the same overrepresented motifs have been detected also in the *C. elegans* connectome [Varshney et al., 2011] and in the mammalian cortex [Song et al., 2005].

Is there a functional reason for the overrepresentions of these motifs in such networks? This question does not have an answer in either of these networks, yet. The overrepresentation of feedforward motifs (motif id = 5) suggests, as we previously speculated, that they are important for generating a head to tail progression.

For the other motif ids (8,11,12 and 13), we found some interesting insights by looking at their connectivity structure. All these overrepresented motifs are characterised by having at least two reciprocally connected nodes. Thus, overrepresentation of these motifs implies that also reciprocal connection are overrepresented. A study on the *C. elegans* [Varshney et al., 2011] suggested that such overrepresentation would arise naturally if proximity was a limiting factor for connectivity. However, since there is no evidence for this, the functional role of motifs is unclear from this study.

Our simulations of the tadpole functional model revealed that reciprocal connections between some neurons (specifically, dINs) are crucial for stable swimming rhythm. Indeed, when we removed ascending connections between the dINs, we found that that the percentage of simulations where swimming oscillations are stable drops from 100% to 36% - the analysis and interpretation of these results are discussed in the last section of this chapter. Remarkably, we found that the motifs with ids = 8,11,12 and 13, and therefore reciprocal connections, are overrepresented also in the subnetwork constituted by only dIN neurons (not shown).

Motif spectrum

It has been hypothesised that the occurrence of specific motif spectra in brain circuits result from evolutionary processes which have extended and combined some primitive and simple connectivity structures (i.e. these motifs) to form complex connectomes, which would guarantee robust and flexible behaviours [Sporns and Zwi, 2004]. According to this hypothesis, the occurrence of similar motifs in connectomes that generate similar functions should be detectable.

To clarify this, in this section we analyse and compare the occurrence of motifs in the tadpole connectome and the connectome of other animal nervous systems: the *C. elegans* complete neuronal network (from Kaiser and Hilgetag [2006]), a

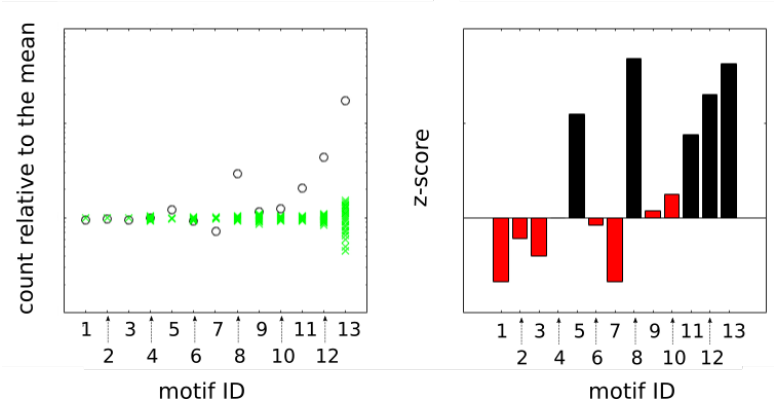

Figure 3.9: Overrepresented triangular motifs in the tadpole connectome. The left panel shows the frequency spectrum (black circles) and in 100 random benchmark networks (green crosses), relative to the average frequencies across the random networks. The y-axis is set to the logarithmic scale to help in the visualisation. Bars in the right panel of Figure 3.9 show the Z-scores, and they are divided between motifs that are overrepresented (black) and non-overrepresented (red). See the text for more details.

connectome model of the zebrafish spinal spinal circuit (extracted from [Stobb et al., 2012]) and the Macaque cortical connectivity (from [Kötter, 2004]). We selected these three circuits because, while the spinal connectomes of both tadpole and zebrafish are (vertebrates) generate similar swimming behaviour [Wiggin et al., 2012], the other two circuits produce very different types of behaviours [White et al., 1986, Rizzolatti et al., 1983] and represent the brain of very different animals: an invertebrate (*C. elegans*) and a mammal (Macaque). We therefore investigated similarities and differences in the occurrence of motifs in these circuits.

Figure 3.10 shows the triangular and square motif spectra for these four circuits. The spectra of triangular and square motifs are shown in the left and right parts of the figure, respectively. In each sub-panel we represent, from left to right, the motif spectra of the original circuit of each selected animal, and of its random and lattice benchmark networks. The x-axis of each sub-figure correspond to the index of the selected motif. To quantify the similarity between the spectra of the benchmark network and the original one we report the value of the normalised

Euclidean distance d between frequency spectra (see Methods for more details). Red circled values report the minimum between these two distances.

Interestingly, a simple visual inspection and the distance values d reveal that the spectra of the tadpole and zebrafish connectomes are both closer to the spectra of a random rather than a lattice topologies. On the contrary, the spectra of the *C. elegans* and Macaque are closer to lattice topology. We obtained similar results also when analysing the functional motifs [Sporns and Kötter, 2004] in these networks, but these results are not presented in this thesis, because they are very similar. The fact that both structural and functional motifs of the tadpole and zebrafish connectomes are more similar to a random rather than a lattice topology shows that these connectomes are also very different from many animal connectomes [Sporns and Kötter, 2004]. Indeed, the study of these connectomes (Macaque visual cortex, Macaque complete cortex, Cat cortex and *C. elegans*) revealed that their motif spectra are more similar to a lattice rather than a random topology. This suggests that the structures of specific neuronal circuits, such as the tadpole and zebrafish, does not necessarily follow "universal" rules, but they are rather built to produce specific functions, including swimming.

PART II: Functional Properties

3.3.6 The distribution of incoming connections from the sensory pathway to CPG neurons explains the shape of spike propagation in the first swimming bout

Swimming in tadpoles can start on either side of the body and this start is marked by the first firings of CPG neurons (see Introduction and Koutsikou et al. [2018]). Recordings have shown these spikes start at RC positions of around 800 μm (distance from the mid-hindbrain border) and propagate in both rostral and caudal directions during time interval of 5-10 ms [Soffe et al., 2009].

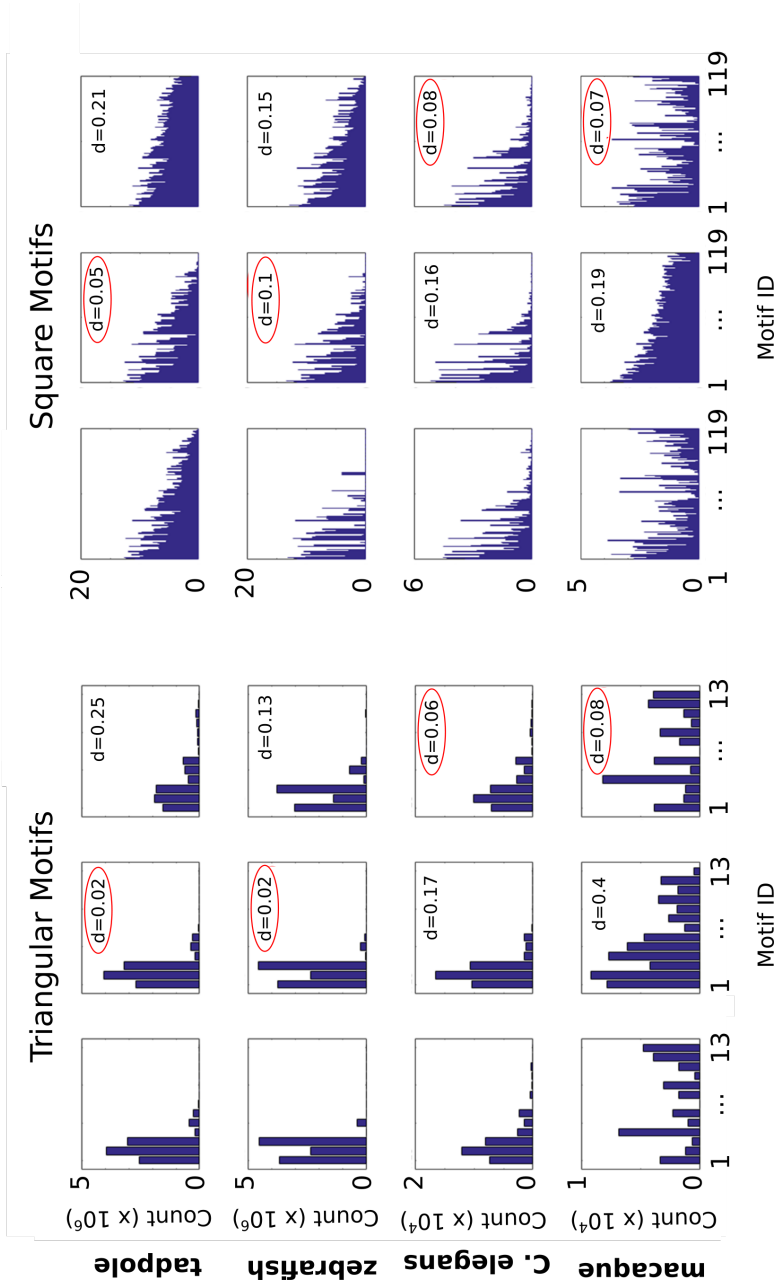

Figure 3.10: Triangle and square motif frequency spectra for different brain networks: tadpole and zebrafish spinal cord, C. elegans global and macaque cortex. While the C. elegans and macaque motif spectra are more similar to benchmark lattice networks, the spectra of tadpole and zebrafish are closer to benchmark random networks. This might be related to properties of vertebrate systems.

In this section, we show examples of three simulations of the probabilistic and functional models to show that they can reproduce the propagation of the first spiking CPG neurons preceding at the start of a swimming episode. We also show that the longitudinal distribution of the number of incoming connections from dlas and dlcs to these CPG neurons can explain this propagation. This proves how a simple structural property of a network such as the degree can be used to estimate a feature related to the function of the network (i.e. the activity propagation).

Figure 3.11A shows the rostro-caudal positions (RC coordinate, y-axis) and the number of connections from dlcs (x-axis) of each CPG neuron, divided according neuronal types (aIN,dIN,cIN,MN - colours identify these types). This number of connections has been extracted from probabilistic matrix (Figure 3.1). Each panel of Figure 3.11B shows raster plots of the spiking activities in two left RBs and of all right CPG neurons for three simulation examples (left,center,right). From left to right, these simulation were obtained by activating a single spike in two RBs (at time 60 ms) located at three different rostro-caudal positions: caudally located (left panel), middle located (central panel), and rostrally located (right panel) at positions shown in figure. Spiking of RBs mimics the touch of the skin which can start swimming in the real animal [Roberts et al., 2014].Simulations last until 85 ms to show only the first bout of swimming dynamics.

Firing of RBs activates dlas and dlcs (not shown), which in turn activate dINs. The combined input from dlcs and dINs then drives the firing of all the other CPG neurons, and initiates swimming. There is a clear propagation of the spiking of all CPG neuron starting from central rostro-causal positions. In these simulations, the start of swimming happens on the opposite side of stimulation because the strengths of synapses from dlcs are higher than the ones from dlas (see the chapter 2 for more details). In other simulations we also tested the effect of reverting these strengths in order to make swimming start on the same

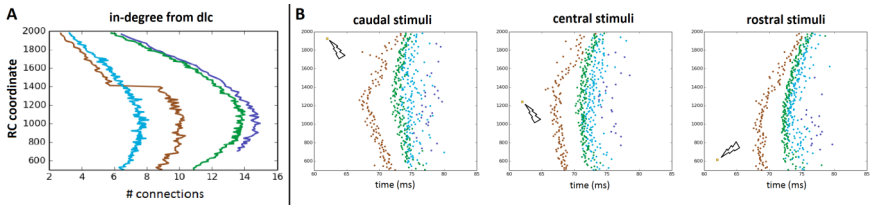

Figure 3.11: Propagation of the first firing of CPG neurons via dlcs A. Flipped figure showing the number of connections from all dlcs to each CPG neuron as a function of the CPG rostro-caudal coordinate, divided according neuronal types. B. Raster plots showing the spiking activities in two left RBs and of all right CPG neurons in three different simulations (left, center, right). The longitudinal position of RB neurons is what changes in these simulation (black thunderbolt). Firings of CPG neurons mark the start of a swimming episode and propagate starting from central longitudinal positions in all the three simulations.

side of stimulation. We do not report these results because they are essentially similar to the ones shown in this figure and presented in the next section.

There is a clear correspondence between the shapes of the number of connections from dlcs to the CPG neurons (Figure 3.11A) and the positions of the CPG neurons of each type which fire first (Figure 3.11B). For example, dINs with RC-coordinate near 1000 μm receive the highest number of incoming connections from dlcs. These positions correspond to the RC-coordinates of dINs that start to fire. These positions vary between approximately 700 μm and 1200 μm in dependence of RC-position of the activated RBs in the three panels. The firing of dINs neurons propagates both rostrally and caudally, and follows the shape of the degrees shown in Figure 3.11A. Similar descriptions are valid also for all other CPG neuronal types. We run 100 random simulations of the functional models in three batches. In each batch we activated the same RBs as the ones shown in 3.11B. All simulations generated qualitatively similar results, including the ones describing the shape of propagation of the CPG firings. Swimming started in the range between approximately 600 and 1350μm.

3.3.7 Reliable swimming anti-phase oscillations

The next stage was to investigate the spiking activity of connectomes to see whether they behaved like those generated anatomically [Borisyuk et al., 2014] and as described behaviourally [Roberts et al., 2014]. This was necessary to evaluate whether the probabilistic model provided a useful tool for exploring biological function.

To investigate the spiking activity of connectomes generated by the probabilistic model, we mapped them onto a functional model composed of single compartment Hodgkin-Huxley type neurons, following the approach described in [Roberts et al., 2014] and described in the chapter 2. To simulate the basic experiment where brief stimulation of the trunk skin initiates swimming in the tadpole, we excited two adjacent sensory RB neurons on one side of the body at a randomly selected RC position. The RB activity propagates along their own axons and then in the sensory pathway (via dla and dlc neurons) to deliver excitation to CPG neurons on both sides of the body. These CPG neurons (cIN, dIN, aIN) generate a pattern of rhythmic spiking alternating between the left and right body sides suitable to drive swimming movements. We repeated this experiment 100 times using different generated adjacency matrices. We found that in all simulations the functional model produced a swimming-like pattern where: firing was rhythmic; neurons that were active fired once per cycle; firing alternated between the two sides; and firing on each cycle was most delayed towards the tail.

However, although connectomes from both the anatomical and probabilistic model produced qualitatively similar swimming activity, the probabilistic model produced a rhythm with significantly longer cycle periods (68.6 $\pm$ 0.8 ms, mean $\pm$ SD, range from 65 to 70 ms) than the anatomical connectomes (58 $\pm$ 1.8 ms), as shown in Figure 3.12. We investigated the underlying cause of this dif-

ference, and in doing so gained an insight into how the structure of the network affects swimming period, a key characteristic of the system's behaviour.

What determines the period of one swimming cycle? A swimming cycle starts when dINs on one side of the body spike. These excite cINs on the same side, which then spike and inhibit dINs on the opposite side, leading to delayed spiking of dINs on the opposite side through post-inhibitory rebound (PIR). Thus, the swimming period can be approximated as $T = 2(\Delta_{DC} + \Delta_{CD})$, where Δ_{DC} is the delay between spiking of dINs and the subsequent spiking of the ipsilateral cINs they excite, and Δ_{CD} is the delay between spiking of cINs and the subsequent PIR spiking of the contralateral dINs they inhibit (Figure 3.12B). Both Δ_{DC} and, particularly, Δ_{CD} were significantly larger with the probabilistic connectome (anatomical model: Δ_{DC}=5.3 ms $\pm$ 0.4; Δ_{DC}=23.7 ms $\pm$ 0.9; probabilistic model: Δ_{DC}=6.2 ms $\pm$ 0.3; Δ_{DC}=28.2 ms $\pm$ 0.4, N=100). Together these two differences account for the overall slower swimming rhythm seen with the probabilistic model, and this is largely as a result of the increased time it takes for dINs to fire PIR spikes in response to contralateral cIN input.

What, then, determines the delay between cIN spikes and contralateral dIN rebound spiking? During swimming dINs are held depolarized by summation of NMDA-receptor-mediated excitation from other dINs, and in this state inhibition from cINs can result in delayed dIN spiking as a result of PIR. Intuitively, and from past investigations, we know that this spiking delay depends on the relative strength of inhibitory and excitatory input from cINs and other dINs respectively. We characterised the relative strength of inhibition and excitation for a given connectome by calculating the average in-degree from cINs and from other dINs. Any cINs that received fewer than 13 connections from dINs were excluded from this calculation, since, as we shall demonstrate in Section 3.5, such cINs are likely to be inactive. We used a linear regression model where cIN-dIN and dIN-dIN in-degrees (independent variables are $I_{cIN>13}$ and I_{dIN}) correlate very

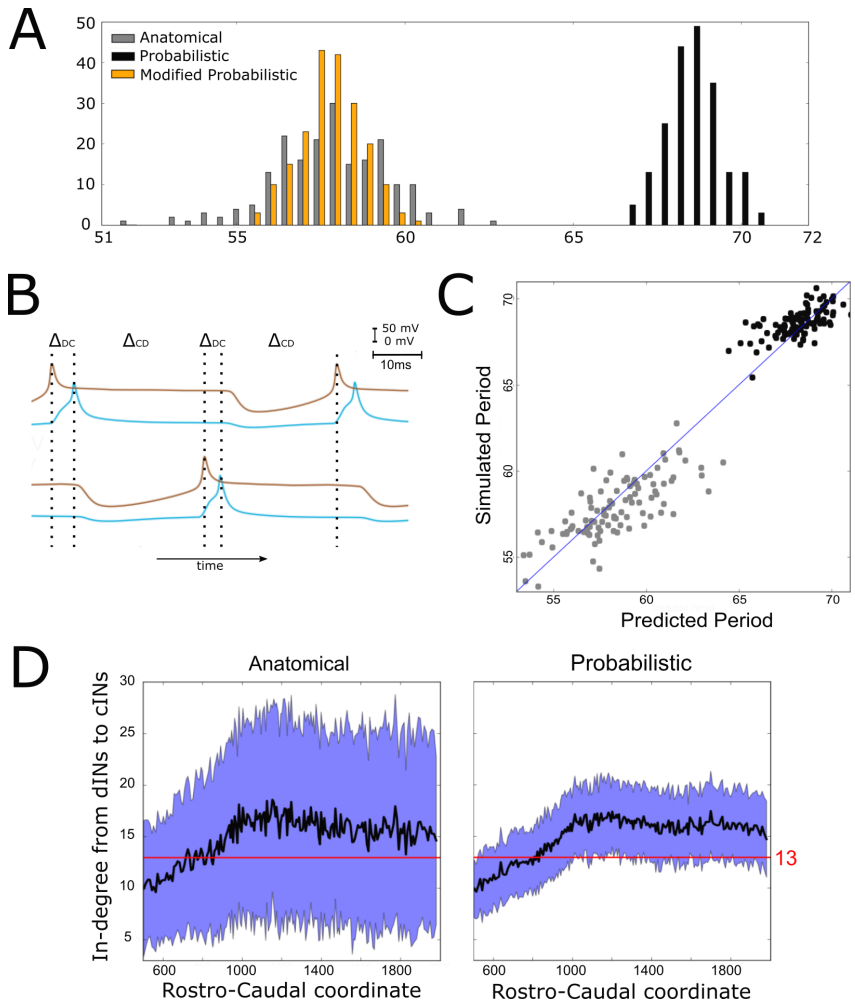

Figure 3.12: Investigating the difference in swimming cycle period between anatomical and probabilistic connectomes. A. Swimming period (as defined by median motoneuron spiking period) for 200 anatomical connectomes (grey), for 200 probabilistic connectomes (black) and 200 probabilistic connectomes where cIN to dIN synaptic strength is reduced (see text for details). B. Example membrane potentials of example dINs (brown) and cINs (blue) on the left and right side during one swimming cycle. The swimming period is a sum of (twice) the delay between dIN and cIN spiking (Δ_{DC} and (twice) the delay between cIN and contralateral dIN spiking (Δ_{CD}). C. Network structure allows us to predict swimming period. Each point shows for one connectome (different from those used in part C and for linear regression) the predicted period based on the connectivity, with the actual period from simulation plotted on the vertical axis. The blue line shows the case where the prediction perfectly matches the simulation. D. More cINs are inactive in anatomical connectomes than in probabilistic connectomes. Although the average in-degree (black line) is similar under both conditions, the standard deviation (blue area) is much higher for anatomical connectomes. This increased variance in anatomical connectomes means that more cINs receive fewer than the 13 connections from dINs that are required for reliable spiking.

strongly with the period of swimming:

$$T = 2.5 \cdot I_{cIN>13} - 3 \cdot I_{dIN}$$

Where T is the period. The coefficient of determination $R^2 = 0.96$.

We used this linear regression model to predict firing period for 200 new connectomes (100 probabilistic, 100 anatomical). The accuracy estimated using the coefficient of determination is $R^2 = 0.94$ (Figure 3.12C). We were therefore able to predict with good accuracy a key characteristic of the network's behaviour based only on its connectivity. Note that this prediction is universal, since it does not require knowledge of whether the connectome was generated using the probabilistic or anatomical model.

Why is inhibition from cINs stronger relative to excitation from dINs, and therefore swimming slower, in connectomes generated by the probabilistic model? This is a difficult question to answer completely, but much of the difference is due to the fact that anatomical connectomes have more cINs that receive fewer than 13 connections from dINs and are thus inactive during swimming (anatomical model: 168 $\pm$ 11 inactive cINs, N=100; probabilistic model: 101 $\pm$ 8 inactive cINs, N=100). Although the mean dIN-cIN in-degree is very similar between anatomical and probabilistic connectomes (and above the threshold of 13), the variance is much higher in the anatomical case (Figure 3.12D).

Therefore, in anatomical connectomes there are more inactive cINs. The underlying reason for this difference in variance is that in the anatomical model neurons have randomly chosen dendritic extents, sampled from the distribution of experimentally measured dendrites (see the thesis Introduction). This means that some neurons have small dendrites and receive very few connections, while others have large dendrites and receive very many connections. In

the probabilistic case this detail is lost, as all incoming connections to a neuron are chosen completely independently of each other.

While we can explain the quantitative difference between anatomical and probabilistic models, this difference clearly illustrates that there are potential pitfalls in applying the probabilistic approach to a particular biological question, and it must be used with caution. In this specific case, there is a problem because the reduction in dIN to cIN in-degree variance produced by the averaging process used to generate the probabilistic connectomes has asymmetric consequences. The decreased number of cINs failing to fire because of weak excitatory input (low in-degree number) is not balanced by the effect of reducing the number of cINs with very strong excitatory input (high in-degree number). This is because, above a threshold input strength, cINs only fire a single spike per cycle (see below); changing the level of excitation above the threshold value does not alter this. The result of this asymmetry is the overall increase in the number of cINs firing with the probabilistic model and hence the lengthened cycle period. To offset this consequence of the probabilistic approach, we therefore reduced the strength of cIN to dIN inhibition (from 0.435 to 0.2 nS). As predicted, this reduced the cycle period to a range overlapping the distribution produced by anatomical connectomes and matches periods seen in the real swimming behaviour (Figure 3.12A).

3.3.8 A core dIN-cIN sub-network can generate swimming

The probabilistic approach allows us to test the reliability of network function after removal of selected connections. As an illustration, we considered a sub-network comprising only the sensory pathway (which is not active during swimming), and dIN and cIN CPG neurons. We excluded aINs and mns simply by setting the probability of connections to and from them to zero. Figure 3.13 shows one simulation of the functional model containing only this sub-network.

Figure 3.13 A, D shows examples of voltage dynamics for individual dIN and cIN neurons on the left and right body sides respectively; Figure 3.13 B, C shows raster plots of spiking activity for all neurons on the left and right sides of the body respectively.

The brown and light blue dots in Figure 3.13 B, C show a typical pattern of anti-phase, left-right swimming activity in the dIN-cIN sub-network. We found that in 100 independent simulations (with different reduced network connectomes) swimming activity was generated that was similar to that in Figure 3.13. The swimming period in these simulations was 57 $\pm$ 0.9 ms. These values are again within the physiological range observed in experimental recordings of swimming.

Previous experiments have shown that the swimming CPG includes dINs, cINs and aINs [Roberts et al., 2010]. However, it is known that aINs have a low probability of firing during swimming, suggesting that their contributions during swimming are minimal and their role in the network is still unclear [Li et al., 2004a]. Our simulation results confirm these experimental findings by showing that the dIN-cIN subnetwork generates reliable swimming.

3.3.9 Removal of commissural connections allows rhythmic firing on the stimulated body side

Experiments have revealed that an isolated side of the tadpole spinal cord without commissural connections can generate regular rhythmic spiking activity in motoneurons, with period that is lower than that of swimming [Soffe, 1989].

Once again, the probabilistic model readily allowed us to simulate these experimental findings by setting the probability of commissural connections from cINs and dlc neurons to zero to disconnect the two body sides. This is equivalent to a sagittal midline lesion experimentally. Figure 3.14 A shows a raster plot of steady oscillatory spiking in motoneurons (green) and dINs (brown), demon-

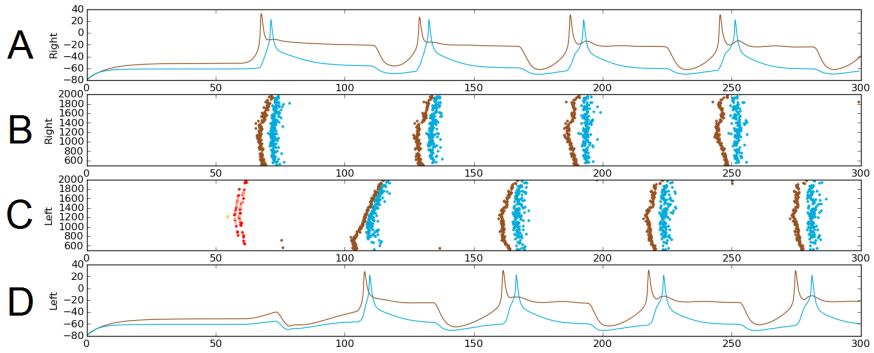

Figure 3.13: Alternating firing ("swimming") in one realization of the dIN-cIN subnetwork in a 300ms simulation, showing activity on the left (A-B) and right (C-D) sides of the spinal cord. B and C show spike times, where the vertical position of each spike corresponds to the rostro-caudal position of the associated neuron. A and D show voltage trace examples for single selected dINs (brown) and cINs (blue) on the left (A) and right (D). Simulated sensory stimulation at 50ms causes an RB neuron (yellow) to spike, which excites dlas and dlcs (pink and red, respectively). Excitation from these sensory pathway neurons causes the dIN and cIN neurons that form the CPG to generate an alternating rhythm.

strating that the rhythmic activity was maintained and stable.

It is important to note that the mechanism that generates this singled-sided rhythm is different to that which generates swimming. In swimming, inhibition from cINs causes contra-lateral dINs to fire post-inhibitory rebound spikes. In the case of separated body sides there is no cIN input to dINs, and the only other inhibitory CPG neurons, the aINs, are inactive. Instead, the rhythmic activity is caused by feedback NMDA excitation within the dIN population, as has been previously observed experimentally [Li et al., 2010] and in modelling [Hull et al., 2016]. Within one simulation dINs fell into a number of different groups, based on their spiking period. In most simulations the majority of dINs spiked rather quickly, with period approximately 24 ms (41 $\pm$ 16 dINs, N=100 connectomes), while most of the remaining dINs spiked with approximately double this period, approximately 53ms (24 $\pm$ 4 dINs). A much smaller group fired twice as slowly again, with a period of approximately 101 ms (2 $\pm$ 3 dINs). Figure 3.14B makes these groups clear, by showing the same set of dIN spikes as Figure 3.14A

but with the neurons sorted according to firing rate. Interestingly, motoneurons tended to fire in-phase with the intermediately sized group of dINs that spiked at approximately 53ms (as shown in Figure 3.14 A), although in some simulations some mns did also spike in-phase with the faster group of dINs; further investigation is required to understand why more mns are not able to fire with the dINs in this group.

We have no direct experimental recordings of dINs following separation of the two body sides, only ventral root recordings showing motor neuron activity. In these experiments [Soffe, 1989] it was found that single-sided rhythmic activity was significantly faster than that seen during swimming (initial average cycle period 60ms vs 43 ms). This was also the case with our simulations, where most mns spiked at approximately 53ms in the single-sided cases, versus approximately 69ms in normal swimming. From our results, we predict that recordings from dINs during single-sided rhythm generation would reveal a relatively large group of dINs that spike much more quickly than ventral root activity, and another much smaller group of dINs that fire much more slowly.

3.3.10 Reliability of cINs spiking depends on their RC-coordinate

Experiments have shown that during swimming the reliability of spiking of some neuron types can vary from cell to cell [Soffe, 1993, Li et al., 2007b]. In simulations of connectomes generated by the anatomical model approximately 50% of cINs fire reliably, whereas in connectomes from the probabilistic model approximately 70% of cINs were reliable. Other cINs were either completely inactive or only fire on some swimming cycles. We investigated the cause of this unreliability by analysing the probabilistic model.

In the functional model, for each pair of cell types, the mean value of synaptic strength was selected in line with experimental data [Roberts et al., 2014] and randomised by addition of the Gaussian random variable with zero mean

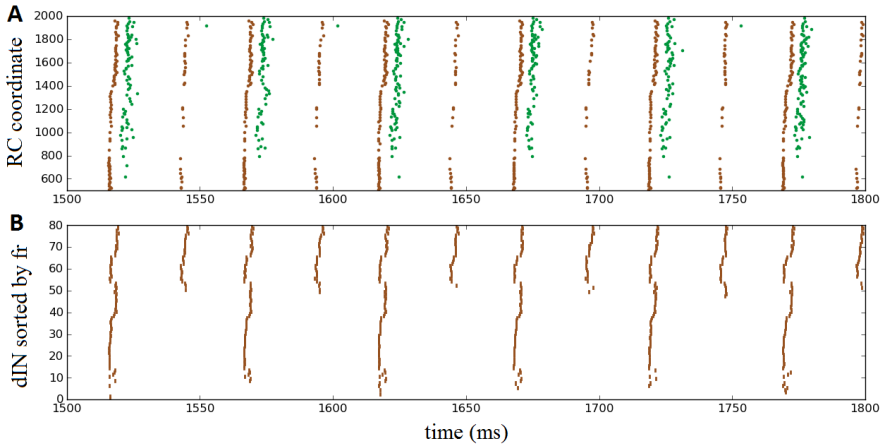

Figure 3.14: Oscillatory activity on one side of the body after removal of commissural connections. A. Raster plot of spiking activity during swimming, showing dINs (brown) and motoneurons (green) on the left side of the spinal cord after removal of commissural connections. B. The same dIN spiking activity as in (A), but with the spike trains sorted vertically based on increasing firing rate. In both cases activity is shown between 1500 and 1800 ms post-stimulation, when the system has settled down into a stable oscillatory state.

and relatively small variance (see chapter 2). In the case of synchronous bombarding, the total input to the neuron depends on both the connection strength and the number of incoming connections, therefore, the degree is an important measure. For the reliability study, we approximate the total input to cIN by the mean dIN to cIN connection strength multiplied by the mean in-degree from dINs to cINs, because dIN spike reliably and synchronously during each swimming cycle.

From simulations of 100 different connectomes, we found that the probability that a cIN spikes reliably depends on the dIN-cIN in-degree (I_{dIN}). If I_{dIN} >15 then a cIN fires once on each swimming cycle, approximately in phase with dINs and mns on the same side; we call this a 'reliable' cIN. If 13 $\leq I_{dIN} \leq$ 15 then firing is irregular, meaning the cIN fires approximately in-phase with dINs and mns but on only some swimming cycles; we call this an 'unreliable' cIN. Those cINs that have I_{dIN}<13 do not fire at all during swimming.

The probabilistic model allowed us to calculate the expected dIN-cIN in-degree

as a function of its rostro-caudal position (Figure 3.15). Note that this result was based only on analysis of the general probability matrix, not individual connectome realisations. The relationship allowed us to hypothesise: (1) it is likely that rostral cINs will not fire; (2) it is likely that cINs with RC-coordinate near 900 μm are unreliable, and (3) it is likely that caudal cINs will fire reliably.

To confirm these hypotheses in the model we used the results of 100 spiking simulations to calculate the probability that a cIN in a certain position will fire reliably. In Figure 3.15 B we show the reliability proportion (the fraction of simulations where the cIN fires reliably) vs RC coordinate. From this, it was clear that cINs at more rostral positions have a significantly lower probability of reliable spiking than cINs in more caudal positions. Using a linear regression model, we determined a strong correlation between the cIN reliability proportion (x) and the average dIN-cIN in-degree (y) given by the linear relationship $y = 0.07 \cdot x - 0.4$ (Figure 3.15 C). Note that there is currently not enough experimental data about the reliability of cIN spiking during swimming in vivo to say whether the level of cIN reliability in our simulations was realistic. However, our general results from the probabilistic model suggest that it is important that any experimental measures of cIN spiking reliability (or that of other neuron types) should take into account the rostro-caudal position of the measured cell.

3.3.11 Ascending axons of dINs are important for swimming

It is a defining feature of dINs in the tadpole that they all have a descending axon, but some dINs which are located more rostrally have a second axon growing in the ascending direction [Borisyuk et al., 2014, Roberts et al., 2014]. Simplified computational models [Li et al., 2006, Wolf et al., 2009] have shown that the swimming activity fails to self-sustain unless some excitatory interneurons have ascending connections. We used the probabilistic model to further clarify the role of ascending dIN axon branches, taking advantage of the fact that

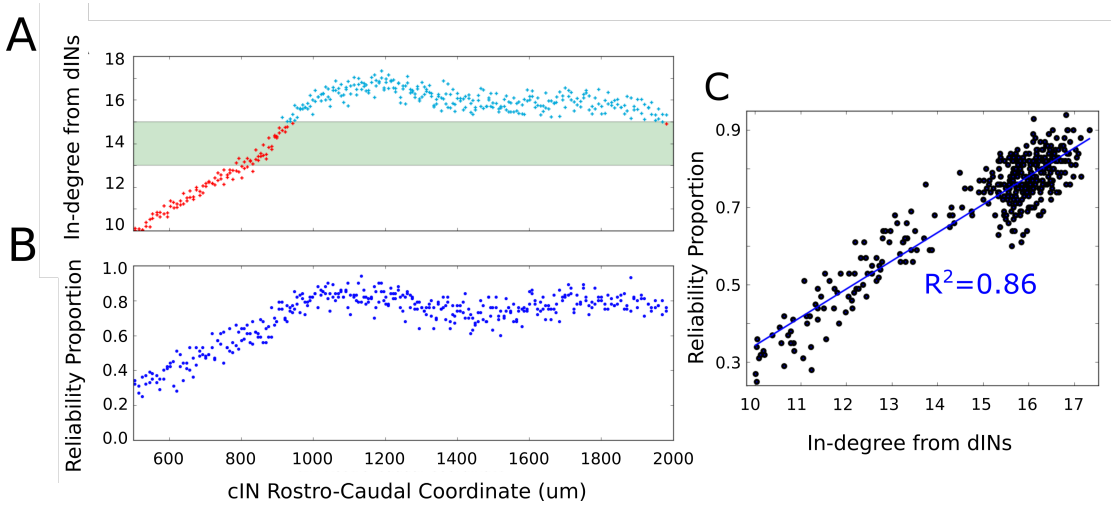

Figure 3.15: Firing reliability of cINs. A. Plot of the average cIN in-degree from presynaptic dINs as a function of rostro-caudal position. Blue dots represent cINs that have on average 15 or more incoming connections from dINs, while red dots represent cINs that have on average fewer than 15 incoming connections from dINs. The cINs with 13-15 incoming connections (green shaded area) are most likely to fire unreliably, whereas those with fewer than 13 connections are likely to be completely inactive. B. cIN reliability proportion vs cIN rostro-caudal position; for each cIN the reliability proportion is the fraction of 100 simulations where the cIN fires reliably. C. Scatter plot of the cIN reliability proportion vs the average in-degree from dINs. The figure shows the linear regression line between these two variables and the corresponding R^2 value.

our new model allows us to run large numbers of simulations and to study the generalised connection structure. Using the probabilistic model, we removed all ascending connections from dINs and generated a modified adjacency matrix (connectome), which we then used to simulate spiking activity.

Figure 3.16 A shows the in-degrees for the dIN sub-network (i.e. the number of incoming connections to each dIN from other dINs) for the standard connectome (black) and one lacking ascending dIN axons (red). In the figure, the horizontal and vertical axes show the in-degrees and the RC-coordinate of dINs, respectively. We consider here only rostral and mid-body dINs in the range of RC-coordinates from 500 to 1400 mm; more caudal dINs do not receive any synapses from ascending dIN axon collaterals, so the in-degrees are the same for both connectomes.

From Figure 3.16 A it is clear that the dIN in-degrees in both cases are similar in the middle body part but are increasingly different for neurons in the rostral part. For the modified connectome, the in-degree (red dots) decays to zero in a linear way as the RC-coordinate approaches 500 mm because the dINs in the most rostral locations have a few if any connections from descending axons. As a result, the most rostral dINs in the modified connectome can only fire due to electrical coupling between dINs, resulting in the appearance of some unusual patterns of spiking activity not observed experimentally. We repeated 100 simulations of the functional model after removing ascending dIN connections. The resulting spiking activity patterns can be divided into three cases:

- Case 1 (63/100): In most simulations, the swimming activity was initiated but failed to persist. Swimming failures begin with rostral dINs failing to spike due to reduced excitatory drive from other dINs (ascending dIN connections are missing); this reduced excitation from the rostral dINs prevents slightly more caudal dINs from firing, and so on, as can clearly be

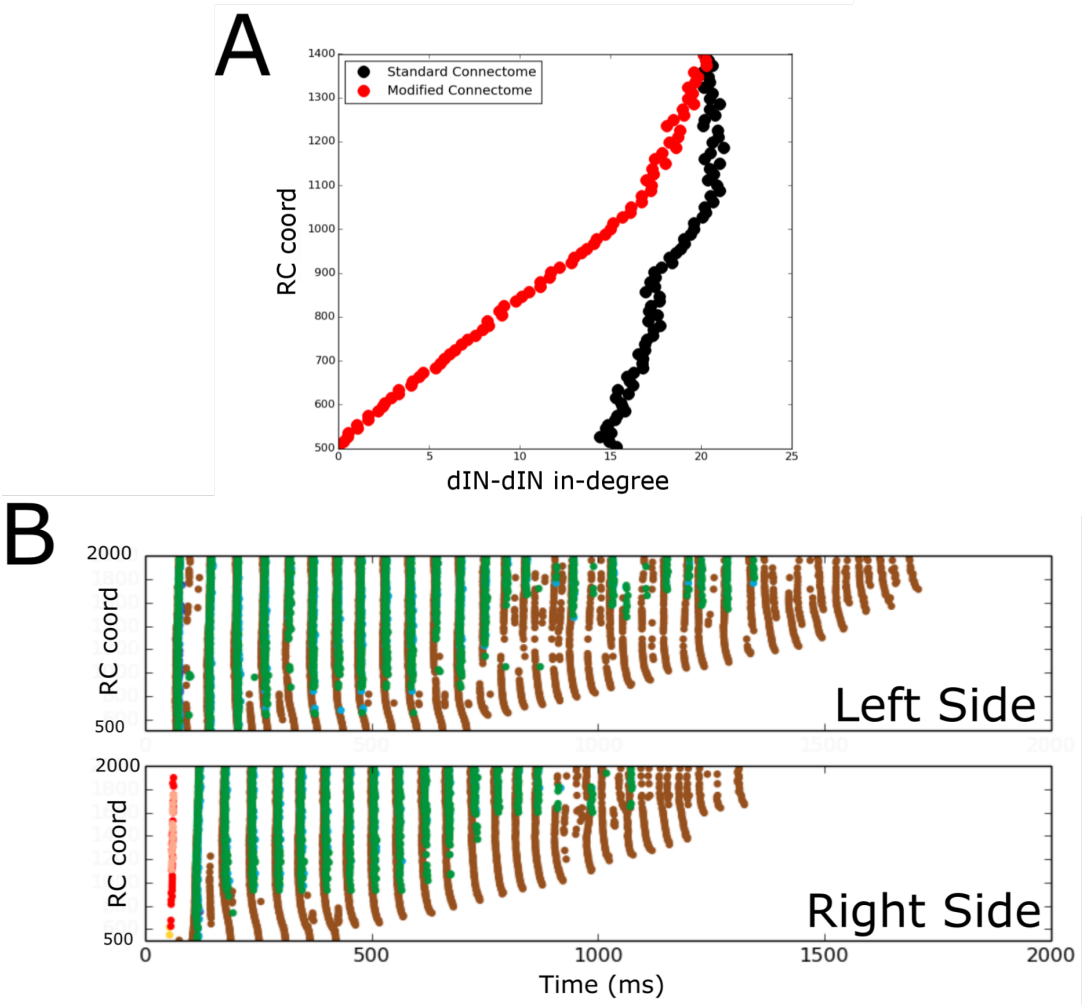

Figure 3.16: Comparison of spiking activity in the normal case and when dIN ascending axons are removed. (A) Average in-degree from dINs to other dINs at different rostro-caudal positions in the standard connectome (black dots) and after removal of ascending dIN axons (red dots). (B) Example of typical spiking activities from connectomes with ascending dIN axons removed (case 1, see text for details).

seen in Figure 3.16 B. This result is in line with previous modelling that showed that feedback excitation is a mechanism that contributes to generating persistent motor activity in a simpler model [Li et al., 2006].

- Case 2 (36/100): In 33 of 36 simulations one side only was active. In 3 of 36 simulations both sides were rhythmically active for the total length of the simulation but they do not fire in antiphase. The pattern of spiking activity on one side is similar to the one shown in Figure 3.14 A.

- Case 3 (1/100): Only one simulation generated sustained swimming alternating firing between left and right sides, but the period of the oscillations was shorter than for the standard connectome (50 ms).

3.4 Discussion

The study of neuronal connectivity is a challenging problem in contemporary neuroscience. One popular and effective method for finding cortical connectivity involved detailed tracing of a small number of individual neurons of each identified type, and then using estimates of the number of location of the different cell types to estimate complete connectivity [Binzegger et al., 2004]. Recent development of new brain imaging techniques allows generation of 3D images of single neurons, tracing their connections and, for example, making progress towards a complete Drosophila connectome [Lin et al., 2015, Shih et al., 2015]. Similar progress has been made by combining molecular, anatomical and physiological techniques to find the neuronal cell types, and connections between them, in mouse retina [Seung and Sümbül, 2014, Kim et al., 2014]. Computational modelling has been successfully applied to find a sensorimotor connectome in larval Zebrafish [Stobb et al., 2012]. In this chapter, available neurobiological data have been used to describe neuronal cell types and formulate a stochastic model of connectivity, which was studied using a graph theory approach.

It is known that brain development involves multiple stochastic processes and that, in most species, individuals' connectomes are different [Seung, 2012]. Despite differences in connectivity, most individuals under normal conditions are able to demonstrate similar functionality. This means that different connectomes include sufficient key structural features to produce a common repertoire of functionalities and behaviours. What are the key connectivity properties that define the network functionality?

Motivated by this question, we derive a probabilistic model of connectivity in the Xenopus tadpole CNS (caudal hindbrain and spinal cord) to study the relationship between the structure and function of the network. To derive the probabilistic model we generate 1000 connectomes using a biologically realistic anatomical model based on the 'developmental' process of axon growth [Li et al., 2007a, Borisyuk et al., 2011, 2014, Roberts et al., 2014]. A similar approach to generating connectivity from a developmental process was used by Bauer et al. [2012]; in this case, a reaction-diffusion model was applied to generate connectivity in a network of excitatory and inhibitory neurons with winner-takes-all functionality. Using a universal ordering of neurons in the tadpole, we have calculated the probability of connection from each neuron i to neuron j as the frequency at which a connection exists among the thousand generated connectomes. In this way, our probabilistic model 'generalizes' structural properties of networks produced by the anatomical model.

Some of the results of our graph theoretical analysis demonstrate that the structure of the tadpole spinal connectome differs from the one of many other brain circuits. For example, using directed measures of clustering, we found that this connectome has a lower number of cycle loops than a benchmark random networks. This implies that the tadpole connectome is not of the small-world type [Watts and Strogatz, 1998], and differs in this respect from most previously analysed brain circuits [Telesford et al., 2011, Sporns and Zwi, 2004]. Another struc-

tural feature that distinguishes the tadpole and zebrafish spinal connectomes from many previously studied connectomes [Sporns and Kötter, 2004], including the ones analysed in this chapter, is that their motif spectra are closer to a randomised rather than a ring-like topologies. All these results are quite important because they show that some graph properties found in the connectomes of different brains are not so "universal" as many suspected [Bassett and Bullmore, 2017]. We suggest that, instead of using graph measure to find universal structural properties in the brain (such as the small-world property), it is more useful to apply these measure to each specific network of study and to make comparisons with networks that share similar functions. Indeed, different neuronal circuits generate different behaviours, and it is well-known that they are built in a specific way to achieve them [Marder and Calabrese, 1996, Bargmann and Marder, 2013].

In the case of tadpoles, we suggest some functional implications of the graph measures used by testing the ability of the connectome to generate swimming behaviours. Specifically, we use the probabilistic model to generate an adjacency matrix representing a particular realisation of neuronal connectivity. Mapping the adjacency matrix to a functional model of spiking neurons of Hodgkin-Huxley type enables us to simulate spiking activity. We compare these simulations of the functional model to the experimental results on swimming initiated by skin touch. All generated adjacency matrixes (connectomes) mapped to the functional model generate similar swimming activity. It seems, then, that the probabilistic model contains some fundamental features of the network connectivity ('proper structure') which ensure correct functioning of the system. For example, experimental recordings show that apparently-pathological activity (synchrony) can sometimes appear soon after swimming initiation: the two body sides spike synchronously during several cycles before then switching to normal anti-phase swimming activity [Li et al., 2014a]. This synchronous activity ap-

pears also in model simulations with connectivity generated by both the anatomical and the probabilistic models. However, the number of synchronously firing neurons is significantly reduced in probabilistic connectomes.

A second type of apparently pathological activity is the additional firing of some dINs near the middle of the swimming cycle (mid-cycle dINs) [Li et al., 2014a]. Mid-cycle dINs appear in model simulations with both anatomical and probabilistic connectivity. However, the number of such mid-cycle dINs is significantly reduced in probabilistic connectomes: 0.8 and 6.3 for probabilistic and anatomical connectomes, respectively (average according to swimming cycles and 100 simulations). These results suggest that synchrony and mid-cycle dINs arise from connectivity imperfections and that the generalised connectivity encapsulated in the probabilistic model improves on the imperfection of some individual realisations.

To design the probabilistic model, we use a minimalistic approach. We use the assumption that directed connections are represented by the matrix of independent Bernoulli random variables. One of the strengths of this approach is that it allowed us to analytically calculate some of the graph's characteristics (the mean and standard deviation of in- and out-degrees, heterogeneity coefficients) directly from the probability matrix, without considerations of a particular (generated) connectome. In the case of the anatomical model, we can only compute graph characteristics for a connectome realization. Here, we study how these characteristics relate to particular functional properties of the network. For instance, the average in- and out-degrees were used to predict the swimming period and to find the positions of reliably firing cINs.

The assumption that the Bernoulli variables are independent is a significant limitation of the probabilistic model. One way to overcome this limitation might be the use of more sophisticated probabilistic processes where the random vari-

ables corresponding to different connections become dependent (e.g. random Markov field approach).

Computational modelling of the tadpole spinal cord reveals the fundamental features of neuronal connectivity that are responsible for robust swimming generation. Unlike simpler organisms such as *C. elegans*, tadpoles have the potential for significant variation between individuals in terms of neuronal connectivity, as a result of the large number of random processes involved in their development. Despite this variation, the behaviour of individuals is approximately the same, suggesting some fundamental organisational principles common across the species. We adopt the philosophy that, for tadpoles at least, there is a theoretical 'perfect' version of the nervous system with individual random variations from this ideal. Although, the probabilistic model arises from 'averaging' of many anatomical connectomes, this model still generates connectomes that reliably swim and this fact presumably reflects the fundamental organisational principles of the system. An interesting property of connectomes generated by the probabilistic model is that their anatomical and functional characteristics are considerably less variable than those generated by our anatomical model (and on whose properties the probabilistic model was based). We hypothesise that due to the 'averaging' process of the probabilistic model, the connectomes generated from it are closer to the theoretical 'ideal' network. Some characteristic features of the connectivity are not clear from an individual realisation, but become evident from the probabilistic model. For example, the shape of degree distributions as a function of cell position cannot be clearly seen from analysing an individual connectome - these shapes are irregular. They are much clearer when calculated directly from the probabilistic model itself. In addition to this, connectomes generated by the probabilistic model generate spiking activity that is considerably less variable and 'messy' than anatomical connectomes, which makes it easier to see and quantify phenomena such as irregularly spiking cINs.

Finding neural connection probabilities under biological constraints is a difficult problem. In the case of the tadpole spinal cord, the system is simple enough that it is possible to reconstruct biologically realistic connectivity [Roberts et al., 2014] (an anatomical connectome) and to define neuronal connection probabilities (probabilistic model). We believe that this is a promising general approach that could be used beyond the particular case of tadpoles. Similar probabilistic approaches have been used for modelling the development of neural networks using limited experimental data [Binzegger et al., 2004, Zubler and Douglas, 2009]. Another possible approach for finding connection probabilities is to minimize an appropriate cost function which reflects both anatomical and functional properties.

3.5 Conclusion

We study the structure and function of the spinal cord neuronal network using experimental data and computational modelling. Our anatomical model generates multiple highly variable and nonhomogeneous connectomes and to deal with this large and complex data we design a very simple mathematical metamodel expecting that this new probabilistic model will reflect (generalise) structural properties of anatomical connectomes and show proper functioning.

The crucial question is: 'Can probabilistic connectomes produce swimming'? The answer to this is not obvious. An earlier paper [Li et al., 2007a] showed that a graph of connections based on probabilities derived from small number of pairwise recordings provides swimming in about 60% of cases only. On the other hand, this new study shows that probabilistic connectomes that include some of the structure of anatomical connectomes reliably swim in all cases. Thus, we can derive an important conclusion that the two properties of the probabilistic model inherited from anatomical connectomes: (1) position of neurons along the rostro-caudal coordinates and (2) frequency of connection appearance, are

sufficient for swimming generation.

Also, it is easy to use the probabilistic approach to generate connectomes compared to the need to 'grow' them using the anatomical model: all traditional characteristics of the connectivity graph can be calculated directly from the probability matrix without consideration of particular connectomes. Some characteristics of the probabilistic connectomes (e.g. the mean of in- and out-degrees) coincide with equivalent characteristics of the anatomical connectomes but some differ (e.g. the variances of in- and out-degrees are significantly smaller for probabilistic connectomes). Although there are some differences between the behaviour of anatomical and probabilistic connectomes, even studying these differences can provide important insights into the relationship between the structure and function of the network. Our investigation in the reasons underlying a difference in swimming frequency between the two types of connectome (see result section) is an example of this, where we found that it was the degree of variance of cIN in-degree from dINs that largely caused the difference. It would have been hard to observe this interesting phenomenon without having the probabilistic model (where in-degree variance is much lower) to compare with the anatomical one.

The probabilistic model provides a different way to look at the information generated by the anatomical model. It is grounded in the previous anatomical model as the anatomical model is grounded in the biological anatomy. It provides a different perspective on data generated by many anatomical models, and it is this different perspective that makes the probabilistic model an advance.

Chapter 4

Bifurcations of Synchrony and Swimming in the Tadpole CPG Controlling Locomotion

During swimming, neurons in the spinal CPG generate antiphase oscillations between left and right half-centres. Experimental recordings show that the same CPG neurons can also generate transient bouts of long-lasting in-phase oscillations between left-right centres. These synchronous episodes are rarely recorded and have no identified behavioural purpose. However, metamorphosing tadpoles require both antiphase and in-phase oscillations for swimming locomotion. Although our previous functional model of the swimming circuit has shown the ability to generate biologically realistic patterns of synchrony and swimming oscillations, a mathematical description of how these oscillations appear is still missing. In this chapter, we study a significant reduction of the CPG swimming circuit that incorporates the key operating principles of tadpole locomotion. This new model generates the various outputs seen in experimental recordings, including swimming and synchrony. To study the model, we perform detailed one- and two-parameter bifurcation analysis. This reveals the critical boundaries that separate different dynamical regimes and demonstrates the existence of parameter regions of bi-stable swimming and synchrony. We show that swimming is stable in a significantly larger range of parameters, and can be initiated more robustly, than synchrony. Our results can explain the appearance of long lasting synchrony bouts seen in experiments at the start of a swimming episode.

Rhythmic neuronal activity is the basis for many locomotor activities, such as swimming, flying and walking [Roberts et al., 1998, Grillner et al., 2008, Golubitsky et al., 1999, Marder and Bucher, 2001, Arshavsky et al., 1993, Dimitrijevic et al., 1998]. Experimental and modelling evidence suggests that such rhythmicity is generated by specialised neuronal networks called central pattern gen-

erators (CPGs) [Marder and Calabrese, 1996, Ijspeert, 2008]. A key property of a CPG is the ability to autonomously generate rhythmic activity without forcing by periodic external input.

Different motor behaviours require different rhythmic patterns, such as left-right antiphase oscillations for walking and running [Grillner, 2006], or in-phase left-right firing for some forms of crawling [Eisenhart et al., 2000] and flying [Marder and Bucher, 2001]. Interestingly, swimming in Xenopus tadpoles follows an anti-phase pattern, but during metamorphosis there is a progressive shift to in-phase limb movements [Combes et al., 2004]. Although experiments show that some CPG neurons can be display either in- or anti-phase oscillations [Li et al., 2014a], it is unclear whether the same group of CPG neurons could be responsible for the generation of these different rhythmic patterns. An alternative is that the CPG includes a repertoire of diverse CPG sub-networks, each responsible for a single motor pattern with its own specific firing [Dickinson et al., 1990, Briggman and Kristan, 2006, Briggman and Kristan Jr, 2008].

In this chapter, we consider a computational model of the Xenopus tadpole CPG. We focus on the neuronal dynamics that drive swimming locomotion in two-day-old tadpoles (two days from fertilisation, developmental stage 37/38). The mechanism for swimming generation is well understood and previous studies have revealed the detailed structure of the CPG circuit. In particular, this circuit is split between left and right sides of the spinal cord (left-right half centres) spanning the spinal cord and caudal hindbrain [Roberts et al., 2008]. A pattern of swimming related activity is generated by excitatory descending interneurons (dINs) and inhibitory commissural interneurons (cINs). These key CPG neurons drive the motor response by firing single action potentials per swimming cycle, with firing occurring in antiphase between left and right half-centres [Roberts et al., 2010].

It has long been known from physiological experiments in tadpoles immobilised with a neuromuscular blocker that the tadpole spinal circuit can also generate transient forms of motor output in which there is synchronous firing of neurons between left and right half centres, with half the swimming period [Kahn and Roberts, 1982a,b, Soffe et al., 1984]. Early simulations suggested that this synchronous output could be stable for neurons excited by positive feedback and coupled by reciprocal inhibition [Roberts et al., 1984, Roberts and Tunstall, 1990]. More recent recordings have confirmed that CPG neurons fire during these transient periods of synchronous activity, which can be spontaneous or induced artificially by injecting constant depolarising currents [Li et al., 2014a]. Transitional synchrony may last for a relatively long time (500-1000 ms) and, in most cases, starts shortly after swimming initiation [Li et al., 2014a, Kahn and Roberts, 1982b]. To date, a behavioural correlate of this pattern has not been characterised, although apparently-pathological 'fluttering' movements have been observed (unpublished). It therefore remains unclear whether synchrony is indeed a pathological behaviour or its appearance is an early preparation for a developmental change. During metamorphosis (happening at around 60 days from fertilisation), in-phase and anti-phase motor patterns have been observed and defined both behaviourally and physiologically (ventral root recordings) [Combes et al., 2004]. We believe that one possible role of synchrony in Xenopus tadpoles is to release glutamate/acetylcholine at double the normal swimming frequency in the CPG and at the neuromuscular junctions. This may boost CPG and muscle excitability and help increase the muscle contraction amplitude/strength at the beginning of swimming.

Our aim is to understand how swimming (anti-phase) and synchrony (in-phase) oscillations can be generated by CPG neurons, find conditions for existence of these two dynamical modes, and for the existence of bi-stability - where both swimming and synchrony can be generated with the same parameters, just by

varying the initial stimulus. Furthermore, we seek to understand the mechanism that produces transitions from long-lasting synchrony to stable swimming. In a related work, anti-phase and in-phase oscillations have been found to be stable outputs in recent computational models of the mammalian respiratory CPG [Molkov et al., 2015]. To achieve our goal, we combine a highly reduced neuronal circuit of two pairs of neurons that are known to be essential for the tadpole CPG function [Arshavsky et al., 1993, Roberts and Tunstall, 1990, Wolf et al., 2009] with a detailed model of single neuron spiking. Consideration of a small network allows us to use bifurcation analysis for studying the possible dynamical modes. A detailed, biologically plausible model of spike generation allows us to mimic specific features of experimental recordings and compare the results of model simulations with experimental data.

The reduced CPG circuit includes one excitatory (dIN) and one inhibitory (cIN) neuron in each half centre. Key features of the model include dIN self-excitation acting as a positive feedback and cIN cross inhibition. A circuit with similar characteristics has been studied in [Laing and Chow, 2002]. During swimming, this circuit works in the following way. Excitation and subsequent spiking of a dIN leads an ipsilateral cIN to spike, inhibiting the dIN in the opposite half centre. A key feature of dIN firing is the potential for post-inhibitory rebound (PIR) spiking. Therefore, after some delay the inhibited dIN generates a spike due to PIR, excites the cIN in the same half centre, and the process repeats to generate an anti-phase spiking pattern between the half-centres. During synchrony, dINs on both half centres fire PIR spikes at similar times, shortly before the arrival of cIN inhibition. When inhibition does arrive, it hyperpolarizes the dINs, which then fire another PIR spike after a relatively slow repolarisation period. If synchrony is stable then the cIN and dIN firing times for the two half-centres become increasingly close together, until both half-centres are firing in perfect synchrony. The activity of dINs drives swimming and other locomotor behaviour

by directly exciting the motorneurons that control muscle movement, though we do not include motorneurons in the reduced model [Li et al., 2006, Soffe et al., 2009].

The model of the neuronal circuit includes six synapses and to model spiking activity we use a detailed single-compartment Hodgkin-Huxley type model with the gating channels' dynamics motivated by voltage-clamp experiments [Dale, 1995, Winlove and Roberts, 2012]. Thus, the reduced model includes 34 ordinary differential equations. To study bifurcations we combine the continuation-based software AUTO-07P [Doedel et al., 2007] and XPPAUT [Ermentrout, 2002]. We study co-dimension one and two bifurcations of the limit cycles corresponding to swimming and synchrony. This analysis reveals the stability regions for these two limit cycles, including regions where the system can support bistable swimming and synchrony. Taking inspiration from initiation of swimming in real experiments, we formulate a biologically-plausible method of initiating the model's dynamics based on input currents onto dINs. This initiation procedure allows us to explore to what extent the time jitter and duration between left and right dIN current inputs can lead to stable synchrony or swimming. We show that the swimming mode has a bigger stability region and it can be initialised for a bigger range of initiation parameter values. This suggests that swimming is the key functional output of young tadpoles. We propose a mechanism for generating long-lasting transient synchrony preceding a swimming episode that is qualitatively similar to synchrony in experimental recordings.

4.1 Methods

4.1.1 Model Description

The model is a significant reduction of the detailed, biologically realistic model of the swimming network in the tadpole caudal hindbrain and rostral spinal cord, which was described in our previous publications [Li et al., 2007a, Borisyuk et al.,

2014, Roberts et al., 2014]. This full model for simulations of the swimming dynamics includes about 2,000 neurons and 90,000 synapses with about 200,000 delay differential equations. This model demonstrates a very reliable swimming dynamic under variation of parameter values [Roberts et al., 2014]. In addition, this model has been used to simulate the experimental data of synchrony activity [Li et al., 2014a].

To use bifurcation analysis for formal mathematical study of the existence and stability of swimming and synchrony, it is necessary to simplify the previous model significantly. Our approach for defining a simplified model for locomotion in tadpoles is to minimise the number of neurons and synaptic connections, and to use a detailed biologically-realistic mathematical description of neurons and synapses. The description of the model comprises two parts.

Firstly, we consider only one "segment" of the spinal cord with the minimal number of neurons in each half-centre needed to characterise the tadpole CPG [Arshavsky et al., 1993, Wolf et al., 2009]: one excitatory dIN and one inhibitory cIN. Thus, the "reduced model" includes four neurons and we assume that the full neuronal network for swimming can be built by expansion of this structure. Figure 4.1 shows the connections in the reduced model. To compensate for a lack of excitation resulting from removal of synaptic input from other dINs, we introduce dIN self-excitation. In the reduced model we consider identical neurons in both half-centres with symmetrical connections. Therefore, the dynamical system is also symmetrical under midline reflection of left and right half-centres (Figure 4.1).

Secondly, we use a detailed model of spike generation and synaptic transmission to mimic important details of firing patterns in different dynamical modes and compare them with experimental recordings from tadpole neurons. To model neurons' membrane potential and transmembrane currents we use the

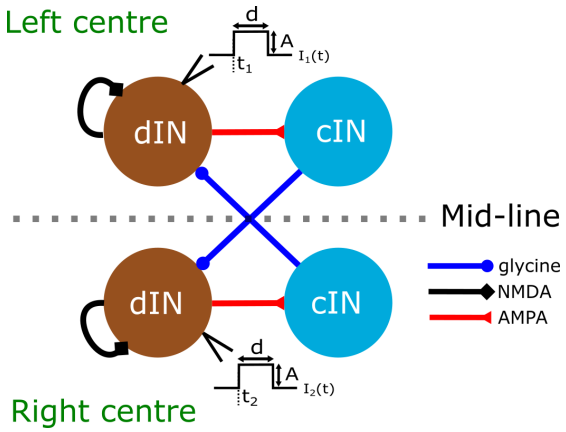

Figure 4.1: Scheme of neurons and connections in the reduced model. Currents $I_1(t)$ and $I_2(t)$represent external depolarising step currents injected to the two dINs to mimic sensory input. Both currents have the same duration d and amplitude A. The current pulses for $I_1(t)$ and $I_2(t)$ are initialised at time t_1 and t_2, respectively.

same modified Hodgkin-Huxley spiking model as in the full functional model (see the Introduction and Roberts et al. [2014]). To model synaptic connections we use an approach similar to the full functional model, the only difference being that in the functional model, synapses were modelled using delay differential equations, while here we use synapse models that are continuously dependent on the pre-synaptic potential. We use a continuous model of synaptic transmission because of the difficulties associated with numerical continuation of systems of delay differential equations.

Neuronal models. Neuronal spike generation is modelled by the single-compartment Hodgkin-Huxley equations, which includes various types of currents flowing through the ion channels. Although several models describing the activity of dINs and cINs have been developed [Wolf et al., 2009, Roberts et al., 2010, 2014, Roberts and Tunstall, 1990, Hull et al., 2015], we believe these models are still not able to reproduce some important properties known from electrophysiology. Here, we use the same neuron models used to model the functional connectome in the previous chapter (see the Introduction and Roberts et al. [2014]), because they incorporate some key physiological firing properties

detected from experimental recordings [Winlove and Roberts, 2012, Dale, 1995, Roberts et al., 2014].

Remark: In the case of dINs, the mechanism of PIR is based on de-inactivation of depolarisation-activated inward currents [Li et al., 2006, Soffe et al., 2009, Angstadt et al., 2005]. However, the complete mechanism underlying PIR in tadpole dINs still awaits physiological characterisation. It is known that, during swimming, dINs are depolarised due to summated, long lasting NMDA-receptor mediated excitation, and the inhibition leading to PIR occurs against the background of this depolarisation [Li et al., 2006].

Figure 4.2A demonstrates the PIR property of the dIN model. During the time interval $[t_0,\ t_1]$ the dIN is in the depolarised state due to constant current injection [Roberts et al., 2014]. During the time interval $[t_1,\ t_2]$ the dIN voltage decreases due to the injection of inhibitory current (blue line). Termination of this inhibitory current at time t_2 (on the background of positive current injection) leads to generation of a dIN spike at time t_2 via the PIR mechanism.

Figure 4.2B-C show the dynamics of the gating variables and ionic currents, respectively. It is clear from these figures that the mechanism of PIR is rather complex, due to the interaction of many model components with different time scales. However, we can see how the PIR spike at time t_2 is triggered by de-inactivation of the sodium current.

Synaptic models. The reduced model includes excitatory and inhibitory connections. We consider both AMPA and NMDA receptors of glutamate excitatory synapses from dINs, and glycinergic receptor for inhibitory synapses from cINs (Figure 4.1). Summation of the slow synaptic transmission mediated by NMDA receptors from dIN to dIN synaptic transmission is essential for generation of swimming activity because PIR spiking in dINs needs inhibition to arrive against a sufficiently high level of depolarization [Roberts and Tunstall, 1990]. For this

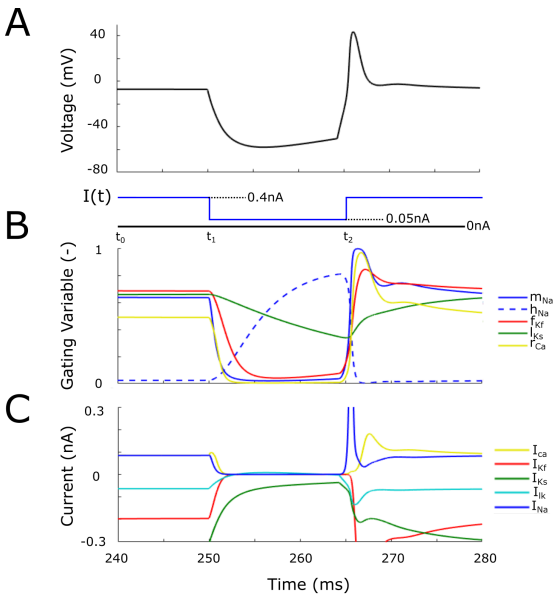

Figure 4.2: Property of PIR in the dIN model. (A) Voltage dynamics in one dIN (black line) during the injection of the current function $I(t)$ (blue line). (B) and (C) show the dynamics of the dIN's gating variables and ionic currents during the same current injection of part (A), respectively.

reason, we consider NMDA driven self-excitatory connections in dINs. As in the full model of the swimming network, dINs in the reduced model are able to fire PIR spikes on release from cIN inhibition. The six synaptic connections of the reduced model (Figure 4.1) encompass the key properties of the tadpole CPG: ipsilateral excitation (driven by NMDA/AMPA synapse), commissural inhibition (driven by glycinergic synapses) and post-inhibitory rebound in dINs.

Equations 4.1-4.5 describe the synaptic currents i_s ($s \in$ {ampa,nmda,inh}). The time evolution of every synaptic transmission event depends on the opening and closing of state variables, τ_c and τ_o respectively. Equation 4.2 describes the dynamics of these variables: y_s, $y_s \in \{c_s, o_s\}$. In this equation, we use a well-known model of synaptic transmission that depends continuously on the pre-synaptic membrane potential v_{pre} [Destexhe et al., 1998] with $g_s = g_s(v_{pre})$ representing the concentration of released neurotransmitter formulated in 4.3. In the case of NMDA receptors, voltage-dependence of the synaptic current is described by the factor $Mg(v)$ representing Mg^{2+} modulation of NMDA recep-

s	NMDA	AMPA	glycine
e_s (mV)	0	0	-75
τ_o^s (ms)	0.5	0.2	1.5
τ_c^s (ms)	80	3	4
$\bar{v}_s$ (mV)	10	10	1
T_s (-)	1.5	4	1

Table 4.1: Parameters of the synaptic models.

tors (Equations 4.4-4.5).

$$i_s = w_s(e_s - v)(c_s - o_s) \tag{4.1}$$

$$\frac{dy_s}{st} = g_s(v_{pre})(1 - y_s) - \frac{y_s}{\tau_y^s} \tag{4.2}$$

$$g_s(v_{pre}) = \frac{T_s}{1 + exp(\bar{v}_2 - v_{pre})} \tag{4.3}$$

$$i_{nmda} = w_{nmda}(e_{nmda} - v)(c_{nmda} - o_{nmda})Mg(v) \tag{4.4}$$

$$Mg(v) = 1/(1 + 0.05exp(-0.08v)) \tag{4.5}$$

Here the values of parameters e_s, τ_o^s, τ_c^s, $\bar{v}_s$ and T_s are given in Table 4.1. Parameters w_s and e_s represent the synaptic strength and reversal potential of each type of synapse, respectively. The time constants τ_o, τ_c of the opening and closing state variables were fitted from pairwise electrophysiological recordings [Sautois et al., 2007] and follow the time course of the different receptors types. The slow de-inactivation of the NMDA is important for a proper functioning of swimming [Sautois et al., 2007]. We do not investigate the variation of these time constants. Parameters w_{ampa}, w_{nmda} and w_{inh} are the bifurcation parameters that we varied during numerical continuation. In the results section we will discuss the values of these parameters.

Remark: Parameter w_{ampa} describes the connection strength of dIN $\rightarrow$ cIN coupling (for simplicity we consider the dynamics of AMPA synapse only). We calculate the physiological range of variation for this parameter using the following experimental findings: (1) The dINs spike reliably and synchronously during

each swimming cycle [Soffe et al., 2009, Li et al., 2014a]; (2) The average number of incoming connections from dINs to cINs participating in swimming is in the range (15, 17) [Ferrario et al., 2018a]; (3) The maximal unitary strength of the AMPA synapse is 0.6nS [Sautois et al., 2007]. Thus, it gives the physiological range of parameter w_{ampa}: (9nS,10.2nS).

Parameter w_{nmda} describes the connection strength of the dIN $\rightarrow$ dIN coupling. For simplicity we consider the dynamics of a slow NMDA synapse only, but adjust the connection strength to reflect the fast AMPA component as well. To calculate the physiological range of this parameter variation, we use experimental findings similar to the consideration above. The average number of incoming connections to dINs from dINs is in the range (13-21) [Ferrario et al., 2018a], and the maximal unitary strengths of the AMPA and NMDA synapses are 0.6nS and 0.15nS, respectively [Sautois et al., 2007]. To take into account the AMPA influence, we adjust the strength by summing these values and multiply by the range of incoming connections to get the physiological range of parameter w_{nmda}: (10nS,15.8nS).

For our numerical study of bifurcations we widen the range for both w_{ampa} and w_{nmda} to clarify the relationship between different bifurcations (e.g. to find the turning point). Therefore, we vary the parameters w_{ampa} and w_{nmda} in the ranges (9nS,20nS) and (8nS,20nS), respectively.

4.1.2 Software

For numerical studies of limit cycles, we combine several software tools. To run numerical integration and find periodic orbits we use XPPAUT [Ermentrout, 2002] with the CVODE variable time step integrator with absolute and relative tolerances equal to 1e-12. We use the stable periodic orbit to start numerical continuation in order to determine stability and find bifurcations. To perform numerical continuation and detect the bifurcations of the reduced model we use

the software package AUTO-07P [Doedel et al., 2007]. We use custom written Python code to transform equations, variables, functions and parameters from XPPAUT to AUTO. To study the initiation of the stable limit cycles and run multiple numerical integrations in parallel, we use both XPPAUT and custom written MATLAB code (MathWorks, Inc) with different variable time step integration schemes (ode23tb, ode45) to confirm the accuracy of our results. To integrate the system with noise, we use standard Euler-Maruyama method with time step dt=0.01.

4.2 Results

4.2.1 Swimming and synchrony limit cycles

In this section, we validate the reduced model by showing that it can produce activity similar to that seen in experimental recordings. To do so, we fix synaptic strengths and simulate the reduced model to reproduce swimming and synchrony dynamics.

In experiments with immobilised tadpoles, CPG neurons are normally at rest before the start of a swimming episode. This start is marked by a gradual depolarisation of the membrane potential that can lead to rhythmic firing [Roberts et al., 1981]. To mimic these experiments, we initialise neurons at rest, and we use the following initiation procedure to control perturbations and move the orbit from the resting state to a basin of attraction of either swimming or synchrony.

Initiation of the dynamics. In experiments, a swimming episode can start after brief head or trunk skin stimulation on one side of the animal [Buhl et al., 2012, Boothby and Roberts, 1995]. Skin stimulation leads to neuronal firing in the sensory pathway which delivers, with some delay, excitation to CPG neurons in both half-centres. Experiments have shown that the start of movement occurs shortly after the first dINs spikes [Buhl et al., 2012], and that dIN activity drives spiking of other neurons during swimming [Soffe et al., 2009].

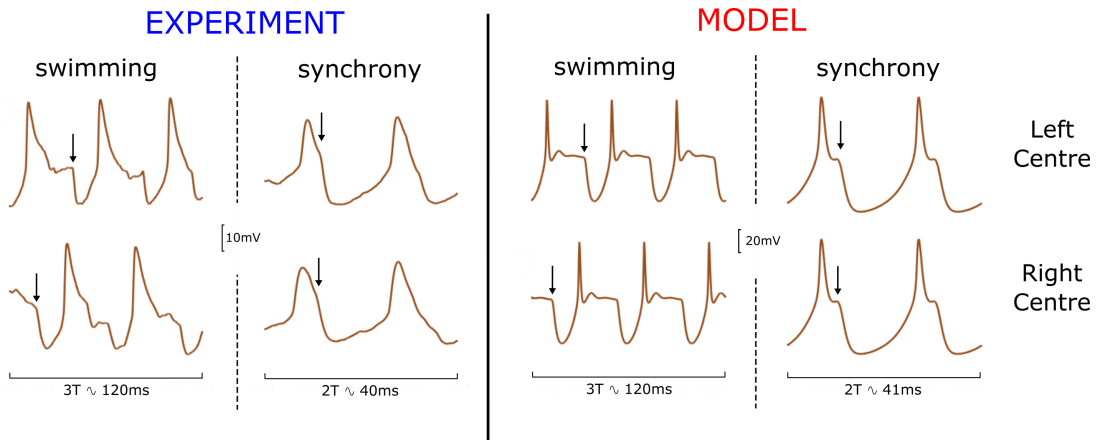

Figure 4.3: Voltage traces of dINs in the reduced model during swimming and synchrony. The left panel shows experimental pairwise recordings from one left-centre dIN and one right-centre dIN during swimming and synchrony. The right panel shows the voltage variable of the two dINs of the reduced model during swimming and synchrony. We show three cycles of swimming (3T) and two cycles of synchrony (2T) to highlight the characteristic shapes of the membrane potential during these two regimes and to compare experiments and model simulations. Arrows indicate the firing of cINs and mark the inhibition preceding PIR spikes in dINs. Model parameters used to obtain swimming are w_{inh} = 23 nS, w_{ampa} = 12 nS and w_{nmda} = 10 nS, with initiation parameters Δ = 140 ms and d = 6 ms. Model parameters used to obtain synchrony are w_{inh} = 55 nS, w_{ampa} = 12 nS and w_{nmda} = 10 nS, and initiation parameters Δ = 0 ms and d = 6 ms. The experimental recordings have been obtained using the same experimental protocols and conditions described in [Li et al., 2014a]

To move the system out of its initial rest state and initiate activity, we inject a depolarising step current i_{ext} with fixed amplitude $A = 0.1$ nA and duration $d = 6$ ms to dINs in the left and right half centres at times t_1 and t_2 respectively, where time delay $\Delta = t_2 - t_1$ (Figure 4.1).

We use the initiation procedure to run numerical integration of the reduced model in order to find stable oscillatory regimes. Figure 4.3 shows both experimental recordings (left panel) and stable regimes of the reduced model (right panel). The left part of each panel shows the membrane potential of dINs in each half-centre of the body during swimming and the right part shows the membrane potentials during synchrony. Parameter values for these simulations are given in the figure caption.

Although the model describes a highly reduced CPG, the pattern of dIN membrane potential trajectories qualitatively matches the experimental recordings well. These typical spiking patterns of swimming and synchrony modes include dIN post-spike depolarisation and deep inhibition (black arrows show time of cIN spikes in the opposite half-centres) causing inhibition and subsequent rebound spiking. These two typical oscillatory patterns correspond to limit cycles in the phase space of the dynamical system. The swimming mode with anti-phase oscillations in opposite half-centres corresponds to the Swimming limit Cycle (SwC), while the synchrony mode of in-phase oscillations corresponds to the Synchrony limit Cycle (SyC).

4.2.2 Symmetry in the reduced model

From Figure 4.1, one can see that the reduced model is invariant under reflection of neurons and synapses on the mid-line. This means that the reduced model is a $\mathbb{Z}_2$-equivariant dynamical system. The reduced model can be written in the general form of an n-dimensional system where $n = 2k$ and k is the number of equations describing the dynamics of the variables related to the left and right half-centres:

$$\dot{y} = f(y), \quad y \in \mathbb{R}^{2k} \tag{4.6}$$

We arrange the equations in such a way that the first k equations describe the state variables of neurons and synapses in the left half-centre as well as the commissural synaptic connection from left cIN to right dIN. All variables related to the left half-centre we denote by vector $y_L(t)$, $y_L \in \mathbb{R}^k$. The other k equations likewise describe neuronal variables and synaptic connections in the right half-centre, as well as the commissural synaptic connection from right cIN to left dIN. We denote these right half-centre variables by vector $y_R(t)$, $y_R \in \mathbb{R}^k$. The system is symmetrical because the equations for variables of the left and right half-centres in Equation 4.6 are identical. If we swap variables y_L and y_R in

Equation 4.6 the equations for y_L become equations for y_R and these equations are equivalent to the y_R equations. An equivalent statement is valid for the y_R equations.

It follows from the system's symmetry that any limit cycle that exists in system 4.6 is of one of four types:

Type (1): **In-phase limit cycle**: $y_L(t) = y_R(t), \forall t$

Type (2): **Anti-phase** limit cycle: $y_L(t) = y_R(t + T/2), \forall t$, here P is period of oscillation.

Type (3): **Out of phase** limit cycle: $y_L(t) = y_R(t + P), \forall t$ here $P \neq T/2$ is phase shift.

Type (4): **Asymmetrical** limit cycle: $y_L(t) \neq y_R(t + P), \forall t, \forall P$.

It is clear that the synchrony limit cycle SyC should be of type (1), and this cycle belongs to the symmetry manifold $Y_k^+ = \{y \in \mathbb{R}^{2k} : y_L = y_R\}$. The swimming limit cycle SwC should be of type (2). All limit cycles of type (3-4) should exist in pairs.

Initiation with symmetry. By selecting proper values for the initiation parameters described in the Methods section, we can initiate limit cycles of different types. For example, to initiate the dynamics inside the in-phase manifold Y_k^+ we select $\Delta = 0$. This means that dINs in both half-centres simultaneously receive the same stimulating input, therefore, the orbit is locked inside the manifold Y_k^+. If $\Delta \neq 0$, the dynamics are initialised outside the manifold Y_k^+, and an orbit can be either attracted to a stable attractor inside of the manifold Y_k^+ or repulsed from the manifold.

4.2.3 Bifurcation analysis under one parameter variation

In this section we use bifurcation theory to study dynamical regimes in the reduced model under variation of one parameter. We begin by outlining our motivations for choosing the bifurcation parameters used for both the codimension-

one and the codimension-two studies.

Choice of the bifurcation parameters. We assume that the values of all model parameters are fixed except for three parameters which we vary in turn using numerical continuation. All parameter values governing the intrinsic dynamics of the neurons are selected according to our previous study of the full physiological model [Ferrario et al., 2018a, Roberts et al., 2014]. Many of these parameter values have been directly measured in experiments, although some were selected from a physiological range in model simulations. Values of these neuronal parameters are fixed for the purposes of bifurcation analysis. The three parameters that we vary, w_{ampa}, w_{nmda} and w_{inh}, correspond to synaptic strengths for excitatory and inhibitory synapses.

We choose to vary these parameters for three reasons. Firstly, although these parameters are important for reliable functioning of the CPG and, in particular, for reliable swimming, it is difficult to measure their values in experiments. Simulations of the full physiological model show that the swimming regime is very robust: swimming exists even when these parameter values are varied in a wide range [Roberts et al., 2014]. However, in a recent work [Davis et al., 2017] we investigated the effect of axon fasciculation in the spinal network, and we found that a proper balance between excitatory and inhibitory connection strengths is needed for generating a reliable CPG swimming activity. Secondly, experimental recordings [Li et al., 2014a] show that occasional synchrony appears more frequently soon after a stimulus that initiates swimming, at a time when the excitatory drive is stronger than during later swimming [Soffe and Roberts, 1982]. Moreover, synchrony appears less frequently when glycinergic inhibition is artificially reduced by application of inhibitory blockers [Li et al., 2014a]. We hypothesise that these excitatory and inhibitory contributions are mainly driven from cINs and dINs. Thirdly, a previous experimental work [Li and Moult, 2012] showed how strong background excitation and phasic inhibition can influence

the swimming period. We used the reduced model to explore how variations in excitatory and inhibitory strengths shape the period of the synchrony and swimming limit cycles. The strength of the conductance driven by dINs and cINs synaptic transmissions represents two major contributions of these two components. By computing the period of synchrony and swimming limit cycles under variation of the synaptic strengths, we explored changes in the swimming and synchrony periods.

By selecting these parameters for bifurcation analysis we aim to find the critical boundaries of stability for the swimming and synchrony modes. Since swimming is the main functional behaviour of the animal at the considered stage of development, we expect that its stability region would most likely occupy a large area in parameter space. Therefore, we first study bifurcations under variation of inhibitory connection strength w_{inh}. We then study codimension-two bifurcations by varying w_{inh} together with either w_{ampa} or w_{nmda}. Throughout the following sections we use the same notation when referring to codimension-one bifurcation points in two-dimensional space and to their horizontal coordinate.

We begin with the study of bifurcations of the swimming and synchrony limit cycles under variation of the inhibitory strength w_{inh}. We use each stable limit cycle as a starting point for a numerical continuation procedure. In Figure 4.4 we show the continuation of the SwC (black curve) and SyC (red curve) under variation of parameter w_{inh}, and we fix parameter values w_{ampa}=12 nS and w_{nmda}=10 nS.

In Figure 4.4 the black curve shows that the SwC is stable for $w_{inh} > w_1$. The critical parameter value w_1 corresponds to a subcritical Neimark-Sacker (torus) bifurcation (TR^-). At this critical parameter value, the stable SwC becomes unstable for $w_{inh} < w_1$ by merging with an unstable torus (torus continuation is not shown in Figure 4.4) which co-exists with the stable SwC for $w_{inh} > w_1$.

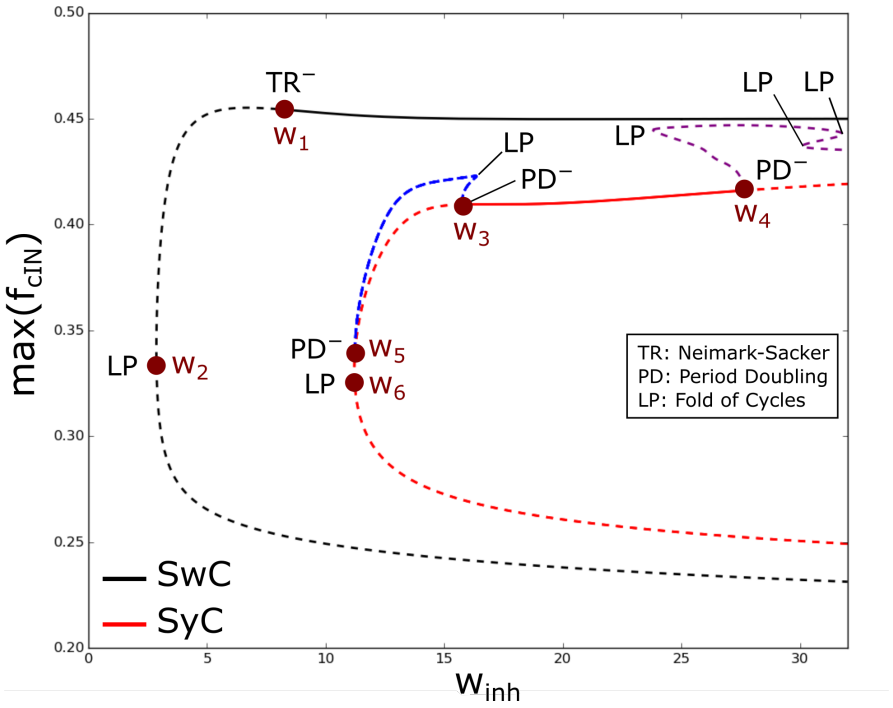

Figure 4.4: One-dimensional bifurcation diagram for the swimming (black) and synchrony (red) limit cycles at varying inhibitory strength w_{ihn}. Blue and purple lines show two unstable limit cycles appearing at bifurcation points w_3 and w_4, respectively. The y-axis shows the maximum of the K_f-gating variable f of the left cIN for each limit cycle. Stable and unstable limit cycles are shown by continuous and dashed lines, respectively. The superscript - refers to subcritical bifurcations. Bifurcation parameter values (in nS) are the following: $w_1 = 8.57$, $w_2 = 2.86$, $w_3 = 15.74$, $w_4 = 27.6$, $w_5 = 11.23$ and $w_6 = 11.21$

Thus, the SwC is unstable (dashed black line) for $w_{inh} < w_1$. At the critical parameter value $w_{inh} = w_2$, ($w_2 < w_1$) this unstable cycle SwC disappears via a fold (limit point) bifurcation (LP) by merging with another unstable cycle.

Remark. Our calculations show that stable SwC can be continued until very large values of $w_{inh} \sim 1000$ nS (not shown).

In Figure 4.4, the solid red line corresponds to the stable SyC for $w_{inh} \in (w_3, w_4)$. Both critical parameter values $w_{inh} = w_3$ and $w_{inh} = w_4$ correspond to subcritical period-doubling bifurcations (PD^-). At a critical parameter value $w_{inh} = w_3$ the stable SyC merges with the unstable limit cycle of double period (blue dashed line) which exists for $w_{inh} > w_3$ and becomes unstable for $w_{inh} < w_3$. Similarly, at the critical parameter value $w_{inh} = w_4$ the stable SyC merges with the unstable limit cycle of double period (purple dashed line) which exists for $w_{inh} < w_4$ and becomes unstable for $w_{inh} > w_4$. The dashed red line shows the unstable SyC.

It is interesting to note that by looking at the trajectories of these two unstable limit cycles of double period we found that these cycles are of two different types. The limit cycle shown by the blue line is of type (1), and this cycle belongs to the symmetry manifold Y_k^+. Further investigation of this blue cycle reveals a fold bifurcation and another subcritical period-doubling bifurcation ($w_{inh} = w_5$). As a result of this subcritical period-doubling bifurcation, the unstable limit cycle of double period (blue dashed line) merges with the unstable SyC (red dashed line) inside of the symmetry manifold Y_k^+. The unstable SyC disappears via a fold bifurcation ($w_{inh} = w_6$).

The limit cycle shown by the purple line is of type (2), and this cycle lies outside the symmetry manifold Y_k^+. Further bifurcations of this unstable limit cycle of double period include several fold bifurcations where two unstable limit cycles merge and disappear.

This analysis shows that there is a region of bi-stability $w_3 < w_{inh} < w_4$ for the

SwC and the SyC limit cycles. We notice that the range of parameter values where the SwC is stable is significantly larger than that of the range where the synchrony cycle is stable.

4.2.4 Stability of swimming and synchrony under variation of 2 parameters

In this section we consider bifurcations of swimming and synchrony cycles under two-parameter variation. We vary the synaptic strength of inhibition w_{inh} with either w_{nmda} or w_{ampa}.

Figure 4.5 shows the 2-dimensional stability regions of swimming and synchrony cycles under variation of parameter pairs (w_{inh}, w_{ampa}) (Figure 4.5A) and (w_{inh}, w_{nmda}) (Figure 4.5B). In both figures, the grey area shows the stability region of the swimming limit cycle, and inside this area is a light red shaded area corresponding to stability of the synchrony cycle. In fact, this light red area shows the region of bi-stability, where both SwC and SyC are stable. The white area in the left part of each panel corresponds to the stationary state without oscillations. From the figures it is clear that the synchrony cycle has a smaller stability region regardless of which excitatory synaptic strength is changed.

In both Figure 4.5A and B, the critical boundary (black line marked by TR^-) of the SwC stability region corresponds to a subcritical Neimark-Sacker (torus) bifurcation. On the left from this line, a stable SwC co-exists with an unstable torus. A swimming cycle and torus merge and disappear on the critical boundary.

The stability region of the SyC is limited by two period-doubling bifurcation lines (red). In Figure 4.5A, both critical boundaries correspond to sub-critical period-doubling bifurcations for larger values of w_{ampa} (red lines marked PD^-). For smaller values of w_{ampa} both period-doubling boundaries become supercritical (red line marked PD^+). We note that everywhere on the period doubling bifur-

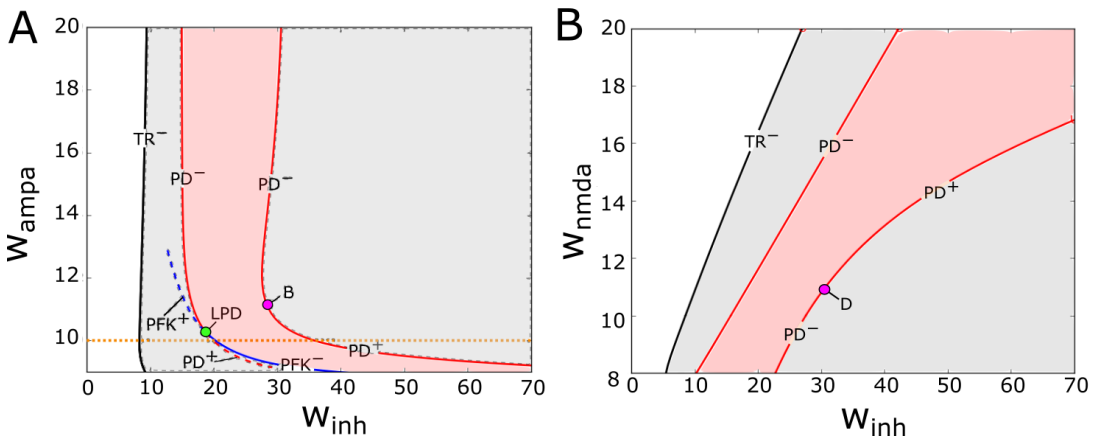

Figure 4.5: Codimension-two bifurcation diagrams showing the stability regions for the swimming (light grey and red) and synchrony (light red) limit cycles under variation of (w_{inh}, w_{ampa}) in (A) and (w_{inh}, w_{nmda}) in (B). Superscripts - and + refer to subcritical and supercritical bifurcations, respectively. To clarify the stability of the limit cycles for low values of w_{ampa}, we computed the codimension-one bifurcation diagram at fixed value $w_{ampa} = 10$nS shown in Figure 4.6 (orange dotted line). Bifurcation points B and D switch the criticality of the PD bifurcation (subcritical to supercritical). The LPD point is a fold-flip bifurcation point. At this point, a pitchfork bifurcation curve (PFK, blue line) interacts with a PD line and both exchange criticality.

cation line (red) one multiplier is (-1).

On the left critical boundary there is a point corresponding to a co-dimension 2 fold-flip bifurcation (green point marked LPD). At this bifurcation point, one additional multiplier becomes equal to the critical value (+1). It is known from [Kuznetsov et al., 2004] that the bifurcation diagram in the vicinity of the LPD critical point is very complex and there are several bifurcation lines, which intersect at the LPD point. [Kuznetsov et al., 2004] shows the bifurcation diagram near the LPD point. It is clear from this diagram that at an LPD point the period doubling line changes from sub- to super-critical. In addition, the diagram shows that the period doubling line and the fold bifurcation line intersect at the LPD point. However, there may be other bifurcation lines interacting in an LPD bifurcation, which we did not find. Since our model is symmetrical, it is possible that our system has a pitchfork line instead of a fold line, and that this pitchfork line interacts with a period doubling line in a symmetrical version of the LPD bifurcation.

To clarify the boundary of SyC stability near the LPD point we fix the parameter value $w_{ampa} = 10$ and vary only one parameter w_{inh} to find bifurcations (horizontal dotted orange in Figure 4.5A). Figure 4.6 shows the results of this. In particular, the panel "ZOOM 1" of Figure 4.6B shows that there are two bifurcations in the area of interest. The critical parameter value $w_{inh} = u_4$ corresponds to the subcritical pitchfork bifurcation of limit cycles (red dot u_4 marked PFK). The SyC is stable in region $w_{inh} > u_4$, and it becomes unstable for $w_{inh} < u_4$. At the PFK^- parameter $w_{inh} = w_4$ a pair of unstable out-of-phase limit cycles of type (4) merge and disappear (green lines in Figure 4.6). This has an important implication used in last section of the Results: when the stable SyC becomes unstable at critical point u_4, the loss of stability is in the transversal direction to the symmetry manifold Y_k^+. In addition, the panel ZOOM1 in Figure 4.6B shows the period doubling bifurcation of the unstable SyC ($w_{inh}^{cr} = u_5$).

We use the critical parameter value of the subcritical pitchfork bifurcation $w_{inh}^{cr} = u_4$ to start a new continuation under variation of two parameters and the result is shown in Figure 4.5A by a solid blue line marked PFK^- . The intersection of this line with the stability region causes the stable SyC to become unstable via subcritical pitchfork bifurcation.

Remark. There are several unstable limit cycles in Figure 4.6 shown by dashed green lines (type (4) out of phase cycles) and blue lines (type (2)) limit cycle of double period.

The critical parameter values $w_{inh}^{cr} = u_5$ and $w_{inh}^{cr} = u_6$ correspond to period doubling bifurcations and $w_{inh}^{cr} = u_7$ corresponds to the pitchfork bifurcation.

Now we return to the SyC stability region in Figure 4.5A and consider the right boundary (red line) which corresponds to the period doubling bifurcation. If w_{ampa}=12, then we know from Figure 4.4 that the period-doubling bifurcation at $w_{inh}^{cr} = w_4$ is subcritical. If w_{ampa}=10 then we know from Figure 4.6A that the

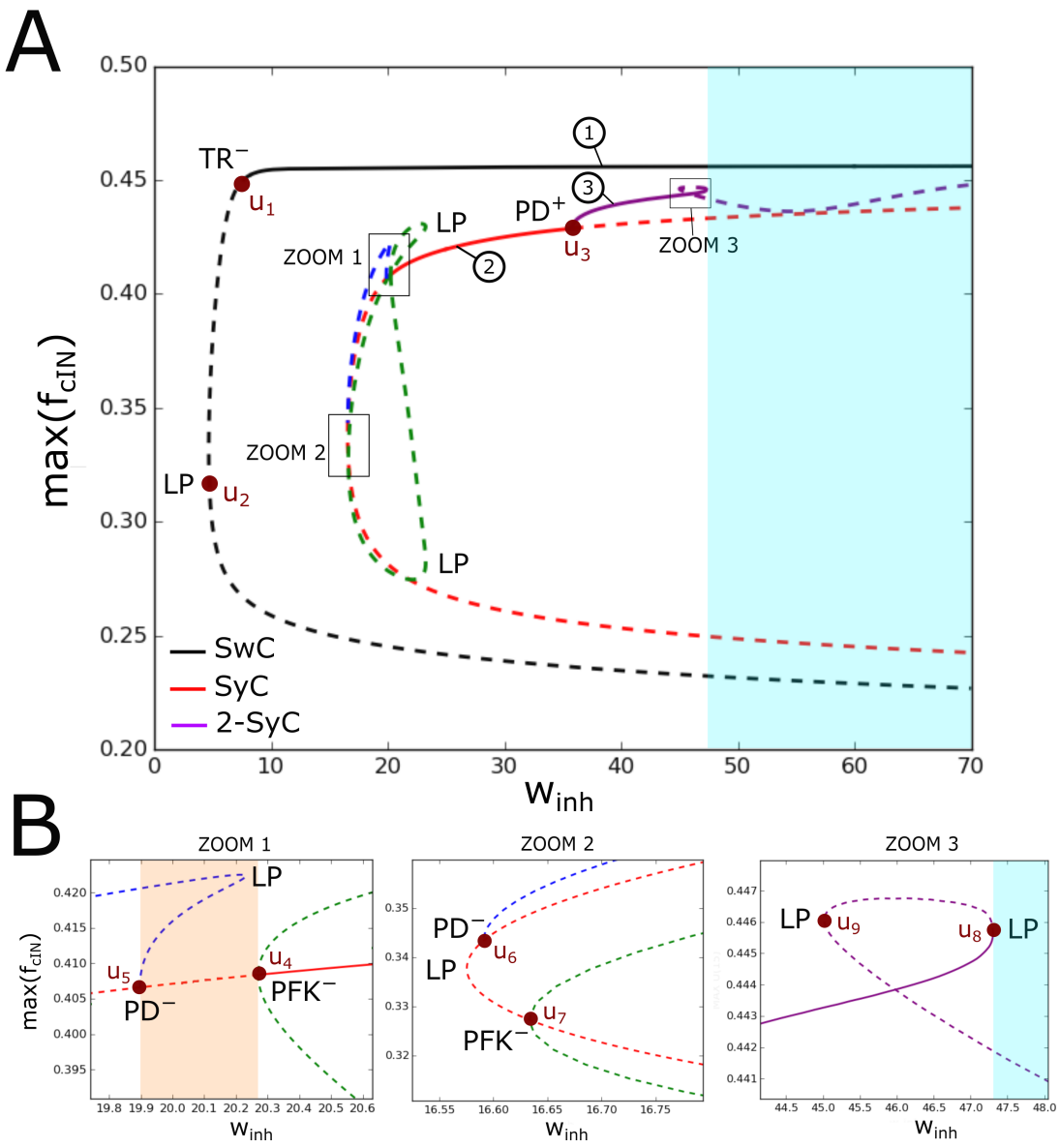

Figure 4.6: (A) One-dimensional bifurcation diagram for the synchrony (red), swimming (black) and double-synchrony (purple) limit cycles at varying inhibitory strength w_{inh} and fixed parameters w_{ampa} = 10 nS and w_{nmda} = 10 nS. The y-axis shows the maximum of the K_f -gating variable f of the left cIN for each limit cycle. Blue and green lines show unstable limit cycles appearing at bifurcation points u_5 and u_4, respectively. Stable and unstable limit cycles are shown by continuous and dashed lines, respectively. The superscript - refers to subcritical bifurcations. (B) Zoom of selected regions of panel A.

period doubling bifurcation at $w_{inh}^{cr} = u_3$ is supercritical: the stable SyC becomes unstable and a stable limit cycle of double period appears. Stable double period cycle is an in-phase type (1) limit cycle. Some additional details of the evolution of this limit cycle (solid purple line in Figure 4.6A) are shown in Figure 4.6B, panel ZOOM 3. This means that somewhere in between these two points on the period-doubling line ($(w_4, 12)$ and $(u_3, 10)$) there should be some codimension-two bifurcation point (B), which corresponds to this change. At this point (B) the red line of subcritical period doubling (marked PD^-) becomes the line of supercritical period-doubling bifurcation (marked PD^- at Figure 4.5A). We are unable to find point B via computational continuation. Therefore, to calculate the coordinates of this point we use multiple simulations of the reduced model to find where the double period limit cycle is stable outside of the SyC stability region. We started simulations from the following point ($\Delta = 0.1, d = 6, w_{ampa} = 10nS, w_{nmda} = 10nS, w_{inh} = 42nS$) and slightly varied parameters (w_{inh}, w_{ampa}), decreasing the value of w_{ampa} to find the double period cycle and define its stability. As a result, we find the coordinates of point B on the period doubling line: (27.8,11.5).

Figure 4.7A shows the voltage traces of the model neurons for each of the three stable limit cycles (SwC, SyC and 2-SyC). Here we introduce notation 2-SyC for the synchrony limit cycle of double period. Each neuron fires once per cycle in the cases of SyC and SwC, and twice per cycle in the case of 2-SyC. For each limit cycle, dIN firing evokes a single spike in the ipsilateral cIN. Clearly, the timing of cIN firing depends on the strength of the AMPA synapses w_{ampa}.

In 4.7B we show the time difference between left cIN and left dIN spikes during swimming as a function of w_{ampa} (for fixed parameters w_{nmda}=10nS and w_{inh}=40nS).

Now we consider Figure 4.5B, which shows the stability region of the SyC cy-

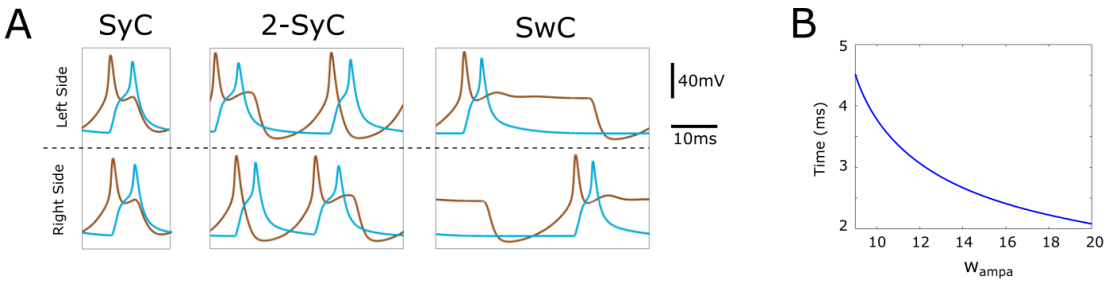

Figure 4.7: (A) Time evolution of the voltage of dINs (brown lines) and cINs (blue lines) during one period of synchrony (SyC), double-synchrony (2-SyC) and swimming (SwC). The three limit cycles are detected by AUTO in Figure 4.6. Synaptic strength parameters used to generate each panel SyC, 2-SyC and SwC, respectively, are $w_{inh} = 30nS, 45nS$ and 40 nS. (B) Time difference between left dIN and left cIN spikes during one cycle of the SwC at varying w_{ampa} . The remaining vector of parameters used to obtain this figure are $w_{inh} = 60nS$, $w_{nmda} = 10nS$, $\Delta = 50ms$ and $d = 6ms$

cle under variation of (w_{inh}, w_{nmda}). This region is shown by red shading, and the two boundaries (left and right red lines) correspond to period-doubling bifurcations. Using simulations of the reduced model we find that the left line corresponds to the subcritical period-doubling bifurcation (marked PD^{-}).

Through the analysis of the right boundary, we find that this period-doubling bifurcation line is supercritical for high values of w_{nmda} and it becomes subcritical for low values of w_{nmda} at the bifurcation point D represented in Figure 4.5B. Point D was not detected by AUTO, so to find its coordinates we used simulations in similar way to the procedure described above for finding the coordinates of point (B) in Figure 4.5A. As a result, we find the coordinates of point D on the period doubling line: (32.6,11.4).

Remark. As we have seen above, the bifurcation software AUTO cannot reliably distinguish whether the period-doubling bifurcation is sub- or supercritical. To clarify this matter for the left stability boundary of SyC, in Figure 4.5B we use multiple continuations and simulations of the model. We found that in a small vicinity on the left of the critical boundary, the bifurcation diagram is rather complex. In fact, some parts of this boundary correspond to a subcritical and other

parts to a supercritical period-doubling bifurcation. In the case of supercritical bifurcation, upon crossing the boundary, the stable synchrony limit cycle becomes unstable and a stable double-period cycle appears. This cycle is stable in a very small vicinity of the period-doubling boundary and becomes unstable via pitchfork bifurcation. We do not report complex bifurcations in this small vicinity on the left of the boundary and indicate that this boundary relates to the subcritical period-doubling bifurcation. Thus, if we do not consider a small region near this boundary, then the only stable attractor is the SwC. A similar remark is valid for the upper part (from the LPD point) of the left critical boundary in Figure 4.5A.

4.2.5 Study of the initiation space

In this Section we study how the dynamical mode depends on initiation parameters. We consider a grid of two parameter pairs: initiation time difference Δ and duration d. The amplitude initiation parameter is a fixed value A=0.01. The rectangular area of the initiation space ($0 \leq \Delta \leq 30$ and $0 \leq d \leq 20$) is covered by a grid of n by n nodes uniformly spaced (n=128). For each node in the grid we initiate the system dynamics. We run the simulations for a long time (3 simulated seconds) so that the trajectory approaches an attractor. This attractor can be either a limit cycle or a fixed point (resting state). In the case of a limit cycle, we calculate the period of oscillations. Figure 4.8 shows the result of simulations with fixed parameters $w_{nmda} = w_{ampa}$=10nS for different values of $w_{inh} \in$ (28,42,60 nS). A black pixel at position (Δ, d) means that initiation with these parameters results in a fixed point (period 0). If the initiated trajectory converges to a limit cycle then we discriminate the limit cycle by computing its period. Parameter value w_{inh}=28nS corresponds to regions of coexistence of stable SwC and stable SyC. Parameter value w_{inh}=42nS corresponds to regions of coexistence of stable SwC and the stable 2-SyC (type (2) cycle). For w_{inh}=60nS only SwC is stable. These particular values for w_{inh} have been selected using the

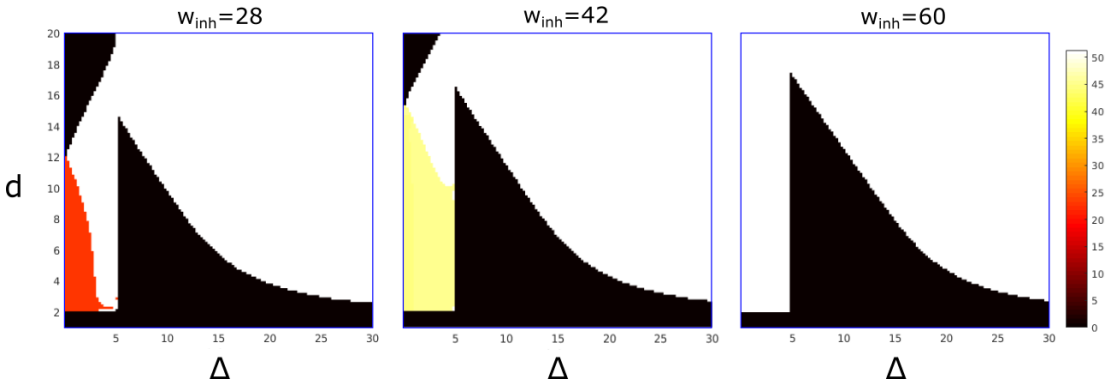

Figure 4.8: Stable attractors of the reduced model at varying initiation parameters (Δ, d) with fixed w_{ampa}=10nS and w_{nmda}=10nS. We show three different values of w_{inh} =28, 42 and 60 nS (title of each subplot). These values correspond to all the possible combinations of stable attractors of the system shown in Figure 4.6. Each coloured region identifies the initialisation parameters (Δ, d) that converge to a stable limit cycle, or converge to the resting state (black regions, fixed point). In the case of convergence to a limit cycle, the colour represents the period of the attractor. The orange region in the case w_{inh} =28nS identifies the initial conditions where the system converges to stable synchrony, the yellow region in the case w_{inh} =42nS corresponds to convergence to the 2-synchrony stable attractor, while the white regions correspond to convergence to stable swimming.

bifurcation diagrams described in the previous sections. This diagram allows us to explore the initiation space for all the stable attractors of the system. In all cases the largest region of initiation space corresponds to stable swimming (period of $\sim$ 50ms) but for some parameter values there is also a relatively small region where simulations converge to either synchrony (period of $\sim$ 20ms) or the double-period synchrony cycle (period of $\sim$ 45ms).

In Figure 4.8 all three panels include a vertical boundary near $\Delta = 5$ms. This boundary separates the white swimming region (or double-synchrony yellow region on the middle panel) from the black rest state region. In fact, the position of this boundary is determined by the time difference between first spikes of the left-dIN and left-cIN which we denote by μ ($\mu \approx 5$ms).

Indeed, if the value of parameter d is limited and the time interval Δ satisfies $\Delta > \mu$, then stimulation of the right dIN will not generate a spike because at the time of stimulation the right dIN will be under strong inhibition. Therefore, the

system will move to the rest state. To explain the right boundary of the black rest state region, we note that after some time the inhibition of the right dIN becomes weaker. Therefore, for some appropriate values of parameter Δ (for a fixed moderate value of parameter d) stimulation of the right dIN will overcome the inhibition, the right-dIN will spike and the system will converge to swimming.

In the case of a short delay $\Delta < \mu$, the right-dIN will spike because the stimulation of this dIN precedes the inhibition from the left-cIN. This dIN spike will trigger a spike in the right-cIN and it will lead to rhythmic activity. This rhythmic spiking can be either double-synchrony (yellow colour region in the middle panel) or swimming (white colour area).

If $d < 2$ms the injected currents of the initiation procedure are too short to activate either of the two dINs, and the system converges to the rest state (small black rectangular region in all three panels).

4.2.6 Interpretation of bifurcation diagrams in terms of experimental recordings

In this section, we speculate on how our study of the reduced model can explain the long-lasting synchronous activity seen in some biological experiments. Firstly, we find that patterns of spiking activity recorded in experiments following skin stimulation are very similar to spiking patterns and voltage traces generated by the reduced model. Secondly, our study of bifurcation enables us to formulate hypotheses on the existence of the synchrony mode and bi-stability regime, where both swimming and synchrony modes co-exist for the same parameter values.

We show that the system's bifurcations and the particular initiation procedure used play important roles in explaining long lasting synchronous activity and a subsequent transition to swimming. To explain this, we consider model parameters near the bifurcation points shown in Figure 4.6.

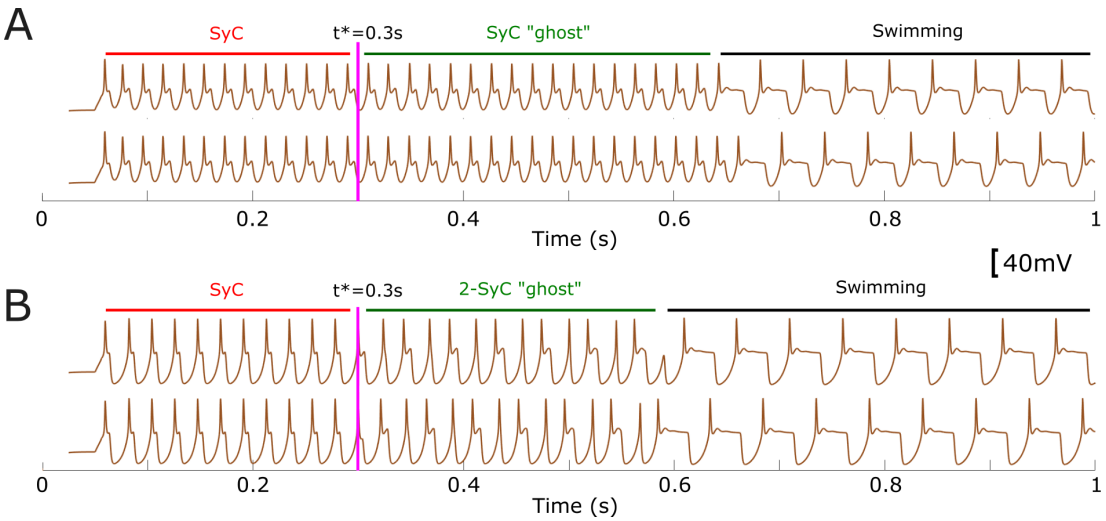

Figure 4.9: Transition from synchrony to swimming. Plot of dINs' voltage recordings at varying time shows synchronous activity before the dynamics are locked into synchronous (A) and double-synchronous regimes (B) before then converging to swimming mode. In both panels A and B, initiation parameters are set to $\Delta = 0$, $d = 6$ and $A = 0.04$. At time $t^\star = 0.3$ms the system is integrated starting from a perturbed initial point. This point is obtained by adding a normally distributed vector of numbers with equal variance $\sigma = 10^{-3}$ to each variable at time $t^\star$. Values of synaptic strengths are $w_{ampa} = 10$, $w_{nmda} = 10$, $w_{inh} = 20.2$ in case A and $w_{inh} = 60$ in case B.

Synchrony (double-synchrony) to swimming transitions. In Figure 4.9A, the selected parameter values correspond to the orange region of the bifurcation diagram in Figure 4.6B (ZOOM 1). For any parameter value inside this region, the SyC is globally unstable, but it is stable inside the symmetry manifold Y_k^+. The initiation parameter value $\Delta = 0$ means that the orbit starts and remains on the invariant symmetry manifold Y_k^+. Although the SyC is unstable, the trajectory converges to this limit cycle. At time $t^\star$ we slightly perturb the last point of the trajectory by adding a normally distributed vector with mean equal to zero and variance $\sigma = 10^{-3}$. We then restart the system integration from the perturbed point. The perturbed point does not belong to the invariant symmetry manifold; therefore, the trajectory diverges from the manifold and tends to SwC. The transitional period from the vicinity of the manifold to SwC is long because the value of w_{inh} is close to the subcritical pitchfork bifurcation (critical parameter value is u_4 in Figure 4.6B, ZOOM 1).

The transition time spent near the "ghost" of the stable synchrony cycle tends to infinity as w_{inh} tends to the critical value of the pitchfork bifurcation. This effect is valid for any parameter in the orange region $w_{inh} \in (u_5, u_4)$ in Figure 4.6B, ZOOM 1. Although both swimming and resting state are stable, for $u_1 \leq w_{inh} \leq u_5$ the system converges to resting state under the initiation procedure with parameter values used in Figure 4.9 ($\Delta = 0$, $d = 6$ and $A = 0.04$). These parameters correspond to the orbit initiation inside the symmetry manifold Y_k^+. For parameter values $u_1 \leq w_{inh} \leq u_5$, the SyC is repulsive inside Y_k^+ (in Figure 4.9B, ZOOM1 both unstable cycles shown by blue and red dotted lines belong to the symmetry manifold), therefore, the orbit stays inside the symmetry manifold and converges to the resting state. By multiple simulations we confirmed that the basin of attraction for the resting state is large, therefore, small perturbations ($\sigma < 0.1$) cannot move the system to another attractor.

In Figure 4.9B, the selected parameter values are inside the light blue region in Figure 4.6A and Figure 4.6B (ZOOM 3). This corresponds to $w_{inh} \geq u_8$. The critical parameter value $w_{inh} = u_8$ corresponds to a fold bifurcation, and the stable 2-SyC disappears. Near the bifurcation a ghost of this limit cycle exists. We start the dynamics with initiation parameter $\Delta = 0$ and the trajectory converges to unstable SyC. At time $t^\star = 0.3$ms we perturb the last point of the trajectory by adding a normally distributed random number to all system variables (the mean is zero and the variance σ). Integration from the perturbed point results in a long transitional period near the ghost of 2-SyC cycle and convergence to the SwC. This long transition can be reproduced for all parameter values $w_{inh} \in (u_8, 70)$ in the light blue region of Figure 4.6A and Figure 4.6B (ZOOM 3). Remarkably, w_{inh} does not need to be too close to the bifurcation point to obtain long lasting transitions, provided values of the perturbation parameter σ are small. For example, with $w_{inh} = 70$nS and $\sigma = 0.01$ we can still obtain a $\sim$ 1s transition time.

In addition, this study of bifurcation provides insights into explanation of some recordings from CPG neurons. Figure 4.6C in Li et al. [2014a] shows that under depolarising current injection, dINs can fire an additional spike at approximately half the swimming period and initiate synchrony. The voltage recordings of these neurons look very similar to the 2-SyC "ghost" part of the trajectory in Figure 4.9B. It is not clear from the experiment why "mid-cycle spikes" appear in the recordings. Our study provides an explanation of this experimental observation.

Distributions of the duration of the synchrony (double-synchrony) bouts. Experimental findings show that the time of transition from synchrony (double-synchrony) to swimming can be distributed in a wide range from 100 to 1000 ms [Li et al., 2014a]. To study how this time of transition depends on the system perturbation we add white noise to the deterministic model 4.6. The following continuous stochastic process describes the model with noise:

$$\dot{du} = f(u) \cdot dt + \phi \cdot dW_t, \quad u(t), f(u), W_t \in \mathbb{R}^{2k} \tag{4.7}$$

where $u(t)$ is the solution 4.7, $f(u)$ is the vector of the right hand side, W_t represents a standard vector of independent Weiner processes and ϕ is a small parameter ($\phi = 0.01$). We use Euler-Maruyama integration to compute the numerical solution of 4.7. We find that in the large majority of random simulations this solution shows transitions from synchrony (double-synchrony) like that in Figure 4.9A,B (with the same parameter values as Figure 4.9).

We run 1000 simulations with independent random seeds. For each simulation we integrate the system for 2s and detect the time of switching from synchrony (double synchrony) to swimming. In 97% of cases the system demonstrates a transition from synchrony to swimming and in 3% the system switches to the resting state. Figure 4.10A shows the histogram of switching time from synchrony to swimming.

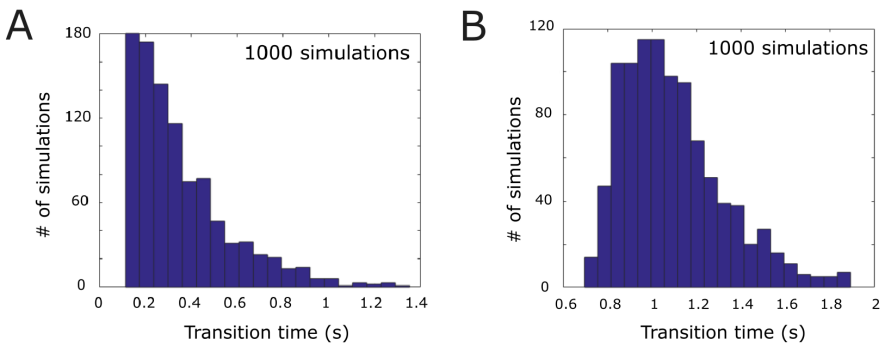

Figure 4.10: Distribution of times spent in the synchrony (double-synchrony) transition in the system with noise. A and B show the histogram of times spent in the synchronous state before switching to swimming. The selected parameter values of A and B are the same as the ones used in Figure 4.7A and B, respectively.

It is clear from this figure that the time of transition from synchrony to swimming is variable and the range of transition times is compatible with those observed in experiments (see Figure 2 in [Li et al., 2014a]). Considering the transition from double-synchrony to swimming we find that for any random seed, the system demonstrates transitions from double-synchrony to swimming. Figure 4.10B shows the histogram of switching time from double-synchrony to swimming.

From swimming to synchrony (double-synchrony) and back. We show that the reduced model can reproduce transitions from swimming to synchrony and switch back to swimming similarly to what is observed in experimental recordings [Li et al., 2014a]. To initiate synchrony from swimming in physiological experiments, one side is stimulated at the middle of the swimming period. We mimic these experiments to initiate synchrony keeping parameter values as in Figure 4.9A. Figure 4.11A shows the injection of a brief positive step current to the left dIN in the middle of the swimming cycle (shown by an arrow). This injection evokes an additional spike which is nearly synchronous with the firing of the right dIN. This additional spike starts a long-lasting synchrony bout before switching back to swimming. This is similar to the experimental recordings [Li et al., 2014a]. Similarly, Figure 4.11B shows that mid-cycle stimulation (shown by an arrow) of

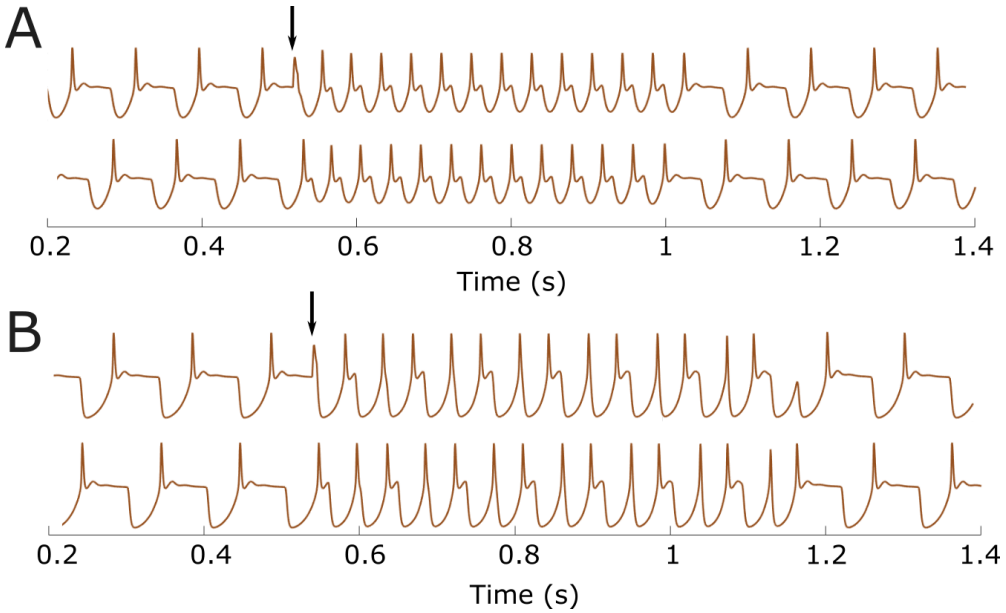

Figure 4.11: Plot of dIN voltage dynamics showing transitions from swimming to synchrony (A) or double-synchrony (B), and back to swimming. In both A and B a brief step current (0.45nA, 5ms) is injected to the left dIN at the time of right dIN firing (black arrows). Parameter values used to obtain A and B are the same as the ones used in Figure 4.9A and B, respectively, except that $\Delta = 50$.

the left dIN during the swimming mode can evoke a long-lasting bout of double-synchrony oscillations.

4.2.7 Breaking symmetry does not change the stability of swimming and synchrony

In this section we analyse the effect of symmetry-breaking in the reduced model. To break the $\mathbb{Z}_2$-symmetry of the system, we slightly perturb the maximal conductance of all ion channels by adding a normally distributed random variable with mean equal to zero and standard deviation $\sigma = 10^{-3}$. This perturbation is applied to all neurons, using a different random seed for each perturbed parameter. All other parameters of neuronal activity and synaptic transmission are identical. As a result of this perturbation, we break the symmetry of the reduced model and consider a non-symmetrical system (NSS).

Studying the bifurcations of the symmetrical system (SS) under variation of two

parameters, we find that there are three stable limit cycles: SyC, SwC and 2-SyC (Figure 4.7). Simulations of the NSS show that the three stable limit cycles ($\overline{SyC}$,$\overline{SwC}$,$\overline{2-SyC}$) have a shape and pattern of firing similar to corresponding cycles for the SS. Figure 4.12A shows projections of stable limit cycles of NSS to the plane of left-right dIN voltages for the three stable limit cycles. For each projection, zooming into part of the phase portrait helps to visualise a small "imperfection" of the limit cycle and a deviation from the diagonal. This figure clearly demonstrates that these three stable cycles are not symmetrical.

To find the stability regions for the stable limit cycles $\overline{SyC}$, $\overline{SwC}$, $\overline{2-SyC}$ of NSS under variation of two parameters (w_{inh},w_{ampa}) and (w_{inh},w_{nmda}) we use massive simulations of the perturbed reduced model. We consider the same region of parameters as in Figure 4.5 and with a uniform n by n grid (n=128). For each node of the grid we simulate the same NSS using the same seed for the random number generator and simulate the trajectory for long times (30 sec), enabling convergence to the limit cycle attractor. Similar to the SS case, we find that the trajectory approaches either a stable limit cycle or a fixed point. In the case of a limit cycle, we compute the period of oscillation. Figure 4.12B (i), (ii) and Figure 4.12B (iii) and (iv) show the results of these computations under variation of (w_{inh},w_{ampa}) and (w_{inh},w_{nmda}), respectively. All simulation parameters used to simulate the trajectories and compute each period are reported in the legend of Figure 4.12.

In Figure 4.12B we use colour coding to show the period of each stable attractor for each pair of parameters (w_{inh},w_{ampa}) and (w_{inh},w_{nmda}). Dark blue corresponds to the zero period, i.e. to the fixed point. Figure 4.12B (i) shows the stability regions for two attractors: a fixed-point attractor (dark blue) and the $\overline{SwC}$ attractor (yellow-red colours indicating periods in the range 35-50 ms). It is clear from the figure that the period of swimming increases with an increase of w_{inh} for any fixed value of w_{ampa}. It is interesting to note that the separation

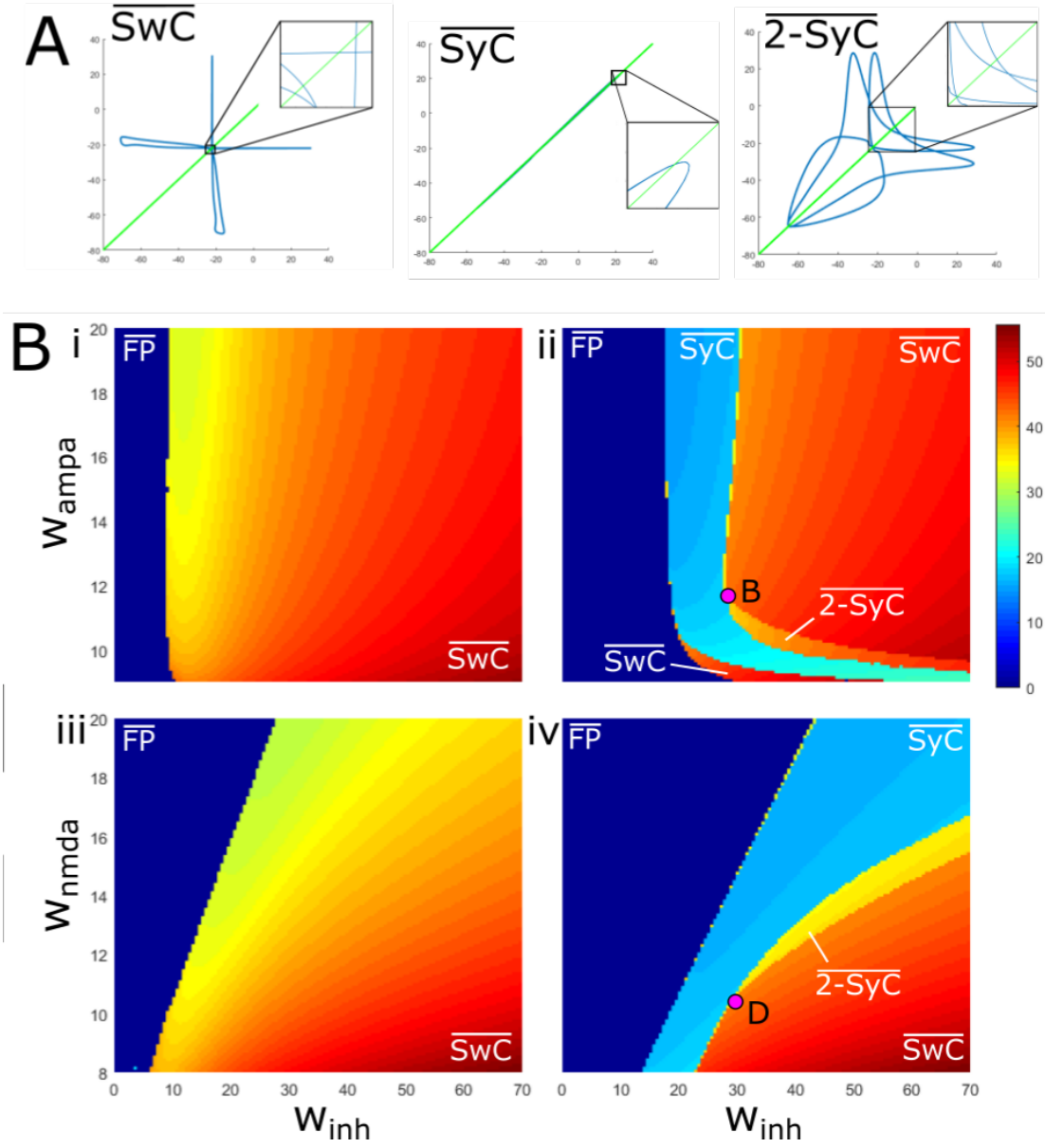

Figure 4.12: Stability of the attractors of after symmetry breaking A. Projection of the three stable limit cycles ($\overline{SyC}$,$\overline{SwC}$,$\overline{2-SyC}$) to the phase plane of dINs voltages and zoom of selected regions (black boxes). The green diagonal line shows the loss of mid-line symmetry of the stable limit cycles. The vector of parameters (w_{inh},w_{ampa},w_{nmda},Δ,d) used for the $\overline{SwC}$ case is (60,10,10,100,6), for the $\overline{SyC}$ case is (25,12,10,10e-4,6), and for the $\overline{2-SyC}$ is (40,10,10,10e-4,6) B. Period of the attracting limit cycle found by numerical simulation at varying (w_{inh},w_{ampa}) and fixed w_{nmda}=10nS in cases (i-ii) and at varying (w_{inh},w_{nmda}) and fixed $w_{ampa} = 12$nS in cases (iii,iv). Initiation parameters for cases (i-iii) are $\Delta = 50$ and $d = 6$, while for cases (ii-iv) are $\Delta = 1e-4$ and $d = 6$.

line between these two regions matches the black line (TR^{-}) in Figure 4.5A corresponding to the subcritical torus bifurcation of the symmetrical system.

Similarly, in Figure 4.12B (iii) there are also different regions (colour coded as in part A). In this case, the period of swimming increases with increase of w_{inh} for any fixed value of w_{nmda}. The separation line between these two regions matches the black line (TR^{-}) in Figure 4.5B again corresponding to the subcritical torus bifurcation of the symmetrical system.

Figure 4.12B (ii) and (iv) show the results of simulations with initiation parameters corresponding to the synchrony mode ($\overline{SyC}$ and $\overline{2-SyC}$). Dark blue again means a trajectory that converges to the fixed point attractor. The light blue area shows the stability region of $\overline{SyC}$. This region and its boundaries match the region and boundaries of the stable synchrony region in the case of SS (Figure 4.5B).

In Figure 4.12B (ii), the left boundary of the $\overline{SyC}$ stability region corresponds to two transitions from the synchrony mode: (1) transition to the fixed point and (2) transition to the swimming mode (dark red area). Both transitions match the bifurcation lines in Figure 4.5A. The right boundary of the $\overline{SyC}$ stability region also corresponds to two transitions: (1) The first is the transition to the swimming mode (red area). The boundary of this transition, above point B in Figure 4.12B (ii), matches the subcritical period-doubling bifurcation line in Figure 4.5A. (2) The second is the transition to the double-period synchrony mode $\overline{2-SyC}$ (yellow-brown area). The boundary of this transition, down-right from point B in Figure 4.12B (ii), fits well to the supercritical period-doubling bifurcation line in Figure 4.5A. This region of stability of the double-period $\overline{2-SyC}$ cycle is narrow with transitions to the swimming mode. Remarkably, our simulations show a stability region of $\overline{2-SyC}$ which was not found by the study of bifurcations.

In Figure 4.12B (iv) the left boundary of the $\overline{SyC}$ stability region (light blue area)

relates to transitions from the "synchrony" mode to the fixed point attractor (dark blue area). The right boundary of the $\overline{SyC}$ stability region relates to two transitions: (1) transition to double-period synchrony mode $\overline{2-SyC}$ (yellow area). The boundary of this transition, up from point D in Figure 4.12B (iv), fits well to the supercritical period-doubling bifurcation line in Figure 4.5B. (2) Transition to the swimming mode. The boundary of this transition, down-left from point D in Figure 4.12B (iv), fits well to the subcritical period-doubling bifurcation line in Figure 4.5B. It is interesting to note that again the simulations show the region of stability of the double-period cycle $\overline{2-SyC}$ (the narrow yellow strip with transitions to the swimming mode) which was not found by the study of bifurcations.

Thus, we conclude that symmetry-breaking by a small perturbation of maximum conductance parameters leads to a minor change of limit cycle stability boundaries. Stability boundaries of NSS fit well to bifurcation lines of the symmetrical system. In addition, the simulation results help to clarify the stability of dynamical regimes in the vicinity of co-dimension-two bifurcation within the complex structure of the bifurcation diagram.

4.3 Discussion

4.3.1 Summary of main findings

In this study we have developed a reduced model of the core neuronal elements of the circuit that drives swimming in the hatchling Xenopus tadpole. We have used bifurcation theory to provide a mathematical description of two main oscillatory modes under variation of key parameters of this model. These modes of anti-phase and in-phase oscillations correspond to swimming and synchrony patterns of spiking activity respectively. Both of these spiking patterns can be observed in physiological experiments where neurons typically fire in alternation (in swimming mode) but can occasionally fire synchronously at half the swimming cycle period (synchrony mode). Bifurcation analysis has shown the

boundaries of the region between two parameters where the stable synchrony regime exists. This synchrony stability region lies within a much larger region corresponding to stable swimming. Therefore, the intersection of these two regions is a region of bistability. We conclude that the same pattern generator circuit can support both swimming and synchrony. A crucial factor in determining which pattern is expressed is the way in which the oscillation is initiated. In addition to swimming and synchrony, we have also described a further stable spiking pattern which we term double period synchrony.

4.3.2 Significance of using the reduced model

We study a reduced model, which can be considered the result of "averaging" of the biologically realistic functional model of the tadpole spinal cord [Roberts et al., 2014]. Specifically, we ignore parts of the functional model corresponding to sensory pathways and consider only the key parts of the tadpole's CPG circuit, as derived from biological measurements and designed to capture the important details. Firstly, the two neuron types included (dIN and cIN) are the core of the CPG. Secondly, the model specification for each is based on available knowledge of their real biological characteristics, including ionic channel currents [Dale, 1995]. The reduction is achieved by minimising the number of neurons considered, leaving just two neurons in each half centre (each side of the body): one excitatory (dIN) and one inhibitory commissural (cIN). Of course, an even smaller circuit constituted by two mutually inhibitory with PIR neurons can generate an anti-phase swimming [Wang and Rinzel, 1992]. However, the mechanism of tadpole CPG functioning is different. In [Arshavsky et al., 1993] there is a comparison of tadpole and Clione CPGs, which, it is believed, work as a chain of two mutually inhibitory neurons.

The essential connectivity between these neurons is maintained. Models of synaptic connections are also biologically realistic; for example, the glutamater-

gic transmission from dINs acts at separate NMDA and AMPA type receptors with different properties [Li et al., 2010]. One additional change made to the model is feedback self-excitation of each dIN. We adopted this change to compensate the lack of excitation between the dINs in the swimming circuit, a property that is lost when reducing the model to a single neuron per type. As a result, the voltage dynamics of the model show patterns of neuron activity that look like those seen in real recordings and previous detailed modelling [Li et al., 2014a, Soffe et al., 2009]. In particular, they show characteristic features of spike dynamics, such as post-inhibitory rebound [Wang and Rinzel, 1992]. The reduced model therefore encapsulates the core features of the full circuit.

Model reduction is essential for allowing a detailed bifurcation analysis of the system. Different approaches for reducing highly complex neuronal systems have been proposed and have been applied to the study of bifurcations in CPG networks [Wojcik et al., 2014, Cymbalyuk et al., 2002, Lodi et al., 2017, Danner et al., 2016]. These approaches tend to reduce the number of differential equations describing neuronal properties by considering simplified neuron models, non-spiking neuron models or phase/amplitude reduction [Izhikevich, 2007, Kepler et al., 1992, Ashwin et al., 2016, Molkov et al., 2015, Rubin et al., 2009]. A further simplification made in CPG circuits is the reduction of the number of synaptic interactions by considering the minimal number of synaptic connections [Marder and Calabrese, 1996, Lodi et al., 2018]. Our approach is different: we do not minimize the number of equations describing the dynamics of single neurons, but we reduce the number of neurons and connections, keeping the important biological properties of spike generation and synaptic interactions. Even with the significant reduction in scale relative to the whole swimming circuit, the dynamical system describing the neuronal activity was still relatively large and included 34 variables. It is a challenging problem to study bifurcations in a dynamical system of such high dimension. For instance, it is known

that the numerical algorithms for continuation of periodic orbits in the case of high dimensional systems are not reliable near the critical parameter value of period-doubling bifurcation. However, using AUTO, and after adjustment of multiple numerical parameters, it was possible to continue the limit cycles and detect bifurcations up to codimension two. Our studies have been restricted to continuation of limit cycles corresponding to swimming and synchrony. The swimming (synchrony) limit cycle is characterised by anti-phase (in-phase) oscillations of equivalent neurons on opposite body sides.

4.3.3 Simplified initiation and the significance of the pattern of initiation

One feature known to be over-simplified in the most recent model of the full swimming circuit [Roberts et al., 2014] is the mechanism for initiating rhythm following a brief stimulus. Fundamentally, the requirement is simply that oscillations on both sides (in each half centre) need to be initiated and coordinated. In the reduced model, the process is also greatly simplified: the triggering stimulus to each side is sufficient to initiate oscillation and this allows us to focus our attention on the effect of timing differences between stimuli to the two sides. We have illustrated effects of also changing the stimulus duration, but we do not consider these further here. Running multiple simulations showed that stimuli are much more likely to initiate swimming than synchrony. To produce synchrony, timing differences between stimuli to the two sides must be very small. This would suggest that, in biological terms, an initiation mechanism is required that avoids such near-simultaneous activation of the two sides (see below).

4.3.4 Stable states and symmetry

Our study of bifurcations provides new insights into the mechanism of CPG spike production. This study reveals three spiking patterns of neuronal activity corresponding to swimming, synchrony and double-period synchrony, each of which is stable in some area of the parameter space. The largest area of stability cor-

responds to the swimming pattern. In swimming, there is typical slow voltage decay after each dIN spike followed by a deep inhibition which leads to a subsequent post inhibitory rebound spike. Spiking in the equivalent dIN neuron in the opposite half-centre is exactly in anti-phase. The stable synchrony pattern is characterised by simultaneous spiking of equivalent neurons on the two sides, with a period of half that seen in swimming. The third stable spiking pattern revealed in our analysis is what we have termed double-period synchrony. The period of this mode is close to the swimming period and the spiking pattern also resembles swimming. But this mode an additional spike with slightly different shape at mid cycle, giving an appearance superficially like that of synchrony. However, in double-period synchrony, spiking of equivalent neurons on the two sides is near-synchronous rather than synchronous. Alternate spikes in the dIN in each half-centre occur just ahead of and then just behind the dIN spike in the opposite half-centre. Like swimming and synchrony, a pattern resembling double-period synchrony has also been described experimentally (see below).

The analysis of bifurcations in the reduced model takes into account the left-right half-centre symmetry. Because of this symmetry, we detect some properties that are exclusive of symmetric dynamical systems [Golubitsky et al., 1999, Kuznetsov et al., 2004]. For example, there are two types of cycles originating from the period-doubling bifurcation of the symmetry cycle. Of the two types of double-period synchrony, one is unstable and left-right symmetrical, while another is stable and its right-half variables are symmetrical to the left-half variables shifted by half-period. Our results on bifurcations are not limited to the symmetric system, but extend to systems where the symmetry is broken by including a small perturbation to some equation parameters. Trivially, all the bifurcations change to non-symmetrical ones (for example, pitchfork becomes fold).

4.3.5 Biological links and significance

As outlined above, our reduced model displays three stable spiking patterns. Remarkably, these three characteristic patterns correspond well to experimental recordings of spiking activity from spinal cord neurons.

Of these, swimming is the most biologically relevant: it is the pattern of activity shown by the CPG neurons that drive muscles to provide the main behavioural response of the tadpole. In experiments, long-lasting swimming is initiated by a brief sensory stimulus (touch) to the head or trunk skin [Roberts et al., 2014, Boothby and Roberts, 1995, Buhl et al., 2012]. The spiking patterns of dIN and cIN neurons in the swimming mode represent the typical activity of CPG neurons and in our analysis, the largest areas of parameter space are for stable swimming.

Synchrony is seen in occasional experimental recordings, where it can last for several hundred milliseconds (perhaps 10-15 cycles) before returning to swimming [Li et al., 2014a]. The synchrony pattern occupies a substantial area of parameter space; however, it lies within the area for swimming, hence it is an area of bistability. Bifurcation analysis shows that both types of stability boundary of the synchrony cycle correspond to subcritical bifurcations (pitchfork and period-doubling bifurcation lines). Therefore, the loss of stability by the synchrony cycle will result in a change of dynamical mode, particularly from synchrony to swimming, just as has been observed experimentally. Like experimentally recorded neurons, this modality change can take several seconds, if model parameters are near the bifurcation points which determine the loss of stability for the synchrony cycle.

Although synchronous activity in the limbs will become a characteristic of the tadpole as it nears metamorphosis to the adult [Combes et al., 2004], there is no evidence that the synchrony pattern modelled here has any function in the

young tadpole. It is more likely, therefore that the goal is to avoid expression of this pattern. Analysis of the initiation parameters in the reduced model suggest that it is important to minimise the likelihood of oscillations on the two sides being initiated within a very short time delay, since such short delays make synchrony more likely. We speculate that the the mechanism of initiation in the real animal introduces some delays that ensure activation on the two sides while avoiding their co-activation.

We have concentrated on analysing the stability of limit cycles corresponding to swimming and synchrony. However, we find that there are several unstable limit cycles, which should be also taken into consideration for clarity of the multiple interlinked bifurcations. Some of these unstable cycles are shown on our bifurcation diagrams for completeness. Moreover, we found one more stable mode - double-period synchrony. As with synchrony, there is no evidence for a biological role for this regime. Double synchrony activity can be observed experimentally, for example by injecting depolarising current into a dIN, or this regime can spontaneously occur during swimming. From a biology viewpoint, the regime corresponding to the double-synchrony in the model appears if the spiking of two dINs on the opposite body sides is not perfectly synchronised, and the jittered cIN inhibition does not suppress dIN spiking on either side [Li et al., 2014a]. Remarkably, the spiking pattern of the double-synchrony in the reduced model perfectly reproduces this experimental finding and the shape of dIN-cIN voltages is very similar to experimental recordings (Figure 4.7A).

Chapter 5

Modelling tadpole locomotor behaviour in response to signals from multiple sensory modalities

In this chapter, we present a detailed computational model of spiking neuron for the network controlling swimming in hatchling Xenopus tadpoles. We define neurons and connections for three sensory pathways controlling the decisions to start/stop the animal locomotion and for the central pattern generator circuit. The model uses numerous biological data and it reproduces biologically realistic patterns of initiation, continuation, acceleration and termination of swimming by mimicking the interactions with the external environment. The input from the environment is integrated and amplified in each sensory pathway and directed to the central pattern generators and motoneurones to select appropriate actions. The model suggests two distinct mechanisms explaining the decision processes for swimming initiation. In the first, slow and variable summation of excitation to threshold generates long and variable decisions. In the second, direct and less variable excitation generates fast and reliable decisions. The model simulates a detailed and biologically plausible sequence of information processing from the internal representation of different sensory modalities, integration and decision-making, action selection, and movement generation.

Animals constantly make movement decisions to survive in a dangerous and complex environment, for example to escape from threats or to find energy resources. Each animal's nervous system represents the external environment by integrating sensory input signals via specialised circuits, which ultimately guide movement decisions. Thus, clarifying the interaction between sensory circuits and the other circuits in the nervous system is key for understanding how animals initiate, continue and stop locomotion [Jin and Costa, 2010, Bargmann

and Marder, 2013, Surmeier, 2013].

Like any other behaviour, locomotion arises from the activity generated by networks of interconnected neurons. What are the key structural and functional properties of these networks that lead to the generation of these activities? Neuroscientists have tried to answer this question by modelling a variety of neuronal networks and behaviours, including swimming and walking in the *C. elegans* [Roussel et al., 2007], the lamprey [Ekeberg, 1993] and the salamander [Ijspeert, 2008], walking in the stick insect [Bässler and Büschges, 1998, Cruse et al., 1998], locomotion in the cat [McCrea and Rybak, 2008], stomach movements in the crab *Cancer Borealis* [Marder and Bucher, 2001]. Despite being remarkably useful to understand many of the neuronal principles beyond the generation of these behaviours, these models and all the other spiking model that we are aware of cannot currently reproduce the complete dynamics of the neuronal activity underlying a whole animal's behaviour. We found confirmations of this from other reviews [Bargmann and Marder, 2013, Marder and Taylor, 2011, Roberts et al., 2010].

One reason is that these models typically aim to simulate only a part of the temporal dynamics of one or of many behaviours. Indeed, these model cannot reproduce the activities of all the neurons that contribute to the start, the modulation and the termination of an entire episode in these behaviours. Models of locomotions have mainly focused on clarifying either the initiation and termination of some movements during decision-making tasks [Surmeier, 2013, Kristan, 2008, Hull et al., 2016]) or the generation and modulation of long-lasting rhythmic patterns of behaviours [Marder and Calabrese, 1996, Marder and Bucher, 2001, McCrea and Rybak, 2008]. There is, however, at least one model that reproduces the whole temporal dynamics of the neuronal populations during both struggling and swimming in the *Xenopus* tadpole [Borisyuk et al., 2017], but it is not a spiking model. Here, however, we focused on developing spiking models,

due to their powerful predictive power.

There are a number of issues that make the problem of reproducing behaviours using such models extremely difficult [Marder and Taylor, 2011, Bargmann and Marder, 2013, Marder, 2015]. One issue is that the circuits in these circuits produce not only one, but a zoo of different and complex behaviours [Marder and Taylor, 2011]. To deal with this problem, models typically have to make strong assumptions, including reducing the study of different sub-circuits in the whole network, each of which generates only a limited number of behaviours. However, since the entire nervous system is connected, these assumptions should be supported by some experimental evidence. One of such evidence could be hypothesised in spinal cord sub-circuits reproducing rhythmic patterns of locomotion. Indeed these circuits can reproduce these patterns even after the spinal cord is removed from the rest of the brain [McCrea and Rybak, 2008, Roberts et al., 2010]. It seems reasonable to believe that explaining how the behaviour works in this sub-circuit could be enough. Another issue is that the structural and/or physiological properties of neurons and connections are largely unknown. In some cases, such as vertebrates' brains, neurons and connections are so many that they cannot be fully identified neither anatomically nor physiologically even for the sub-circuits discussed above [Bargmann and Marder, 2013]. In other cases, such as the brain of some invertebrates, although all neurons and connections have been identified anatomically, their physiological properties are largely unknown [Bargmann and Marder, 2013, Roberts et al., 2010].

Due to its simplicity, the hatchling *Xenopus* tadpole represents a unique animal for studying how a circuit can achieve a complete motor behaviour (swimming) using both experiments and models. Several biological data have been collected over the years and have identified the properties and connections of most of the neurons that contribute to the initiation, continuation, modulation and

termination of swimming [Roberts et al., 2010, Li, 2011]. These neurons have been classified in only a few number of types based on anatomy and physiology [Li et al., 2007a, Sautois et al., 2007]. This has allowed previous models to replicate a biologically-realistic partial reconstruction of the neuronal connectivity in the swimming circuit and to simulate the spiking dynamics of most of the neurons in this circuit [Roberts et al., 2014, Ferrario et al., 2018a]. Thanks to this model and to other experimental studies, the role of most neurons in the swimming circuit have been clarified, and we know that they are essentially divided between neurons that participate in the sensory integration of the external signals by initiating and terminating swimming, and neurons in the central pattern generator that produce the swimming alternating activity [Roberts et al., 2010, Li, 2011]. Secondly, the number of neurons and connections in the swimming circuit is relatively low [Roberts et al., 2010], and it is therefore possible to simulate biologically-realistic models using a relatively low computational power and memory.

In this chapter, we model the whole swimming behaviour of the hatchling *Xenopus* tadpole by improving and extending our previous anatomical and functional models (see chapter 2, chapter 3 and [Roberts et al., 2014, Ferrario et al., 2018a]). We include the neuronal populations and connections of three sensory pathways, and we integrate these into the previous models of the central pattern generator.

Experimental recordings have shown that there are four sensory pathways that lead to the initiation, continuation, modulation and termination of swimming via the interaction with the external environment. The same experiments have defined the identity, properties and connections of neurons in three of these pathways. Swimming can be reliably started by trunk skin touch (TS), head skin touch (HT) or by activation of photo-receptors in the pineal eye by light dimming (LD), and it can be reliably stopped by head skin pressure (HP). Addition-

ally, stimulating the TS and LD pathways during swimming transiently accelerates swimming [Sillar and Roberts, 1988]. In our model, we do not include the LD pathway as this pathway is not yet well defined. The extended network includes 1732 neurons and $\sim$ 100,000 connections. Among them, there are 1198 CPG and motor neurons and the remaining 532 neurons are sensory and sensory pathway neurons. We name this new, extended computational model as "Virtual Tadpole" (VT). In building the connectivity in this model we use some ideas and findings from our probabilistic model (described in chapter 3; Ferrario et al. [2018a]) and recent biological evidence [Buhl et al., 2015, Koutsikou et al., 2018]. Specifically, unknown connections between the newly included sensory populations are established from the distributions of known connection probabilities of other neuronal types included in the probabilistic model.

The VT anatomical model generates the architecture of connections which we project to the VT functional model of Hodgkin-Huxley type spike generating neurons. The final model represents the biggest reconstruction of the tadpole's swimming neuronal network that we are aware of. It can reproduce the initiation, continuation, acceleration and termination of the animal's swimming behaviour in response to stimulation of the TS, HT and HP pathways, which mimic the normal interaction with the external environment. The model can also reproduce spontaneous slowing down and termination of swimming. We simulate a detailed and biologically plausible sequence of interactions and information processing from the internal representation of environment, sensory integration and decision-making, action selection, and generation of movements. The VT model provides a framework for exploring multi-sensory integration and simple motor decision making, as well as generating new ideas and hypotheses for experimental testing. The VT is the only spiking neuronal model we are aware of that (1) accounts for the sensory initiation, modulation and termination of a whole animal's locomotor behaviour and (2) represents most of the functioning

neurons in the system.

One of the most interesting results from the VT functional model relates to the decision-making neuron populations. It is known from recent experiments that the time delay between the spiking of sensory neurons and first motor responses are long and variable (range 20-150 ms; Koutsikou et al. [2018]). To explain this experimental finding we develop a model of decision-making neuron populations. Recordings from the brainstem reticulospinal neurons driving swimming show that they receive slow, variable synaptic excitation which would allow integration of sensory inputs and explain the long, variable delays to swimming. Experiments and model simulations suggest that extended firing in currently undefined presynaptic hindbrain neurons can generate slow, variable summation of excitation leading to the variable delays in the decision to swim found in experimental recordings [Koutsikou et al., 2018].

Our simulations allow us to explain the difference in reaction times between the TH/HP pathways and the TS pathway. The TH and HP pathways include hindbrain tIN and MHR neurons respectively, which fire shortly after the sensory stimulus and lead to faster decisions to initiate or terminate swimming compared to the TS initiation pathway. Our results suggest the following two distinct mechanisms for decision-making: (1) the TS pathways generate slow and variable summation of excitation to threshold, and include a simple mechanism of sensory memory. (2) The HP and HT pathways can provide faster and less variable decisions, with response times more comparable to reflexes.

Model simulations also suggest that the activity of inhibitory neurons with contralateral connections (called cINs and forming part of the CPG circuit; Roberts et al. [2010]) are extremely important for coordinating the initiation of swimming in the TH and TS pathways. The incoming signal from the skin sensory pathways arrives at the hindbrain population driving the decision-making process on

the two sides at approximately at the same time (but see Buhl et al. [2015]) and this will lead to two issues. On one hand it will tend to generate synchronous activity on both sides rather than alternating swimming activity. On the other hand, if the activation of muscles on one side occurs before those on the other side, the latter muscles must be activated after approximately half a swimming cycle. CIN inhibition ensures that excitation arrives with a suitable delay between the two sides. Firstly, this inhibition allows a type of winner-take-all mechanism to select on which body side swimming will start, by suppressing the activity of CPG neurons on the opposite side and avoiding the synchronous activation of muscles. Secondly, it delays the firing of CPG and motor neurons and allows a coordinated alternation.

The massive simulations of the VT model reproduce patterns of neuronal activity that correspond to those recorded experimentally, from the activity of brain and spinal cord neurons to the motor behaviour. To show that the VT model generates a plausible and complete swimming behaviour similar to a real tadpole we consider combinations of input signals to different sensory pathways. The VT functional model converts these signals into the tadpole motor behaviour. These simulations demonstrate how the integration of different sensory modalities of environmental signals can lead to appropriate motor behaviours.

5.1 Model description

5.1.1 Biological details of the VT neuronal circuit

In this section we report the neurobiological details of the sensory pathway neuronal populations and their role in decisions to start/stop swimming locomotion. These details include anatomical and functional properties of neurons, synaptic connections and the activities of each neuronal type. We use these details to extend the previously defined anatomical and functional models of the swimming circuit by establishing neuron-to-neuron connectivity and by modelling the

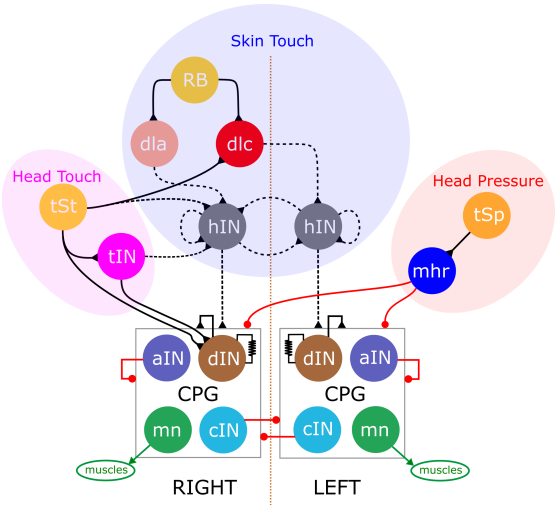

Figure 5.1: Diagram of connectivity in the VT model. Coloured circles represent neuronal populations and lines with markers represent directed connections between these populations (black=excitatory, red=inhibitory). All neuronal populations except hIN have been defined anatomically and physiologically in experiments. Continuous lines show connections established by evidence from recordings. Dotted lines are at present inferred from indirect evidence. Shaded coloured regions highlight the neuronal populations and connections within the three sensory pathways included in the VT model. Colours in each populations are used hereafter to show the activity of the different neuronal types.

dynamical properties of the different neuronal types and their synapses. Figure 5.1 shows a diagram representing all populations included in the VT model and their connections. These include the populations and connections described in the following sections.

5.1.1.1 Trunk skin initiation pathway - TS

Sensory pathway and the start of swimming. In biological experiments, touch to the trunk skin usually leads to tadpole swimming [Boothby and Roberts, 1995]. To measure response times to the first flexion of swimming in immobilised tadpoles a single spike is evoked in sensory RB neurons using a current pulse stimulus to ventral trunk skin [Clarke et al., 1984]. These spikes excite sensory pathway dlc and dla neurons which project axons into the contralateral and ipsilateral part of the hindbrain, respectively. Paired recording failed to find any evidence for direct synaptic excitation of hindbrain CPG hdIN neurons by

dlcs [Buhl et al., 2015]. We have focused exclusively on dlcs because we are confident that they provide the only skin sensory pathway activating swimming on the unstimulated side of the body Li et al. [2003]. We have not investigated the ipsilateral pathway from the skin to the hindbrain, which is formed by the ascending axons of both sensory RB neurons and the dlas which they excite [Li et al., 2004b].

Long and variable reaction times. Latency measures showed that response times made in intact animals are long and variable (median: 102, inter-quartile-range: 81-136 ms; Koutsikou et al. [2018]). In immobilised tadpoles, motor nerve recordings were used to define delays to the start of fictive swimming following a threshold stimulus to the left trunk skin. Swimming started on either side. The median delay to the first motor burst on the unstimulated side was 40 ms (range: 20-150ms; inter-quartile range: 33-61 ms) from the stimulation time. These delays to the start of fictive swimming, when the central nervous system is exposed to physiological saline, were shorter than delays measured behaviourally. However, both were long and variable compared to *Xenopus* motoneuron firing delays in a simple flexion reflex to a trunk skin stimulus (7.0-13.8 ms; Li et al. [2003]). These measures suggest that delays to the start of tadpole swimming are longer and more variable than simple reflexes or the ballistic escape responses seen in fish [Korn and Faber, 2005]. To investigate the timing of sensory firing, dlc whole-cell recordings were used to measure responses to a current pulse to the trunk skin. EPSP onset latencies in dlc neurons indicated that the firing delays of the single spikes in sensory RB neurons were short and consistent (mean 4.7 $\pm$ 0.6 ms). The dlc spike latencies were a little longer and more variable (mean 6.5 $\pm$ 1.1 ms).

The role of hindbrain dINs. The latency and variability of firing times in the sensory and sensory pathway neurons cannot explain the length and variability of response times to the start of swimming. Recordings were therefore made

from the dINs located in the hindbrain (hdINs) that drive swimming to examine the pattern of synaptic input that leads to their firing and the start of swimming following a sensory stimulus to the skin [Koutsikou et al., 2018]. These recordings showed that the hdINs on each side are equivalent to reticulospinal neurons in adult vertebrates and are critical for the initiation and generation of swimming (see chapter 1 and Li et al. [2006], Soffe et al. [2009]). In summary, hdINs initiate swimming following sensory stimulation [Buhl et al., 2012, 2015] but also sustain it through their mutual electrical and chemical excitatory synapses [Hull et al., 2016], cellular and pacemaker properties, and rebound from reciprocal inhibition between the two sides [Li, 2011]. These critical roles make the reticulospinal hdINs the key neurons to account for the long and variable delays to the start of swimming. As expected from the delays to the start of swimming, delays to the first spikes in hdINs are also long and variable (median 35.4 ms, IQR 27.8-65.7, range 25-140 ms).

A new proposal for the mechanism that initiate swimming. When the trunk skin is stimulated, hdINs receive excitation for up to 1.5 seconds in the form of a series of summating EPSPs which can depolarise the hdINs to firing threshold (Figure 5 in Koutsikou et al. [2018]). The amplitudes and timings of these EPSPs is variable. The dispersed pattern of these summating EPSPs cannot be explained by the short latency, single firing patterns of the RBs, dlas and dlcs. Instead, the timing of these EPSPs raises the possibility of that there is a population of excitatory neurons, which we call hindbrain interneurons (hINs), presynaptic to the hdINs, that are excited by a brief sensory stimulus but fire later, and can fire for much longer extending the firing the sensory pathway. Therefore, we hypothesise that the hIN populations on each body side receive input signals from dlc and dla neurons, sustain their activity by making recurrent excitatory connections, and excite hdINs and other hindbrain CPG neurons. We explore the plausibility of this proposal by integrating a model of the hIN network

into the VT model.

5.1.1.2 Head touch initiation pathway - HT

Similar to the TS, stimulation or touch to the head can also initiate swimming. Here, we briefly summarise some of these results.

The HT pathway (see Figure 5.1) is innervated by touch-sensitive trigeminal sensory neurons (tSts) in the head. Similar to RBs, tSt neurons fire single action potentials in response to brief current pulses and excite trigeminal interneurons (tINs) and rostral dlcs (rdlcs) and make them fire [Buhl et al., 2012, 2015]. Single tINs make direct excitatory connections onto ipsilateral hdINs, but rdlcs do not make equivalent connections onto contralateral hdINs. However, rdlcs remain strong candidates for exciting contralateral hdINs (and possibly other CPG neurons) indirectly via some unidentified neuronal population (discussed in the next paragraph). Stronger stimuli lead to firing of many tINs and this can activate hdINs and initiate swimming on the stimulated side at short latencies. However, lesion experiments show that surgical removal of tINs does not block the initiation of swimming at short latencies. This suggests the existence of at least two different mechanisms that can lead to the start of swimming. Overall, swimming in response to HT stimulation can start on either sides, but it starts more frequently on the stimulated side.

Weak stimulation of the head does not initiate swimming and leads to a variable pattern of summating EPSPs in hdINs, similar to the ones observed in response to weak stimulation of the trunk skin [Buhl et al., 2015]. In response to stimulation near swim threshold, both the delay to the first firing of hdINs and reaction times are long and variable. These results suggest that an undentified neuronal population is involved in extending the effect of sensory stimuli to the head. Since rdlcs are excited by both head and trunk skin stimuli, it seems certain that they will excite the same hindbrain neurons on the opposite side in both

cases. Therefore, we hypothesise that these unidentified neurons are the hINs recruited during stimulation of the trunk skin (Figure 5.1). Stronger stimuli lead to the firing of hdINs and evoke swimming more reliably and at much shorter delays than weaker stimuli.

5.1.1.3 Head pressure termination pathway - HP

Trigeminal neurons innervating the cement gland and head skin (tSps) fire in response to head pressure [Roberts, 1980]. These neurons excite and activate inhibitory mid-hindbrain reticulospinal neurons (MHRs) which can in turn terminate swimming [Perrins et al., 2002, Li et al., 2014b]. In response to head pressure MHR neurons directly inhibit CPG neurons via GABAergic synapses. It is remarkable that the activation of a single MHR can stop swimming [Perrins et al., 2002]. Therefore, as a population, MHRs must deliver a powerful inhibitory signal to the CPG neurons that reliably stops swimming.

5.1.2 Modelling the pathways and swimming initiation

In this section we describe the neuronal populations (or types) and connectivity in the VT model. We consider a total of 12 populations (Figure 5.1), which are schematically represented by coloured circles in Figure 5.1. Four of these populations form the CPG circuit (dIN,cIN,aIN,mn) and their connectivity is established from the anatomical connectome model and previous experimental studies (see chapter 1). The remaining 8 populations relate to the new sensory pathways included in the VT model.

We consider two excitatory sensory pathways, skin touch and head touch, which are organised in a similar way. In both pathways, sensory neurons (RBs and tSts, respectively) fire single spikes in response to touch of the skin and of the head, respectively. The signal from these sensors propagates to the processing populations (dla/dlc and tIN, respectively), which in turn deliver excitatory inputs to a hypothetical hindbrain neuronal population (hINs). We hypothesise

that hINs extend this brief input signal by producing irregular and variable firing patterns that can last for up to 2 seconds. The hINs then project to the CPG and they initiate swimming by exciting dINs. Also, we include direct connections from tINs to dINs which have been detected also in pairwise recordings [Buhl et al., 2012, 2015]. The inhibitory head pressure pathway is organised in a simpler way. The signal from sensory neurons (tSps) goes to a processing population (MHRs), which delivers inhibitory inputs to the all the CPG populations to stop swimming.

In the next sections, we describe the neuron and connection models of the different sensory pathways shown in Figure 5.1. All neuronal models and synaptic connectivity in the CPG circuit are the same as the previous anatomical and functional models described in the chapter 1 and in [Ferrario et al., 2018a, Roberts et al., 2014, Sautois et al., 2007].

5.1.3 Number and rostro-caudal positioning of neurons

Each neuronal population in the VT model is formed by a fixed number of neurons, and each neuron is defined by its cell type and its rostro-caudal distance (simply referred to "position" hereafter). On each side of the spinal cord, the positions of these neurons are defined by the distance of the cell bodies from the mid-hindbrain border.

The number and positions of neurons in each population have been assigned based on experimental data except for hINs. We fix the same neuron numbers and positions for each population included in the probabilistic model (RB, dla, dlc, dIN, cIN, aIN, mn). To define the connectivity to CPG neurons from the sensory pathway populations, we divide CPG neurons between hindbrain and spinal CPG neurons. Simply, hindbrain CPG neurons (including hdINs) are CPG neurons with soma positions less than 900μm. The remaining CPG are defined as spinal neurons.

	hIN	tSt	tIN	tSp	MHR
number of cells	60	130	40	80	40

Table 5.1: Number of cells for newly included neuronal populations in the VT model. Populations on each side contain exactly half of these numbers.

The number of neurons in each of the remaining populations in the VT model are estimated based on prior experimental knowledge and they are reported in table 5.1. For more detalis see Koutsikou et al. [2018], Buhl et al. [2012], Perrins et al. [2002].

These distances are estimated based on anatomical measurements of each class of neuron, except for hINs. The positions of tSts are independently uniformly distributed in the interval [-50,0]μm, while tIN positions are uniformly distributed in the interval [150,330]μm (based on Buhl et al. [2012]). The positions of tSps are also independently uniformly distributed in the interval [0,10]μm, based on Hayes and Roberts [1983]). MHRs are uniformly distributed in the interval [400,550]μm, based on Perrins et al. [2002]. Since we have no anatomical data on hINs, we assume that their positions are uniformly distributed in the hindbrain in the interval [-130,500]μm.

5.1.4 Spiking neuron models

To model all neuronal types except hINs we use the same single-compartment Hodgkin-Huxley equations used to define all neuronal types in the previous functional model of the swimming circuit (described in the chapter 1). Parameters in these equations have been chosen specifically for each neuronal type to mimic their electrophysiological properties known from neurobiology.

For the RB, dIa, dIc and CPG neuronal types except dINs we use the same parameter values as in [Roberts et al., 2014]. The motivations of the choice of these parameters have been provided in this paper. For dINs, we also use the same model and parameters as in [Roberts et al., 2014], except for changing

the maximal conductance of the sodium ionic current in the dIN model (from 210.5nS to 180nS dINs). This change helps in reducing the number of simulations where the dIN activity starts in left-right synchrony in response to inputs from the TH and TS pathways (see Results and Discussion sections). For the same reason we reduce the value of electrical coupling between hdINs from 0.2nS to 0.05nS. For tSt and tSp sensory neurons we use the same model parameters as sensory cells as in the spinal cord given in [Sautois et al., 2007], because they have not been physiologically characterised.

tIN neurons - To model tIN neurons, we match some of the basic electrophysiological properties of these neuronal type from data reported in Buhl et al. [2012]. We start from the parameter values of the aIN model given in Sautois et al. [2007] because both aINs and tINs have similar firing properties: repetitive firing to current injection at any depolarisation level, no firing adaptation, no delayed firing and no after-spike depolarisation block. We then adopt the following parameter changes to match the specific properties of tINs:

- Leak conductance and leak reversal potential are set to match the average input resistance $R_{in} = 459M\Omega$ and resting potential $V_{rest} = -55mV$ recorded in experiments [Buhl et al., 2012].
- We use the approach discussed in [Roberts and Tunstall, 1990] to obtain a qualitatively similar current threshold for firing. Specifically, we decrease by 25mV parameter Ds defining the rate functions in all ionic channels to obtain current threshold of $\sim 50pA$ similar to tINs (from Figure 6D in Buhl et al. [2012]).
- To obtain a similar dependence of firing frequency in response to variable current injection (I-f curve) and match the range of firing frequencies of tINs (compare Figure 5.2A with Figure 6D in Buhl et al. [2012]), the maximal conductance of the sodium, fast potassium and slow potassium is modified

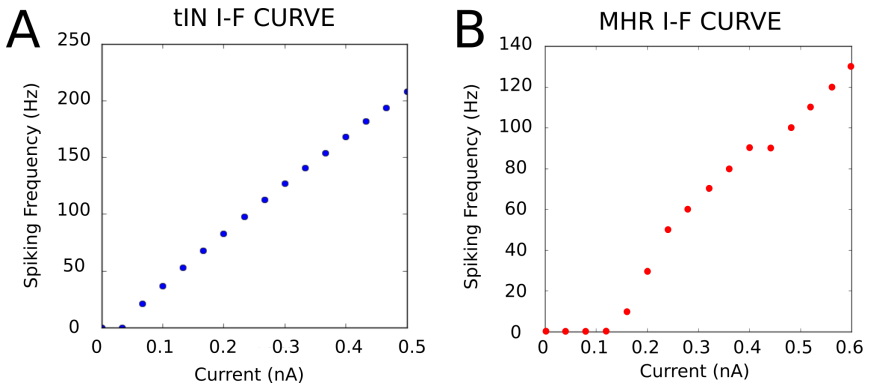

Figure 5.2: Current-frequency curves in the model tIN (A) and MHR (B). To compute these curves, we inject a step depolarising current with increasing amplitude and measure the spiking frequency. Spiking frequencies are plotted against these varying current amplitudes. These curves match the current frequency curves measured experimentally (compare with Figure 6D in Buhl et al. [2012] and Figure 5 in Perrins et al. [2002] for tIN and MHR, respectively).

to values $g_{na} = 680nS$, $g_{Kf} = 40nS$ and $g_{Ks} = 20nS$, respectively.

- Parameter A of the β_m sodium rate function is decreased by $2ms^{-1}$ to give a better match of the voltage amplitude of spikes during high current injections.

MHRs - Similar to tINs, we model MHR neurons to match some key electrophysiological properties reported in [Perrins et al., 2002]. We start from dlc model paramters [Sautois et al., 2007] because the dlcs' resting potential and input resistance are closer to the average MHR values than all other neuronal types in the swimming circuit. Moreover, MHRs have similar firing properties to dlcs: multiple action potential firing in response to positive current injection and firing adaptation [Perrins et al., 2002, Roberts and Sillar, 1990]. We then adopt the following changes to model parameters to mimic other properties of MHRs:

- The leak conductance and leak reversal potential are set to match the average input resistance $R_{in} = 262M\Omega$ and resting potential $V_{rest} = -68mV$ of experimentally recorded MHRs. These values were measured from sharp microelectrodes, which record more negative resting potential val-

ues than more precise patch electrodes. To correct these imprecise measurements, we manually select a lower value of the resting potential $V_{rest} = -60mV$. This change was suggested by multiple comparisons between neuronal recordings made using both types of electrodes (microelectrodes and patch clamps).

- We decrease parameter D defining the rate functions of all ionic channels by 10mV to obtain a similar current threshold for firing to MHRs, following the same approach discussed in the case of tINs.

- To match the I-f curve and firing frequencies of MHRs , obtain multiple firing at any level of injected current, lower the spike frequency to realistic values and avoid single-spikes to current injection the values of parameter A of the α_m sodium rate function was decreased by $3ms^{-1}$ and of parameter A of the β_f of the fast potassium rate function was decreased by $0.9ms^{-1}$ (compare Figure 5.2B with Figure 5 in Perrins et al. [2002]).

hINs - This model neuron consists of two electrically connected compartments, one representing the combined dendrites and soma and the other representing the axon. The equations governing the dynamics of both compartments are based on the same Hodgkin-Huxley equations used to model all other cell types (see chapter 1), but with the membrane properties of an unspecialised, generic tadpole neuron (spinal motoneuron; Koutsikou et al. [2018], Sautois et al. [2007], Roberts et al. [2014]). The parameters for the dendrite/soma and axonal compartments are identical, except that the maximum conductance values of all active channels (Na, K fast , K slow) are increased by a factor of five in the axonal compartment. The total capacitance of each compartment is 5pF, and the inter-compartment conductance is 10nS. We use a two-compartment model because random networks of single compartment neurons with motoneuron properties are not able to produce persistent rhythmic firing when coupled by

glutamatergic synapses with NMDA receptors. During strong excitatory synaptic input, the neurons in such networks became very depolarised and stopped firing because of depolarisation block. A more realistic model incorporating a second compartment representing the axon did not have this problem; when the soma/dendrite compartment was depolarised by excitatory synaptic input the axonal compartment could continue to spike repetitively.

5.1.5 Modelling the neuronal connectivity in the VT circuit

Connections from dlas/dlcs to hINs. In the model, connections from dlas to hINs and from dlcs to hINs are randomly prescribed by sampling from independent Bernoulli variables with probabilities p_1 and p_2, respectively. We infer probabilities p_1 and p_2 from physiological recordings of unidentified neurons in the mid-brain which are believed to be analogous to the hINs. These recordings revealed that 45% of hINs receive EPSPs earlier than 13ms after the stimulation of the skin which leads to a swimming episode. Previous experiments suggested that dlas and dlcs fire only once in response to RB input and they are the only active neurons before 13ms apart from RBs [Koutsikou et al., 2018]. Therefore, we can assume that these early EPSPs are a result of direct connections from active dlas or active dlcs to hINs. Assuming that the trunk skin stimulation activates n_1 dlas and n_2 dlcs, any randomly picked hIN receives a binomially distributed number of EPSPs $Y_1 \sim B(n_1, p_1)$ from the active dlas and $Y_2 \sim B(n_2, p_2)$ from the active dlcs. We assume that the inputs from both sides are equal ($Y_1 = Y_2$). Thus we can derive formulas for the probability that a randomly picked hIN receives EPSPs from either dlas or dlcs before 13ms:

$$0.45 = \text{Pr(hIN received EPSPs < 13ms)} = \text{P}(Y_1 \geq 1)+\text{P}(Y_2 \geq 1) = 2*\text{P}(Y_i \geq 1) = 2 * [1 - 1 * (1 - p_i)^{n_i}]$$

From the functional model simulation we found that the average numbers of active dlas and dlcs following activation of the trunk skin from 100 realisations of

the functional connectome model [Roberts et al., 2014] is 19 and 31, respectively. With simple calculations we thus obtain the probabilities p_1 and p_2.

Connections from tSts/tINs to hINs. tSt and tIN axons grow ipsilaterally in the hindbrain, where they are well-placed to make synaptic connections with the dendrites of hINs. We have no anatomical nor physiological data to use to establish these connection probabilities. However, since both dlas and tSts/tIN are sensory/sensory pathway cells with ipsilateral axons, we expect similar tSt/tIN→hIN and dla→hIN connection probabilities. However, since tSts and tINs are located closer to hINs than dlas, we expect higher probability of connections from tSts/tINs. Therefore, we used the same model as was used to establish dla→hIN connections to establish both tSt→hIN and tIN→hIN connections, but adding 0.05 to each probability.

Connections from hINs to hindbrain CPG neurons. One of the current hypotheses is that hINs make ipsilateral connections with CPG neurons in the hindbrain (including hdINs). Since we have no available information on hINs nor on their connections to CPG neurons, we opted for a simple model of connectivity: any pair of pre-synaptic hIN and post-synaptic CPG neurons located in the hindbrain connect with probability p=0.1. We fixed this low probability value because some pilot studies suggest that these connections are rare, id they exist at all (unpublished data).

5.1.5.1 Probabilistic approaches to defining the other connection probabilities

To establish some of the synaptic connections between sensory pathway neurons in the VT circuit we used two approaches based on the probabilistic model [Ferrario et al., 2018a], which we will call hereafter the "probabilistic approach". The idea of the probabilistic approach is to use the probabilities contained in the probability matrix P (Figure 3.1) to infer unknown connection probabilities of the new neuronal pathways included in the VT model. This approach allows us

to estimate these unknown probabilities based on the assumption that neuronal types in these pathways have similar anatomical and/or functional properties to the neuronal types contained in the probabilistic model. The probabilistic approach allows us to infer unknown connections without simulations of the growth of axons and synaptic formation as in the anatomical model.

Although the probabilistic approach is based on several strong assumptions, there are some encouraging motivations for using it. First, the probabilistic and anatomical models have shown that cell types with similar anatomical and/or functional properties (such as sensory interneurons or CPG neurons) tend to form a similar pattern of connection probabilities (see Figure 3.1). Second, we use this approach because there are no (or only a few) available and reliable anatomical measurements and/or pairwise recordings which can be used to establish these new connections. Third, if the connectivity determined using the probabilistic approach can realise the function of the network, then this would suggest that more complicated models are not required.

We use two different modified versions of the probabilistic approach:

1. PROBABILISTIC APPROACH 1 - Let us assume that we need to define the probability of connection between two new cell types, and detailed anatomical information is unavailable. In this case we select two neuronal types that exist in the probabilistic model with anatomical and/or functional properties the most similar to the two new cell types. These properties will be discussed when we describe the neuronal connectivity between two particular neuronal types (see below). We extract all connection probabilities from the probability matrix for these two selected cell types and apply the generalisation procedure [Borisyuk et al., 2014] to generate connection probabilities for each pair of neurons for two new cell types.

2. PROBABILISTIC APPROACH 2 - The second approach is similar to the

first one, but in this case we use available measurements of axon lengths to generate connection probabilities. We notate a cell type as "old" if it is already included in the probabilistic model and as "new" if it is not in the probabilistic model. Let us assume that we need to generate probabilities of connection from neurons of a new cell type (N) to neurons of an old cell type ($O1$). We notate this connections $N \rightarrow O1$. We know from experiments that there is a similarity in the axon length distribution between neurons of another old cell type ($O2$) and N neurons. We use this axon length distribution to generate connection probabilities from neurons of type N.

For each neuron k of cell type $O2$ and neuron m of cell type $O1$ the difference between rostro-caudal coordinates is $l(k,m) = c_k - c_m$, where c_j is the rostro-caudal coordinate of neuron $j = k$ or m. We assume that neurons of cell type $O2$ and $O1$ are ordered according to strictly increasing rostro-caudal coordinates; k numerates ordered $O2$ neurons; m numerates ordered $O1$ neurons. From the probability matrix we know the probability of connection $p(k,m)$ from neuron k to neuron m. The correspondence between $l(k,m)$ and $p(k,m)$ defines the function $p = f(l)$. This function describes how the probability of connection depends on the difference of rostro-caudal coordinates. We use this function to specify the probability of connection from each neuron r of type N to neuron t of type $O1$. To do that, we consider the piece-wise linear interpolation of function f, and calculate the difference $l(r,t)$ in rostro-caudal coordinates between neuron r and neuron t. We use this distance to find the probability of connection $p(r,t) = f(l(r,t))$.

5.1.5.2 Connections determined using the probabilistic approach 1

Connections from tSts to tINs. Buhl et al. [2012] provides direct evidence from pairwise recordings that the probabilities of connections from tSts to tINs

are relatively high. We use approach 1 and we assume that these connection probabilities are similar to the probability of connections from RB cells to dlas. The motivations for choosing these connections are twofold. Firstly, Figure 3.1 shows that these probabilities are the highest values in the probabilistic matrix. Secondly, we expect that connections from tSts and tINs and connections from RBs to dlas are similar because they are both ipsilateral projections from sensory neurons (tSts and RBs) to sensory interneurons (dlas and tINs). Thus we use the generalisation procedure [Borisyuk et al., 2014] to prescribe the individual connection probabilities from tSts to tINs.

Connections from tSts to rdlcs. Buhl et al. [2015] provides indirect evidence that the probabilities of connections from tSps to rdlcs are high. Also in this case we use approach 1 and select the probabilities of connections from sensory RB cells to dlcs from the probabilistic model. The motivations for choosing these connections are twofold. Figure 3.1 shows that probabilities of connection from RBs to dlcs are high. Secondly, both connections from tSts and dlcs and connections from RBs to dlcs are both ipsilateral descending connections projecting from sensory neurons (tSts and RBs) with similar functional properties to the same dlc interneuron class. The generalisation procedure is then used to find individual connection probabilities.

Connections from tSts to hdINs. tSt axons grow ipsilaterally in the hindbrain, where they could potentially make synaptic connections with the dendrites of hdINs [Buhl et al., 2012]. Again, we use approach 1 to establish these connections probabilities by assuming that they are similar to connection probabilities from dlas to hdINs. The motivations for choosing these probabilities are the following. Firstly, both dlas and tSts are ipsilateral. Secondly, both dlas and tSts are sensory cells active briefly after stimulation. Thirdly, both connection probabilities consider the same post-synaptic cells (hdINs).

Connections from tSps to MHRs. Perrins et al. [2002] provides indirect evidence that the probabilities of connections from tSps to MHRs are relatively high. In this case, we also use approach 1 and select the probabilities of connections from sensory RB cells to dlas in the probabilistic model. We choose these probabilities because they are high and because sensory RB neurons have similar functional properties to tSps. Thus we use the generalisation procedure to find individual connection probabilities from tSps to MHRs.

5.1.5.3 Connections determined using the probabilistic approach 2

Connections from tINs to hdINs. We know from experiments that tINs are descending neurons and their axons are relatively long ($1750 \pm 480\mu m$, mean $\pm$ standard deviation, Buhl et al. [2012]) and comparable to the axon lengths of dlas ($1820 \pm 470\mu m$, Li et al. [2001]). Additionally, both tIN and dla neurons have a similar anatomical properties and functional roles in the swimming behaviour. Anatomically, axons of both types have similar length distributions and project ipsilaterally. Functionally, they are both sensory interneurons, fire transiently in response to skin touch (in the touch of the head or the skin) and excite other interneurons in the CPG [Buhl et al., 2012, Li et al., 2004b]. Thus we expect tINs and dlas to have similar connection probabilities towards hdINs. We follow the probabilistic approach 2 and use dla to hdIN connection probabilities from the probabilistic model to define the function $p = f(l)$. However, since dlas are ascending neurons and tINs descending neurons, we consider the symmetric reflection of f by applying the change of variables $p = f(-l)$. This function provides the probability of connection from tINs to hdINs. Figure 5.3 A shows the graph of this function which was calculated from the probabilistic model.

Inhibitory Connections from MHR to CPG neurons. Perrins et al. [2002] provides indirect evidence that MHR neurons connect with high probability to CPG neurons in the rostral part of the spinal cord. We follow the probabilistic

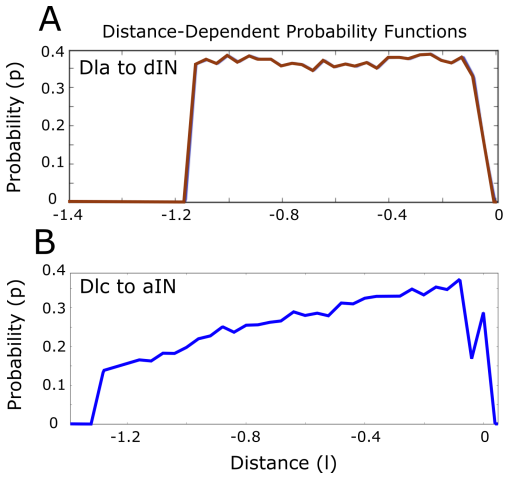

Figure 5.3: Graph of probability functions $p = f(l)$ showing the probability of connections from dlas to hdINs (A) and from dlcs to aINs (B), where l is the distance between pre- and post-synaptic cell bodies positions.

approach 2 by selecting dlc to CPG connection probabilities from the probabilistic model to define the function $p = f(l)$ for establishing ipsilateral MHR to CPG connection probabilities. In fact, we separate connection probabilities from dlcs to any of the CPG types (dIN,cIN,aIN,mn). For each of these types we build function f and use it to define connection probabilities from MHRs to this selected type. Figure 5.3 B shows the graph of this function in the case of connection probabilities from dlcs to aINs. The reasons for choosing dlc to CPG connection probabilities are twofold. First, the axon lengths of MHR neurons ($1180 \pm 350\mu m$, Perrins et al. [2002]) are comparable to the axon lengths of dlc neurons ($1190 \pm 410\mu m$, Li et al. [2001]). Second, both MHR and dlc neurons have a similar functional role in the swimming network. They are both sensory pathways neuronal types, fire transiently in response to sensory input and connect to CPG neurons. We therefore expect dlcs and MHRs to have similar connection probabilities to CPG cell types. However, since dlcs are ascending neurons and MHRs descending neurons, we consider the symmetric change of variables $p = f(-l)$. Since activation of MHRs sends powerful signal to CPG neurons [Perrins et al., 2002], we expect these connection probabilities to be higher than dlc to CPG connection probabilities. For this reason, we multiply

function f by factor 2, so that these probabilities can reach values up to p=0.8. Moreover, we know from [Perrins et al., 2002] that MHR neurons have primary ipsilateral axons, and about 20% of MHRs also have a secondary contralateral axons. For this reason, we randomly select 20% MHRs in the model and use the same function $p = f(-l)$ to define contralateral connections from MHRs to CPGs.

5.1.5.4 Establishing the hIN recurrent connections using an alternative probabilistic approach

We hypothesise that hINs are able to generate sustained firing in response to transitory input from the sensory pathways (dla/dlc/tIN/tSt) as a result of excitatory recurrent connections within their population. To establish this recurrent connectivity we used the probabilistic approach, since we have no anatomical or physiological information that can be used to infer these connection probabilities. We suspect hINs to be located in a relatively compact longitudinal region of the hindbrain, which would suggest connections between hINs to be local. The most local connectivity amongst neurons in the probabilistic model is the mn to mn connection probabilities (Figure 3.1). Therefore, we select the first 30 rows and columns of sub-matrix containing to the mn to mn ipsilateral connectivity and we select these as the connection probabilities between ipsilateral hINs. These first rows and columns are selected because they represent the connectivity between the most-rostral mns, near positions where hINs are presumably located. To allow sustained activity within the hIN population in response to input from active dlas/dlcs it was necessary to multiply these probabilities by a factor of 2. In addition to ipsilateral connections, we add contralateral connections between the left and right hIN populations. The reasons behind adding these connections are twofold. Firstly, there is anatomical evidence from some neurons in the midbrain called mIN (midbrain interneuron) neurons, which we believe are anatomically and physiologically analogous to the hINs, have such

contralateral connections (unpublished data). On the other side, preliminary simulations of the functional model suggested that contralateral connections between hINs are necessary to sustain activity at a similar frequency on both sides and to avoid unbalanced excitation of CPG neurons on either side, which would not allow a coordinated initiation of swimming. To include contralateral connections between hINs we use the same approach used to model ipsilateral hIN-hIN connections using the same sub-matrix containing to the mn to mn probabilities, except that each of these probabilities connections is established randomly by drawing a Bernoulli variable with probability p=0.3. We choose this probability value because anatomical experiments tracing mIN axons revealed that about 20 % of them run contralaterally (unpublished data).

5.1.6 Adjacency matrix in the VT model

In the previous section we have described how we assigned the connection probabilities of the new classes of neuronal types in the VT model. These probabilities, combined with the previous anatomical model, can be used to generate an adjacency matrix of directed connections $A = (a_{i,j})$, where $a_{ij} \in \{0, 1\}$ and $a_{ij} = 1$ indicates existence of a connection from neuron i to neuron j. We use these probabilities to sample the connectivity of the new populations included in the VT connectome using Bernoulli variables. The remaining connections in A have been generated from single realisations of the anatomical model. One random realisation of the full adjacency matrix A for the VT connectome is shown in Figure 5.4. We use white colour to show existing connections ($a_{ij} = 1$) and black colour to show no connections ($a_{ij} = 0$). Neurons have been indexed and sorted according to rostro-caudal positions as in Figure 3.1.

5.1.7 Synaptic parameters

In this section we describe the parameters used to model synapses. The VT functional model includes different types of excitatory and inhibitory synapses.

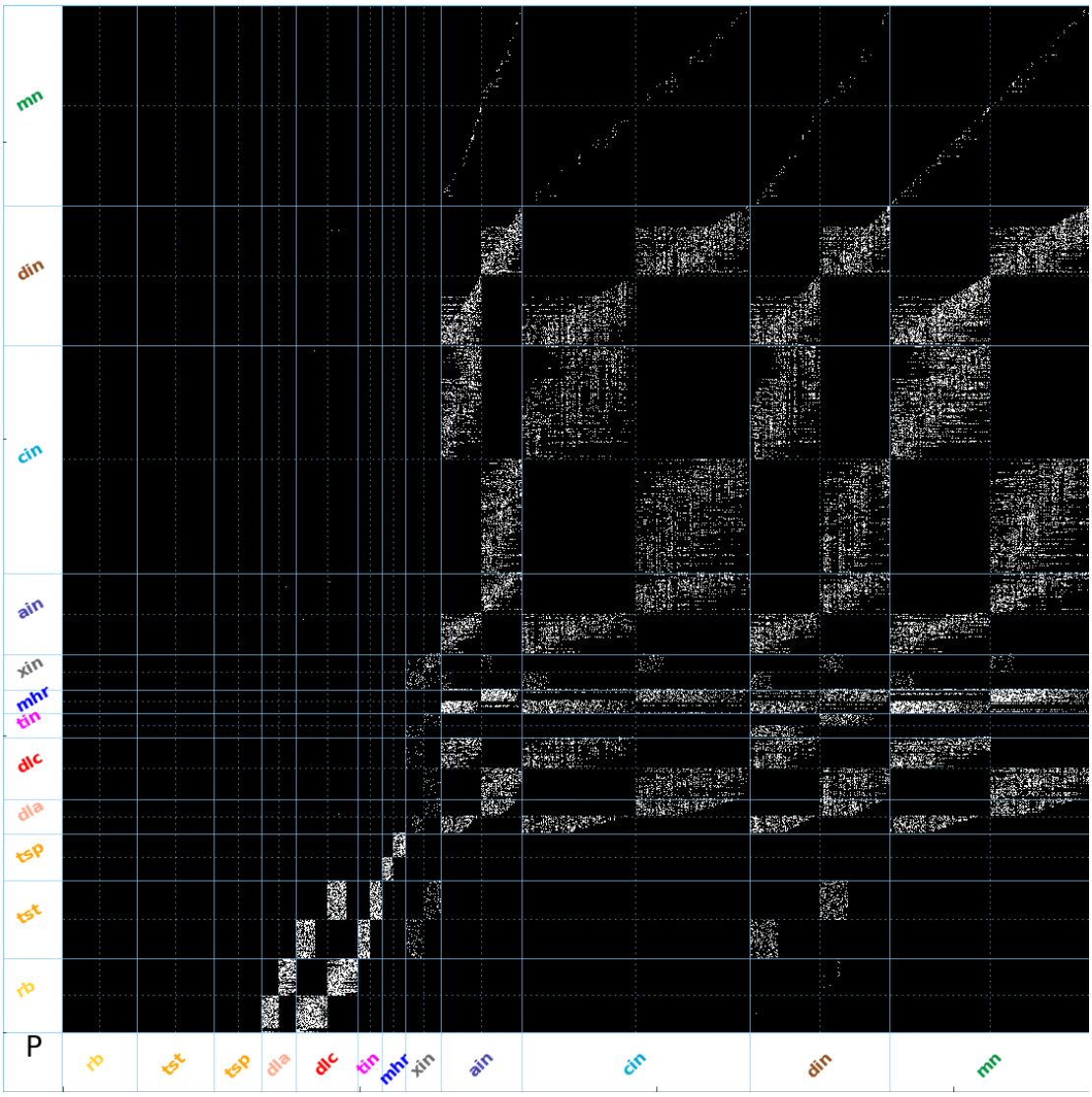

Figure 5.4: Visualisation of one realisation of the adjacency matrix A of the VT connectome, where white colours show existing connections ($a_{ij} = 1$) and black colour no connections ($a_{ij} = 0$). The remaining description of this figure is the same as the one of Figure 3.1. Rows and columns corresponding to neurons of each of the 12 types in the VT model are separated by solid blue lines. Light blue lines separate the matrix into symmetrical sub-blocks. Within each sub-block vertical and horizontal dotted lines separate the left body side (top rows and left columns) from the right body side (bottom rows and right columns). In each sub-block neurons are ordered according to increasing rostro-caudal position.

Two of these models mimic excitatory synapses by releasing glutamate and activating AMPA and NMDA receptors to the post-synaptic neurons, and the other two models mimic inhibitory synapses releasing glycine (INH) and Gamma-Aminobutyric acid (GABA-A) and activating inhibitory receptors to the post-synaptic neurons. The AMPA, NMDA and INH synaptic models used in the VT model follow the same model equations and time constants described in the previous functional connectome model (see chapter 1). The values of these parameters were selected to match physiological properties of neurons or pairwise recordings [Sautois et al., 2007]. To model synaptic variability, the maximal conductance value of most synapses are normally distributed with fixed mean and standard deviation. If not stated otherwise in the description below, the values of standard deviations of each conductance is 5% of the mean conductance value. Synaptic parameters of synapses that were already included in the previous functional model [Roberts et al., 2014, Ferrario et al., 2018a] are maintained the same, except for the changes described in the following sections.

5.1.7.1 Changes to previous synaptic parameters

rb $\rightarrow$ dla/dlc - One of the possible sources of variability in the start of swimming is the difference in the synaptic input levels between left and right sides. For trunk skin stimulation the current belief is that part of this difference derives from the difference in the input from RBs to dlas and to dlcs. This difference in inputs will contribute to deciding the side where first firing of CPG neurons and first motor responses occur [Buhl et al., 2012]. Like the previous functional model, we assume that RB to dla/dlc synapses include only an AMPA component and that their conductance is normally distributed. To avoid simultaneous co-activation of the two sides, which leads to pathological left-right synchrony, [Li et al., 2014a], we increase the original standard deviation value of the of the AMPA conductance by a factor 10. The mean value of these conductance are varied to mimic a difference in the input from RBs.

For the mean conductance values in the model, we selected two values: the original value of conductance suggested in previous functional model (8nS), and a reduced value (5nS). The motivation for using the first value (8nS) is given in Roberts et al. [2014]. However, it is possible that this original is too high, since the input from only 2 active RBs activates roughly half of the dlas and dlcs in any swimming simulation of the functional model (average of 19 dlas and 31 dlcs). Koutsikou et al. [2018] shows that there is a threshold stimulus above which tadpoles start to swim reliably on each repeated trial, and below which the same animals do not move (called swimming threshold). We aim to reproduce the physiological conditions where the stimulation is just above swimming threshold in the VT model. To do so, we assume that lowering the stimulation levels reduces the sensory input and, as a result, also the number of active dlas/dlcs in the network. In order to test this in the model, we used a second mean conductance value to model these synapses (5nS). Using this value we reduce the average number of active dlas and dlcs by an average of 7 and 9 units, respectively.

rb/dla/dlc $\rightarrow$ CPG neurons - These connections are excitatory glutamatergic connections with separate AMPA and NMDA receptors. The mean value of conductances in both receptors are reduced to 0.04nS from the previous functional model. We reduced these values because there is evidence suggesting that dlas and dlcs excite dINs and other CPGs only weakly [Koutsikou et al., 2018, Li et al., 2004b].

dIN $\rightarrow$ dIN - We reduced the mean conductance of the AMPA self-excitation in dINs to 0.3nS in order to decrease the number of simulations that produce pathological synchronous activity at the beginning of swimming episodes via trunk skin stimulation (see Results below).

5.1.7.2 Synaptic parameters in the new sensory pathway connections

There is only a small amount of available data that can be used to infer the values of synaptic parameters of the new connections included in the VT model. When synaptic data is available, we use it to fit synaptic parameters. In the case that such data is not available, we explored the parameter space in order to find ranges of values that gave the desired behaviour.

dla/dlc/tSt/tIN $\rightarrow$ hIN - We hypothesise that these synapses are glutamatergic, similar to all other excitatory synapses in tadpoles. We selected a mean conductance of 3nS for both AMPA and NMDA components and standard deviation value 2.

hIN $\rightarrow$ hIN - We model these connections as glutamatergic synapses activating AMPA and NMDA receptors, which allow sustained firing in the hIN population following transitory excitatory input from dlas and dlcs. The maximal conductance values for these synapses are not normally distributed like all previously described synapses and have maximum values of 5.5nS and 1.4nS for AMPA and NMDA, respectively. To include trial-to-trial variability, the strength of hIN-hIN synapses varied across simulations. Specifically, the maximum conductance of each synapse was scaled down by a randomly chosen value (0.8, 0.6, 0.4, 0.2 or 0) at the start of each simulation, with the scaling factor for each synapse chosen independently. To stop the firing of hINs, we introduced a simple model of synaptic depression in these synapses: the value of AMPA and NMDA synaptic strengths of each individual synapse is multiplied by parameter $\alpha = 0.995$ at the occurrence of a pre-synaptic spike (exponential decreasing of synaptic strength). Parameter α was selected to stop the firing of hINs after about 1.5 seconds. The synaptic delays between hINs are fixed: for ipsilateral and contralateral connections between hINs these delays are fixed to 1ms and 5ms respectively. Parameters in the model have been selected to reproduce

sustained firing in hINs that last for about 1.5 seconds after skin stimulation, similar to experiments [Koutsikou et al., 2018].

hIN $\rightarrow$ CPG neurons - We hypothesise that hINs are connected via mixed AMPA and NMDA synapses to CPG neurons. To model these synapses we use the same model of synaptic depression like hIN to hIN synapses with depression parameter $\alpha = 0.99$. Both AMPA and NMDA synapses have maximum conductance of 0.3nS, and we use the same random variability of synaptic strengths as the one introduced in the case of hIN to hIN synapses.

tSt $\rightarrow$ rdlc - Buhl et al. [2015] provides indirect evidence for direct excitatory connections from tSts to rdlcs. For simplicity we included only the AMPA component and the same standard deviation like in RB to dla/dlc synapses, and we select a mean conductance value of 4nS.

tSt $\rightarrow$ tIN - Buhl et al. [2012] provides indirect evidence that these synapses activate glutamatergic AMPA and NMDA receptors, and it provides data of EPSP recordings on tINs following stimulation of the head skin at varying intensity. Large EPSPs are produced in tINs by trigeminal afferents in response to weaker stimuli, which presumably activate single tSt neurons. Therefore, we hypothesise that these data result from a single tSt spike and one connection from this tSt to the tIN. The analysis of these data include measures of EPSP amplitudes, rise time from 10 to 90% amplitude, time to peak after the stimulus and duration at 50% amplitude. These data are provided separately for mixed AMPA and NMDA components, and for the AMPA component (obtained by blocking the NMDA component via applications of NBOX). We use both sets of data to fit the synaptic conductance parameters of the AMPA and NMDA components using a python derivative-free optimisation algorithm based on a user defined cost function [Mayer, 2017]. Our cost function is defined as the sum of the difference between experimental and simulated measures of single EPSPs (amplitude, 10-

NMDA	model	exp	AMPA+NMDA	model	exp
Amplitude (mV)	4.7	4.7		13.7	14.2
10-90 % rise time (ms)	9.9	10.4		2	2.5
50 % amplitude time (ms)	70.6	54.4		13.9	17.8
Time to peak (ms)	24.4	16.6		10.4	8.7

Table 5.2: Comparison between different measures of tIN EPSPs from NMDA (left) and mixed AMPA and NMDA (right) in model simulations and experiments (exp). These measures are EPSP amplitudes, rise time from 10 to 90% amplitude, time to peak after the stimulus and duration at 50% amplitude. Experimental measures are averaged across many neurons, from Buhl et al. [2012]. The measures obtained from simulations are obtained by modelling a single synapse from one tSt to one tIN with parameters $g_{AMPA} = 1nS$ and $g_{NMDA} = 0.78nS$.

90% rise time, time to peak and duration at 50% amplitude). Simulated EPSPs are obtained by modelling a single connection from one model tSt to one model tIN, and by injecting a brief step current to the tSt sufficient to activate one spike. We start the fitting of the NMDA maximal conductance using the data obtained by applications of NBOX, which gives best fitting value $g_{NMDA} = 0.78nS$. We then fixed $g_{NMDA} = 0.78nS$ and we used the same fitting method to approximate the AMPA conductance using the data on mixed AMPA and NMDA components, which gives value $g_{AMPA} = 1nS$. We started the fitting procedure from several initial condition and confirmed convergence of the optimisation algorithm to these values of parameters. Table 5.2 shows a good agreement between of the measures of EPSPs in experiments and and simulations obtained using the fitted parameters.

tIN $\rightarrow$ dIN - Buhl et al. [2012] provides direct evidence of direct glutamatergic AMPA and NMDA synapses from tINs to rostral reticulospinal dINs and hdINs. Similar to the case of tSt to tIN connections (see above), the paper provides measures of EPSP recordings on dINs, including EPSP amplitudes, rise time from 10 to 90% amplitude and time to peak after the stimulus (no data on the duration at 50% amplitude is provided, and therefore omitted in the model). In this case, however, these data are obtained from pairwise recordings of tINs

AMPA+NMDA	model	exp
Amplitude (mV)	2.5	2.6
50 % amplitude time (ms)	14.7	14
Time to peak (ms)	4.1	5.2

Table 5.3: Comparison between measures of single EPSPs in dINs from mixed AMPA and NMDA (right) in model simulations and experiments single tIN→dIN synapses. These measures are EPSP amplitudes, rise time from 10 to 90% amplitude, time to peak after the stimulus and duration at 50% amplitude. Experimental measures are averaged across many neurons, from [Buhl et al., 2012]. The measures obtained from simulations are obtained by modelling a single synapse from one tIN to one dIN with parameters $g_{AMPA} = 0.37nS$ and $g_{NMDA} = 0.23nS$.

and dINs. Therefore, we are confident that that these EPSPs are a result of single pre-synaptic spiking and single connections from tIN to a dIN. The data has been analysed for mixed AMPA and NMDA components. We use a similar optimisation algorithm and cost function used to fit synaptic parameters of tSt to tIN synapses (see previous paragraph). The only two differences are that we fit the AMPA and NMDA synaptic strengths simultaneously using two-parameter fitting and that the cost function is defined as the sum of the difference between experimental and simulated EPSP amplitudes, time to peaks and durations at 50% amplitude. EPSPs are reproduced by a single connection model from one tIN to one dIN, and by injecting a brief step current to the tIN sufficient to evoke one spike in the tIN. Additionally, since the voltage dynamics of dINs depends on the electrical coupling in the dIN population, the post-synaptic dIN is electrically coupled to other 15 dINs with coupling coefficient value of 0.2nS (selection of these dIN numbers and coupling coefficients are based on analysis of the previous functional model). The result of the fitting gives values of parameters $g_{AMPA} = 0.37nS$ and $g_{NMDA} = 0.23nS$. The fitting procedure was started from several initial condition to confirmed convergence of the optimisation algorithm to these parameters values. Table 5.2 shows a good agreement between of the measures of EPSPs in experiments and and simulations obtained using the fitted parameters.

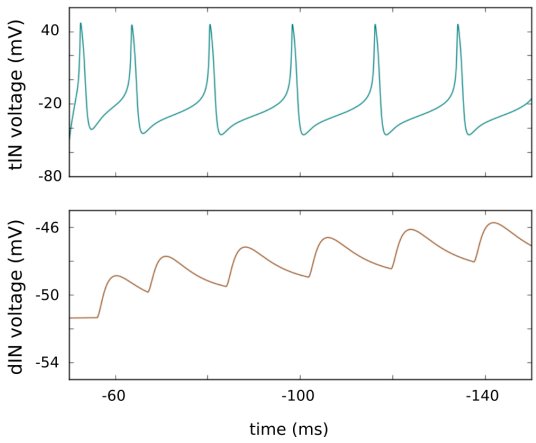

Figure 5.5: Voltage of one tIN (top) connected to one dIN (bottom) via mixed AMPA and NMDA excitatory synapse in a model simulation. A depolarising step current evokes a train of spikes in a single tIN and generates summation of EPSPs in the dIN. Conductance parameters used in this simulation are $g_{AMPA} = 1nS$ and $g_{NMDA} = 0.78nS$ (the best fitted parameters, see text for more details).

Figure 5.5 shows the voltage recording of one tIN connected via a single excitatory synapse (AMPA+NMDA) with parameters given in Table 5.3. The tIN is injected with positive current that activates 6 spikes in the tIN. It is remarkable that the tIN-evoked EPSPs in the dIN show temporal summation similar to that seen in electophysiological recordings (see Figure 9 in [Buhl et al., 2012]).

tSt $\rightarrow$ dIN neurons - Buhl et al. [2012] suggest the existence of direct excitatory synapses from tSts to dINs. Since there is no available data that can be used to estimate synaptic parameters, we assume that these synapses have mixed AMPA and NMDA receptors and that parameter values of these synapses are the same as tIN to dIN synapses.

tSp $\rightarrow$ MHR neurons - Perrins et al. [2002] provides indirect evidence for excitatory synapses from tSps to MHRs. We seleted excitatory synapses with mixed AMPA and NMDA components with mean conductance of $5nS$ and $1nS$, respectively.

MHR $\rightarrow$ CPG neurons - Perrins et al. [2002] shows that these synapses are

inhibitory and activate GABA-A. These GABA-A synapses are modelled using the same equations and parameters of glycine inhibitory synapses included also in the previous functional model (INH), except for the closing time constant $tau_c = 20ms$ and reversal potential $E_{GABA-A} = 70mV$. These parameters are based on current clamp recordings of inhibitory postsynaptic potentials produced in tadpole spinal neurons by MHR stimulation [Hull et al., 2016].

Synaptic delays - The delays in the synaptic transmissions depend on the rostro-caudal distance between cell bodies. We use the same model used to define this delay in the previous functional model (see chapter 1).

5.2 Results

In the previous section we described the new elements of the VT model which include head skin sensory modalities and hindbrain sensory processing neuronal populations. In this section we combine these populations with CPG neurons to demonstrate how the model can generate appropriate behaviour in response to different sensory stimuli. We show that the VT model can reproduce and explain the neuronal processes underlying the initiation, continuation, acceleration and termination of swimming in response to sensory signals. First, we demonstrate how swimming activity can be initiated by the TS and HT sensory pathways. Second, we show that swimming activity can be stopped by activation of sensory neurons from the head pressure pathway or can stop spontaneously. Third, we show that the stimulation of the trunk skin can lead to acceleration of swimming. For each of these behaviours, the model can mimic the experimentally recorded spiking neuronal activity of many of the key cell types. Therefore, these simulations could provide an incredibly useful platform to help understand the neuronal mechanisms that generate each of these behaviours, and for experimental testing.

5.2.1 Extended firing in hINs leads to long and variable swimming initiation delays in a first test of the model

The long and variable pattern of EPSPs in hdINs observed before the start of a swimming episode (see model description and Koutsikou et al. [2018]) suggests that the spiking of neurons in the TS sensory pathway is extended. A simple and commonly proposed mechanism to explain extended firing is that some population of neurons form small recurrent networks (see, for example, Durstewitz et al. [2000]) on each side of the hindbrain (hINs), lying between the trunk skin sensory pathway and the hdINs. To explore the plausibility of this proposal, we start by building a first, simplified "test" network model of the trunk skin pathway (Figure 5.6). All details of this model (including model parameters) can be found in Koutsikou et al. [2018]. We use this "test model" to show the working principles underlying the decision-making process for swimming initiation. This test model uses the same functional specifications of neurons and synapses as the ones used in the VT model, except for some adjustments in synaptic parameters. In this test model, we only consider one side of the spinal cord (opposite to the stimulation side), and the number of neurons and connections is reduced compared to the VT model.

In this model, 30 sensory pathway dlcs, with nearly synchronous spike times, produce glutamatergic excitation in a group of 30 hINs with a contact probability of 0.4. To form a recurrent network, the hINs make mutual glutamatergic synapses, activating AMPA and NMDA receptors; each hIN receives input on average from three other, randomly chosen, hINs. hINs connects randomly to any hdINs with probability of 0.2 and these connections also activate AMPA and NMDA receptors.

The synaptic strength varies randomly across trials as in the VT model and as is found experimentally [Li et al., 2002, 2003, 2006, 2007b, Buhl et al., 2012].

Similar results hold also for the VT model and are reported in the next section.

In preliminary tests, we found that brief sensory dlc firing produced continuous, self-sustained firing of all hINs. This showed the effectiveness of recurrent excitation but did not provide significant variability. Synaptic strengths and connection probabilities of dlc to hINs were therefore reduced until only some hINs fired as a direct result of dlc excitation. Sustained firing was then variable across the hIN population, and on some trials hIN firing was transient (Figure 5.6 B-D). These patterns of hIN firing lead to slow and variable summation of EPSPs in the five hdINs, connected to the hINs to monitor their output (Figure 5.6A). The summating EPSPs could fail to reach hdIN firing threshold or lead to firing with variable delays (34-190 ms; n = 30 trials). Single hIN spikes led to small hdIN EPSPs (0.6-2.3 mV) but larger hdIN EPSPs occurred when two or more hIN spikes were nearly synchronous.

The simplified test model described above demonstrate that a recurrent network of hINs can generate extended and variable firing following transient input from the sensory pathway and produce a pattern of summating EPSPs in hdINs with which they synapse. These results illustrate the plausibility of the proposal that activity in a group of neurons forming a simple recurrent network could act as a short sensory memory, extending firing to a brief sensory stimulus and providing summating excitation to produce long and variable delays in the initiation of hdIN firing and the activation of the first motor responses.

5.2.1.1 Swimming initiation via trunk skin stimulation

The simplified test model described in the previous section can explain the neuronal processes underlying the initiation of swimming on one side of the body. In this section, we test if this explanation can be extended to the VT model by including the hIN populations on each side of the body. A major issue is then to explain how the two sides are coordinated at the start of swimming. More

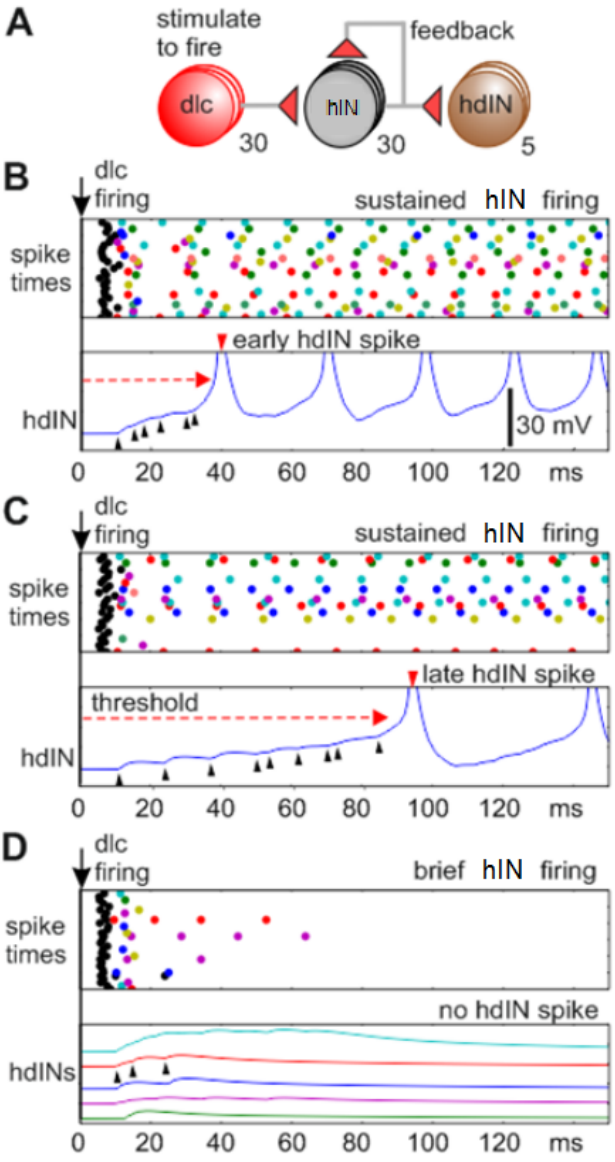

Figure 5.6: Simplified recurrent model of hdIN excitation and recruitment from Koutsikou et al. [2018]. Details about the model connectivity and parameters can be found this paper. In A we show a diagram of connectivity and neuronal populations in the test model: we consider a recurrent hIN network excited by single spikes in 30 sensory pathway dlcs and 5 hdINs to monitor output (A). All neurons are considered to be on one side of the spinal cord. Parts B-D show raster plots of spike times for dlcs (black) and hINs (colours); in response to 30 DLC spikes at time t=0 (arrow). Lower panels show selected hdIN voltage records. HINs generate sustained firing with variable durations and produce variable, summating EPSPs in hdINs (black arrowheads). EPSP summation can reach threshold (dashed red line) and lead to hdIN firing (red arrowhead) after variable delays. In part D, when hIN firing is brief, EPSPs sum but do not reach hdIN firing threshold (all five traces separated for clarity).

precisely, we can formulate this issue with the following two related aspects:

1. **Muscle alternation.** Assuming that swimming starts when muscles on one side contract, how can muscles on the opposite side be activated half a swimming cycle later?

2. **Muscle synchronisation.** If the same process that leads to the hdINs spiking and first motor responses happens on both sides, how is the network able to avoid synchronous activation of antagonist muscles?

Clarifying how the network is able to produce the initial alternation of muscles and avoid their synchronisation is not trivial. For the first aspect, we cannot assume that the same mechanism of PIR in dINs controlling the alternation of antagonist muscles during swimming can coordinate alternation also of the first two swimming cycles. This is because dINs' voltages are at low levels of depolarisation at the time when these two cycles occur (presumably driven by hINs), and we know that dINs cannot fire on rebound under such conditions [Soffe et al., 2009]. For the second aspect, although we know that synchronous activation of antagonist muscles during the first few swimming cycles can be observed (Chapter 3; Li et al. [2014a]), this phenomenon is rare and usually lasts for only a brief period of time. These observations suggest that the occurrence of this left-right muscle synchronisation should be minimised by the circuit. However, the current proposal for the start of swimming could lead to several cases where this phenomenon might occur.

We start by reproducing the start of swimming in response to trunk skin stimulation using the VT model. Figure 5.7 shows one simulation of this model, where all neurons are initialised at rest at time 0. The top and bottom panels of Figure 5.7 show examples of voltage dynamics for individual neurons for each type on the right and left body sides (three randomly selected hINs and one neuron for each of the other active neuronal types). Neurons of all the other neuronal types

are omitted because they are inactive. The central panels in Figure 5.7 show raster plots of spiking activity of all neurons on the right and left sides of the body. The maximal conductance of RBs to dlas/dlcs synapses in this simulation is 8nS (we then tested changes to 5nS, see below). We mimic skin touch (or stimulation) by generating single-spikes into two sensory RB neurons on the left side of the spinal cord. These spikes trigger single-spike responses in a group of sensory interneurons (dlas and dlcs), which in turn excite and cause the firing of some hINs on both sides. Due to their recurrent excitation, hINs on both sides generate sustained irregular firing (lasting for about 1.5 seconds on both sides) and produce similar variable and summating EPSPs in hdINs as in experimental recordings [Koutsikou et al., 2018] and in the previous test model (Figure 5.6B-C). However, in the VT model, EPSPs are also produced in all other CPG neurons. When the EPSP summation reaches threshold for spiking, left CPGs start to fire (typically, hdINs fire first).

It is important to notice that results similar to the one presented in this figure hold also when generating random simulations with new network connectivities (see Methods). Additionally, these repeated simulations show that swimming oscillations can start on both left and right sides of the body and in response to the stimulation of the skin on either of these sides (see results below).

Due to their contralateral connections, the hIN populations on both sides display similar firing patterns, and that these two patterns build up with time at similar rates. This property guarantees that left and right CPG neurons receive a similar build-up of excitation from left and right hINs, respectively, enabling their firing. Simulations that are not reported in this chapter revealed that including a sufficient number of these connections is important. If this number is too low, a high percentage of random simulations show that the first firing of CPG neurons on one side is not followed by the firing of CPG neurons on the opposite side, and swimming oscillations are not properly initiated. This activity pattern

is discussed in more details below.

The inhibition from cINs helps to guarantee the initial alternation of muscles and avoid their synchronisation (see point 1-2 above). Due to the similarity of hIN inputs to the CPG neurons on both sides, right CPGs in Figure 5.7 could in theory fire shortly after the firing of left CPGs. However, the inhibition from the left cINs prevents and delays the firings of the right CPG. In fact, due to the interplay between the excitatory input from left hINs and the inhibition from right cINs, these firings occurs at approximately half a swimming cycle after the firing of left CPGs, establishing the alternation of antagonist muscles for the first swimming cycle (see point 1 above). Additionally, results from multiple random simulations revealed that the cIN inhibitory strength helps to avoid co-activation of the two sides (see point 2 above). Simulations with reduced cIN inhibitory conductance showed that episodes of synchronous activation of antagonist muscles occurred more frequently (see results below).

The first firings of left and right mns defines the first half-cycle of swimming. Once this cycle is completed, CPG neurons continue to generate anti-phase left-right oscillatory firings, which is essentially controlled by contralateral inhibition from cINs and PIR spikes of dINs during their mutual re-excitation. We do not explain this pattern in detail because it has been studied in detail in chapter 3 and chapter 4. It is worth highlighting, however, that CPG neurons are able to generate this pattern while receiving continuous excitatory drive from the background firing of hINs, which is a feature that was not explored in these previous chapters.

We then repeated 100 independent random simulations of the VT model using the same parameters and stimulation protocol as in Figure 5.7 to test the robustness of these results and compare them with experimentally observed patterns of neuronal activities. In all the simulations tested, the pattern of neuronal ac-

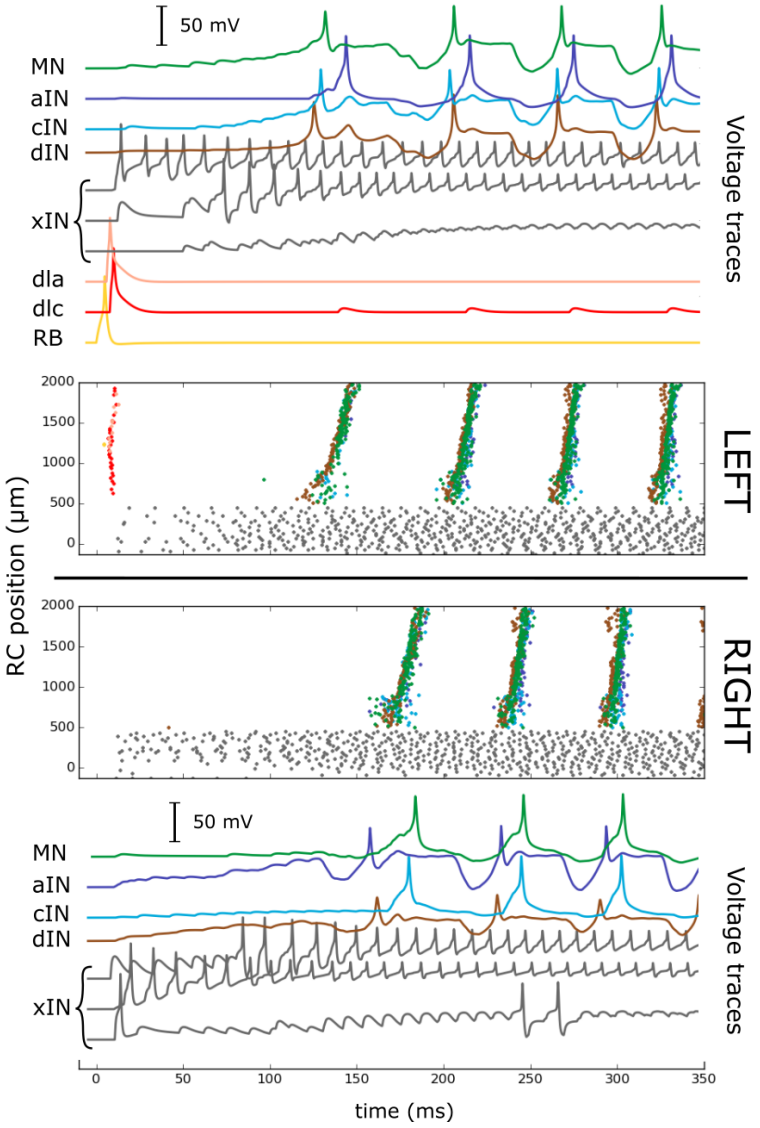

Figure 5.7: Start of swimming in response to trunk skin stimulation. The horizontal line in the middle of the figure separates the activity of neurons on the left (top) and right (bottom) body side. Central panels show spike times, where the vertical position of each spike corresponds to the rostro-caudal position of the associated neuron. Top and bottom panels show the voltage traces from selected neurons that represent the activity of the population: three hINs and of one neuron for each of the other active neuronal types. Neurons of all the other neuronal types are omitted because they are inactive. Two sensory RB neurons fire one spike each in response to a brief stimulation at time 0. RBs excite and lead to the firing of dlas and dlcs, which in turn excite and recruit a number of hINs on both sides. HINs fire repetitively and irregularly, and they produce variable summating EPSPs in CPG neurons. The first firing of CPG neurons on the left side is followed by the firing of CPG neurons on the right side half a swimming cycle later and by left-right anti-phase alternation of the CPG activity. The mean maximal conductance of RBs to dlas/dlcs in this simulation is 8nS. We use the standard colour coding described in Figure 5.1 to show both voltages and spikes.

tivity of RBs, dlas, dlcs and hINs is similar to the one shown in Figure 5.6B-C and Figure 5.7. Briefly, single spikes in sensory and sensory pathway neurons activate the hIN populations on both sides. These neurons spike irregularly and at variable times between 1 and 2 seconds and they generate variable EPSPs in CPG neurons, similar to those in experimental recordings [Koutsikou et al., 2018]. The summation of these EPSPs can fail to reach firing threshold on both sides, and in these cases all neurons eventually return to their resting steady-state (19/100 simulations). We do not show the results of these simulations because they are similar to the ones shown in Figure 5.6D in the case of hdINs, except that the same pattern of EPSPs reported for hdINs appears also in all CPG neurons on both sides. Similar to Figure 5.6B-C, the same summation can lead to firing in at least one of the two sides (81/100 simulations). The description of these 81 simulations can be divided in the following three groups:

1. 75 simulations showed neuronal activity patterns similar to the ones shown in Figure 5.7. First motor responses, measured as the first mn firing times, could occur on either of the two sides (41 times on the left, 34 times on the right), and their delays from the time of stimulation were long and variable, ranging from 45 ms to 199 ms.

2. In 3 simulations CPG neurons on both sides fired at approximately the same time (synchrony). This synchronous firing persisted for 1-3 swimming cycles (see point 2 above). In all these simulations, this synchronous activity was followed by swimming with anti-phase firing of CPG neurons on each side. These results suggest that synchrony is unstable. Interestingly, synchrony has also been seen in experimental recordings [Li et al., 2014a] and, in both model and experiments, is a rare event. In chapter 4 we have reported a detailed study of how this pattern can occur in a simplified model of the CPG circuit. In particular, we have observed that syn-

chrony can be initiated when CPG neurons receive a similar input on both sides and occurring at nearly the same time. Similarly, synchrony in these simulations is driven by the irregular spiking of hINs neurons, which can occasionally provide CPGs on both sides receive a similar input occurring at nearly synchronous times.

3. In 1 simulation, CPG neurons on one side start to fire, but CPG neurons never fire during the entire simulation time, and all neurons converge to the resting state. A similar activity pattern where single motor responses are activated on one cycle but does not persist was observed also in experiments [Roberts et al., 1985].

We then tested the impact of reducing cINs' inhibition by repeating 100 random simulations with modified maximal cIN maximal conductance from 0.435nS to 0.2nS. In 22/100 of these simulations CPG neurons on both sides fail to reach firing threshold and return to their resting steady-state. The description of the remaining simulations can be divided in the same three groups previously described (points 1-3 above). 63/100 simulations showed neuronal activity patterns similar to the ones shown in Figure 5.7 (see point 1 above). In 2/100 simulations the firing of CPG neurons on one side is not followed by the firing of CPG neurons on the opposite side (see point 3 above). In the remaining 13/100 simulations CPG neurons on both sides start to fire in synchrony (see point 2 above).

Therefore, we observe a significant reduction in the number of cases where the firing of CPG neurons is initiated in antiphase alternation and a significant increase in the number of cases where firing of CPG neurons starts in synchrony. These results suggest that the strength of cIN inhibition helps to avoid the co-activation of antagonist muscles (see point 2 above).

Koutsikou et al. [2018] summarises the biological experiments supporting these

predictions of the VT model. Additionally, the experiments presented in this paper demonstrated that sub-threshold stimulation of the skin may lead tadpoles to make a decision to start to swim or to stay still. Buhl et al. [2012] shows that also head skin stimulation can lead tadpoles to make the same decisions. After repeated trials with variable stimulation levels, Buhl et al. [2012] concludes that swimming starts more frequently and with less reaction times variability when stimulation levels are stronger.

We therefore tested if the VT model can also predict this experimental finding. So far, our model mimics strong stimuli levels to the trunk skin by using high conductance values in the synapses from sensory RB neurons and sensory pathway dla and dlc neurons. To investigate responses to weaker skin stimuli, we presume that lower stimulation levels activate less dlas and dlcs in the network. We therefore tested if the VT model responses were different after reducing the number of active dlas and dlcs in the network. Although we are aware that lower stimulation levels are likely to decrease also the number of active RBs, we did not test the effect of reducing this number for two reasons. Firstly, because we wanted to keep this number equal to the one described in the previous functional model [Roberts et al., 2014], as changing it would require to drastically modify the strengths of synapses from RBs to dlas and dlcs (of an order of magnitude of more than 10), which are based on physiological evidence [Roberts et al., 2014]. Secondly, because we could still reduce the input from RBs to the network simply by lowering these strengths from 8nS to 5nS (see Model description). In future tests, we aim to explore further this feature of the model.

We therefore repeated 100 random simulations of the VT model after the application of these changes and tested the reliability of the start of swimming. In these simulations the voltage and spiking activities of RBs, dlas and dlcs is similar to the ones shown in 5.7, except that fewer dlas and dlcs are activated,

due to the reduced input from RBs (see previous section). In some simulations, the hINs spike at variable times between 1 and 2 seconds, and their dynamics is similar to the one of hINs in Figure 5.7. In the remaining simulations, hINs stop to fire briefly after stimulation on both sides (between 60 and 150 ms), similar to Figure 5.6D. In both cases, however, hINs generate variable EPSPs in CPG neurons. The summation of these EPSPs often failed to reach threshold for the spiking (64/100 simulations). In 36 simulations, spiking of CPG neurons and swimming was initiated. The activity of CPG neurons is similar to the one shown in Figure 5.7. Firing of mns on either side of the spinal cord (19 times on the left, 17 times on the right), and delays to the first mn firing ranged from 50 to 170ms. These simulation results suggest that lower levels of TS stimulation lead to less reliable initiations of swimming and to more variable delays to the first motor responses. It is also interesting that these simulations can produce transitory pattern of hdINs' EPSPs that has been seen also in experiments [Koutsikou et al., 2018].

The results of these 200 simulations demonstrate that the VT model can reproduce neuronal activities that lead to the initiation of swimming that are similar to those seen in experimental recordings. In agreement with experiments, the VT model shows that TS stimulation may or may not lead to the start of swimming. Moreover, when swimming starts, the first motor response can occur on either side after long and variable delays from stimulation. These results suggest that the VT model mimics closely the neurobiological details of the swimming circuit and it can be used to study the neuronal mechanisms leading to the initiation of swimming in response to the TS stimulation. These results endorse the neuromechanistic proposal suggested by the test model to explain the long and variable delays to the start of swimming [Koutsikou et al., 2018]. Moreover, they provide additional insights that demonstrate the neuronal principles beyond the alternation and de-synchronisation of antagonist muscles during the first swim-

ming cycle.

5.2.2 Initiation of swimming by head touch

In this section, we simulate the start of swimming in response to head touch (or electrical stimulation) in the VT model. Figure 5.8 shows an example where the top and bottom panels show the voltage dynamics of representative neurons of each type and the central panels show the spiking activity of all neurons as in Figure 5.7. To mimic the neuronal responses to head touch, 8 sensory tSt neurons on the left side were stimulated to fire a single spike each at time 0. The firing of tSts excites and causes single spiking in 8 tINs and 30 rdlcs. tSts, tINs and rdlcs contribute to excite hINs and hdINs on both sides. Due to this mixed transitory input and their recurrent excitation, hINs fire repetitively and irregularly, similar to model simulations of the TS pathway (Figure 5.7) and excite CPG neurons on both sides. The mixed inputs from left tSts, tINs and hINs summate to generate high amplitude EPSPs and cause the early firing of left hdINs, which in turn activate CPG neurons on the left side. Meanwhile, the population of right hINs excites and causes the firing of right CPGs approximately half a swimming cycle after the firing of left CPGs. As in the case of TS stimulation, left cIN inhibition is crucial for making sure that the firing of right CPG neurons occurs after approximately half a swimming cycle delay, and not before. When the first half-cycle of swimming is complete, left-right anti-phase oscillatory activity of the CPG neurons is established and continues as in the case of TS stimulation.

100 random simulations of the VT model were used to confirm the validity of these results. For 99/100 simulations the stimulation protocol led to the initiation of swimming oscillations and to neuronal activities similar to Figure 5.8. The number of tINs and rdlcs recruited in all simulations was also similar (9 $\pm$ 2.4 tINs and 31 $\pm$ 1 rdlc, mean $\pm$ std). First spiking of CPG neurons started on

the stimulated left side in all 99 simulations, and the first motor response was at 29.9±2.4 ms (mean±std, calculated from the vector of median first firing times in left mns). In the remaining 1/100 simulation the summation of EPSPs did not reach threshold for activating CPG neurons on either sides. These EPSPs were long and variable as in the case of TS stimulation.

We notice that, in contrast to TS stimulation, none of these 100 simulations demonstrated coactivation of antagonist muscles. The reason for this is that the dINs on the left stimulated side receive stronger excitatory sensory inputs than right dINs, because of input from tINs. Another consequence of this high level of excitation is that hdINs tend to fire at much shorter delays from the start of stimulation which leads to much shorter first reaction times, as found in recordings from tadpoles [Buhl et al., 2015].

Buhl et al. [2015] showed that changing the intensity of electrical stimulation to the head skin can have a great impact on both the side where swimming will start and the delays to first motor responses. After repeated trials experiments show that, with stronger stimulations (above swim threshold), swimming starts always on the stimulated side and first motor responses occur at shorter and less variable delays (approximately 30-40ms). Other experiments showed that lower stimulation levels (just above swim threshold) can lead to the initiation of swimming on either side of the body and that the first motor responses occur at much longer and more variable delays, similar to the delays to swimming following TS stimulation [Koutsikou et al., 2018]. Additionally, these second experiments show that hdINs on both sides of the spinal cord receive a similar pattern of summating EPSPs which can make them to fire at long and variable times. These results suggest that a similar mechanisms to the one described for the TS pathway might be responsible for the initiation of swimming when low stimulation levels are applied to the head skin.

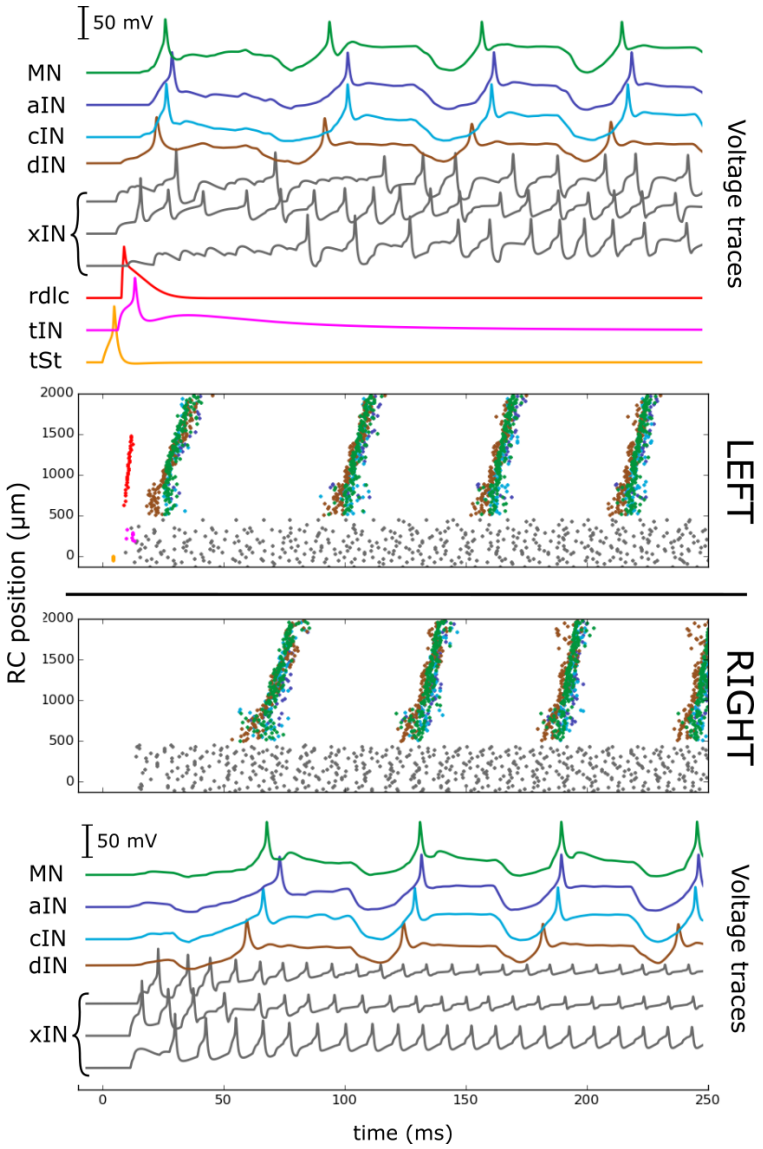

Figure 5.8: Simulation of the start of VT model swimming in response to head stimulation. Panels are organised as in Figure 5.7. Top and bottom panels show the voltage activities of selected active neurons in response to head pressure. Eight sensory tSts fire one spike each in response to a brief stimulation at time 0. These neurons excite and lead to the firing of tINs and rdIcs, which in turn excite and recruit a number of hINs on both sides. hINs fire repetitively and irregularly, and they produce variable summating EPSPs in CPG neurons. The strong excitation from tINs to dINs mixed with hIN to dIN excitation leads to the firing of dINs and other CPGs and to the start of swimming on the stimulated side. Meanwhile, right hINs excite and activate CPG neurons on the opposite side approximately half a swimming cycle after the firing of left CPG neurons. After this first half-cycle of swimming, left-right anti-phase alternation of the CPG activity is established and continues.

Our previous simulations of the TH pathway showed that activation of tSts, tINs and hINs on the stimulated side is sufficient to activate ipsilateral hdINs and initiate swimming (in 99/100 simulations). The first firing of CPG neurons and the first motor responses always occur on the same stimulated side and at a shorter and less variable delays compared to TS stimulation. This would suggest that our stimulation protocol was similar to the high level intensity stimulation of the head skin. We therefore tested if lowering this level can still lead to the initiation of swimming and, if this is the case, whether the delay to the first motor responses was longer and more variable, as found in the experimental recordings [Buhl et al., 2015].

To mimic the lower intensity of head skin stimulation we reduced the number of activated tSts from 8 to 6 in the VT model. We then repeated 100 random simulations of the model and obtained the following results. The number of active tINs decreased to 2.8 $\pm$ 1.6 (mean $\pm$ std). Swimming oscillations were initiated in 52/100 simulations on either side of the animal (28 times on the left side, 18 on the right side). Delays to first motor responses were long and variable (range 30.2-173ms), similar to simulations of the TS pathway. CPG neurons received long and variable patterns of EPSPs caused by the firing of hINs. The neuronal mechanism leading to the start of swimming in these simulations is analogous to the one described for the TS pathway. In 46/100 simulations CPG neurons on either sides received similar long and variable EPSPs, but the summation of these EPSPs did not reach threshold for firing and swimming was not initiated. In 2/100 simulations synchronous activity of CPG neurons lasting 3 swimming cycles was observed, similar to the synchrony pattern seen in response to TS stimulation. In one of these simulations this synchrony was followed by antiphase swimming oscillations, similar to the synchrony in simulations of the TS pathway. In the other simulation, swimming oscillations did not appear and dynamics of CPG neurons returned to the rest. This pattern has been reported

also in chapter 4.

In summary, these results suggest two distinct mechanisms for the initiation of swimming in response to TH stimulation. In the first mechanism, direct excitation from tINs to dINs sums, causing the firing of dINs on the stimulated side, which in turn activates the other CPG neurons on the same side. On the opposite side, the sustained and variable firing of hINs excites CPGs and leads to their firing after approximately half the swimming cycle, effectively initiating swimming. This mechanism leads to quick and less variable delays to the first muscle activation which are comparable to reflexes. In the second mechanism, long and variable summation of excitation caused by irregular firing in hINs may or may not initiate swimming. When swimming is initiated, delays to first motor responses are longer and more variable, like delays to first motor responses in the case of stimulation of the TS (discussed in the next section).

5.2.3 Summaries of results on the initiation pathways

Figure 5.9 shows an analysis of simulations of the VT model in response to stimulation of the TS and TH (the data used are from the 400 simulations described in the previous two sections). We divide simulations between the ones obtained by applications of high levels of stimulation (High TS, High TH) and the ones obtained by applications of low levels of stimulation (low TS, low TH), following the same division that was described previously (therefore, we use 100 simulations for each group). The neuronal activity of each simulation is classified into four distinct groups. The first group is formed by simulations where CPG neurons eventually generate antiphase swimming oscillations (swim, blue colour). The second group is formed by simulations where CPG neurons receive variable EPSPs that do not reach threshold for firing in these neurons, and therefore swimming oscillations do not start (no swim, red colour). The third group is formed by simulations where CPG neurons on both sides start to fire in synchrony and

either switch to swimming or return to rest after some time (sync, green colour). The fourth group is formed by simulations where only CPG neurons on one side fire (one-sided, purple colour). Each bar in Figure 5.9A shows the size of each of these groups of simulations. Boxlplots in Figure 5.9B show separate distributions of the reaction times of the first motor responses for each of the four tested stimulation protocols (High/Low TS, High/Low TH). These data were calculated from simulations where swimming with anti-phase oscillatory firing of CPG neurons was initiated. Reaction times are calculated in each simulation as the median across all active rostral mns (rostro-caudal positions < 1000μm). Above these boxplots we show the percentages of simulations where swimming started on the left (L) and on the right sides (R).

This analysis summarises the quantitative agreements between model simulation and experimental recordings, which were discussed in the previous sections. In summary, we observe the following (Figure 5.9A). High levels of TS stimuli lead to a higher probability to initiate swimming than lower levels of TS stimuli. However, in both cases swimming can start on either side of the spinal cord (Figure 5.9B). High levels of HT stimuli start swimming oscillations in almost all cases (99/100), while lower levels of HT stimuli may or may not start swimming. Coactivation of antagonist muscles (synchrony) occurred in 5/400 simulations. In a single simulation the CPG neurons on one side of the body were activated while the ones on the opposite side remained inactive (one-sided activation). Remarkably, both the simulations showing synchronous coactivation of antagonist muscles and the simulation showing one-sided CPG activity correspond to activity patterns that have been recorded in experiments in [Li et al., 2014a] and [Roberts et al., 1985], respectively.

From Figure 5.9B we observe the following. The TS pathway can lead to long and variable decisions to swim and lower levels of the TS stimuli lead to longer and more variable reaction times than stronger TS stimuli. These distributions

of reaction times correspond to the ones measured in experiments from ventral root recordings, which measure inter-quartile ranges of 33-61 ms and 80-113 ms in responses to stimulations near threshold for initiating real and fictive swimming, respectively [Koutsikou et al., 2018]. In particular, we remark that these distributions (low TS and high TS) are skewed towards those like the ones reported in this paper (Figure 1 in Koutsikou et al. [2018]). The TH pathway can lead to either reliable and quick (high TH) or to long and variable (low TH) delays to swimming. These distributions of reaction times also correspond to the ones gathered from experiments shown in Buhl et al. [2015]. For stimulations near the threshold for initiating fictive swimming these times range of 15-87 ms median of 25ms, while for stronger stimulations the inter-quartile range is 19-40 ms and median of 23 ms. Lastly, our results correspond to experiments by predicting that all stimulation protocols except High TH can initiate swimming on either side, and that the High TH pathway leads to initiation of swimming always on the stimulated side.

5.2.4 Termination of swimming

5.2.4.1 Head pressure reliably stops swimming

In this section, we simulate the termination of swimming in response to head pressure. Figure 5.10 shows the activities of CPG, tSp and MHR neurons, which belong to this pathway. The top and bottom panels of Figure 5.10 show the voltage dynamics of selected neurons for each of these cell types and central panels the spiking activity of all neurons. We activate single firing in 10 tSts to initiate swimming. To mimic responses of sensory neurons to head pressure like in experiments [Perrins et al., 2002], we stimulated 10 sensory tSp neurons on the left side by injecting each tSp with a step current from 1.95s to 2.35s with independent random normally generated amplitudes (mean=0.2nA, std=0.02). During this stimulation tSp sensory neurons fired rhythmically with amplitude

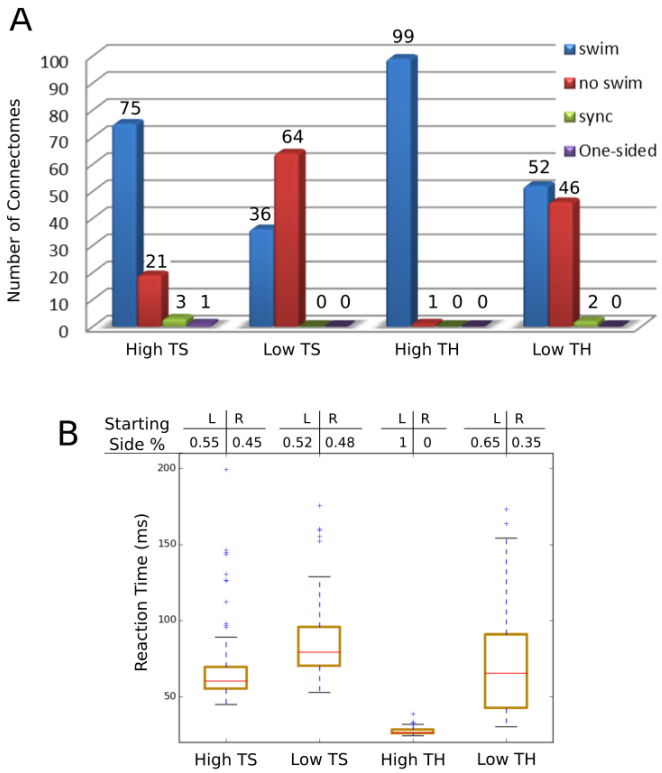

Figure 5.9: Summary of statistics in simulations of the VT model in response to TS and TH sensory pathway stimulation. Random simulations of the TS and HT pathways are divided between high and low levels of stimulation intensities. A. Bar charts showing the number of simulations where swimming is initiated for each of four groups of simulations. These groups are based on the activity of CPG neurons. We group simulations where CPG neurons display antiphase oscillations (swim, blue), no firing on either side (no swim, red), synchronous activity (sync, green) and firing on one-side only (one-sided, purple). B. Box plots showing the reaction time distributions of the first motor responses for each of the stimulation protocols (high/low TS, high/low TH). These distributions are calculated only from simulations that displayed CPG swimming activities. Top: percentages of simulations where swimming starts on the left (L) and on the right sides (R) in each of the stimulation protocols.

dependent frequencies. The frequency of the tSp neuron shown in the upper panel of Figure 5.10 is 32.5Hz. Stimulation of 10 tSps leads to the activation of all ipsilateral MHRs, which produced irregular spiking activity and inhibited CPG neurons on both sides via ipsilateral and commissural connections. As a result of the stimulation of the head pressure pathway the swimming oscillatory activity of all neurons stops after 2.4 seconds.

We repeated 100 random simulations of the VT model with the same stimulation protocol to confirm the reliability of these results. In each simulation we activate single spikes in 10 tSts, which reliably initiate the swimming dynamics in all 100 simulations. All active neuronal types show similar voltage and spiking dynamics to the ones shown in Figure 5.10. Following tSp stimulation, swimming was reliably stopped in all 100 simulations. Similarly, experiments in immobilised tadpoles suggest that pressure of the skin can reliably be stopped stopping swimming (97% of tadpoles are stopped by application of head pressure; Perrins et al. [2002]).

Physiological experiments have shown that firing of single MHRs can reliably stop swimming (in 7 of 9 MHR tested; see Perrins et al. [2002]). We simulated these experiments using the VT model. Figure 5.11A and B show the activities of CPG and MHR neurons in two random simulations of the model. Top and bottom panels show voltage dynamics of selected cells and central panels the spiking activity of all the CPGs and MHRs in the network. In each simulation, we initiate the swimming dynamics by activating single spikes in 10 tSts. We apply the same stimulation protocol used to activate individual MHRs in experiments [Perrins et al., 2002]. We inject 5 equal current pulses to a randomly selected MHR starting 2 seconds after the stimulation tSts. The selected MHR fires two spikes in response to each pulse (amplitude 0.2nS lasting 30ms). In Figure 5.11A the activity of the selected MHR inhibits CPG neurons on left side (this neuron only forms ipsilateral connections), while in B the selected MHR inhibits

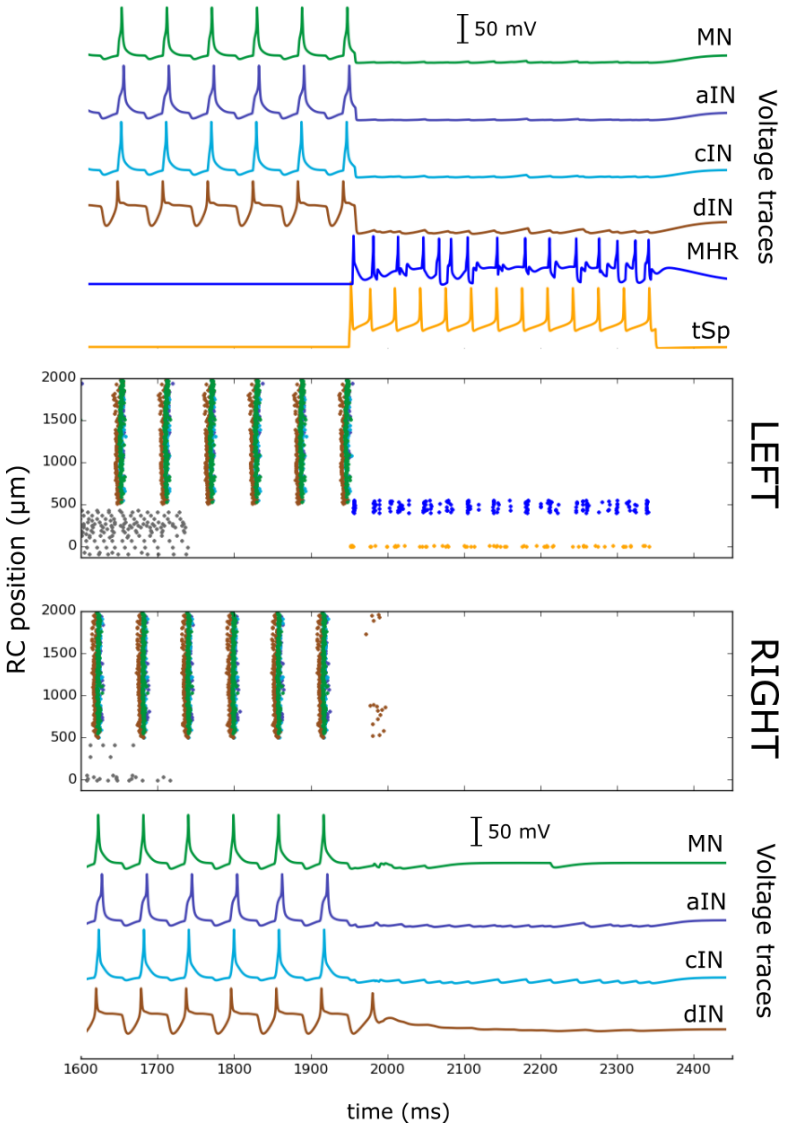

Figure 5.10: Simulation of the VT model mimicking the termination of swimming in response to head pressure stimulation. Panels are organised as in Figure 5.7. Top and bottom panels show the voltage activities of selected active neurons in response to head pressure. CPG neurons started by displaying swimming oscillations. 10 sensory tSp neurons were injected with step current and fired rhythmically to activate all ipsilateral MHRs, which inhibited CPG neurons and stopped swimming oscillations.

CPGs on both sides (neuron with both ipsilateral and contralateral connections). In the first case (A) the swimming dynamics continued after the inhibition, while in the second case (B) swimming is terminated. In case (A) some of the left CPG neurons fire additional spikes at half the cycle of swimming.

We repeat a total of 100 random simulations using the same stimulation protocol for the activation of single MHRs. In all these simulations the activities of the MHR and all CPG neurons is similar to the ones shown in Figure 5.10. Swimming was stopped in 62/100 simulations, and continued in the remaining 38/100 simulations. For the second set of simulations when swimming did not stop (38/100), CPG neurons on either side tended to fire additional spikes synchronously with those on the opposite side, during the period of stimulation. In simulations where swimming ends after MHR input (62/100), anti-phase activity in CPGs is not immediately interrupted after spiking of MHR neurons inhibition, but it can continue for up to 3 cycles after the last MHR spike. The termination or continuation of swimming cannot be determined based solely on whether the selected MHR forms only ipsilateral connections or both ipsi and contralateral connections. Swimming can stop or continue both if the activated MHR forms only ipsilateral connections to CPGs or if it forms both ipsilateral and contralateral connections to CPGs.

5.2.4.2 Spontaneous termination of swimming

When swimming is initiated in biological experiments, it normally starts with short cycle periods. The cycle period then increases to a stable plateau, before eventually slowing again before swimming stops [Dale and Roberts, 1984]. To mimic this phenomenon in the VT model we introduced a mechanism of synaptic depression into the NMDA recurrent connections amongst dINs. We use the same mechanism of synaptic depression as in hIN to hIN synapses, with a depression parameter $\alpha = 0.99$. Essentially, the strengths of each of these NMDA

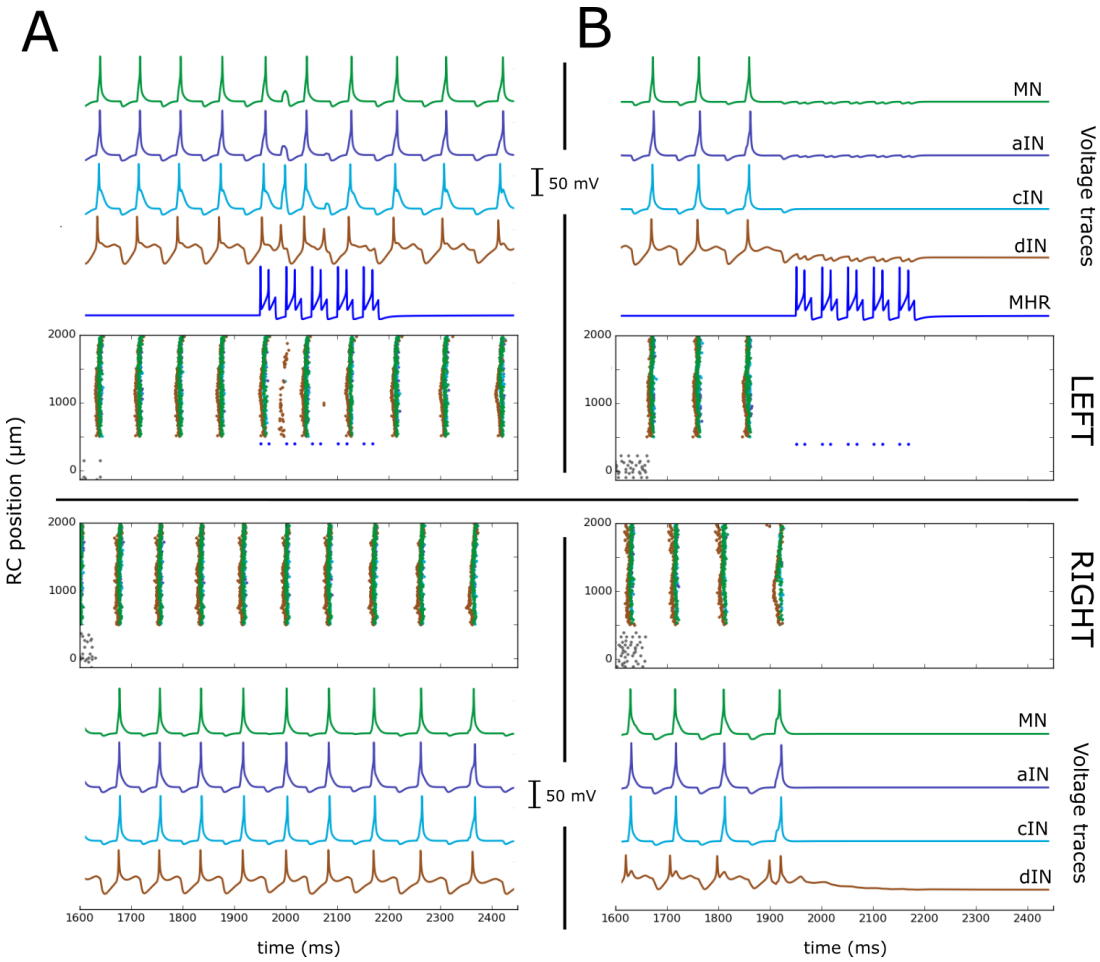

Figure 5.11: Activation of single MHR neurons can terminate swimming. In both A and B, panels are organised as in Figure 5.7. Top and bottom panels show the voltage activities of CPGs and the only active MHR. In both A and B, CPG neurons start by displaying swimming oscillations. We inject 5 equal current pulses to a randomly selected MHR starting 2 seconds after the stimulation of tSts which initiates swimming. The selected MHR fires two spikes in response to each pulse (amplitude 0.2nS lasting 30ms). In A firing of the MHR does not stop swimming oscillations. In B the firing of the MHR stops swimming oscillations.

synapses are multiplied by α after each pre-synaptic spike.

Figure 5.12 shows the last 800 ms of a 3.4 second simulation of the VT model which demonstrates the spontaneous termination of swimming CPG activity. The top and bottom panels of Figure 5.8 show the voltage dynamics of selected CPG neurons, and central panels show the spiking activity of all neurons. Swimming was initiated by stimulating 10 tSts at the start of the simulation. The simulation is then run for a long enough time to observe the swimming termination time. At the last cycle of right CPG firings, left dINs are inhibited by right cINs, but do not fire on rebound as in the previous cycles. Therefore, the failure of left dIN rebound spiking at approximately 3.2 seconds causes the end of the spiking in left CPGs. This stops the left cIN inhibition and PIR spiking in right dINs. Thus, the swimming episode stops at around 3.2 seconds. The period of swimming in the last few cycles increases significantly compared to the when swimming started, going from 50-60ms to about 100ms (compare Figures 5.7 with Figures 5.12), as in biological experiments [Li and Moult, 2012]. We will discuss the time course of the cycle period in during a full simulation of swimming in the next section.

In this case, as previously, we repeat 100 random simulations of the VT model with equal parameters and stimulation procedures. Each simulation is run for a long time to observe spontaneous swimming terminations. Swimming ended in all simulations, either on the left or right side, and stopping times ranged between 2.6 and 3.9 seconds. The activity of CPG neurons when swimming stopped was similar in all simulations to Figure 5.12. The termination of swimming always occurred in the same way, starting with missed rebound in dINs on one side and missed inhibition on the opposite side.

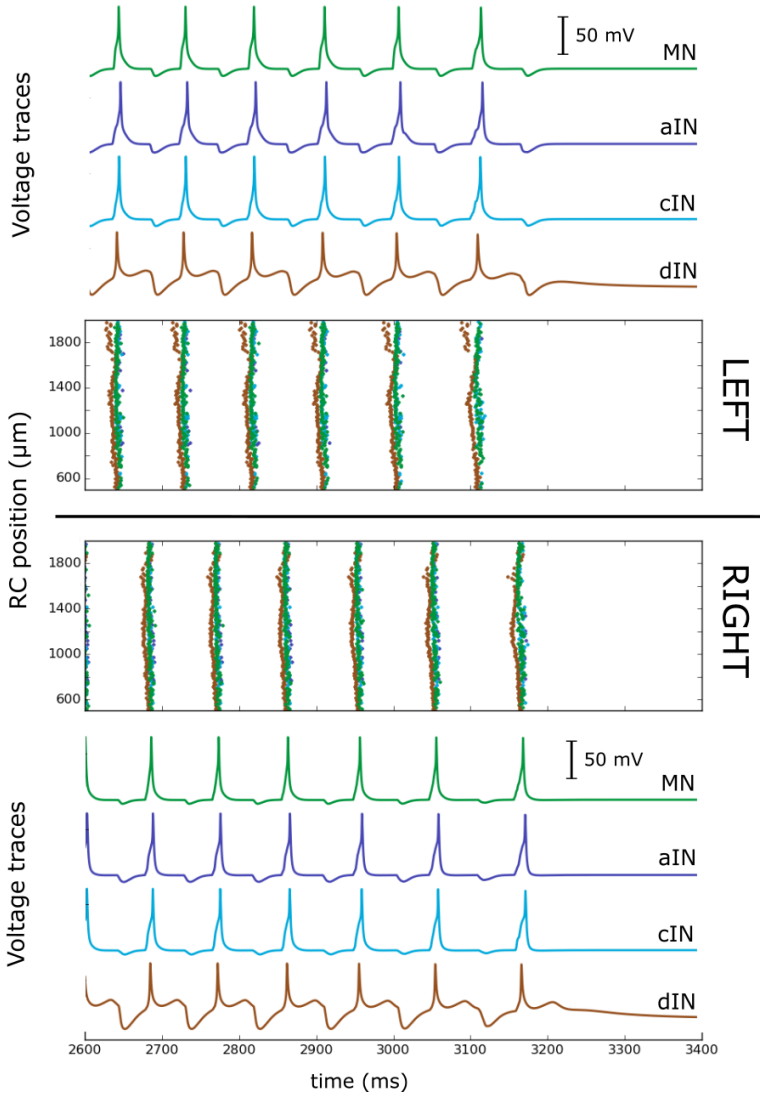

Figure 5.12: Spontaneous termination of swimming. Panels are organised as in Figure 5.7. Top and bottom panels show the voltage traces of one selected CPG neuron per type on the left and right side, respectively. All other neurons are inactive, and their voltages are omitted. In the last cycle of right CPG neuron firing, left dINs are inhibited by right cINs, but do not fire one rebound as in the previous cycles. Therefore, the termination of left dIN rebound spiking at approximately 3.1 seconds causes the end of the spiking in left CPGs and to the termination of swimming.

5.2.5 Simulating a tadpole's swimming behaviour and interactions with the external environment

In this section we present massive simulations of the VT model that aim to reproduce a biologically plausible, neuronal activity during a complete swimming episode of a tadpole that includes interactions between sensory pathways and the CPG populations. These simulations aim to reproduce a realistic sequence of events where a tadpole receives external inputs from multiple sources, internally represents and processes this information and modifies its behaviour accordingly.

We describe one hypothetical sequence of events that might be observed during the life of a tadpole. The sequence lasts for 8 seconds and the events are summarised in Table 5.4. We assume that the tadpole is motionless before time t=0 (rest state). At time t=0 the tadpole is touched on the left side of the trunk skin for a brief period of time (Event #1), the TS pathway becomes active and the animal starts to swim. At time t=2s the animal finds shade and attaches under a plant floating on the water surface. Pressure receptors in the cement gland become active in response to the pressure of the left side of the head against the plant for 0.4 seconds and activate the HP pathway. The signal from this pathway inhibits the CPG during the time interval [2,2.4]s (Event #2), stops swimming after 2.4 seconds and the tadpole returns to the rest state. At time t=2.5s the head of the animal is briefly touched on the left side, the HT pathway becomes active and the animal starts to swim for a second time (Event #3). The last event happens at time t=4.5s, when the tadpole skin is touched briefly on the right side (Event #4). The TS pathway becomes active and causes the acceleration of swimming for a limited time period. After this acceleration, swimming stops spontaneously.

Figure 5.13A shows a simulation of the sequence of events for the VT model.

Event #	Initial Time (s)	Final Time (s)	Stimulation Pathway (side)
1	0	0.005	Skin Touch (left)
2	2	2.4	Head Pressure (left)
3	2.5	2.505	Head Touch (left)
4	4.5	4.505	Skin Touch (right)

Table 5.4: Sequence of events

The top and bottom panels show the voltage dynamics of selected active neurons and central panels the spiking activity of all neurons. The top two panels and the bottom two panels show the activities of left and right neurons, respectively. Events in the sequence are shown by black arrows and are summarised in Table 5.4. Coloured horizontal bars under the voltages in the top and bottom panels show the duration of these events (colours mark the event type). Each event represents the signal from the external environment that modulates the dynamics of the neuronal populations in each sensory pathway. These populations then influence the activities of the CPG populations and, in the case of Events #1-2-3, lead to the initiation or termination of swimming. The dynamics of active neurons in each of these events is similar to those described in the previous sections. The intensities of stimulation of the TS and HT pathways are selected to be high enough to initiate swimming. In the case of Event #4 the stimulation of the TS pathway leads to the acceleration of swimming. A simple explanation for the shorter periods at the start of a swimming episode and during acceleration lies in the properties of hINs and dINs. When acceleration occurs, the hIN population is active and excites dINs during swimming. This excitation increases the voltage level of after-spike depolarisation in dINs [Li and Moult, 2012]. Due to this higher depolarisation and the intrinsic properties of dINs, PIR firing in dINs occurs at shorter times after the release of cIN inhibition than during periods when hINs are inactive. An experimental confirmation of this explanation comes from Li and Moult [2012]. This paper shows that injecting positive currents into dINs during swimming leads to the same results:

higher level of after-spike voltage depolarisation in dINs, faster PIR spiking in dINs and acceleration of swimming.

Figure 5.13B shows the swimming period versus time. Periods are calculated at the half of each swimming cycle as the median firing of left active mns. The values of these periods are within the physiological range measured in experiments [Roberts et al., 2014]. At the first start of swimming (Event #1) the period starts at ∼63ms, quickly decreases to ∼ 53ms during the first 300ms, and slowly increases. This is in line with experimental recordings [Sillar and Roberts, 1992, Li and Moult, 2012]. When the HP pathway is activated (Event #2), swimming stops (red rectangle). When swimming restarts via stimulation of the HT pathway (Event #3), the period of swimming follows the same temporal dynamics as at the previous start of swimming. When the right TS occurs (Event #4), the period quickly decreases (acceleration), and slowly increases until it reaches a value of ∼ 100ms and spontaneously stops.

5.3 Conclusions and discussion

The Virtual Tadpole model (VT) presented in this chapter is a biologically-realistic reconstruction of the tadpole swimming neuronal circuit that reproduces the activity of most of the active neurons during a swimming episode, from its start to its end. Thus, the VT model is the only spiking neuronal model that we know of that (1) accounts for the sensory initiation, modulation and termination of a whole animal's locomotor behaviour and (2) represents most of the functioning neurons in that animal.

To define the VT model we extended and improved previous biologically realistic anatomical and functional models [Roberts et al., 2014, Ferrario et al., 2018a]. These previous models aimed to reproduce the processes of swimming initiation in response to touching the trunk skin and rhythmic pattern generation [Roberts et al., 2014, Ferrario et al., 2018a]. However, recent experimental evidence

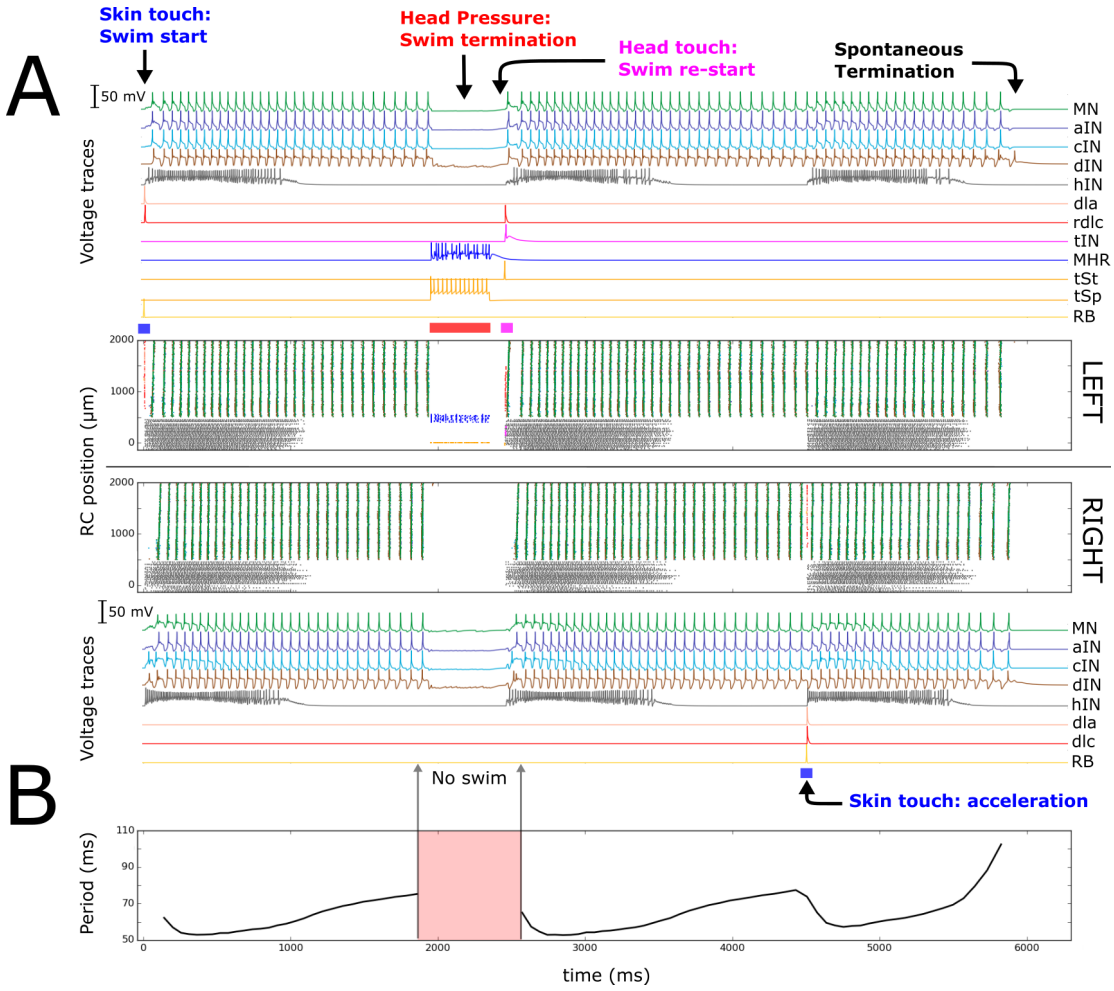

Figure 5.13: Sequence of events of multi-sensory pathways. A. Panels in this subfigure are organised as in Figure 5.7, except for showing the voltage traces of one neuron of each type, provided that at least one neuron in that type fires at least once during the simulation time. B. Swimming period vs time.

suggested that the initiation process described in these models was oversimplified in at least two ways. Firstly, the synaptic strengths of the sensory pathway neurons to the CPG neurons were adjusted to start the swimming oscillations. However, recent evidence suggests that these synapses are only weak, if they even exist [Koutsikou et al., 2018, Buhl et al., 2015]. Secondly, these models cannot predict the long and variable delays to the first firing of dINs and of first motor responses [Koutsikou et al., 2018].

In addition to that, the VT model also extends these previous models by incorporating two other sensory pathways which can initiate and terminate swimming in response to head touch and pressure, respectively. Simulations of VT model can now explain the processes beyond the initiation and termination of swimming in response to the stimulation of each of these three pathways. Moreover, it predicts the acceleration of ongoing swimming when the skin is stimulated [Sillar and Roberts, 1988]. By including a mechanism of synaptic depression between the dINs in the VT model that can also reproduce the slowing down and spontaneous termination of swimming [Dale and Gilday, 1996].

To define the properties of the connections in the VT model we incorporate significant anatomical data collected in experiments. In some cases we prescribed connections using our probabilistic model [Ferrario et al., 2018a] and by taking into account the available experimental data. In particular, we use the morphological similarities between the neurons with known connections and neurons with unknown connectivity. Using these similarities we consider the known probabilities and use a generalisation procedure to generate the probabilities for new cell type connections which have similar properties to the known ones, based on the anatomical and functional properties of these cell types. For example, since both tINs and dlas have similar anatomical and functional properties, unknown connection probabilities from tINs are generalised from known connection probabilities from dlas. As a result, the total number of generated synaptic

connections in the VT model is about 100,000.

Model equations and parameters have been selected to either match available experimental data [Buhl et al., 2012, 2015, Koutsikou et al., 2018, Perrins et al., 2002] or to obtain physiologically plausible initiation/termination of the swimming dynamics. As a result of this, the VT model imitates a chain of information processing of external signals to sensors, through a sensory pathway, decision making and execution of action by generating physiological patterns of neuronal activities.

The model of the swimming decision making process is based on physiological evidence and on our previous simplified model [Koutsikou et al., 2018]. Activation of model hINs generated a pattern of sustained activity which was highly variable due to the random distribution of connection strengths between these neurons. This type of variable and sustained activity is what was expected from the experimental evidence and is similar to processes of decision-making [Kristan, 2008, Surmeier, 2013]. The VT model includes populations of hIN neurons on both sides of the body and we found that commissural connections between these neurons are important to ensure that the start of swimming is properly coordinated. The inclusion of hINs in the model can explain why the response to trunk skin stimulation have such long and variable delays [Koutsikou et al., 2018].

The model of connectivity includes several random elements that mimic the variability of the connectivities of multiple tadpole individuals. Due to this randomness, repeated simulations of the model produce different pattern of activities and lead to variable behaviours. For example, first motor responses and swimming stopping times of in VT model simulations vary in the ranges of $\sim$ 20-200 ms and $\sim$ 2.6 and 4 seconds, which correspond to the ranges observed in the real animals [Koutsikou et al., 2018, Buhl et al., 2015, Dale and Roberts, 1984,

Li et al., 2006]. This means that the VT model has complex and unpredictable behaviour, like a real tadpole, and it shows that the randomness included in the model can explain some aspects of the variability in the animal behaviour.

We demonstrated how stimulation can initiate or stop swimming by showing that model simulations produce spiking patterns similar to the experimental recordings in all three sensory pathways. When modelling the response to TS stimuli, the large majority of random simulations of the VT model reproduce the initiation of swimming antiphase spiking activity in left and right CPG neurons (swimming oscillations).

Our simulation results suggest that commissural inhibition from cINs is important for a coordinated start of the first swimming cycle. This inhibition makes sure that the firing between left and right CPG neurons occurs at a time interval of approximately half a cycle of swimming.

We have shown that stimulation of the TS pathway can lead to two other activity patterns. In the first, left and right CPG neurons start to fire in-phase oscillations (synchrony oscillations), favouring the coactivation of antagonist muscles. In the second, the firing of CPG neurons on one side is not followed by the spiking of CPGs on the opposite side (one-sided CPG firing). Synchrony oscillations and one-sided CPG firing have been observed also in experiments [Li et al., 2014a, Roberts et al., 1985]. These experiments and in random simulations of the VT model have confirmed that these two activity patterns occur only seldomly. For this reason we believe that they are pathological activities that the circuit is structured to avoid. Thus, some of the parameters in the VT model were appropriately selected to reduce the number of simulations producing these activities.

This calibration of the model revealed some of the critical features of the VT model which can help to prevent these pathological activities. Specifically, we

found that higher numbers of commissural connections between hINs help to minimise the number of random simulations producing one-sided CPG firing. Thanks to these connections hINs on both sides fire at similar rates and deliver a similar excitatory input to both left and right CPG neurons, which typically lead to the firing of CPG neurons on both sides. However, including too many of these contralateral hIN connections increases the number of random simulations producing left-right synchronous oscillations of CPG neurons. We therefore selected an intermediate number of these connections, which was suggested by anatomical data of neurons analogous to the hINs. In particular, each hIN in the model has 30 % chance to form the same average number of connections to contralateral hINs as it has for ipsilateral ones. Remarkably, using this paramter value pathological synchronous or one-sided CPG firings happen only rarely (3/100 simulations of the TS pathway). Another important parameter that acts to reduce the production of synchrony oscillations is the strength of contralateral inhibition. In fact, repeated simulations of the VT model with reduced cIN inhibitory strengths showed that episodes of synchronous CPG activity occur more frequently.

Finally, we suggest that future model development should include several important details which have not been considered in the current VT model:

1. The pineal eye sensory pathway should be included. This pathway provides information about light dimming and it leads to the initiation and acceleration of swimming [Jamieson and Roberts, 2000].

2. The spontaneous initiation of swimming is an interesting feature of tadpole behaviour [Roberts et al., 2010]. Swimming tadpoles can spontaneously stop and sink to the ground to stay at rest for some time, after which they spontaneously starts swimming without any apparent external stimulation.

3. It is known [Kahn and Roberts, 1982c, Soffe, 1993, Li et al., 2007b] that

the repertoire of tadpole behaviours includes both swimming and struggling. During struggling (or escaping behaviour) the tadpole body moves backward with a higher amplitude and lower frequency in comparison with swimming.

4. Previous works suggested that the slow-down and termination of swimming are mediated by purinergic transmitters ATP and adenoside released during swimming by changing the excitability of spinal neurons by inhibiting K^+ and Ca currents, respectively [Dale and Gilday, 1996, Dale, 2003, 2002, 1998]. In the VT model, this rhythmic modulation is caused by the depression of NMDA synapses in the dIN population. Similar to the effect of adenosine, this mechanism causes a decrease in neuronal excitability and leads to the slow-down and termination of swimming. Since neuronal models incorporating the effect of ATP and adenosine in tadpoles have been previously developed [Dale, 2002], these could be incorporated in the VT model. This modulation could then be compared with our current results obtained by NMDA synaptic depression and with experiments.

Chapter 6

An Action Selection Mechanism based on Partial Synchronization in a Spiking Model of the Basal Ganglia

In this chapter we investigate a plausible role of oscillations and synchronisation for the action selection problem using a spiking model of the basal ganglia. The model includes neurons in the sub-thalamic nucleus (STN), globus pallidus indirect pathway (GPi) and an oscillatory forcing input that mimics the cortical contribution to the circuit. The model assumes that the activation of a set of GPi units corresponds to a specific motor action. Simulations of the model show that the cortical input can entrain STNs into complex regions of phase-locking synchronisation, called "Arnold tongues". This synchronisation and a winner-take-all mechanism enables the cortical input to activate a selective group of GPi neurons. Multiple changes in the frequency and amplitude of this input activate different sets of GPi units, enabling the switching between different motor programs. The model suggests that the strength and decay time of synapses from STNs to GPis are important for regulating the times of switching. A proper adjustment of these parameters allows switching these times to be in the physiological range.

In chapter 2 we reviewed some of the existing evidence on the structure and function of the basal ganglia. In this review, we highlighted that the basal ganglia (BG) are a group of subcortical nuclei thought to play an important role in the control of movements and action selection. Additionally, we provided evidence suggesting that the BG is organised into multiple oscillatory parallel "channels", with each channel corresponding to actions and/or body regions and/or specific muscles. For instance, a previous model of the basal ganglia [Merrison-Hort et al., 2013] suggested that both physiological and Parkinsonian oscillations can

be generated if we consider this hypothetical organisation.

In this chapter we consider this hypothesis and we investigate a plausible mechanism of action selection in a spiking neuronal model of the BG. We consider a simplified neuronal circuit, consisting of Izhikevich neurons in the subthalamic nucleus (STN) and in the internal segment of the globus pallidus (GPi). Oscillatory input, assumed to originate in the cortex, entrains subsets of STN neurons via partial synchronization. Excitatory connections from the STN to the GPi and inhibitory connections within the GPi allow this input to "select" groups of active GPi neurons. We assumed that each of these groups corresponds to one parallel channel, and thus to a specific motor program.

In order to study the entrainment of the STNs, we distribute amplitudes and frequencies of the cortical input and we show that a complex structure of phase-locking regions of Arnold tongue bifurcations exists on the plane of these parameters. This revealed how many different groups of STN neurons could be entrained for a given input strength. Moreover, it shows that, at increasing amplitudes, STN neurons with intrinsic frequencies lower than the input can synchronise to the input at ratios other than 1:1 locking. This corresponds to the activation of different sets of GPi neurons (or "channels"). Moreover, this suggests that input amplitude cannot be too high if a one-to-one mapping between frequencies and selected channels is required. By considering cases with multiple forcing frequencies, we showed that more complex scenarios are possible.

We model the switches between different actions by changing the amplitude and frequency of the cortical input. These changes mimic the cortical encoding of stimuli coming from the the external environment. By simulating action switching in the model, we found that the strength and time constant of the STN-GPi synapses changes on the action switching time. After repeated trials we found that a proper set of these synaptic parameters can lead to physiologically plau-

sible switching times. Conversely, if these parameters are much higher than these values, all GPi units become active and it becomes impossible to distinguish which action is selected. This condition may correspond to the motor impairments in Parkinson's disease.

6.1 Methods

6.1.1 Neuronal models

We model all neurons using a simple Izhikevich spiking model with parameter values describing class 1 excitabile cells [Izhikevich, 2003]. This model is computationally tractable yet still reproduces two important features of basal ganglia neurons: excitability and spiking behaviour.

The circuit model consists of two populations of neurons representing the STN and GPi, containing $N_s = 200$ and $N_g = 25$ neurons, respectively. Each unit is modelled according to the two dimensional Izhikevich model, where the equations governing the dynamics of neuron i are:

$$V_i' = 0.04 \cdot V_i^2 + 5V_i + 140 - u_i + I_i + I_{ext} + I_{syn} + \nu_i$$
$$u_i' = a(bV_i - u_i)$$
$$if \quad V_i > 30 : V_i \leftarrow c; u_i \leftarrow u_i d$$

We used standard values for all the parameters ($a = 0.02$, $b = 0.2$, $c = 65$, $d = 6$), which correspond to neurons that are normally quiescent and have a class 1 excitability according to Izhikevich's classification. The term I_i corresponds to a constant external current that is different for each neuron and has the effect of giving each neuron a different intrinsic spiking frequency. The term I_{ext}, which is defined more fully below, is the oscillatory cortical input, which is identical for each neuron in the population. The term I_{syn} represents the sum of all the synaptic currents flowing in neuron i. Finally, ν_i is a Brownian input of white

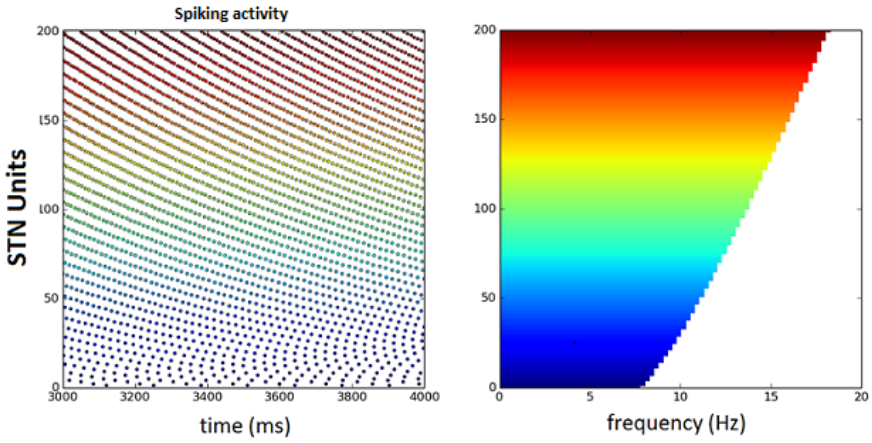

Figure 6.1: STN spiking activity without external input. Left: Raster plot showing each neuron's spike train. Right: The intrinsic spiking frequency of each STN neuron.

noise. Initially we set $\nu_i = 0$ to consider the simpler deterministic case as this makes it easier to determine the different partial synchronisation regimes, but we later added noise to obtain more realistic results.

In the model, we choose values of I_i for the STN population uniformly, from the range 4 to 7, so that without external input the STN units all spike independently, with a linear range of frequencies from 7-18Hz. A similar range of frequencies are observed in pacemaker STN neurons recorded in monkeys [Bergman et al., 1994]. We consider STN neurons arranged on a line, with the injected current I_i (and therefore frequency of spiking) varying monotonically along the line (y-axis of Figure 6.1). For GPi neurons we set $I_i = 0$, so that the neurons in the GPi do not intrinsically spike. Figure 6.1 shows the intrinsic spiking activity of the STN population.

In order to simulate oscillatory cortical input to the STN we apply an identical external current comprising multiple frequency components to all STN neurons:

$$I_{ext} = \sum_j a_j sin(2\pi\omega_j t)$$

Where a_j and ω_j are the amplitude and frequency of oscillatory component j,

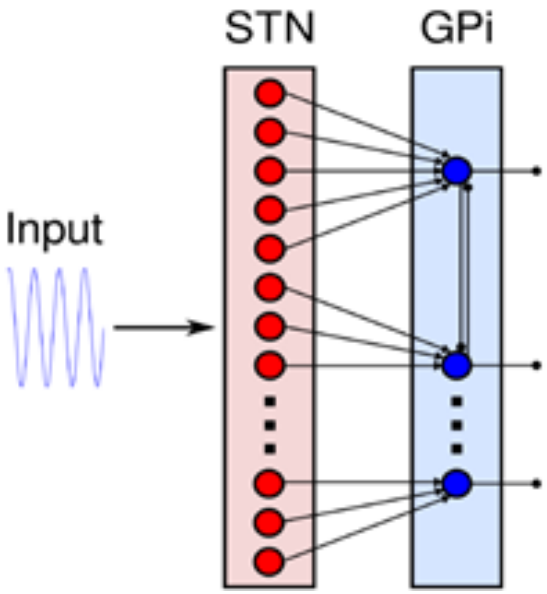

Figure 6.2: Overview of the populations in the model and their connections.

respectively. For the GPi neurons we set $I_{ext} = 0$.

6.1.2 Synaptic transmission

Each STN neuron makes an excitatory synapse onto one GPi neuron in a uniform manner, such that each GPi neuron receives $N_s/N_g = 8$ synapses. Like in the STN, we also consider the GPi units to be arranged on a line, with the STN→GPi projection organised in a topographical fashion, such that each GPi neuron receives input from a group of STN neurons that are adjacent to each other (and therefore have similar intrinsic spiking frequencies). Additionally, since there is biological evidence for inhibitory synaptic connections between nearby neurons in the globus pallidus [Terman et al., 2002], model GPi neurons are coupled via inhibitory connections from their $N_{gg} = 4$ neighbouring neurons on each side (Figure 6.2). The mutual inhibition amongst the GPi establishes a regime of competition.

For both excitatory and inhibitory connections we used standard exponential chemical synapses. The total synaptic current flowing at each time t in neuron

i is given by:

$$I_{syn}(t) = I_E + I_I = g_E(t)(E_{rev} - V_i(t)) - g_I(I_{rev} - V_i(t))$$

Where $E_{rev} = 0mV$ and $I_{rev} = -80mV$ are the reversal potentials, and determine if the synapse is inhibitory (I) or excitatory (E). We initially set $g_E = g_I = 0nS$ to study the behaviour of the STN population in response to cortical input. If two cells are connected through a synapse of type x (where x is E or I), the postsynaptic response in neuron j in correspondence of each presynaptic action potential rises by an increment of the conductance $g_x \leftarrow g_x + w_x$, where w_x is a parameter. The synaptic conductance follows an exponential decay determined by equation:

$$g'_x = -g_x/\tau_x$$

Here τ_x is the decay time of each synapse $x \in \{E, I\}$. Each STN neuron i can form excitatory synapses onto the output GPi units. We scaled the excitatory impact of STN units according to their intrinsic frequency using the following procedure. For each $x \in \{E, I\}$ we fixed the maximal weight w_x^1 and decay time τ_x^1 representing the highest frequency STN unit and we scaled these values down uniformly with decreasing frequency, reaching minimum weight $w_x^2 = w_x^1 - 0.15nS$ and decay time $\tau_x^2 = \tau_x^1 - 0.015$ for the lowest frequency STN unit.

For the moment we do not specify the values of w_x and τ_x because we will discuss them later in more detail, and show that they play a very important role in the switching time between selected actions.

6.1.3 Phase-locking synchronisation

In this section, we review principles of synchronisation of non-linear oscillators which are important for understanding the results presented in this chapter.

It is well known that single neurons can generate oscillatory activity. Current be-

lief is that, when many of these neurons interact, their oscillatory activities can synchronise and cause entire brain regions to oscillate at different frequencies [Buzsáki and Draguhn, 2004]. For example, [Timmermann and Florin, 2012] showed that excessive β oscillations recorded in entire regions of the basal ganglia are associated with synchronisation at the neuronal level.

One of the simplest cases of synchronisation in oscillatory regimes can be observed in a self-sustained oscillator driven by an external force. Such mechanisms can describe many biological phenomena that can be observed in nature, such as synchronisation of clocks that govern the circadian rhythm [Pikovsky et al., 2003] or simultaneous flashing of fireflies [Strogatz, 2018]. Assuming the frequency of forcing is close enough to the oscillator's intrinsic frequency, the steady state solution of a periodically-forced oscillator is synchronous with the periodic input. Under this condition the phase difference of the two oscillators approaches a constant value - this is a stable fixed point of the system. In dynamical system theory the oscillator in this state is called phase-locked, because its frequency is locked to the forcing frequency.

We can extend the concept of phase-locking to two neurons coupled by single or multiple synapses. It is important to note that phase-locking does not necessarily mean that the two cells are firing at the same time, but rather they may fire with some constant delay between spikes. However, when a subset of spiking neurons in a population have similar phases and are phase-locked to the same periodic force they will fire in unison. We will call such behaviour partial synchronisation.

Synchronisation in a periodically forced oscillator may also appear at other frequencies besides the one close to the driving frequency. In fact, we can generalise the concept of phase-locking when the ratio between the period of the force and the period of the oscillator is a rational number. We will say that a

forced oscillator with period T is $p:q$ - phase-locked to the force with period T_f if $pT \approx qT_f$ where p and q are positive integers. If the period of forcing (T_f) is kept constant, then two parameters affect the ability of an oscillator to phase-lock: the strength of the forcing input (k) and the oscillator's intrinsic period of oscillation (T_i). For each pair p, q we may thus calculate the region in the (k, T) parameter space of where $p:q$ - phase-locking occurs; these regions are called Arnold tongues.

Phase locking can appear also in maps that act as non-forced oscillators. Let us consider a simple clarifying example: the circle-map. In dynamical systems a map is defined as an equation with discrete times, and it can be represented through an evolving sequence $\theta = \{\theta_n\}_{n=1}^{\infty}$. The circle map is a particular sequence θ that solves:

$$\theta_{n+1} = \theta_n + \Omega - \frac{K}{2\pi} sin(2\pi\theta_n) \quad mod \quad 1$$

Starting from a fixed initial value θ_0, mod is the standard modulo operator, Ω and k are system parameters. The sequence θ represents the angle variation over a circle. We define rotational number:

$$r = \lim_{n\to\infty} \frac{\sum_{i=1}^{n}}{n}$$

Thus $p:q$ - phase-locked Arnold tongues are defined as a region in the space of parameters where there the system solution has is locally constant rotational number $r = p/q$. In Figure 6.3 the different coloured regions indicate the different rotational numbers obtained by varying $(\Omega, K) \in [0,1] \times [0, 2\pi]$ are shown. Some values of the rotational number in Figure 6.3 are rational, and eventually are surrounded by other equal values of r, in this case, they will form an Arnold tongue region in the parameter space.

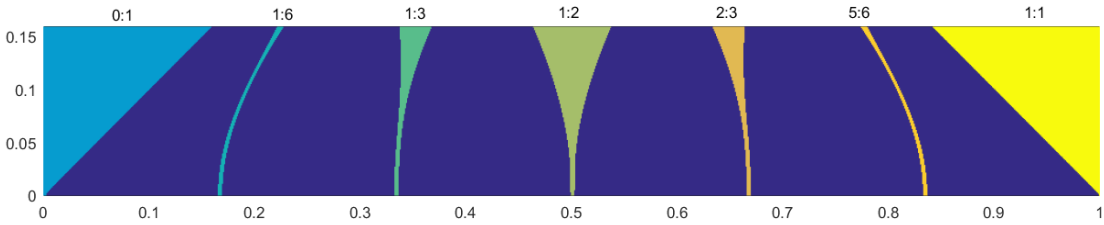

Figure 6.3: Coloured plot of the rotational number r for circle map at varying Ω in $[0, 1]$ (x-axis) and K in $[0, 1/2\pi]$ (y-axis). Not every value of r corresponds to a rational number, and thus to an Arnold's tongue.

6.1.4 Software

Simulations of unconnected periodically forced Izhikevich oscillators were performed in MATLAB (MathWorks, Inc), while simulations of connected neural networks were developed in NEURON [Carnevale and Hines, 2006] interfaced with Python [Hines et al., 2009].

6.2 Results

6.2.1 Single forcing frequency on STNs

We first studied the effects of a cortical input with a single sinusoidal oscillatory component $I_{ext} = a_0 sin(2\pi\omega_0 t)$ on the STN population under a deterministic regime. With this forcing input applied to each of the STN neural oscillators, the system produces regions of partial synchronisation with a set of p:q-phase-locked regions for any fixed input frequency. Each STN neuron remains an oscillator under forcing but its period of oscillation may be different to its intrinsic period. When the period of oscillation of an STN neuron is such that it completes p cycles for every q cycles of the forcing signal, we describe that neuron as being p:q phase-locked. In Figure 6.4 (left panel) we show three phase-locked regions found with fixed $w = 16.5$ and $a_0 = 1$. Figure 6.4 (right panels) shows plots against time and phase portraits from STN neurons in the different phase-locked regions.

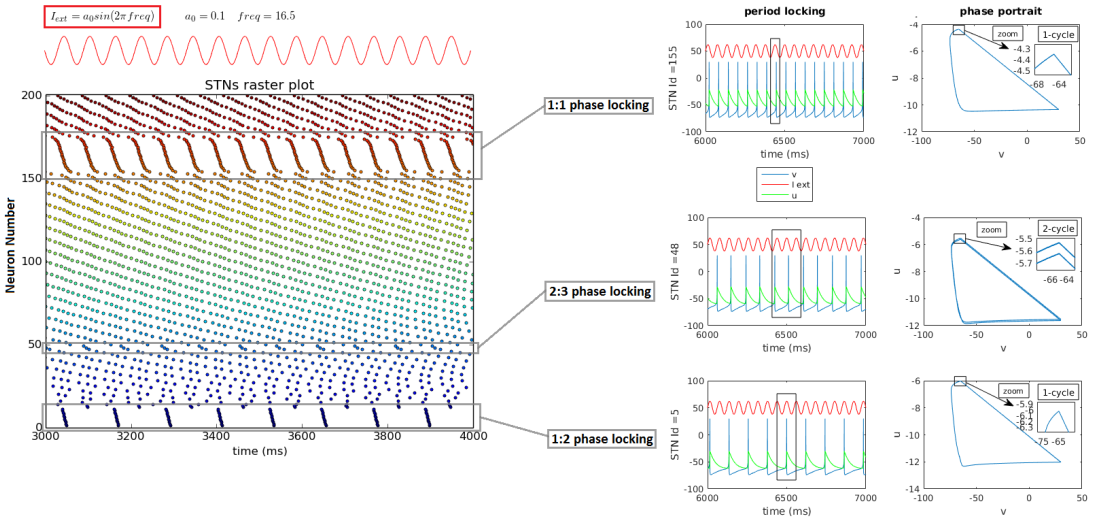

Figure 6.4: (Left panel) Activity in STNs using a single sinusoidal input with parameters $\omega = 16.5$ and $A = 0.1$. Three regions of partial synchronisation appear, corresponding to different p and q values. (Right panels) A member of each locked region is represented with the plot of u, v, and I_{ext}. In order to make u and I_{ext} visible in the plot they were multiplied by values 5 and 120, respectively. A small rectangle shows the period of q input oscillations and the number of p spikes in such period. The phase portrait of the two solutions u and v shows the correspondence between the number of p-cycles and the value p in the phase-locking.

6.2.2 Arnold tongues on STNs

Arnold tongues illustrate the multiple synchronisations found in STN cells depending on their intrinsic frequencies. The Arnold tongue diagrams in Figure 6.5 help us to visualise the different areas of partial synchronisation obtained for three different external frequencies in STN neurons at varying external amplitude.

Each coloured region in Figure 6.5 corresponds to a partial synchronisation region, showing that a single frequency cortical input can synchronise multiple groups of STN neurons depending on their intrinsic frequencies. Increasing the input oscillation amplitude expands each 1:1 phase-locked region (orange colour), squeezing together the other p:q locked regions. Changing the forcing frequency shifts the phase-locked regions up and down, whilst largely pre-

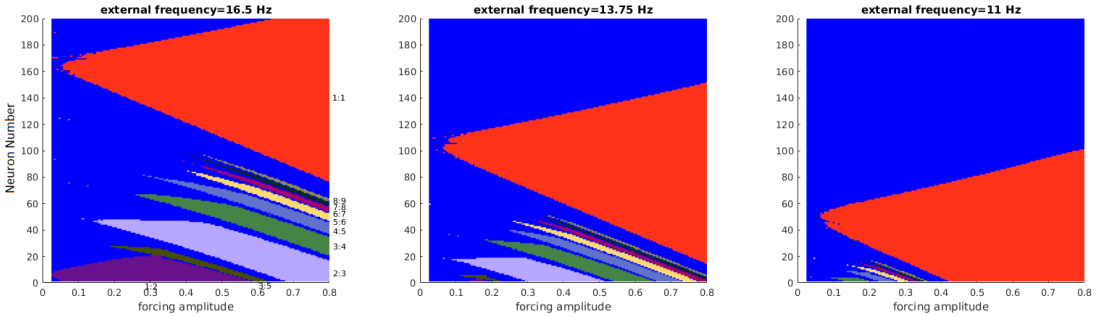

Figure 6.5: Phase-locked regions of Arnold tongues. Each colour represents a single p:q pair for three different values of external frequencies: 16.5Hz,13.75Hz and 11Hz from left to right. The horizontal axis shows the strength of external forcing and the vertical axis shows the STN number (arranged in order of increasing intrinsic frequencies). The biggest coloured region (orange) of partial synchronisation corresponds to 1:1 locking. From the plot with external frequency of 11Hz we notice that no Arnold tongues are present above the 1:1 locking region. Decreasing the external frequency does not change the area of the 1:1 region, but shifts the synchronised regions downwards while slightly squeezing together the other phase locked regions.

serving the total area of each region. Arnold tongues provide a useful tool for determining the correct parameters to obtain a desired number of synchronised cells. The Arnold tongues suggest that neurons with intrinsic frequencies above that of the forcing input cannot become synchronised, and this appears to be a universal property.

For example, Figure 6.6 shows a simulation with a large number of neurons that have intrinsic frequencies above that of the input, yet none of these neurons become synchronised. As we will explain shortly, this feature is no longer true when the forcing input contains multiple frequency components. In this simulation, we consider 2000 STNs with white noise component $\nu_i \sim N(0, \sigma^2)$, where N represents a Brownian random variable. We choose the value of σ ranging from 0.002 to 0.01, such that lower-frequency neurons receive weaker noise than higher frequency ones.

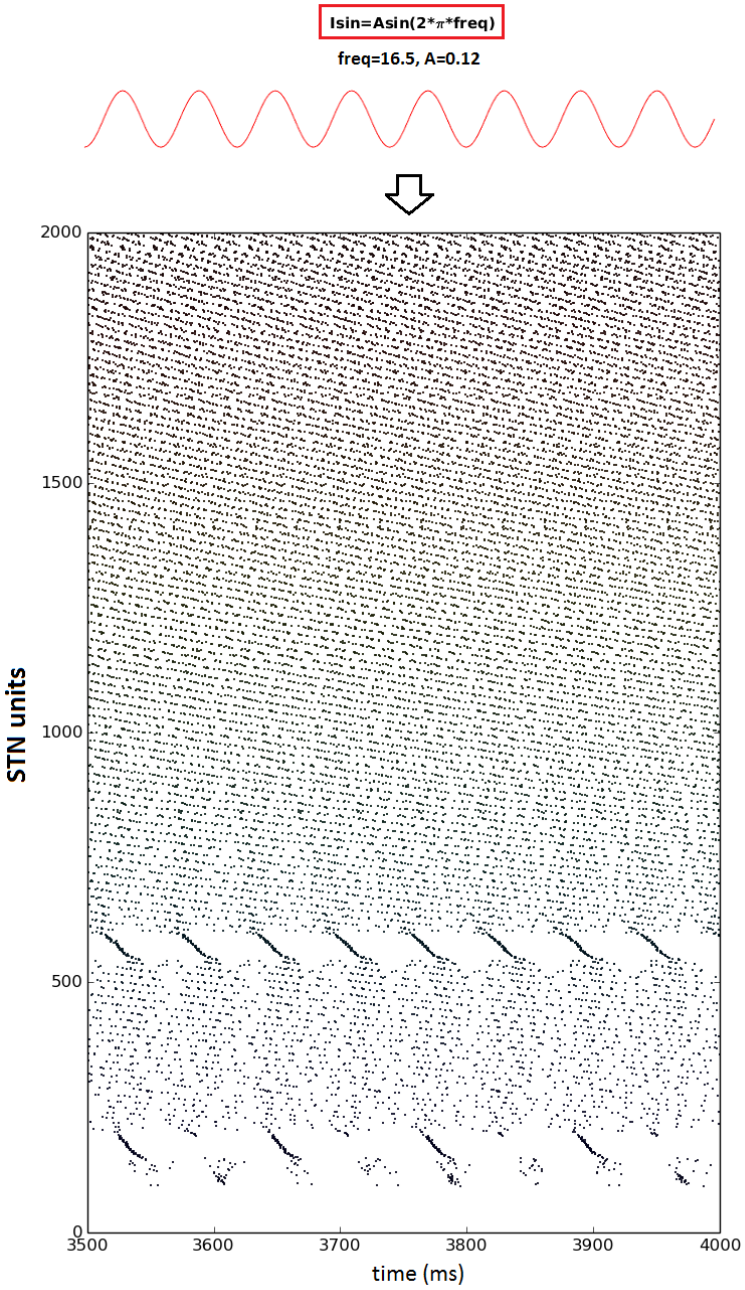

Figure 6.6: Raster plot of 2000 STN units forced by a 16.5Hz single-frequency sinusoidal force with $a_0 = 0.12$. The STN have frequencies ranging from 0Hz (bottom) to 40Hz (top). White noise component ν_i was added in these units as described in the text. No phase locked units appear in cells with a frequency above 16.5Hz. This important property is not maintained when we have inputs with multiple frequency components.

6.2.3 The selection of action via GPi output channels

The phenomena of partial synchronisation may lead to the selection of different channels via activation of GPi units. To make GPi units active in the network, we define non-zero weights for the excitatory and inhibitory connections. We chose maximum weights $w_I^1 = -2$, $w_E^1 = 1.2$ and decay times $\tau_I^i = \tau_E^i = 0.1$. We also added the white noise component $\nu_i \sim N(0, \sigma^2)$ as discussed in the previous section.

In our model, actions are selected via activation of groups of GPi neurons, which we assume belong to different "channels" of information flow through the basal ganglia. Figure 6.7 shows the spiking activity of the same network of STN and GPi neurons in response to a single-frequency (16.5Hz) oscillatory input of varying amplitude. When the amplitude is low (bottom panel), two small groups of partially synchronised STN neurons appear via 1:1 and 1:2 phase-locking, and their synchronised firing activates two groups of GPi neurons. GPi neurons with above-average firing rates are considered "activated", and are indicated by the solid black bar on the far right of the figure. However, at higher amplitudes a single-frequency oscillatory input can give rise to other selected channels' combinations, as shown in Figure 6.7 (top panel). This follows from the result of the Arnold tongue diagrams shown in Figure 6.5, as these showed that multiple phase-locked groups of STN neurons can appear for a single oscillatory input if the input amplitude is big enough.

6.2.4 Arnold tongues via two forcing frequencies

We now consider external inputs that contain multiple frequency components. Figure 6.8 shows how an input containing two, three or four frequency components can select groups of GPi neurons. The strength of the oscillatory input in Figure 6.8 was chosen such that in each case, the selected neurons in the GPi are activated by groups of STN neurons that are in 1:1 phase-locked syn-

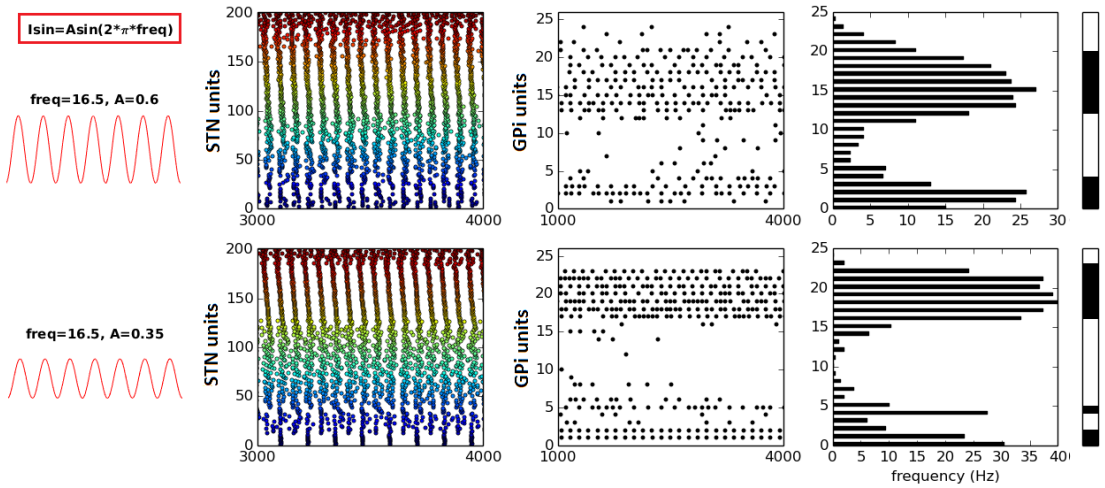

Figure 6.7: A single-frequency (16.5Hz in this case) oscillatory input can give rise to multiple synchronisation regions, in agreement with the Arnold tongues. The bars on the far right of the figure show which GPi neurons are considered selected, which is defined as those that have an above-average firing rate. An input amplitude of 0.6 selects only two clear output channels despite the high number of different p:q phase-locked regions in the Arnold tongue diagram (Figure 6.5), while an amplitude of 0.35 selects three channels. Unsurprisingly, the size of the channels (number of GPi neurons recruited) increases with the amplitude of forcing.

chronisation. The ability to select multiple combinations of output channels in response to mixed-frequency input may be the basis of action selection in the basal ganglia.

Arnold tongues are determined using a deterministic regime, but they can still give us an idea of how many different channels may be open in a stochastic approach and predict the amplitude required for synchronising a desired amount of cells. A small amount of white noise preserves the mean number of partially synchronised cells identified by the tongues. If this number is sufficiently high, the STN excitatory strength will activate a single channel in the GPi neurons.

As in the single frequency case, regions of partially synchronised STN units in phase locked regimes other than 1:1 can cause additional channels to be selected. To investigate this, we calculated Arnold tongue diagrams for the case with multiple forcing frequency components. Figure 6.9 shows Arnold tongues

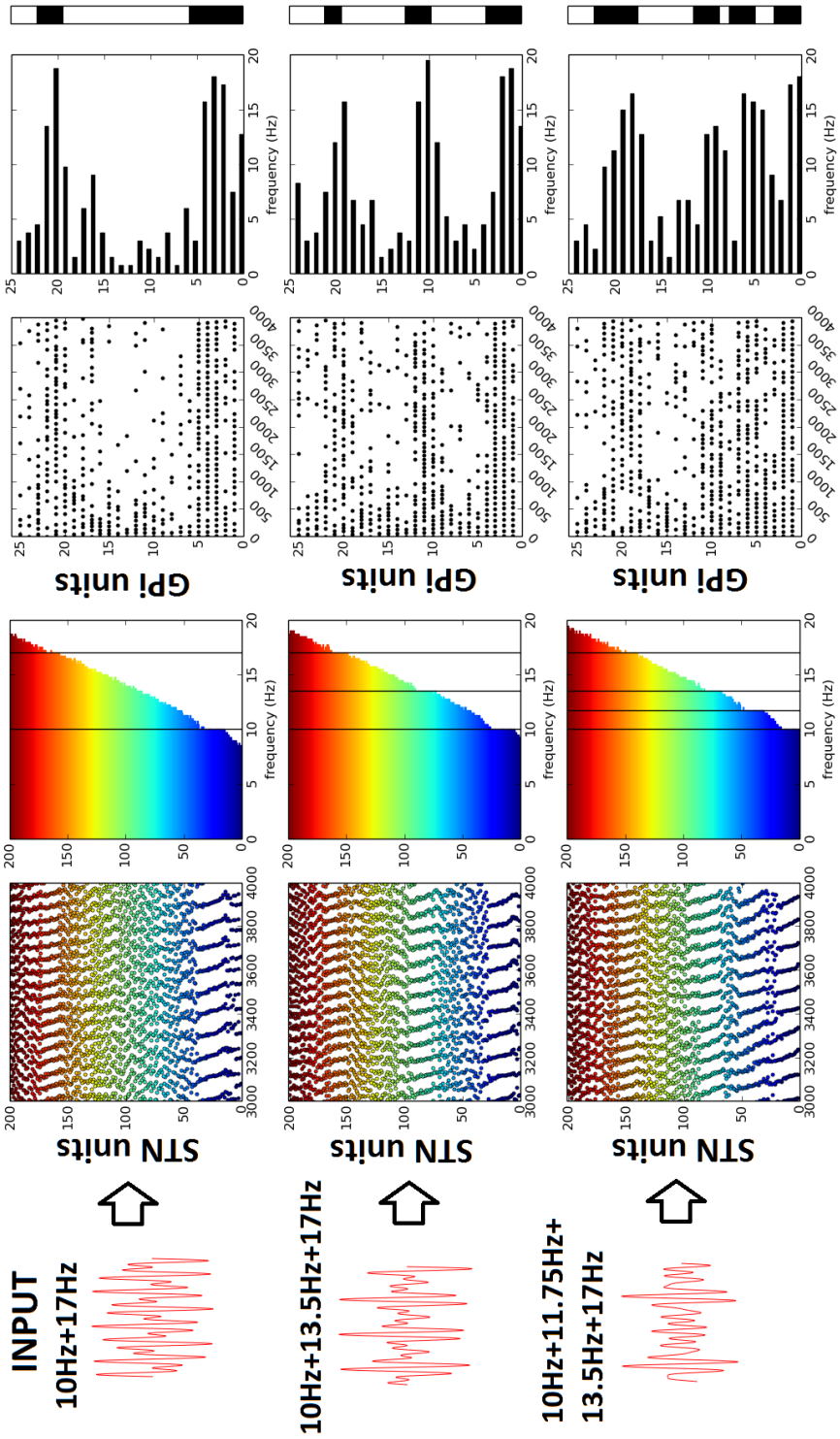

Figure 6.8: A single forcing input with multiple frequency components having amplitude of 0.12 activates multiple GPi "channels" via partial synchronisation. This figure shows, from top to bottom, the activation of two, three or four output channels by an oscillatory input containing two, three or four frequency components. The number of active channels is in one to one correspondence with the number of forcing frequencies.

for an external input that has two frequency components: 16.5Hz and 13.75Hz. In this figure there are 400 STN units with intrinsic firing rates from 0 to 40Hz. Arnold tongues were computed according to the definition of p:q - phase locking, considering the two input periods separately to produce two diagrams. The shapes of the Arnold tongues in Figure 6.9 are the same for the two frequencies, since each neuron is forced by both frequency inputs, thus its period is a multiple of both the two-forcing periods. However, the values of p and q for any given region differ between the two plots. For example, the biggest region of partial synchronisation (green on the left, dark blue on the right) corresponds to 1:1 phase-locking for the 16.5Hz component of the input and to 6:5 phase-locking for the 13.75Hz component 13.75. The second biggest region (cyan on the left, sea green on the right) corresponds to 1:1 phase-locking for the 13.75Hz component and 5:6 phase-locking for the 16.5Hz component.

The two main regions of partial synchronisation thus correspond to 1:1 phase-locking in the case of two forcing frequencies, which is similar to the results in Figure 6.5. However, these regions have a decreased area compared to the single-frequency case and they squeeze together, forming more tongues between them. Also, in contrast to the single-frequency component case, other Arnold tongues appear for intrinsic frequencies higher than the biggest phase-locked regions, leading to more complex situations. The input signal coming from the cortex is likely composed of many frequency components and amplitudes, thus our consideration of only single and double frequency input is a simplification. Nevertheless, we discovered that large regions of 1:1 phase-locking are preserved for each frequency, and their impact on GPi units is maintained even within a noisy regime.

Finally, we consider the time taken to select different channels in the output GPi population. Physiologically, the switching time between different actions is thought to be in the order of hundreds of milliseconds [Anderson and Lebiere,

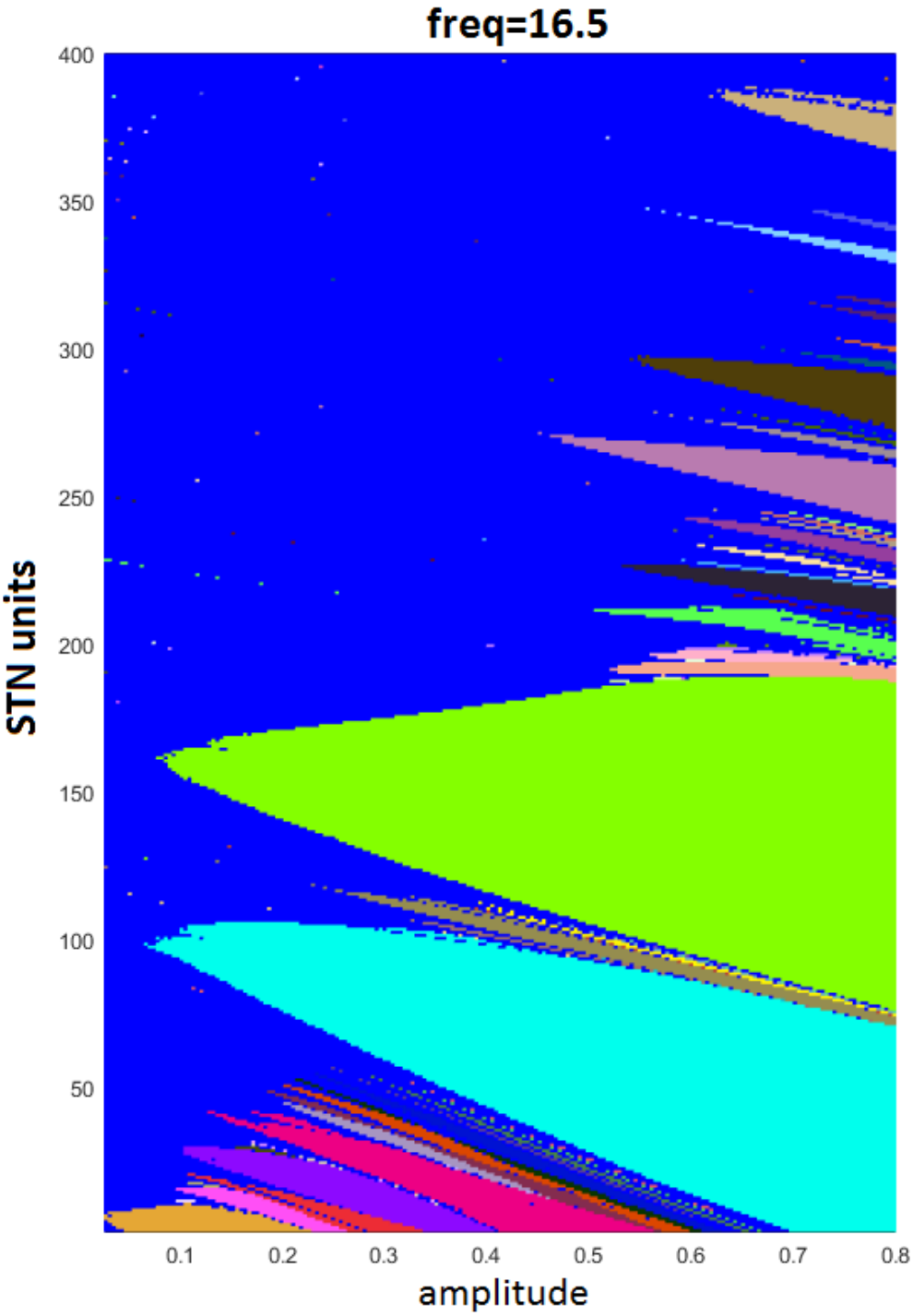

Figure 6.9: Two forcing frequencies Arnold's tongues bifurcation diagram. Values for p and q are computed from the definition of p:q phase-locked regions using each of the two frequency components. Only the Arnold tongues calculated in relation to the 16.5Hz is shown, as the figure for the 13.75Hz component in analogous.

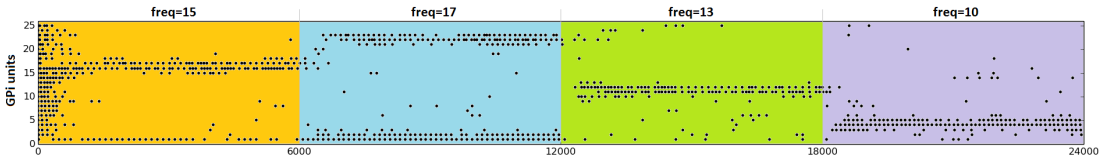

Figure 6.10: Changing selected channels by switching the forcing input. Each coloured region corresponds to a different input frequency, which changes every 6 seconds. The amplitude is fixed at 0.12 for the entire simulation time. In this simulation $(w_E^1, \tau_E^1) = (0.5, 0.16)$.

2003].

6.2.5 Multiple action switches

We investigated the effects of synaptic weights and decay time constants on the time taken to switch between sets of activated channels. Specifically, we varied the maximal weights and decay times for the excitatory synapses, and looked for changes in the action selection time. Figure 6.10 reproduces four different activated channel switches and each switch takes approximately 400ms, here we use the fixed coupling strength and decay time: $(w_E^1, \tau_E^1) = (0.5, 0.16)$.

6.2.6 Effect of increasing excitatory synaptic parameters on the switching time

Figure 6.11 demonstrates that increasing the maximum excitatory conductance and decay time of synapses decreases the switching time. The switching time was calculated as the first firing of the GPi units (having indexes in the set Ω) with closest intrinsic frequency to the switching forcing frequency in the deterministic case, so that sporadic situations caused by noise could be avoided. Moreover, in order to obtain a correct comparison, we maintained the same noise for different values of synaptic conductance and decay time. We define the vector of spike timings for each unit i (i.e. spike train) as spk_i, so that the formula used to calculate the switching time has the form:

$$t_{switch} = min_{i \in \Omega}(min_{t \geq tstop/2}(spk_i(t)))$$

6.3 Discussion

We are interested in oscillations arising in the firing rate of the neuronal activity of the basal ganglia, since experimental evidence has shown that excessive oscillatory synchronisation is positively correlated with the symptoms of Parkinson's disease [Holgado et al., 2010]. Moreover, oscillations are thought to play a fundamental role in the functional physiology of the basal ganglia [Joundi et al., 2012].

In the past, several computational models were developed that reproduced pathological oscillations in the basal ganglia. Different approaches showed how oscillations could be generated either intrinsically within the basal ganglia circuitry [Ebert et al., 2014, Terman et al., 2002] or extrinsically by an oscillatory input coming from an external source, such as the cortex. Experiments on rats by [Magill et al., 2001] suggest that increased low-frequency oscillations in the STN and GP are due to inappropriate processing of rhythmic cortical input. Ebert et al. [2014] included STN self-excitation in their model, but experimental evidence [Parent and Parent, 2007] shows that STN axonal arborisation is not self-targeted, but rather it projects into the globus pallidus (either external or internal part), the substantia nigra pars reticulata and the striatum. Terman et al. [2002] focused on the interplay between STN excitation on the GP and the back-inhibition on the STN from the GP and on the STN strong hyperpolarisation during back-inhibition.

Here we have presented a model in which an oscillatory cortical input partially synchronises unconnected STN neurons, and consequently selects different combinations of output channels in the GPi through excitation. Our results support the idea that the input coming from the cortex could be separated into multiple frequency components. The dominant components (higher amplitudes) would influence the STN by creating regions of partial synchronisation, and it

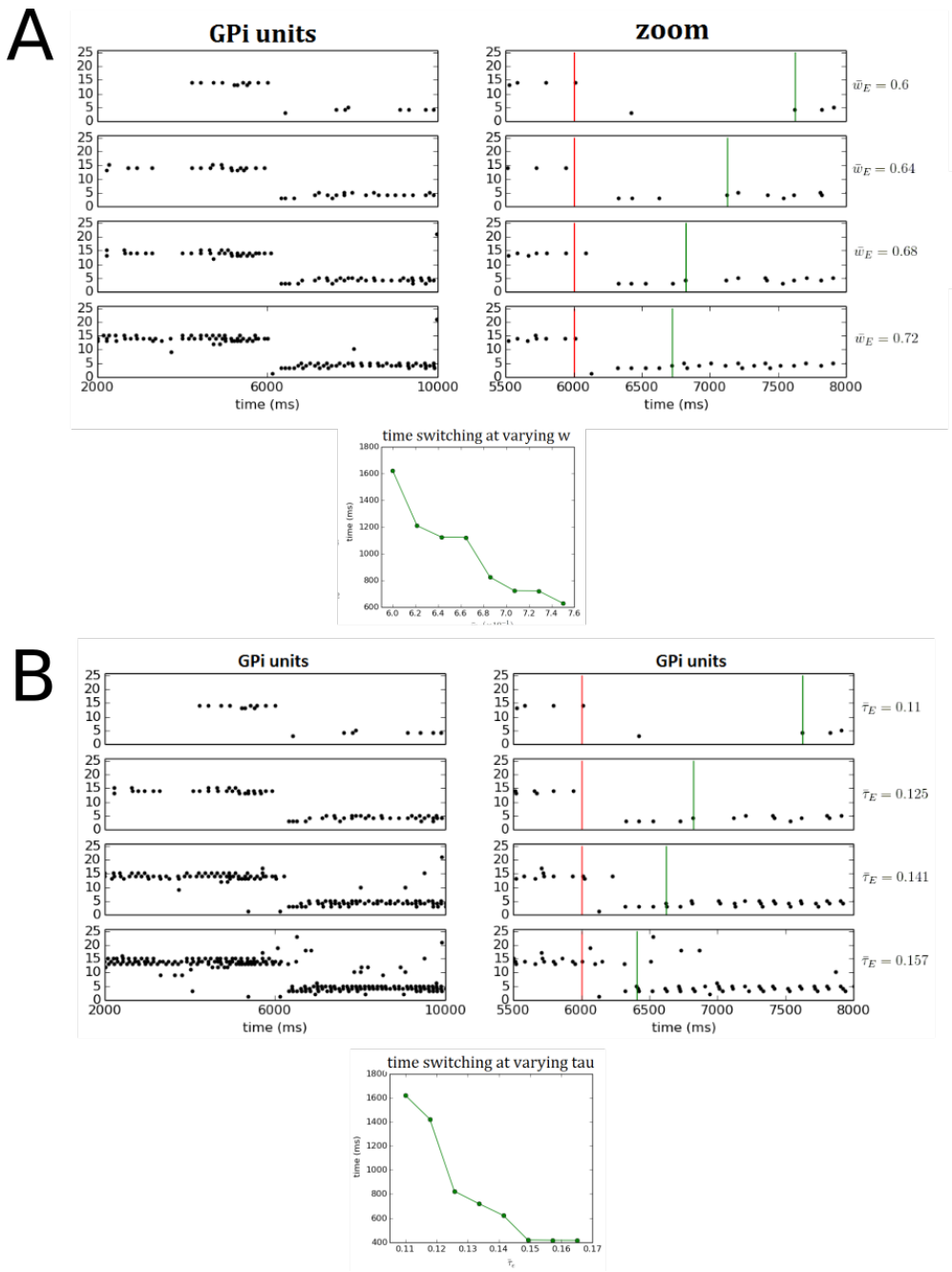

Figure 6.11: Decrease in the action selection switching time at increasing excitatory strength (A) and decay time (B). Conductance values w_E^1 vary in the interval [0.6, 0.75] with fixed maximal decay time 0.12. Decay times τ_E^1 vary in the interval [0.11, 0.165] with fixed maximal conductance 0.65. All simulations last 12s. The switch takes longer than a second with low w_E^1 and τ_E^1, but we can achieve realistic results increasing g_E and τ_E. Forcing amplitude is equal to 0.12 for the entire simulation, while the frequency switches from 14Hz to 10Hz at 6s. The set $\Omega = \{3\}$ contains the index of the GPi unit excited by most STN units. This unit has intrinsic frequency closer to 10Hz and it has been used to calculate the switching time.

would then activate a combinations of different channels on the output GP. We assumed the existence of inhibitory connections between GPi units, because there is evidence for self-inhibition in the GPe [Goldberg and Bergman, 2011] but similar data for the GPi is lacking. However, this feature is not a critical part of the model, and similar results can be achieved without it.

The switching time between different actions is strongly dependent on the synaptic strength and decay time, and we were able to find a proper set of parameters that fit the realistic switching time [Anderson and Lebiere, 2003]. Future development of the model could study how dopamine receptors influences the switching time of new actions and compare parkinsonian (lack of dopamine) conditions to healthy ones. Experimental evidence suggests that dopamine increases the activity of the inhibitory GPe projection on the STN [Kultas-Ilinsky and Ilinsky, 2012], and the activity in the STN neurons is consequently reduced [Magill et al., 2001]. According to Holgado et al. [2010], advanced Parkinson's disease increases specific synaptic weights in the basal ganglia, in particular the increase in the STN excitation towards the GP. According to this predictions our results would demonstrate that switching time of new actions would much be faster during the Parkinsonian state. Drastic increases of synaptic conductance and decay time lead to almost instantaneous switching. If we further increase the synaptic parameters (g_E^1 and τ_E^1), most GPi units get activated, and therefore we cannot clearly recognise which channels are selected. Thus Parkinsonian conditions may lead to critical values of synaptic strengths in which the selection of new actions are hardly processed by the brain. This finding may be related to the motor symptoms of the disease.

Oscillations may play a physiological role in the basal ganglia in terms of action selection and in Parkinson's disease, as shown by electrophysiologcal recordings (reviewed in the Introduction). Biologically realistic models of the basal ganglia could help to clarify the neuro-dynamical principles that regulate the

pathological activity, and they could be used to visualise the effects of treatment, which could provide aid to clinicians. Such studies can then allow one to explore how to minimise pathological activity and promote healthy activity. Our results show how computational modelling allows to test hypotheses on how physiological and pathological activity in the basal ganglia might arise. In the longer term, the understanding of the basal ganglia and PD that such models give us might permit even more advanced novel treatments to be developed.

Both experimental and theoretical studies strongly support a concept of oscillatory neural activity in the basal ganglia. Irregular and regular oscillations of different frequencies, synchronised, coherent and not synchronised can be observed both in healthy and pathological cases. The goal of computational modelling in this respect is to clarify the correspondence between oscillatory dynamics and the functional state, in both healthy or pathological conditions. These computational studies aim to reveal the neuronal mechanisms of movement and action selection in the healthy brain, to try to understand how these mechanisms go wrong in disease. Our modelling of oscillatory dynamics shows that partial synchronisation is a powerful theoretical approach and can be used for formulation of new theories on brain functioning. In particular, we demonstrate how partial synchronisation can be applied to model action coding and movement selection.

Chapter 7

Thesis contribution

A new method to generate and study pairwise neuronal connectivity: the probabilistic model Ferrario et al. [2018a]. In chapter 3, we define a new probabilistic meta-model to generate connections between neurons in the *Xenopus* tadpole swimming circuit using a previously developed anatomical model of connectivity (connectome) [Borisyuk et al., 2014, Roberts et al., 2014]. The probabilistic model generalises the structure of multiple variable anatomical connectomes and it shows proper neuronal activity patterns of swimming oscillations when mapped into the functional network. Using the probabilistic model we study the key structural and functional properties of tadpole networks generating this behaviour and we clarify some experimental findings. We suggest that the probabilistic model can be used to define connectivity in case of limited experimental data. In chapter 5 we demonstrate how this approach works: we use the probabilistic model to define the complete connectome of the expanded model where we combine CPG neurons and their connections with additional populations of sensory pathway cells (see below).

Mathematical theory helps to explain experimental relationship between synchrony and swimming regimes in tadpole Ferrario et al. [2018b]. In chapter 4 we use bifurcation analysis to study synchrony and swimming regimes observed in electrophysiological recordings. We built a reduced spiking neuronal model that incorporates the key operating principles of the *Xenopus* tadpole central pattern generator. This model generates all the experimentally-

observed outputs, including swimming and synchrony. We show that swimming is stable in a significantly larger range of parameters, and can be initiated more robustly, than synchrony. Moreover, the model can explain the experimental observation of synchrony appearance at the start of a swimming episode.

The first spiking neuronal model that accounts for the sensory initiation, modulation and termination of a whole animal's locomotor behaviour: the virtual tadpole (VT) Koutsikou et al. [2018]. In chapter 5 we expanded our previous anatomical, probabilistic and functional models of the swimming circuit [Roberts et al., 2014, Ferrario et al., 2018a] to include the sensory pathways. The VT model is based on multiple biological data which we use to reconstruct the connectivity and define dynamical properties of neurons and synapses. The model simulates a detailed and biologically plausible sequence of information processing events from the internal representation of different sensory inputs, integration and decision-making, action selection, and movement generation. We believe that the VT is the first spiking neuronal model that accounts for the sensory initiation, modulation and termination of a whole animal's behaviour and describes a significant part of the tadpole nervous system corresponding to movement initiation and control.

Study of partial synchronisation of neuronal activity in a model of action selection Merrison-Hort et al. [2017]. In chapter 6 we present a new spiking neuronal model of the basal ganglia and propose a plausible mechanism of action selection. This model supports the idea that the oscillatory input from the cortex to the basal ganglia could be represented as a superposition of a single or multiple components (channels) with fixed frequencies. The components with higher amplitudes will create regions of partial synchronization in the subthalamic nucleus (STN). We hypothesise that these partially synchronised STN regions represent some particular action. The model explains the switching between actions and relationship between synaptic strengths and switching times.

We show that the decreasing synaptic strength slows the switching times, a condition that may correspond to the motor impairments in Parkinson's disease.

The software that I developed during my PhD project is publicly available.

1. Probabilistic and functional models for reproducing the spiking activity of the tadpole spinal circuit in Neuron-Python language - the code be found in the following link Model DB.

2. I developed a PYTHON code that automatically converts XPPAUT files to FORTRAN-95 files of AUTO-07. This code can be used to run numerical continuation using AUTO-07 instead of the XPPAUT. The main advantage of using AUTO-07 instead of XPPAUT is that AUTO-07 uses multiple computer cores for parallelisation and drastically increases a speed of the numerical continuation in high-dimensional systems. Also, my code could be used by people that known how to write XPPAUT code, but have no experience with FORTRAN-95.

List of references

Eve Marder. Understanding brains: details, intuition, and big data. *PLoS biology*, 13(5):e1002147, 2015.

Eve Marder and Ronald L Calabrese. Principles of rhythmic motor pattern generation. *Physiological reviews*, 76(3):687–717, 1996.

Eric R Kandel, James H Schwartz, Thomas M Jessell, Department of Biochemistry, Molecular Biophysics Thomas Jessell, Steven Siegelbaum, and AJ Hudspeth. *Principles of neural science*, volume 4. McGraw-hill New York, 2000.

Arkady Pikovsky, Michael Rosenblum, Jurgen Kurths, and Jürgen Kurths. *Synchronization: a universal concept in nonlinear sciences*, volume 12. Cambridge university press, 2003.

Yakov Kazanovich and Roman Borisyuk. An oscillatory neural model of multiple object tracking. *Neural computation*, 18(6):1413–1440, 2006.

Hans Berger. Über das elektrenkephalogramm des menschen. *Archiv für psychiatrie und nervenkrankheiten*, 87(1):527–570, 1929.

György Buzsáki and Andreas Draguhn. Neuronal oscillations in cortical networks. *science*, 304(5679):1926–1929, 2004.

Christoph S Herrmann, Daniel Strüber, Randolph F Helfrich, and Andreas K Engel. Eeg oscillations: from correlation to causality. *International Journal of Psychophysiology*, 103:12–21, 2016.

Raphael Ritz and Terrence J Sejnowski. Synchronous oscillatory activity in sensory systems: new vistas on mechanisms. *Current opinion in neurobiology*, 7(4):536–546, 1997.

Wolf Singer. Synchronization of cortical activity and its putative role in information processing and learning. *Annual review of physiology*, 55(1):349–374, 1993.

Logan Voss and Jamie Sleigh. Monitoring consciousness: the current status of eeg-based depth of anaesthesia monitors. *Best practice & research Clinical anaesthesiology*, 21(3):313–325, 2007.

Andreas K Engel, Pascal Fries, and Wolf Singer. Dynamic predictions: oscillations and synchrony in top–down processing. *Nature Reviews Neuroscience*, 2(10):704, 2001.

Michael J Kahana, David Seelig, and Joseph R Madsen. Theta returns. *Current opinion in neurobiology*, 11(6):739–744, 2001.

Charles M Gray, Peter König, Andreas K Engel, and Wolf Singer. Oscillatory responses in cat visual cortex exhibit inter-columnar synchronization which reflects global stimulus properties. *Nature*, 338(6213):334, 1989.

Rodolfo Llinas and Urs Ribary. Coherent 40-hz oscillation characterizes dream state in humans. *Proceedings of the National Academy of Sciences*, 90(5): 2078–2081, 1993.

Erol Başar, Canan Başar-Eroglu, Sirel Karakaş, and Martin Schürmann. Gamma, alpha, delta, and theta oscillations govern cognitive processes. *International journal of psychophysiology*, 39(2-3):241–248, 2001.

Pascal Fries, John H Reynolds, Alan E Rorie, and Robert Desimone. Modulation of oscillatory neuronal synchronization by selective visual attention. *Science*, 291(5508):1560–1563, 2001.

Roman M Borisyuk and Yakov B Kazanovich. Oscillatory model of attention-guided object selection and novelty detection. *Neural Networks*, 17(7):899–915, 2004.

Peter Lakatos, George Karmos, Ashesh D Mehta, Istvan Ulbert, and Charles E Schroeder. Entrainment of neuronal oscillations as a mechanism of attentional selection. *science*, 320(5872):110–113, 2008.

James Rankin, Elyse Sussman, and John Rinzel. Neuromechanistic model of auditory bistability. *PLoS computational biology*, 11(11):e1004555, 2015.

DeLiang Wang and Peter Chang. An oscillatory correlation model of auditory streaming. *Cognitive Neurodynamics*, 2(1):7–19, 2008.

Francisco Varela, Jean-Philippe Lachaux, Eugenio Rodriguez, and Jacques Martinerie. The brainweb: phase synchronization and large-scale integration. *Nature reviews neuroscience*, 2(4):229, 2001.

RY Moore. Organization and function of a central nervous system circadian oscillator: the suprachiasmatic hypothalamic nucleus. In *Federation proceedings*, volume 42, pages 2783–2789, 1983.

Thomas B Schillen and Peter König. Binding by temporal structure in multiple feature domains of an oscillatory neuronal network. *Biological cybernetics*, 70 (5):397–405, 1994.

Andreas K Engel, Pascal Fries, Peter König, Michael Brecht, and Wolf Singer. Temporal binding, binocular rivalry, and consciousness. *Consciousness and cognition*, 8(2):128–151, 1999.

Wolf Singer and Charles M Gray. Visual feature integration and the temporal correlation hypothesis. *Annual review of neuroscience*, 18(1):555–586, 1995.

RM Borisyuk, GN Borisyuk, and YB Kazanovich. The synchronization principle in modelling of binding and attention. *Membrane & cell biology*, 11(6):753–761, 1998.

David Kahn, Edward F Pace-Schott, and J Allan Hobson. Consciousness in waking and dreaming: the roles of neuronal oscillation and neuromodulation in determining similarities and differences. *Neuroscience*, 78(1):13–38, 1997.

Mircea Steriade, David A McCormick, and Terrence J Sejnowski. Thalamocortical oscillations in the sleeping and aroused brain. *Science*, 262(5134): 679–685, 1993.

Sten Grillner and S Kashin. On the generation and performance of swimming in fish. In *Neural control of locomotion*, pages 181–201. Springer, 1976.

Alan Roberts, SR Soffe, ES Wolf, M Yoshida, and F-Y Zhao. Central circuits controlling locomotion in young frog tadpoles. *Annals of the New York Academy of Sciences*, 860(1):19–34, 1998.

Sten Grillner, Peter Wallén, Kazuya Saitoh, Alexander Kozlov, and Brita Robertson. Neural bases of goal-directed locomotion in vertebratesï£¡an overview. *Brain research reviews*, 57(1):2–12, 2008.

Martin Golubitsky, Ian Stewart, Pietro-Luciano Buono, and JJ Collins. Symmetry in locomotor central pattern generators and animal gaits. *Nature*, 401(6754): 693–695, 1999.

Eve Marder and Dirk Bucher. Central pattern generators and the control of rhythmic movements. *Current biology*, 11(23):R986–R996, 2001.

Yu I Arshavsky, GN Orlovsky, Yu V Panchin, Alan Roberts, and SR Soffe. Neuronal control of swimming locomotion: analysis of the pteropod mollusc clione and embryos of the amphibian xenopus. *Trends in neurosciences*, 16(6):227–233, 1993.

Milan R Dimitrijevic, Yuri Gerasimenko, and Michaela M Pinter. Evidence for a spinal central pattern generator in humans a. *Annals of the New York Academy of Sciences*, 860(1):360–376, 1998.

Sten Grillner. Biological pattern generation: the cellular and computational logic of networks in motion. *Neuron*, 52(5):751–766, 2006.

F James Eisenhart, Timothy W Cacciatore, and William B Kristan Jr. A central pattern generator underlies crawling in the medicinal leech. *Journal of Comparative Physiology A*, 186(7-8):631–643, 2000.

Eugene M Izhikevich. *Dynamical systems in neuroscience*. MIT press, 2007.

Peter Ashwin, Stephen Coombes, and Rachel Nicks. Mathematical frameworks for oscillatory network dynamics in neuroscience. *The Journal of Mathematical Neuroscience*, 6(1):2, 2016.

A.L. Hodgkin and A.F. Huxley. A quantitative description of membrane current and its application to conduction and excitation in nerve. *The Journal of physiology*, 117(4):500, 1952a.

E. M. Izhikevich. Simple model of spiking neurons. *IEEE Trans Neural Netw*, 14(6):1569–72, 2003.

Romain Brette and Wulfram Gerstner. Adaptive exponential integrate-and-fire model as an effective description of neuronal activity. *Journal of neurophysiology*, 94(5):3637–3642, 2005.

Leon Glass and Michael C Mackey. *From clocks to chaos: the rhythms of life*. Princeton University Press, 1988.

Leon Chua, Valery Sbitnev, and Hyongsuk Kim. Neurons are poised near the edge of chaos. *International Journal of Bifurcation and Chaos*, 22(04): 1250098, 2012.

Eugene M Izhikevich. Neural excitability, spiking and bursting. *International journal of bifurcation and chaos*, 10(06):1171–1266, 2000.

John Rinzel and G Bard Ermentrout. Analysis of neural excitability and oscillations. *Methods in neuronal modeling*, 2:251–292, 1998.

Stephen R Soffe, Alan Roberts, and Wen-Chang Li. Defining the excitatory neurons that drive the locomotor rhythm in a simple vertebrate: insights into the origin of reticulospinal control. *The Journal of physiology*, 587(20):4829–4844, 2009.

John Guckenheimer and Philip Holmes. *Nonlinear oscillations, dynamical systems, and bifurcations of vector fields*, volume 42. Springer Science & Business Media, 2013.

Yuri A Kuznetsov. *Elements of applied bifurcation theory*, volume 112. Springer Science & Business Media, 2013.

Andrey L Shilnikov and Nikolai F Rulkov. Subthreshold oscillations in a map-based neuron model. *Physics Letters A*, 328(2-3):177–184, 2004.

Xiao-Jing Wang and John Rinzel. Alternating and synchronous rhythms in reciprocally inhibitory model neurons. *Neural computation*, 4(1):84–97, 1992.

Steven M Baer, Thomas Erneux, and John Rinzel. The slow passage through a hopf bifurcation: delay, memory effects, and resonance. *SIAM Journal on Applied mathematics*, 49(1):55–71, 1989.

Mathieu Desroches, John Guckenheimer, Bernd Krauskopf, Christian Kuehn, Hinke M Osinga, and Martin Wechselberger. Mixed-mode oscillations with multiple time scales. *Siam Review*, 54(2):211–288, 2012.

Charles M Gray and David A McCormick. Chattering cells: superficial pyramidal neurons contributing to the generation of synchronous oscillations in the visual cortex. *Science*, 274(5284):109–113, 1996.

Robert J Butera Jr, John Rinzel, and Jeffrey C Smith. Models of respiratory rhythm generation in the pre-botzinger complex. i. bursting pacemaker neurons. *Journal of neurophysiology*, 82(1):382–397, 1999.

Krasimira Tsaneva-Atanasova, Hinke M Osinga, Thorsten Rieß, and Arthur Sherman. Full system bifurcation analysis of endocrine bursting models. *Journal of theoretical biology*, 264(4):1133–1146, 2010.

Maurice Gola and Allen Selverston. Ionic requirements for bursting activity in lobster stomatogastric neurons. *Journal of comparative physiology*, 145(2): 191–207, 1981.

Clayton T Dickson, Jacopo Magistretti, Mark H Shalinsky, Erik Fransén, Michael E Hasselmo, and Angel Alonso. Properties and role of i h in the pacing of subthreshold oscillations in entorhinal cortex layer ii neurons. *Journal of Neurophysiology*, 83(5):2562–2579, 2000.

Theodore Vo, Richard Bertram, Joel Tabak, and Martin Wechselberger. Mixed mode oscillations as a mechanism for pseudo-plateau bursting. *Journal of computational neuroscience*, 28(3):443–458, 2010.

Stephen Coombes and Paul C Bressloff. *Bursting: the genesis of rhythm in the nervous system*. World Scientific, 2005.

Martin Golubitsky, Kresimir Josic, and Tasso J Kaper. An unfolding theory approach to bursting in fast–slow systems. In *Global analysis of dynamical systems*, pages 282–313. CRC Press, 2001.

Allen I Selverston and Maurice Moulins. Oscillatory neural networks. *Annual review of physiology*, 47(1):29–48, 1985.

Roman Borisyuk. Oscillatory activity in the neural networks of spiking elements. *BioSystems*, 67(1-3):3–16, 2002.

Wen-Chang Li, Stephen R Soffe, Ervin Wolf, and Alan Roberts. Persistent responses to brief stimuli: feedback excitation among brainstem neurons. *Journal of Neuroscience*, 26(15):4026–4035, 2006.

KG Pearson and S Rossignol. Fictive motor patterns in chronic spinal cats. *Journal of neurophysiology*, 66(6):1874–1887, 1991.

David A McCrea and Ilya A Rybak. Organization of mammalian locomotor rhythm and pattern generation. *Brain research reviews*, 57(1):134–146, 2008.

Cornelia I Bargmann and Eve Marder. From the connectome to brain function. *Nature methods*, 10(6):483, 2013.

Frances K Skinner, Nancy Kopell, and Eve Marder. Mechanisms for oscillation and frequency control in reciprocally inhibitory model neural networks. *Journal of computational neuroscience*, 1(1-2):69–87, 1994.

Eve Marder and Adam L Taylor. Multiple models to capture the variability in biological neurons and networks. *Nature neuroscience*, 14(2):133, 2011.

Alan Roberts, Wen-Chang Li, and Stephen R Soffe. How neurons generate behaviour in a hatchling amphibian tadpole: an outline. *Frontiers in behavioral neuroscience*, 4:16, 2010.

Andrea Ferrario, Robert Merrison-Hort, Stephen R Soffe, and Roman Borisyuk. Structural and functional properties of a probabilistic model of neuronal connectivity in a simple locomotor network. *eLife*, 7:e33281, 2018a.

Alan Roberts, Deborah Conte, Mike Hull, Robert Merrison-Hort, Abul Kalam al Azad, Edgar Buhl, Roman Borisyuk, and Stephen R Soffe. Can simple rules control development of a pioneer vertebrate neuronal network generating behavior? *Journal of Neuroscience*, 34(2):608–621, 2014.

Bart Sautois, Stephen R Soffe, Wen-Chang Li, and Alan Roberts. Role of type-specific neuron properties in a spinal cord motor network. *Journal of computational neuroscience*, 23(1):59–77, 2007.

Stella Koutsikou, Robert Merrison-Hort, Edgar Buhl, Andrea Ferrario, Wen-Chang Li, Roman Borisyuk, Stephen R Soffe, and Alan Roberts. A simple decision to move in response to touch reveals basic sensory memory and mechanisms for variable response times. *The Journal of physiology*, 2018.

Wen-Chang Li, Tom Cooke, Bart Sautois, Stephen R Soffe, Roman Borisyuk, and Alan Roberts. Axon and dendrite geography predict the specificity of synaptic connections in a functioning spinal cord network. *Neural Development*, 2(1):17, 2007a.

Roman Borisyuk, Abul Kalam al Azad, Deborah Conte, Alan Roberts, and Stephen R Soffe. A developmental approach to predicting neuronal connectivity from small biological datasets: a gradient-based neuron growth model. *PLoS One*, 9(2):e89461, 2014.

Roman Borisyuk, Tom Cooke, and Alan Roberts. Stochasticity and functionality of neural systems: mathematical modelling of axon growth in the spinal cord of tadpole. *Biosystems*, 93(1-2):101–114, 2008.

Roman Borisyuk, Abul Kalam al Azad, Deborah Conte, Alan Roberts, and Stephen R Soffe. Modeling the connectome of a simple spinal cord. *Frontiers in neuroinformatics*, 5:20, 2011.

Oliver Davis, Robert Merrison-Hort, Stephen R Soffe, and Roman Borisyuk. Studying the role of axon fasciculation during development in a computational model of the xenopus tadpole spinal cord. *Scientific reports*, 7(1):13551, 2017.

Nicholas Dale. Experimentally derived model for the locomotor pattern generator in the xenopus embryo. *The Journal of Physiology*, 489(2):489–510, 1995.

Crawford IP Winlove and Alan Roberts. The firing patterns of spinal neurons: in situ patch-clamp recordings reveal a key role for potassium currents. *European Journal of Neuroscience*, 36(7):2926–2940, 2012.

A.L Hodgkin and A.F Huxley. Currents carried by sodium and potassium ions through the membrane of the giant axon of loligo. *Journal of Physiology*, 116: 449–472, 1952b.

Alan L Hodgkin and Andrew F Huxley. A quantitative description of membrane current and its application to conduction and excitation in nerve. *The Journal of physiology*, 117(4):500–544, 1952c.

C Morris and H Lecar. Voltage oscillations in the barnacle giant muscle fiber. *Biophysical Journal*, 35(1):193–213, 1981. ISSN 0006-3495. doi: 10.1016/S0006-3495(81)84782-0.

R FitzHugh. Impulses and physiological states in theoretical models of nerve membrane. *Biophysical Journal*, 1(6):445–466, 1961.

Wen-Chang Li, Alan Roberts, and Stephen R Soffe. Locomotor rhythm maintenance: electrical coupling among premotor excitatory interneurons in the brainstem and spinal cord of young xenopus tadpoles. *The Journal of physiology*, 587(8):1677–1693, 2009.

Alan Roberts. The function and role of two types of mechanoreceptive free-nerve endings in the head skin of amphibian embryos. *Journal of comparative physiology*, 135(4):341–348, 1980.

JD Clarke, BP Hayes, SP Hunt, and ALAN Roberts. Sensory physiology,

anatomy and immunohistochemistry of rohon-beard neurones in embryos of xenopus laevis. *The Journal of Physiology*, 348(1):511–525, 1984.

KM Boothby and A Roberts. Effects of site of tactile stimulation on the escape swimming responses of hatchling xenopus laevis embryos. *Journal of Zoology*, 235(1):113–125, 1995.

Alan Roberts. Conducted impulses in the skin of young tadpoles. *Nature*, 222 (5200):1265–1266, 1969.

Edgar Buhl, Alan Roberts, and Stephen R Soffe. The role of a trigeminal sensory nucleus in the initiation of locomotion. *The Journal of physiology*, 590(10): 2453–2469, 2012.

Edgar Buhl, Stephen R Soffe, and Alan Roberts. Sensory initiation of a coordinated motor response: synaptic excitation underlying simple decision-making. *The Journal of physiology*, 593(19):4423–4437, 2015.

Russell G Foster and Alan Roberts. The pineal eye inxenopus laevis embryos and larvae: A photoreceptor with a direct excitatory effect on behaviour. *Journal of comparative physiology*, 145(3):413–419, 1982.

Alan Roberts. Pineal eye and behaviour in xenopus tadpoles. *Nature*, 273 (5665):774–775, 1978.

D Jamieson and ALAN Roberts. Responses of young xenopus laevis tadpoles to light dimming: possible roles for the pineal eye. *Journal of Experimental Biology*, 203(12):1857–1867, 2000.

David Jamieson and Alan Roberts. A possible pathway connecting the photosensitive pineal eye to the swimming central pattern generator in young xenopus laevis tadpoles. *Brain, behavior and evolution*, 54(6):323–337, 1999.

Alan Roberts, NA Hill, and Robin Hicks. Simple mechanisms organise orientation of escape swimming in embryos and hatchling tadpoles of xenopus laevis. *Journal of Experimental Biology*, 203(12):1869–1885, 2000.

KATE M Boothby and Alan Roberts. The stopping response of xenopus laevis embryos: pharmacology and intracellular physiology of rhythmic spinal neurones and hindbrain neurones. *Journal of Experimental Biology*, 169(1): 65–86, 1992.

Alan Roberts and AR Blight. Anatomy, physiology and behavioural role of sensory nerve endings in the cement gland of embryonic xenopus. *Proc. R. Soc. Lond. B*, 192(1106):111–127, 1975.

Ray Perrins, Alison Walford, and Alan Roberts. Sensory activation and role of inhibitory reticulospinal neurons that stop swimming in hatchling frog tadpoles. *Journal of Neuroscience*, 22(10):4229–4240, 2002.

P Van Mier and HJ Ten Donkelaar. Early development of descending pathways from the brain stem to the spinal cord in xenopus laevis. *Anatomy and embryology*, 170(3):295–306, 1984.

Keith T Sillar and R Meldrum Robertson. Thermal activation of escape swimming in post-hatching xenopus laevis frog larvae. *Journal of Experimental Biology*, 212(15):2356–2364, 2009.

JONATHAN A Kahn and ALAN Roberts. The central nervous origin of the swimming motor pattern in embryos of xenopus laevis. *Journal of Experimental Biology*, 99(1):185–196, 1982a.

JA Kahn and Alan Roberts. Experiments on the central pattern generator for swimming in amphibian embryos. *Phil. Trans. R. Soc. Lond. B*, 296(1081): 229–243, 1982b.

SR Soffe, JD Clarke, and A Roberts. Activity of commissural interneurons in spinal cord of xenopus embryos. *Journal of Neurophysiology*, 51(6):1257–1267, 1984.

Wen-Chang Li, Robert Merrison-Hort, Hong-Yan Zhang, and Roman Borisyuk. The generation of antiphase oscillations and synchrony by a rebound-based vertebrate central pattern generator. *Journal of Neuroscience*, 34(17):6065–6077, 2014a.

Robert Merrison-Hort, Nada Yousif, Andrea Ferrario, and Roman Borisyuk. Oscillatory neural models of the basal ganglia for action selection in healthy and parkinsonian cases. In *Computational Neurology and Psychiatry*, pages 149–189. Springer, 2017.

Peter Redgrave, Tony J Prescott, and Kevin Gurney. The basal ganglia: a vertebrate solution to the selection problem? *Neuroscience*, 89(4):1009–1023, 1999.

Raed A Joundi, Ned Jenkinson, John-Stuart Brittain, Tipu Z Aziz, and Peter Brown. Driving oscillatory activity in the human cortex enhances motor performance. *Current Biology*, 22(5):403–407, 2012.

Nicolas Mallet, Alek Pogosyan, László F Márton, J Paul Bolam, Peter Brown, and Peter J Magill. Parkinsonian beta oscillations in the external globus pallidus and their relationship with subthalamic nucleus activity. *Journal of neuroscience*, 28(52):14245–14258, 2008.

Ned Jenkinson and Peter Brown. New insights into the relationship between dopamine, beta oscillations and motor function. *Trends in neurosciences*, 34 (12):611–618, 2011.

William D Hutchison, Jonathan O Dostrovsky, Judith R Walters, Richard Courtemanche, Thomas Boraud, Joshua Goldberg, and Peter Brown. Neuronal os-

cillations in the basal ganglia and movement disorders: evidence from whole animal and human recordings. *Journal of Neuroscience*, 24(42):9240–9243, 2004.

Lonneke ML De Lau and Monique MB Breteler. Epidemiology of parkinson's disease. *The Lancet Neurology*, 5(6):525–535, 2006.

Robert Merrison-Hort, Nada Yousif, Felix Njap, Ulrich G Hofmann, Oleksandr Burylko, and Roman Borisyuk. An interactive channel model of the basal ganglia: bifurcation analysis under healthy and parkinsonian conditions. *The Journal of Mathematical Neuroscience*, 3(1):14, 2013.

Garrett E Alexander and Michael D Crutcher. Functional architecture of basal ganglia circuits: neural substrates of parallel processing. *Trends in neurosciences*, 13(7):266–271, 1990.

David Williams, Marina Tijssen, Gerard Van Bruggen, Andries Bosch, Angelo Insola, Vincenzo Di Lazzaro, Paolo Mazzone, Antonio Oliviero, Angelo Quartarone, Hans Speelman, et al. Dopamine-dependent changes in the functional connectivity between basal ganglia and cerebral cortex in humans. *Brain*, 125 (7):1558–1569, 2002.

Joseph Jankovic. Parkinsonï£¡s disease: clinical features and diagnosis. *Journal of neurology, neurosurgery & psychiatry*, 79(4):368–376, 2008.

Fabian Chersi, Marco Mirolli, Giovanni Pezzulo, and Gianluca Baldassarre. A spiking neuron model of the cortico-basal ganglia circuits for goal-directed and habitual action learning. *Neural Networks*, 41:212–224, 2013.

Izhar Bar-Gad, Shlomo Elias, Eilon Vaadia, and Hagai Bergman. Complex locking rather than complete cessation of neuronal activity in the globus pallidus of a 1-methyl-4-phenyl-1, 2, 3, 6-tetrahydropyridine-treated primate in

response to pallidal microstimulation. *Journal of Neuroscience*, 24(33):7410–7419, 2004.

JL Perez Velazquez, R Guevara Erra, and Michael Rosenblum. The epileptic thalamocortical network is a macroscopic self-sustained oscillator: evidence from frequency-locking experiments in rat brains. *Scientific reports*, 5:8423, 2015.

Peter J Magill, J Paul Bolam, and Mark D Bevan. Relationship of activity in the subthalamic nucleus–globus pallidus network to cortical electroencephalogram. *Journal of Neuroscience*, 20(2):820–833, 2000.

PJ Magill, JP Bolam, and MD Bevan. Dopamine regulates the impact of the cerebral cortex on the subthalamic nucleus–globus pallidus network. *Neuroscience*, 106(2):313–330, 2001.

David Terman, Jonathan E Rubin, AC Yew, and CJ Wilson. Activity patterns in a model for the subthalamopallidal network of the basal ganglia. *Journal of Neuroscience*, 22(7):2963–2976, 2002.

Jonathan E Rubin and David Terman. High frequency stimulation of the subthalamic nucleus eliminates pathological thalamic rhythmicity in a computational model. *Journal of computational neuroscience*, 16(3):211–235, 2004.

Cameron C McIntyre and Philip J Hahn. Network perspectives on the mechanisms of deep brain stimulation. *Neurobiology of disease*, 38(3):329–337, 2010.

Mark D Humphries, Robert D Stewart, and Kevin N Gurney. A physiologically plausible model of action selection and oscillatory activity in the basal ganglia. *Journal of Neuroscience*, 26(50):12921–12942, 2006a.

David Willshaw, Zhaoping Li, et al. Subthalamic–pallidal interactions are critical in determining normal and abnormal functioning of the basal ganglia. *Pro-*

ceedings of the Royal Society of London B: Biological Sciences, 269(1491): 545–551, 2002.

Alejo J Nevado Holgado, John R Terry, and Rafal Bogacz. Conditions for the generation of beta oscillations in the subthalamic nucleus–globus pallidus network. *Journal of Neuroscience*, 30(37):12340–12352, 2010.

Alejo J Nevado-Holgado, Nicolas Mallet, Peter J Magill, and Rafal Bogacz. Effective connectivity of the subthalamic nucleus–globus pallidus network during parkinsonian oscillations. *The Journal of physiology*, 2014.

Olaf Sporns, Giulio Tononi, and Rolf Kötter. The human connectome: a structural description of the human brain. *PLoS computational biology*, 1(4):e42, 2005.

Mark EJ Newman. The structure and function of complex networks. *SIAM review*, 45(2):167–256, 2003.

Mark EJ Newman, Duncan J Watts, and Steven H Strogatz. Random graph models of social networks. *Proceedings of the National Academy of Sciences*, 99(suppl 1):2566–2572, 2002.

Réka Albert and Albert-László Barabási. Statistical mechanics of complex networks. *Reviews of modern physics*, 74(1):47, 2002.

Ed Bullmore and Olaf Sporns. Complex brain networks: graph theoretical analysis of structural and functional systems. *Nature Reviews Neuroscience*, 10 (3):186, 2009.

Marcus Kaiser. A tutorial in connectome analysis: topological and spatial features of brain networks. *Neuroimage*, 57(3):892–907, 2011.

Mikail Rubinov and Olaf Sporns. Complex network measures of brain connectivity: uses and interpretations. *Neuroimage*, 52(3):1059–1069, 2010.

Danielle S Bassett and Olaf Sporns. Network neuroscience. *Nature neuroscience*, 20(3):353, 2017.

Lav R Varshney, Beth L Chen, Eric Paniagua, David H Hall, and Dmitri B Chklovskii. Structural properties of the caenorhabditis elegans neuronal network. *PLoS computational biology*, 7(2):e1001066, 2011.

Marcus Kaiser and Claus C Hilgetag. Nonoptimal component placement, but short processing paths, due to long-distance projections in neural systems. *PLoS computational biology*, 2(7):e95, 2006.

Michael Stobb, Joshua M Peterson, Borbala Mazzag, and Ethan Gahtan. Graph theoretical model of a sensorimotor connectome in zebrafish. *PLoS One*, 7 (5):e37292, 2012.

Olaf Sporns, Christopher J Honey, and Rolf Kötter. Identification and classification of hubs in brain networks. *PloS one*, 2(10):e1049, 2007.

Marcel A de Reus and Martijn P van den Heuvel. Rich club organization and intermodule communication in the cat connectome. *Journal of Neuroscience*, 33(32):12929–12939, 2013.

Mark D Humphries, Kevin Gurney, and Tony J Prescott. The brainstem reticular formation is a small-world, not scale-free, network. *Proceedings of the Royal Society of London B: Biological Sciences*, 273(1585):503–511, 2006b.

Duncan J Watts and Steven H Strogatz. Collective dynamics of ï£¡small-worldï£¡networks. *nature*, 393(6684):440, 1998.

Emma K Towlson, Petra E Vértes, Sebastian E Ahnert, William R Schafer, and Edward T Bullmore. The rich club of the c. elegans neuronal connectome. *Journal of Neuroscience*, 33(15):6380–6387, 2013.

Sophie Achard, Raymond Salvador, Brandon Whitcher, John Suckling, and ED Bullmore. A resilient, low-frequency, small-world human brain functional network with highly connected association cortical hubs. *Journal of Neuroscience*, 26(1):63–72, 2006.

Victor M Eguiluz, Dante R Chialvo, Guillermo A Cecchi, Marwan Baliki, and A Vania Apkarian. Scale-free brain functional networks. *Physical review letters*, 94(1):018102, 2005.

Sreedevi Varier and Marcus Kaiser. Neural development features: Spatio-temporal development of the caenorhabditis elegans neuronal network. *PLoS computational biology*, 7(1):e1001044, 2011.

Réka Albert, Hawoong Jeong, and Albert-László Barabási. Error and attack tolerance of complex networks. *nature*, 406(6794):378, 2000.

Albert-László Barabási and Réka Albert. Emergence of scaling in random networks. *science*, 286(5439):509–512, 1999.

Hai-Bo Hu and Xiao-Fan Wang. Unified index to quantifying heterogeneity of complex networks. *Physica A: Statistical Mechanics and its Applications*, 387 (14):3769–3780, 2008.

Ernesto Estrada. Quantifying network heterogeneity. *Physical Review E*, 82(6): 066102, 2010.

SR Soffe. Roles of glycinergic inhibition and n-methyl-d-aspartate receptor mediated excitation in the locomotor rhythmicity of one half of the xenopus embryo central nervous system. *European Journal of Neuroscience*, 1(6):561–571, 1989.

DA Sprott. The method of maximum likelihood applied to the poisson binomal distribution. *Biometrics*, 14(1):97–106, 1958.

Robert Tarjan. Depth-first search and linear graph algorithms. *SIAM journal on computing*, 1(2):146–160, 1972.

Edsger W Dijkstra. A note on two problems in connexion with graphs. *Numerische mathematik*, 1(1):269–271, 1959.

Giorgio Fagiolo. Clustering in complex directed networks. *Physical Review E*, 76(2):026107, 2007.

Ed Bullmore and Olaf Sporns. The economy of brain network organization. *Nature Reviews Neuroscience*, 13(5):336, 2012.

Sergei Maslov and Kim Sneppen. Specificity and stability in topology of protein networks. *Science*, 296(5569):910–913, 2002.

Olaf Sporns and Rolf Kötter. Motifs in brain networks. *PLoS biology*, 2(11): e369, 2004.

Ron Milo, Shai Shen-Orr, Shalev Itzkovitz, Nadav Kashtan, Dmitri Chklovskii, and Uri Alon. Network motifs: simple building blocks of complex networks. *Science*, 298(5594):824–827, 2002.

Danielle S Bassett, Perry Zurn, and Joshua I Gold. On the nature and use of models in network neuroscience. *Nature Reviews Neuroscience*, page 1, 2018.

Nicholas T Carnevale and Michael L Hines. *The NEURON book*. Cambridge University Press, 2006.

Avis H Cohen, Philip J Holmes, and Richard H Rand. The nature of the coupling between segmental oscillators of the lamprey spinal generator for locomotion: a mathematical model. *Journal of mathematical biology*, 13(3):345–369, 1982.

Qawi K Telesford, Karen E Joyce, Satoru Hayasaka, Jonathan H Burdette, and Paul J Laurienti. The ubiquity of small-world networks. *Brain connectivity*, 1 (5):367–375, 2011.

Marco Iosa, Leonardo Gizzi, Federica Tamburella, and Nadia Dominici. Neuromotor control and feed-forward models of locomotion in humans. *Frontiers in human neuroscience*, 9:306, 2015.

JA Kahn and A Roberts. The neuromuscular basis of rhythmic struggling movements in embryos of xenopus laevis. *Journal of Experimental Biology*, 99(1): 197–205, 1982c.

Sen Song, Per Jesper Sjöström, Markus Reigl, Sacha Nelson, and Dmitri B Chklovskii. Highly nonrandom features of synaptic connectivity in local cortical circuits. *PLoS biology*, 3(3):e68, 2005.

Olaf Sporns and Jonathan D Zwi. The small world of the cerebral cortex. *Neuroinformatics*, 2(2):145–162, 2004.

Rolf Kötter. Online retrieval, processing, and visualization of primate connectivity data from the cocomac database. *Neuroinformatics*, 2(2):127–144, 2004.

Timothy D Wiggin, Tatiana M Anderson, John Eian, Jack H Peck, and Mark A Masino. Episodic swimming in the larval zebrafish is generated by a spatially distributed spinal network with modular functional organization. *Journal of neurophysiology*, 108(3):925–934, 2012.

John G White, Eileen Southgate, J Nichol Thomson, and Sydney Brenner. The structure of the nervous system of the nematode caenorhabditis elegans. *Philos Trans R Soc Lond B Biol Sci*, 314(1165):1–340, 1986.

G Rizzolatti, M Matelli, and G Pavesi. Deficits in attention and movement following the removal of postarcuate (area 6) and prearcuate (area 8) cortex in macaque monkeys. *Brain*, 106(3):655–673, 1983.

W-C Li, Shin-ichi Higashijima, DM Parry, Alan Roberts, and SR Soffe. Primitive roles for inhibitory interneurons in developing frog spinal cord. *Journal of Neuroscience*, 24(25):5840–5848, 2004a.

Wen-Chang Li, Alan Roberts, and Stephen R Soffe. Specific brainstem neurons switch each other into pacemaker mode to drive movement by activating nmda receptors. *Journal of Neuroscience*, 30(49):16609–16620, 2010.

Michael J Hull, Stephen R Soffe, David J Willshaw, and Alan Roberts. Modelling feedback excitation, pacemaker properties and sensory switching of electrically coupled brainstem neurons controlling rhythmic activity. *PLoS computational biology*, 12(1):e1004702, 2016.

SR Soffe. Two distinct rhythmic motor patterns are driven by common premotor and motor neurons in a simple vertebrate spinal cord. *Journal of Neuroscience*, 13(10):4456–4469, 1993.

Wen-Chang Li, Bart Sautois, Alan Roberts, and Stephen R Soffe. Reconfiguration of a vertebrate motor network: specific neuron recruitment and context-dependent synaptic plasticity. *Journal of Neuroscience*, 27(45):12267–12276, 2007b.

Ervin Wolf, Steffen R Soffe, and Alan Roberts. Longitudinal neuronal organization and coordination in a simple vertebrate: a continuous, semi-quantitative computer model of the central pattern generator for swimming in young frog tadpoles. *Journal of computational neuroscience*, 27(2):291–308, 2009.

Tom Binzegger, Rodney J Douglas, and Kevan AC Martin. A quantitative map of the circuit of cat primary visual cortex. *Journal of Neuroscience*, 24(39): 8441–8453, 2004.

Chi-Wen Lin, Hsuan-Wen Lin, Mei-Tzu Chiu, Yung-Hsin Shih, Ting-Yuan Wang, Hsiu-Ming Chang, and Ann-Shyn Chiang. Automated in situ brain imaging for

mapping the drosophila connectome. *Journal of neurogenetics*, 29(4):157–168, 2015.

Chi-Tin Shih, Olaf Sporns, Shou-Li Yuan, Ta-Shun Su, Yen-Jen Lin, Chao-Chun Chuang, Ting-Yuan Wang, Chung-Chuang Lo, Ralph J Greenspan, and Ann-Shyn Chiang. Connectomics-based analysis of information flow in the drosophila brain. *Current Biology*, 25(10):1249–1258, 2015.

H Sebastian Seung and Uygar Sümbül. Neuronal cell types and connectivity: lessons from the retina. *Neuron*, 83(6):1262–1272, 2014.

Jinseop S Kim, Matthew J Greene, Aleksandar Zlateski, Kisuk Lee, Mark Richardson, Srinivas C Turaga, Michael Purcaro, Matthew Balkam, Amy Robinson, Bardia F Behabadi, et al. Space–time wiring specificity supports direction selectivity in the retina. *Nature*, 509(7500):331, 2014.

Sebastian Seung. *Connectome: How the brain's wiring makes us who we are*. HMH, 2012.

Roman Bauer, Frederic Zubler, Andreas Hauri, Dylan R Muir, and Rodney J Douglas. Developmental origin of patchy axonal connectivity in the neocortex: a computational model. *Cerebral Cortex*, 24(2):487–500, 2012.

Danielle S Bassett and Edward T Bullmore. Small-world brain networks revisited. *The Neuroscientist*, 23(5):499–516, 2017.

Frederic Zubler and Rodney Douglas. A framework for modeling the growth and development of neurons and networks. *Frontiers in computational neuroscience*, 3:25, 2009.

Auke Jan Ijspeert. Central pattern generators for locomotion control in animals and robots: a review. *Neural networks*, 21(4):642–653, 2008.

D Combes, SD Merrywest, J Simmers, and KT Sillar. Developmental segregation of spinal networks driving axial-and hindlimb-based locomotion in metamorphosing xenopus laevis. *The Journal of physiology*, 559(1):17–24, 2004.

Patsy S Dickinson, Carol Mecsas, and Eve Marder. Neuropeptide fusion of two motor-pattern generator circuits. *Nature*, 344(6262):155, 1990.

Kevin L Briggman and William B Kristan. Imaging dedicated and multifunctional neural circuits generating distinct behaviors. *Journal of Neuroscience*, 26(42): 10925–10933, 2006.

Kevin L Briggman and WB Kristan Jr. Multifunctional pattern-generating circuits. *Annu. Rev. Neurosci.*, 31:271–294, 2008.

Alan Roberts, W-C Li, SR Soffe, and Ervin Wolf. Origin of excitatory drive to a spinal locomotor network. *Brain research reviews*, 57(1):22–28, 2008.

Alan Roberts, N Dale, and SR Soffe. Sustained responses to brief stimuli: Swimming in xenopus embryos. *Journal of Experimental Biology*, 112(1): 321–335, 1984.

Alan Roberts and MJ Tunstall. Mutual re-excitation with post-inhibitory rebound: a simulation study on the mechanisms for locomotor rhythm generation in the spinal cord of xenopus embryos. *European Journal of Neuroscience*, 2(1): 11–23, 1990.

Yaroslav I Molkov, Bartholomew J Bacak, Adolfo E Talpalar, and Ilya A Rybak. Mechanisms of left-right coordination in mammalian locomotor pattern generation circuits: a mathematical modeling view. *PLoS computational biology*, 11(5):e1004270, 2015.

Carlo R Laing and Carson C Chow. A spiking neuron model for binocular rivalry. *Journal of computational neuroscience*, 12(1):39–53, 2002.

Eusebius J Doedel, Thomas F Fairgrieve, Björn Sandstede, Alan R Champneys, Yuri A Kuznetsov, and Xianjun Wang. Auto-07p: Continuation and bifurcation software for ordinary differential equations. 2007.

Bard Ermentrout. *Simulating, analyzing, and animating dynamical systems: a guide to XPPAUT for researchers and students*, volume 14. Siam, 2002.

Michael J Hull, Stephen R Soffe, David J Willshaw, and Alan Roberts. Modelling the effects of electrical coupling between unmyelinated axons of brainstem neurons controlling rhythmic activity. *PLoS computational biology*, 11 (5):e1004240, 2015.

James D Angstadt, Jeffrey L Grassmann, Kraig M Theriault, and Sarah M Levasseur. Mechanisms of postinhibitory rebound and its modulation by serotonin in excitatory swim motor neurons of the medicinal leech. *Journal of comparative physiology A*, 191(8):715–732, 2005.

Alain Destexhe, Zachary F Mainen, and Terrence J Sejnowski. Kinetic models of synaptic transmission. *Methods in neuronal modeling*, 2:1–25, 1998.

Alan Roberts, JA Kahn, SR Soffe, and JDW Clarke. Neural control of swimming in a vertebrate. *Science*, pages 1032–1034, 1981.

SR Soffe and Alan Roberts. Activity of myotomal motoneurons during fictive swimming in frog embryos. *Journal of neurophysiology*, 48(6):1274–1278, 1982.

Wen-Chang Li and Peter R Moult. The control of locomotor frequency by excitation and inhibition. *Journal of Neuroscience*, 32(18):6220–6230, 2012.

Yu A Kuznetsov, Hil GE Meijer, and Lennaert van Veen. The fold-flip bifurcation. *International Journal of Bifurcation and Chaos*, 14(07):2253–2282, 2004.

Jeremy Wojcik, Justus Schwabedal, Robert Clewley, and Andrey L Shilnikov. Key bifurcations of bursting polyrhythms in 3-cell central pattern generators. *PloS one*, 9(4):e92918, 2014.

Gennady S Cymbalyuk, Quentin Gaudry, Mark A Masino, and Ronald L Calabrese. Bursting in leech heart interneurons: cell-autonomous and network-based mechanisms. *Journal of Neuroscience*, 22(24):10580–10592, 2002.

Matteo Lodi, Andrey Shilnikov, and Marco Storace. Cepage: A toolbox for central pattern generator analysis. In *Circuits and Systems (ISCAS), 2017 IEEE International Symposium on*, pages 1–4. IEEE, 2017.

Simon M Danner, Simon D Wilshin, Natalia A Shevtsova, and Ilya A Rybak. Central control of interlimb coordination and speed-dependent gait expression in quadrupeds. *The Journal of physiology*, 594(23):6947–6967, 2016.

Thomas B Kepler, LF Abbott, and Eve Marder. Reduction of conductance-based neuron models. *Biological Cybernetics*, 66(5):381–387, 1992.

Jonathan E Rubin, Natalia A Shevtsova, G Bard Ermentrout, Jeffrey C Smith, and Ilya A Rybak. Multiple rhythmic states in a model of the respiratory central pattern generator. *Journal of Neurophysiology*, 101(4):2146–2165, 2009.

Matteo Lodi, Andrey Shilnikov, and Marco Storace. Design of synthetic central pattern generators producing desired quadruped gaits. *IEEE Transactions on Circuits and Systems I: Regular papers*, 65(3):1028–1039, 2018.

Xin Jin and Rui M Costa. Start/stop signals emerge in nigrostriatal circuits during sequence learning. *Nature*, 466(7305):457, 2010.

D James Surmeier. Neuroscience: to go or not to go. *Nature*, 494(7436):178, 2013.

Nicolas Roussel, Christine A Morton, Fern P Finger, and Badrinath Roysam. A computational model for c. elegans locomotory behavior: application to multiworm tracking. *IEEE transactions on biomedical engineering*, 54(10):1786–1797, 2007.

Örjan Ekeberg. A combined neuronal and mechanical model of fish swimming. *Biological cybernetics*, 69(5-6):363–374, 1993.

Ulrich Bässler and Ansgar Büschges. Pattern generation for stick insect walking movements-multisensory control of a locomotor program. *Brain Research Reviews*, 27(1):65–88, 1998.

Holk Cruse, Thomas Kindermann, Michael Schumm, Jeffrey Dean, and Josef Schmitz. WalknetâĂŤa biologically inspired network to control six-legged walking. *Neural networks*, 11(7-8):1435–1447, 1998.

William B Kristan. Neuronal decision-making circuits. *Current Biology*, 18(19): R928–R932, 2008.

Roman Borisyuk, Robert Merrison-Hort, Steve R Soffe, Stella Koutsikou, and Wen-Chang Li. To swim or not to swim: A population-level model of xenopus tadpole decision making and locomotor behaviour. *BioSystems*, 161:3–14, 2017.

Wen-Chang Li. Generation of locomotion rhythms without inhibition in vertebrates: the search for pacemaker neurons, 2011.

Keith T Sillar and Alan Roberts. A neuronal mechanism for sensory gating during locomotion in a vertebrate. *Nature*, 331(6153):262, 1988.

Wen-Chang Li, Stephen R Soffe, and Alan Roberts. The spinal interneurons and properties of glutamatergic synapses in a primitive vertebrate cutaneous flexion reflex. *Journal of Neuroscience*, 23(27):9068–9077, 2003.

W-C Li, Stephen R Soffe, and Alan Roberts. Dorsal spinal interneurons forming a primitive, cutaneous sensory pathway. *Journal of neurophysiology*, 92(2): 895–904, 2004b.

Henri Korn and Donald S Faber. The mauthner cell half a century later: a neurobiological model for decision-making? *Neuron*, 47(1):13–28, 2005.

Wen-Chang Li, Monica Wagner, and Nicola J Porter. Behavioral observation of xenopus tadpole swimming for neuroscience labs. *Journal of Undergraduate Neuroscience Education*, 12(2):A107, 2014b.

BP Hayes and Alan Roberts. The anatomy of two functional types of mechanoreceptive'free'nerve-ending in the head skin of xenopus embryos. *Proc. R. Soc. Lond. B*, 218(1210):61–76, 1983.

Alan Roberts and Keith T Sillar. Characterization and function of spinal excitatory interneurons with commissural projections in xenopus laevis embryos. *European Journal of Neuroscience*, 2(12):1051–1062, 1990.

W-C Li, R Perrins, SR Soffe, M Yoshida, A Walford, and Alan Roberts. Defining classes of spinal interneuron and their axonal projections in hatchling xenopus laevis tadpoles. *Journal of Comparative Neurology*, 441(3):248–265, 2001.

Andreas Mayer. Noisyopt: A python library for optimizing noisy functions. *Journal of Open Source Software*, 2, 2017.

Daniel Durstewitz, Jeremy K Seamans, and Terrence J Sejnowski. Neurocomputational models of working memory. *Nature neuroscience*, 3(11s):1184, 2000.

W-C Li, SR Soffe, and Alan Roberts. Spinal inhibitory neurons that modulate cutaneous sensory pathways during locomotion in a simple vertebrate. *Journal of Neuroscience*, 22(24):10924–10934, 2002.

Alan Roberts, N Dale, WH Evoy, and SR Soffe. Synaptic potentials in motoneurons during fictive swimming in spinal xenopus embryos. *Journal of Neurophysiology*, 54(1):1–10, 1985.

N Dale and ALAN Roberts. Excitatory amino acid receptors in xenopus embryo spinal cord and their role in the activation of swimming. *The Journal of Physiology*, 348(1):527–543, 1984.

Keith T Sillar and Alan Roberts. The role of premotor interneurons in phase-dependent modulation of a cutaneous reflex during swimming in xenopus laevis embryos. *Journal of Neuroscience*, 12(5):1647–1657, 1992.

Nicholas Dale and Deborah Gilday. Regulation of rhythmic movements by purinergic neurotransmitters in frog embryos. *Nature*, 383(6597):259, 1996.

Nicholas Dale. Coordinated motor activity in simulated spinal networks emerges from simple biologically plausible rules of connectivity. *Journal of computational neuroscience*, 14(1):55–70, 2003.

Nicholas Dale. Resetting intrinsic purinergic modulation of neural activity: an associative mechanism? *Journal of Neuroscience*, 22(23):10461–10469, 2002.

Nicholas Dale. Delayed production of adenosine underlies temporal modulation of swimming in frog embryo. *The Journal of physiology*, 511(1):265–272, 1998.

H Bergman, T Wichmann, B Karmon, and MR DeLong. The primate subthalamic nucleus. ii. neuronal activity in the mptp model of parkinsonism. *Journal of neurophysiology*, 72(2):507–520, 1994.

Lars Timmermann and Esther Florin. Parkinson's disease and pathological oscillatory activity: is the beta band the bad guy?ï£¡new lessons learned from low-frequency deep brain stimulation. *Experimental neurology*, 233(1):123–125, 2012.

Steven H Strogatz. *Nonlinear dynamics and chaos: with applications to physics, biology, chemistry, and engineering*. CRC Press, 2018.

Michael Hines, Andrew P Davison, and Eilif Muller. Neuron and python. *Frontiers in neuroinformatics*, 3:1, 2009.

John R Anderson and Christian Lebiere. The newell test for a theory of cognition. *Behavioral and brain Sciences*, 26(5):587–601, 2003.

Martin Ebert, Christian Hauptmann, and Peter A Tass. Coordinated reset stimulation in a large-scale model of the stn-gpe circuit. *Frontiers in computational neuroscience*, 8:154, 2014.

Martin Parent and André Parent. The microcircuitry of primate subthalamic nucleus. *Parkinsonism & related disorders*, 13:S292–S295, 2007.

Joshua A Goldberg and Hagai Bergman. Computational physiology of the neural networks of the primate globus pallidus: function and dysfunction. *Neuroscience*, 198:171–192, 2011.

Kristy Kultas-Ilinsky and Igor A Ilinsky. *Basal Ganglia and Thalamus in health and movement disorders*. Springer Science & Business Media, 2012.

Andrea Ferrario, Robert Merrison-Hort, Stephen R Soffe, Wen-Chang Li, and Roman Borisyuk. Bifurcations of limit cycles in a reduced model of the xenopus tadpole central pattern generator. *The Journal of Mathematical Neuroscience*, 8(1):10, 2018b.